International Journal of Navigation and Observation

Future GNSS Signals

Guest Editors: Olivier Julien, Gérard Lachapelle, and Letizia Lo Presti

Future GNSS Signals

International Journal of Navigation and Observation

Future GNSS Signals

Guest Editors: Olivier Julien, Gérard Lachapelle,
and Letizia Lo Presti

Contents

Future GNSS Signals, Olivier Julien, Gérard Lachapelle, and Letizia Lo Presti
Volume 2008, Article ID 683242, 1 page

Experimental Results for the Multipath Performance of Galileo Signals Transmitted by GIOVE-A Satellite, Andrew Simsky, David Mertens, Jean-Marie Sleewaegen, Martin Hollreiser, and Massimo Crisci
Volume 2008, Article ID 416380, 13 pages

Multiple Gate Delay Tracking Structures for GNSS Signals and Their Evaluation with Simulink, SystemC, and VHDL, Heikki Hurskainen, Elena Simona Lohan, Xuan Hu, Jussi Raasakka, and Jari Nurmi
Volume 2008, Article ID 785695, 17 pages

Data and Pilot Combining for Composite GNSS Signal Acquisition, Daniele Borio and Letizia Lo Presti
Volume 2008, Article ID 738183, 12 pages

Design of Short Synchronization Codes for Use in Future GNSS System, Surendran K. Shanmugam, Cécile Mongrédien, John Nielsen, and Gérard Lachapelle
Volume 2008, Article ID 246703, 14 pages

Joint L-/C-Band Code and Carrier Phase Linear Combinations for Galileo, Patrick Henkel and Christoph Günther
Volume 2008, Article ID 651437, 8 pages

Bayesian Time Delay Estimation of GNSS Signals in Dynamic Multipath Environments, Michael Lentmaier, Bernhard Krach, and Patrick Robertson
Volume 2008, Article ID 372651, 11 pages

Comparison between Galileo CBOC Candidates and BOC(1,1) in Terms of Detection Performance, Fabio Dovis, Letizia Lo Presti, Maurizio Fantino, Paolo Mulassano, and Jérémie Godet
Volume 2008, Article ID 793868, 9 pages

Hindawi Publishing Corporation
International Journal of Navigation and Observation
Volume 2008, Article ID 683242, 1 page
doi:10.1155/2008/683242

Editorial

Future GNSS Signals

Olivier Julien,[1] Gérard Lachapelle,[2] and Letizia Lo Presti[3]

[1] *Signal Processing and Telecommunications Laboratory, École National de L'Aviation Civile (ENAC),*
31055 Toulouse, France
[2] *Department of Geomatics Engineering, University of Calgary, Calgary, AB, Canada T2N 1N4*
[3] *Dipartimento di Elettronica, Politecnico di Torino, 10129 Torino, Italy*

Correspondence should be addressed to Gérard Lachapelle, gerard.lachapelle@ucalgary.ca

Received 15 April 2008; Accepted 20 April 2008

This special issue of the International Journal of Navigation and Observation deals with future global navigation satellite system (GNSS) signals. It is a timely issue in view of the current US GPS modernization efforts, the deployment of the EU's Galileo, the replenishment of Russia's GLONASS, and China's plan to launch COMPASS. These systems, either individually or as a group, will provide tremendous availability, accuracy, and reliability enhancements to a consumer's market that is growing at an annual double-digit rate. Research is taking place not only to enhance the methods and algorithms to process the signals already in place but also to propose and optimize future signals and combinations thereof.

The seven papers presented in this issue cover a variety of topics, ranging from Galileo signal testing to signal multipath reduction, and represent a good cross-section of current activities in this area. A study of multipath performance of the initial Galileo signals transmitted by the GIOVE-A satellite using actual data is described by Simsky et al., and a new generic approach called multiple gate delay tracking structures to reduce GNSS signal multipath is proposed and evaluated with different software approaches by Heikki Hurskainen et al. Also, Borio et al. discuss two strategies for the joint acquisition of data and pilot channels that are available on emerging signals. Shanmugam et al. present a short synchronization code design for future GNSS based on the optimization of specific performance criteria. Joint L/C-band code and carrier phase linear combination methods for Galileo are discussed by Henkel et al. Moreover, Lentmaier et al. discuss Bayesian time delay estimation based on particle filters for use in dynamic multipath environments. Finally, a comparison between Galileo CBOC candidates and BOC(1,1) signals in terms of detection performance is presented by Dovis et al.

Olivier Julien
Gérard Lachapelle
Letizia Lo Presti

Hindawi Publishing Corporation
International Journal of Navigation and Observation
Volume 2008, Article ID 416380, 13 pages
doi:10.1155/2008/416380

Research Article

Experimental Results for the Multipath Performance of Galileo Signals Transmitted by GIOVE-A Satellite

Andrew Simsky,[1] David Mertens,[1] Jean-Marie Sleewaegen,[1] Martin Hollreiser,[2] and Massimo Crisci[2]

[1] *Septentrio, Ubicenter, Philipssite 5, Leuven 3001, Belgium*
[2] *The European Space Research and Technology Centre, The European Space Agency, Keplerlaan 1, Postbus 299, 2200 AG Noordwijk, The Netherlands*

Correspondence should be addressed to Andrew Simsky, a.simsky@septentrio.com

Received 6 July 2007; Accepted 17 March 2008

Recommended by Olivier Julien

Analysis of GIOVE-A signals is an important part of the in-orbit validation phase of the Galileo program. GIOVE-A transmits the ranging signals using all the code modulations currently foreseen for the future Galileo and provides a foretaste of their performance in real-life applications. Due to the use of advanced code modulations, the ranging signals of Galileo provide significant improvement of the multipath performance as compared to current GPS. In this paper, we summarize the results of about 1.5 years of observations using the data from four antenna sites. The analysis of the elevation dependence of averaged multipath errors and the multipath time series for static data indicate significant suppression of long-range multipath by the best Galileo codes. The E5AltBOC signal is confirmed to be a multipath suppression champion for all the data sets. According to the results of the observations, the Galileo signals can be classified into 3 groups: high-performance (E5AltBOC, L1A, E6A), medium-performance (E6BC, E5a, E5b) and an L1BC signal, which has the lowest performance among Galileo signals, but is still better than GPS-CA. The car tests have demonstrated that for kinematic multipath the intersignal differences are a lot less pronounced. The phase multipath performance is also discussed.

1. INTRODUCTION

The first Galileo signals were transmitted on January 12, 2006, by the GIOVE-A satellite. The first results for the tracking noise, signal power, and code multipath performance of the live GIOVE-A signal obtained with the use of Septentrio's GETR receiver have been presented in October 2006 [1]. The overview of the on-going GIOVE-A signal experimentation activity including results obtained at ESA, Septentrio NV, and Alcatel Alenia Space can be found in [2]. Results of GIOVE-A signal testing have also been reported in [3, 4].

The purpose of the current paper is to summarize the analysis of the multipath performance of the GIOVE-A signal performed at Septentrio since the beginning of the GIOVE-A mission up to the time of this publication that is during the first one and half years of the satellite operation. Estimations of code multipath errors specific to ranging signals are of particular interest to the user community because they make significant contribution to the error budget of user applications. Unlike many other error sources, multipath errors are essentially modulation-dependent, hence there is a significant interest to improving multipath performance by optimizing the signal definition.

The ranging signals of Galileo are based on advanced code modulation schemes, which are expected to provide significant improvement of the tracking and multipath performance as compared to the current GPS. With the advent of GIOVE-A these expectations have been verified. The first analysis [1] has clearly shown the advantages of the Galileo signals in comparison to current civilian signals of GPS (C/A and L2C). Further experience based on a wider array of data has confirmed these results. In this paper, we summarize the results from a number of data sets obtained at few antenna sites at different geographic locations as well as the results of kinematic tests in different environments.

The GIOVE-A transmits ranging signals using all the currently foreseen Galileo modulations: L1BC, L1A, E5a, E5b, E5 (or E5AltBOC), E6BC, and E6A [1, 5]. The GETR receiver has been custom-built by Septentrio for the reception of GIOVE signals. The GETR is capable of tracking all the

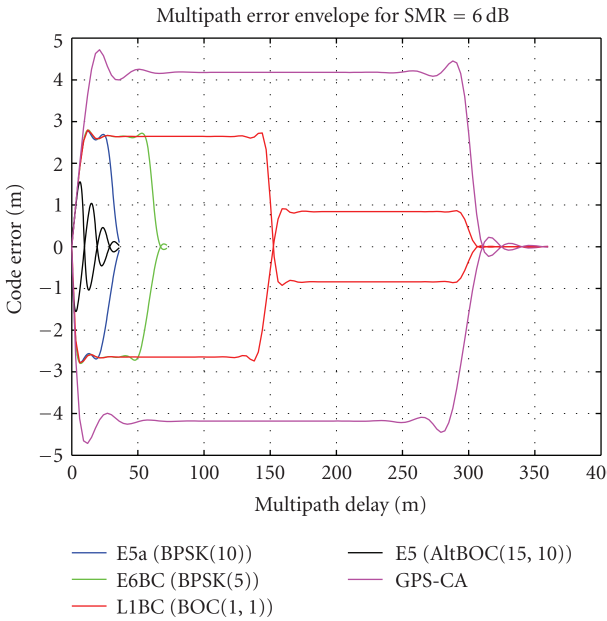

Figure 1: Multipath error envelopes of GNSS code modulation at signal/multipath ratio of 6 dB: GPS-C/A (magenta), Galileo L1BC (red), E6BC (green), E5a (blue), E5AltBOC (black).

transmitted modulations. The output of GETR includes raw measurements, navigation bits and, optionally, correlation function, and the samples of the RF signal at the intermediate frequency. The signal acquisition in GETR is implemented with the use of a custom-tailored fast acquisition unit [6].

This paper is based on the analysis of GETR measurements (pseudoranges, phases, Dopplers, C/N_0). The emphasis is on the evaluation of the code multipath performance, which is statistically characterized by the dependence of the averaged multipath noise upon elevation. Our approach is to compare empirical data for different sites and different signals and to classify the signals in accordance with their average multipath performance.

2. MULTIPATH ERROR ENVELOPES OF GALILEO CODE MODULATIONS

Multipath error envelopes for GPS-CA and Galileo code modulations are presented in Figure 1. The error envelopes were computed using the standard simulation of the tracking process of a straight code modulation superimposed with a single reflected signal at a signal/multipath ratio of 6 dB. The simulation of the tracking process involves the computation of the correlation peaks of the original code and the code superimposed with multipath. The bandwidth of RF filtering simulated by the algorithm was 40 MHz for all the codes (55 MHz for E5AltBOC).

The results shown in Figure 1 prove that the error envelopes for all the Galileo modulations are well within the error envelope of the GPS-CA code. From the shape of the error envelopes it is evident that the biggest advantage of Galileo modulations is in the suppression of long-delay multipath. E5AltBOC is the only modulation, which is expected to provide a high degree of suppression of a short-range multipath as well. Exceptional multipath performance of E5AltBOC has been confirmed in all the hitherto processed data.

As for the other Galileo codes, their performance significantly depends upon the typical spectra of multipath delays on a particular site. For example, with a multipath delays of about 200 m, the L1BC multipath is expected to be much lower than with GPS-CA, while with multipath delays of about 100 m, the advantage of L1BC would be less pronounced. More precisely, the improvement of Galileo BOC (1,1) with respect to BPSK(1) in the first 150 m is due to the wider transmit bandwidth of Galileo than GPS, and not really due to the signal structure. Indeed, if both Galileo and GPS had the same transmit BW, the multipath envelopes would be similar for the first 150 m. The improvement due to signal structure only comes between 150 and 300 m. All the Galileo codes presented in the plot (except for E5AltBOC) are expected to have the same multipath errors for delays shorter than 10 m, while for the delays between 50 and 100 m, E5a and E6BC modulations will have lower multipath errors than L1BC.

In practice, this means that relative performance of different code modulations will be site-dependent. Of course, a modulation with a smaller theoretical multipath error envelope is never expected to be worse (on average) than the modulation with a bigger error envelope. However, the advantages of more advanced code modulations will be more evident for the sites where long-delay multipath is dominant but may disappear for the sites with significant short-range mulitpath.

All the above considerations directly apply only to static multipath. Code multipath errors visible by the GNSS receiver in the movement, such as in car tests, are subject to averaging at the level of tracking. Although these modulations, which look better in Figure 1 are still expected to show lower multipath errors in the car test, it is hard to predict theoretically the measure of their advantage. Our experimental results presented later in the paper show relatively small differences between all the codes except for E5AltBOC which still is a definite champion. The exceptional qualities of E5AltBOC are due to its exceptionally high bandwidth. The tracking of E5AltBOC signal is implemented in the GETR in accordance with the algorithm outlined in [7].

3. CALCULATION OF CODE MULTIPATH ERROR BASED ON EXPERIMENTAL DATA

In our data analysis we computed code multipath using a well-known formula:

$$M_i = P_i - \Phi_i + 2\lambda_i^2 \frac{\Phi_j - \Phi_i}{\lambda_j^2 - \lambda_i^2}, \tag{1}$$

where M_i is the estimate of the code multipath error on a pseudorange P_i, while Φ_i and Φ_j are the carrier phase observables (in units of length) for wavelengths λ_i and λ_j for the same satellite. j represents any band which is different

Figure 2: Space Engineering antenna mounted on the rooftop of the Septentrio office.

than i. With multifrequency Galileo signals, several values of j are possible, but the particular selection of j does not significantly affect the results. Formula (1) estimates a combination of multipath and tracking noise, but the contribution of the tracking noise can be neglected in most practical cases. For those signals which have pilot and data components, we used the pilot component; the multipath is exactly the same for both components but the tracking noise is independent. In (1), all the effects of the movement are canceled out, hence it is applicable to both static and kinematic data.

4. STATIC DATA COLLECTED IN LEUVEN AT SEPTENTRIO TEST SITE

Most of the data presented in this paper have been collected at the rooftop of the Septentrio office building. The wideband GPS/Galileo antenna provided by Space Engineering is shown in Figure 2. The antenna was mounted on the support structure and was located higher than the other objects on the rooftop. However, the adjacent building, which is seen at the photo, was still higher than the antenna and acted as a source of reflected signals. Therefore, the short-range multipath at our site is relatively low, but long-range multipath systematically affects our data especially at low elevations when a satellite is rising or setting in the direction opposite to the adjacent building, which was in fact quite typical for GIOVE. The reflector building stretches in the North/South direction while GIOVE-A would often (but not always) rise directly in the East. In fact, day-dependent variations of multipath on our site were to a great extent due to the variations of the direction of rising/setting of GIOVE-A with respect to this reflecting wall.

Table 1 shows the availability of the data for individual Galileo signals in the Leuven data sets processed for this report. Although GIOVE-A is able of transmitting all the experimental Galileo signals, it can transmit only in two frequency bands at a time. In reality, the satellite is transmitting either a combination of L1+E5a+E5b or a combination of L1+E6.

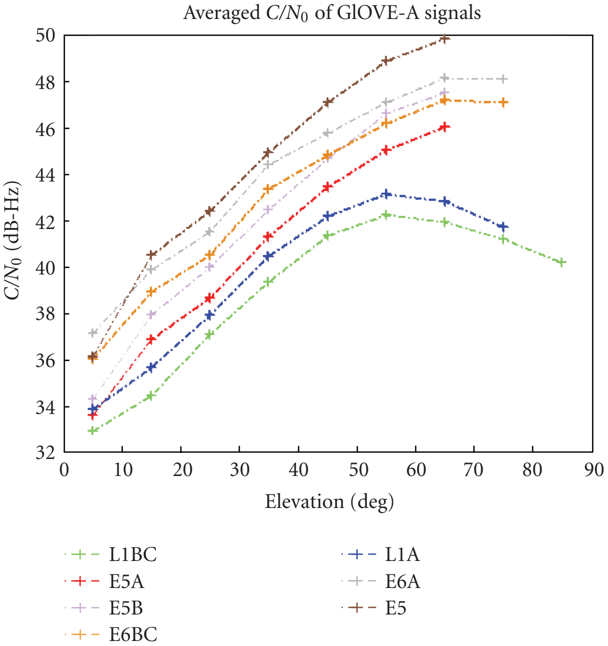

Figure 3: Averaged signal power for all the tests in Leuven.

In our analysis, we have joined all the processed data for averaged signal power and code multipath errors as functions of elevation into one global array. This data is presented in Figures 3 and 4 for signal power and multipath, respectively. The signal power matches the specifications of GSTB-V2, but it is not representative of the final Galileo satellites, which will use different transmitters. The drop of C/N_0 at zenith for L1 signals is peculiar to the Space Engineering antenna (see [1] for more details).

Figure 4 contains standard deviations of code multipath for 10-degree bins of the elevation angle. Because the distance to the adjacent building is about 100 m, typical delays of generated multipath are about 200 m (for satellites rising or setting in the direction opposite to the building), hence at low elevations L1BC and all the other Galileo codes perform significantly better than GPS-C/A, where this component of multipath is dominant. On the contrary, at high elevations where short-range multipath is dominating, GPS-CA and 4 Galileo codes (L1-BC, E5a, E5b, E6BC) have similar values of multipath errors.

It is also clear that at low elevations L1BC has the highest multipath compared to other Galileo modulations. For the best modulations, such as E5AltBOC and L1A the long-range multipath is almost completely suppressed, hence corresponding curves in Figure 4 are almost flat and show little increase at low elevations. The Leuven site is well-suited to compare the suppression of long-range multipath by different code modulations.

Figure 4 contains also the comparison of the multipath performance of GPS-CA for 2 GPS receivers: GETR and PolaRx2. The difference between the two (black curves) can be seen as a measure of difference between the magnitude of multipath errors in two different receivers even if both do not use multipath mitigation (PolaRx2 uses multipath mitigation by default but it was turned off for this test). The difference

Table 1: GIOVE-A signal components recorded during static tests in Leuven.

Data set	Max elevation (deg)	L1A	L1BC	E5A	E5B	E5AltBoc	E6A	E6BC
15 January 2006	44.8	X	x				x	x
16 January 2006	60.0	X	x	x	x	x		
08 March 2006	83.8	X	x				x	x
19 May 2006	65.3	X	x	x	x	x		
28 May 2006	84.4		x	x	x	x		
13 October 2006	75.6	X	x				x	x

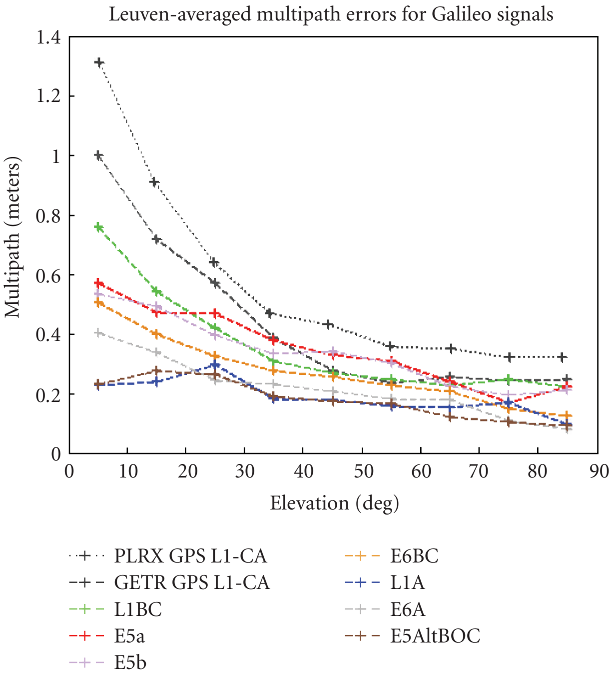

Figure 4: STD of code multipath for Galileo signals in comparison to GPS-CA for the tests in Leuven.

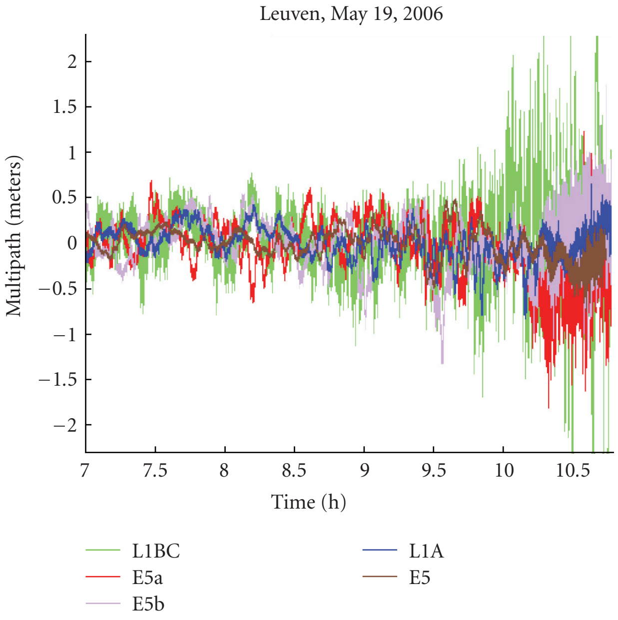

Figure 5: Time series of code multipath for the test of May 19.

is due to a combination of receiver parameters such as front-end bandwidth and the type of a discriminator.

Comparison of low-elevation and high-elevation multipaths is also presented in Table 2. In this table, the Galileo modulations are grouped into 3 groups: (i) high-performance group, which included E5AltBOC and the two PRS modulations (L1A and E6A), (ii) medium-performance group, which includes E5a, E5b, and E6BC, and (iii) low-performance group, which includes only L1BC and has still better performance as compared to CPS-CA. The values of multipath typical for the high-performance group are comparable to the values of tracking noise for GPS-CA code and are for most of the tests nearly equal at low and high elevations. This ranking of Galileo modulations in terms of multipath performance is practically identical to the ranking obtained by computer simulations in [8].

Successful suppression of long-range multipath can also be directly observed in the time series of multipath which we present here for some of the tests.

In Figure 5, the long-range multipath manifests itself in high-frequency variations of multipath error near the right edge of the graph. The same ranking of the Galileo modulations as in Table 2 can be observed; the multipath errors of L1BC are the highest, while the multipath of E5AltBOC is the lowest and the others fall in-between.

The high-amplitude high-frequency variations of L1BC multipath shown in Figure 5 and other similar plots correspond in fact to a quasiperiod about 20 seconds. The zoomed plot of these variations is shown in Figure 6. This plot clearly demonstrates how complete the suppression of long-range multipath by the best Galileo modulations is. A similar example, which includes E6A, is shown in Figure 7. In Figure 5 and other plots with time series, the part of the plot with higher-amplitude and higher-frequency multipath always corresponds to lower elevations, when the satellite is rising and setting. The variation of multipath with elevation is illustrated by the multipath versus elevation plots (Figure 4 and similar plots).

TABLE 2: Multipath STD error (m) of Galileo signals as compared to GPS C/A code.

Signal	Chip rate,	Jan. 15		Jan. 16		Mar. 08		May. 19		May. 28		Oct. 13	
	MHz	>10°	<10°	>10°	<10°	>10°	<10°	>10°	<10°	>10°	<10°	>10°	<10°
GPS-C/A	*1.023*	*0.60*	*1.19*	*	*	*	*	*	*	*	*	*	*
L1BC	1.023	0.36	0.93	0.40	0.55	0.39	0.41	0.38	0.86	0.38	0.93	0.34	0.79
E5a	10.23	—	—	0.55	0.62	—	—	0.33	0.51	0.25	0.51	—	—
E5b	10.23	—	—	0.33	0.44	—	—	0.35	0.47	0.27	0.55	—	—
E6BC	5.115	0.28	0.28	—	—	0.27	0.42	—	—	—	—	0.30	0.67
L1A	2.5575	0.24	0.37	0.21	0.20	0.24	0.20	0.23	0.22	—	—	0.18	0.37
E6A	5.115	0.24	0.22	—	—	0.23	0.17	—	—	—	—	0.23	0.58
E5AltBOC	10.23	—	—	0.25	0.23	—	—	0.20	0.30	0.14	0.23	—	—

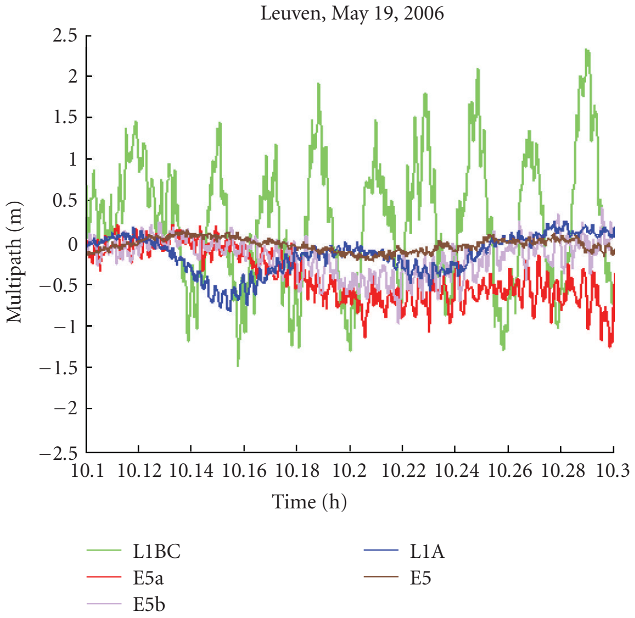

FIGURE 6: Zoomed view of the high-elevation part of the previous plot.

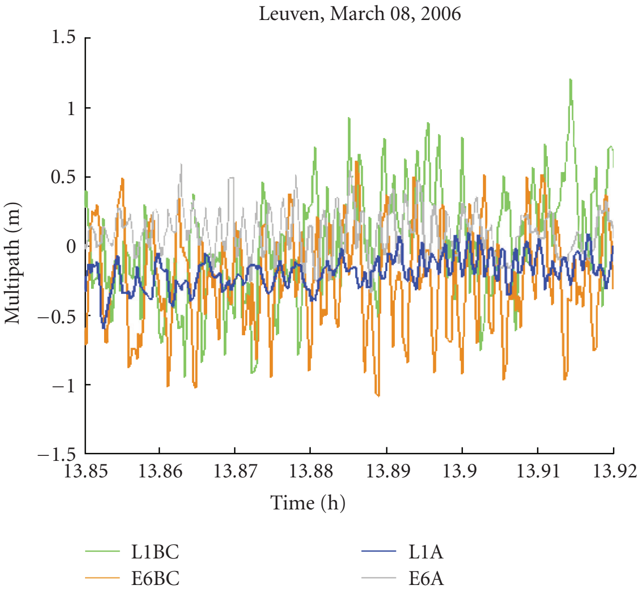

FIGURE 7: Similar example from another dataset which includes E6A.

Although most of the Leuven data demonstrate similar behavior for all the 3 modulations of the best group (E5, L1A, E6A), a more careful analysis gives the impression that on average the magnitude of multipath errors increases in the sequence E5AltBOC→L1A→E6A (which is quite in line with theoretical expectations), and that the performance of E6A in some cases comes close to the values typical for the "medium-performance" group. An example is presented in Figure 8. In fact, even in a summary plot (Figure 4), the E6A modulation shows visibly higher multipath errors at low elevations than E5AltBOC+L1A. Some other tests presented later in this paper also suggest that the best-performance group in fact includes only E5AltBOC and L1A, while E6A gravitates to the medium-performance group. The E5AltBOC, on the other hand, always shows an exceptionally stable performance; its values of multipath errors are always the lowest as compared to other modulations (see Figures 9, 10, and 11)

5. ANTENNA SITE IN LEUVEN WITH MORE INTENSIVE SHORT-RANGE MULTIPATH

In order to investigate the effect of short-range multipath on Galileo signals, we placed the Galileo antenna at another more multipath-rich position on the same rooftop. This antenna position was located on the roof floor between the two metal ventilation outlets (identical to these in the right bottom corner of Figure 2). The antenna was located lower than many other reflective objects on the rooftop, so it was expected to get more short-range and middle-range multipath compared to the main site. The comparison of the two sites is presented in Figure 12.

Figure 12 shows that the multipath at the "multipath-rich" location is indeed higher, the difference being particularly great for E5a. At higher elevations the difference between the two sites is statistically insignificant, which indicates that the local objects generate multipath predominantly

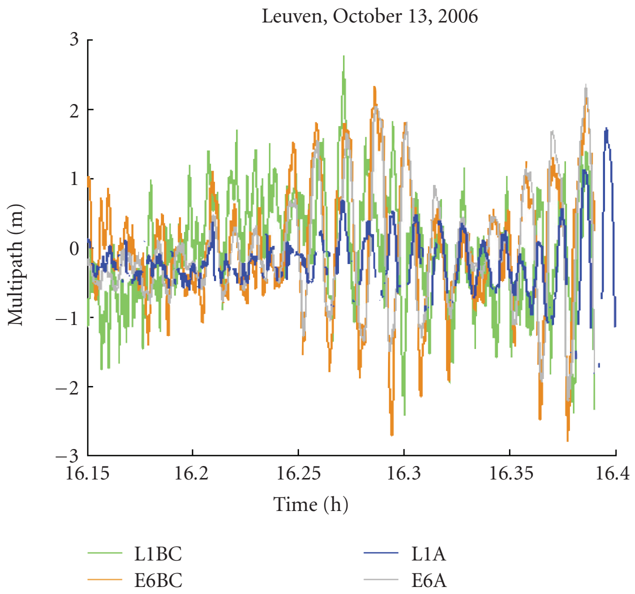

FIGURE 8: An occasion of relatively high multipath errors by L1A/E6A.

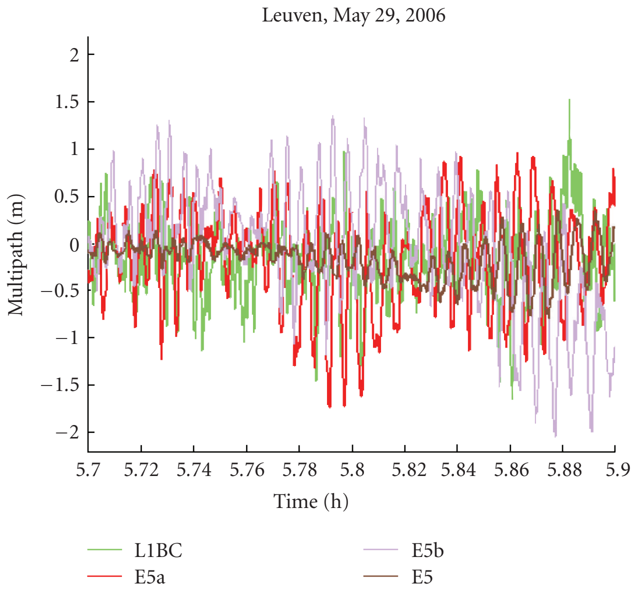

FIGURE 10: Multipath time series for May 29, 2006.

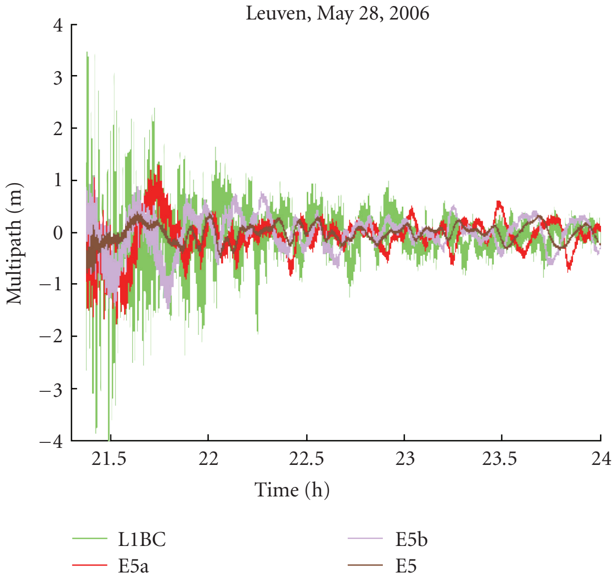

FIGURE 9: Multipath time series for May 28, 2006.

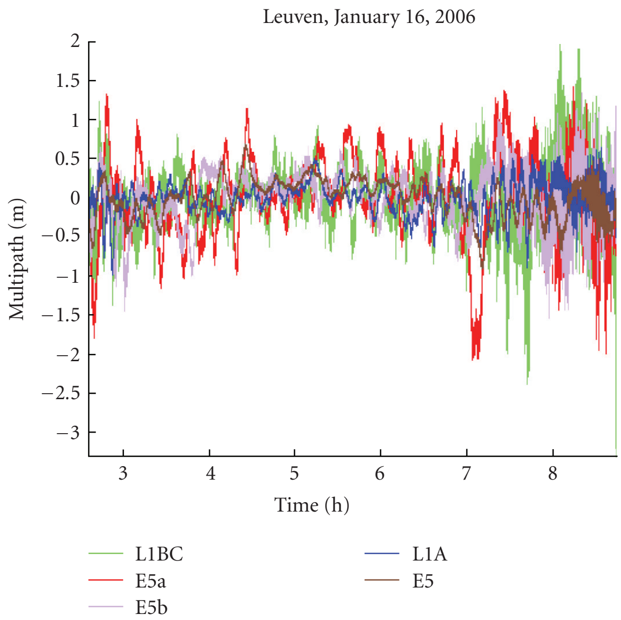

FIGURE 11: Multipath time series for January 16, 2006.

for low-elevation satellites. The multipath statistics for the two tests at the “multipath-rich” site is presented in Table 3.

The time series of code multipath is presented in Figures 13 and 14. It is evident that in both plots the multipath of E5a is unusually high in comparison to all the other tests. The reason for this strange behavior, different from all the other tests, is not clear.

6. STATIC DATA COLLECTED AT LA PLATA AND WUHAN GESS SITES

On top of processing the data collected by ourselves, we also processed the GIOVE-A data collected at 2 other geographic locations and available via GESS network: La Plata in Latin America and Wuhan in China.

The analysis of multipath data from these two sites confirms in broad terms the tendencies reported in the first section. In particular, the superior performance of L1A and E5AltBOC has been confirmed. However, some important differences must be mentioned. First of all, the E6BC signal has high multipath comparable to L1BC (even higher than L1BC at low elevations). Secondly, at the Wuhan site the elevation dependence is much less pronounced than for the rest of the tests, probably due to the peculiarities of local reflectors. Thirdly, the E6A signal shows worse performance

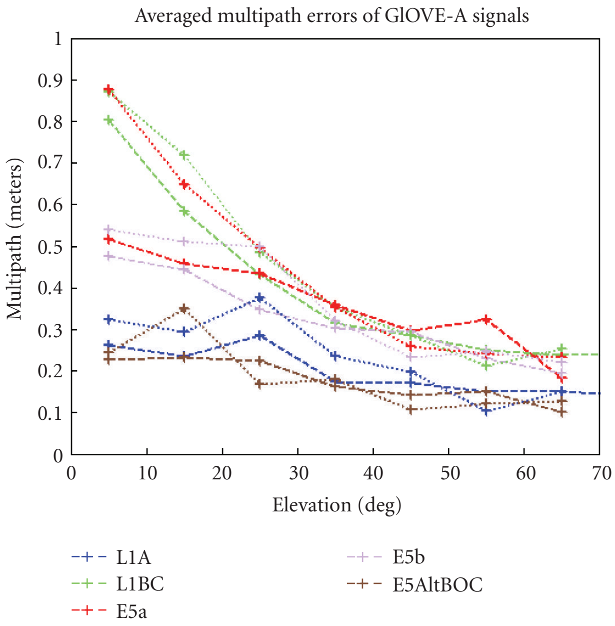

FIGURE 12: Dotted line: tests of December 12 and 13 at a "multipath-rich" site. Broken line: average of tests during March–October, 2006, at the open-sky site.

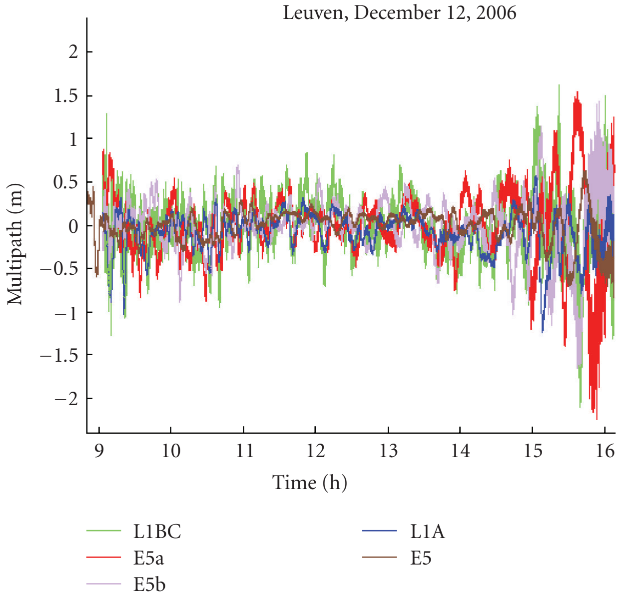

FIGURE 13: Time series for code multipath for December 12, 2006.

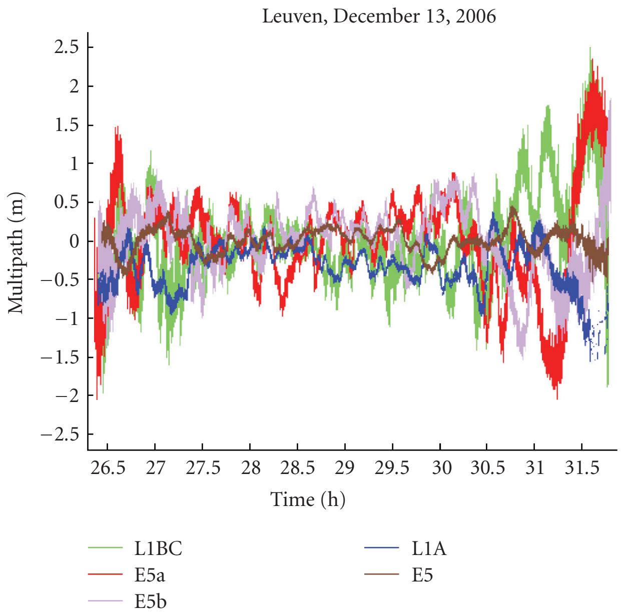

FIGURE 14: Time series for code multipath for December 13, 2006.

TABLE 3: Multipath STD error (m) of Galileo signals for a more "multipath-rich" antenna site.

Signal	Chip rate (MHz)	Dec. 12		Dec. 13	
		>10°	<10°	>10°	<10°
L1BC	1.023	0.33	0.48	0.48	0.96
E5a	10.23	0.35	0.82	0.45	0.89
E5b	10.23	0.31	0.32	0.39	0.60
L1A	2.5575	0.23	0.20	0.28	0.36
AltBOC	10.23	0.16	0.30	0.21	0.22

than L1A and E5AltBOC. At low elevations it still gravitates to the "high-performance group," while at higher elevations it shows about the same average multipath errors than other signals.

It is also quite clear that performance of GPS-CA on both sites is about the same as the performance of L1BC. This can probably be attributed to the prevalence of the multipath delays shorter than 150 m, in which case both modulations are supposed to be about equivalent. The strange behavior of GPS multipath at elevations less than 10 degrees for the La Plata site can at least partly be explained by high masking angles from a wide range of directions which leads to the lower than normal availability of GNSS signals (see photo of the La Plata site, Figure 25).

Peculiarities of these sites can also be illustrated by the time series of multipath errors (Figure 17–20). Figure 17 illustrates relatively high multipath errors for E6BC. Figures 19 and 20 show that the multipath for the Wuhan stations has indeed atypical elevation dependence; at lower elevations the frequency of the variations of multipath are increasing, while their amplitude remains the same. The multipath results for different stations depend of course upon the peculiarities of the multipath environment, in particular upon the presence of reflectors oriented in a certain way relative to the GIOVE-A lines of sight at its rising and setting.

Figure 21 demonstrates how different the multipath environments at different stations indeed are. At La Plata station, the multipath is generally the highest (almost a double at high elevations compared to Leuven), while at Wuhan the multipath is not only higher in general, but also its elevation dependence is flatter. Logically enough, the

Table 4: Availability of GIOVE-A signals for the data sets from La Plata and Wuhan.

Stations	Date	Max. elevation (deg)	L1A	L1BC	E5A	E5B	E5AltBoC	E6A	E6BC
La Plata	10 & 11 Sep 2006	88.9	x	x				x	x
	5, 6 & 7 Apr 2007	87.7	x	x	x	x	x		
Wuhan	18 & 19 Oct 2006	88.5	x	x				x	x
	20 & 21 Mar 2007	88.8		x	x	x	x		

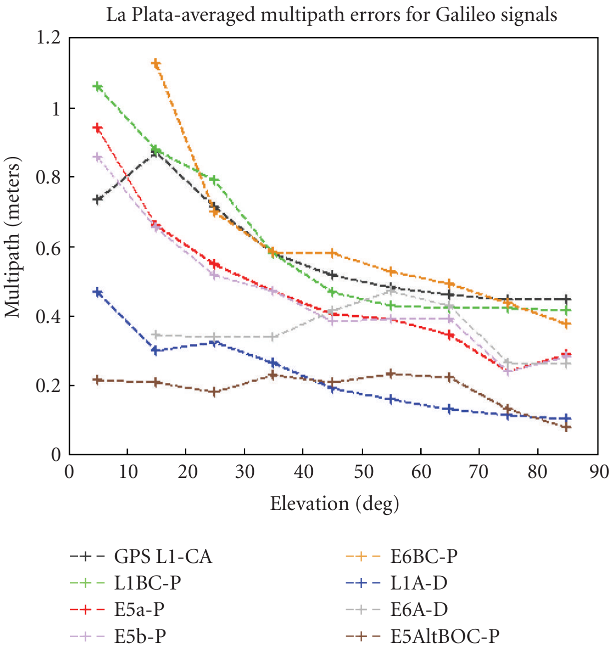

Figure 15: Multipath performance at the La Plata GESS site.

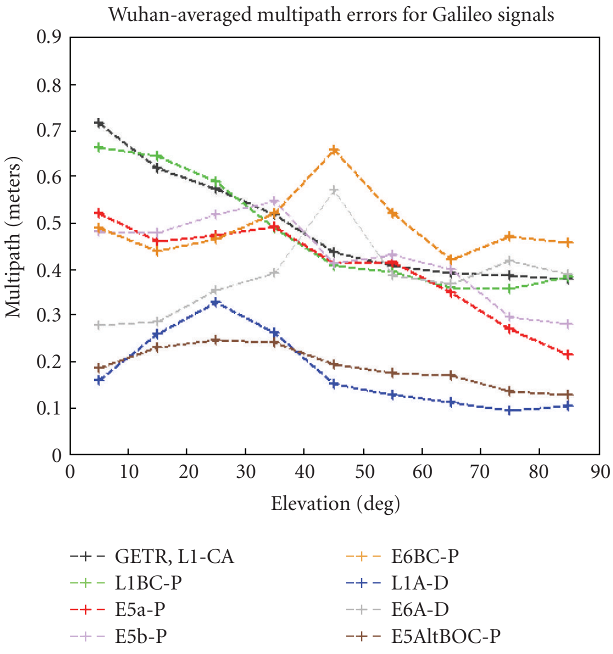

Figure 16: Multipath performance at the Wuhan GESS site.

biggest differences can be seen for L1BC, where multipath errors are the highest, while for E5AltBOC, where multipath errors are significantly suppressed, the differences are almost undetectable (Figure 22).

Investigation of the reasons for site-dependent differences is beyond the scope of this paper. The photos of La Plata and Wuhan antenna sites from public IGS sources show significant amount of local reflectors. The La Plata site (Figure 25) resembles a park and is surrounded with high trees which are apparently responsible for high multipath and masking of the signal at low elelvations. The Wuhan site (Figure 26) is on the rooftop of a two-storeyed building and is surrounded by remote trees which are likely to serve as a source of scattered signals. The multipath caused by scattered signals is expected to be present at all the elevations and may be responsible for the flatter elevation dependence of multipath at Wuhan (Figure 21). It should also be mentioned that at the La Plata site the signal power is systematically lower than in Leuven and Wuhan (cf. Figures 3, 23, and 24).

The total statistics of multipath for all the processed data for La Plata and Wuhan is presented in Table 5. The averages presented in this table illustrate the same tendencies already visible from the plots, in particular the low elevation dependence of multipath at the Wuhan site.

7. KINEMATIC TESTS

The code multipath errors for kinematic tests with GIOVE-A signals where first presented in [1]. The kinematic multipath is very different from a static one in that its variations are dominated by fast changes of the reflectors due to movement, and that a high degree of multipath suppression is achieved at the tracking level due to averaging of the rapid oscillations of in-phase/out-of-phase multipath. The time series of kinematic multipath consists of random structure-less variations, where the differences between the modulations are much less pronounced that in the static case.

In this paper, we present the results of two car tests performed in different environments: rural and urban. Separate statistics was computed for the periods when the car was static and the periods when the car was moving. As shown in Table 6, the signal availability during the tests

TABLE 5: Multipath 1-sigma error (m) for the data sets of La Plata/Wuhan.

Signal	Chip rate (MHz)	La Plata				Wuhan			
		Sep. 10		Apr. 05		Oct. 18		Mar. 20	
		>10°	<10°	>10°	<10°	>10°	<10°	>10°	<10°
L1BC	1.023	0.56	—	0.62	1.06	0.53	0.66	0.54	0.66
E5a	10.23	—	—	0.46	0.94	—	—	0.42	0.52
E5b	10.23	—	—	0.46	0.86	—	—	0.46	0.48
E6BC	5.115	0.59	—	—	—	0.50	0.49	—	—
L1A	2.5575	0.28	—	0.28	0.47	0.29	0.16	—	—
E6A	5.115	0.38	—	—	—	0.39	0.28	—	—
AltBOC	10.23	—	—	0.21	0.22	—	—	0.21	0.19

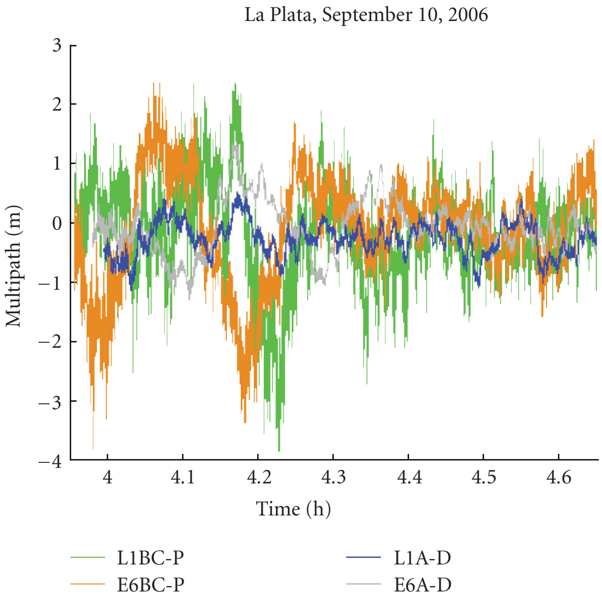

FIGURE 17: Time series of code multipath for La Plata, September 10, 2006.

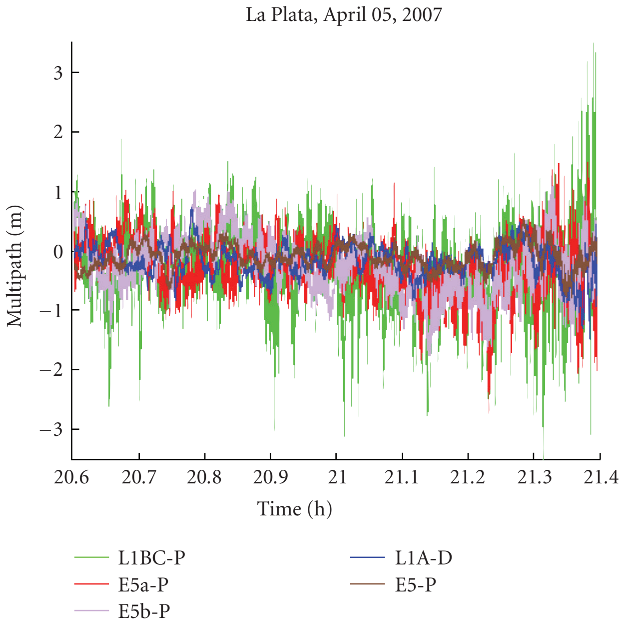

FIGURE 18: Time series of code multipath for La Plata, April 05, 2007.

was different; during the urban test, L1 and E6 were being transmitted, while during the rural test L1 and E5 signals were available.

Although the static portions of the car tests still show the same tendencies as the data collected on the rooftop, the data collected during the movement demonstrates much smaller values of multipath errors, much smaller advantage of Galileo modulations as compared to GPS-C/A, and much smaller differences between Galileo modulations. The differences between static and kinematic multipath can be clearly seen in Figures 27 and 28. Figure 29 illustrates that code multipath during the urban test was generally somewhat higher due to obviously greater amount of reflectors in the urban environment.

In particular, the results of the car tests suggest that the replacement of L1 BOC(1,1) with MBOC will not have any significant impact on the multipath performance in the automotive environment. Indeed, MBOC is expected to show the performance intermediate between L1BC and E6BC, while both modulations have about the same intensity of kinematic multipath according to Table 6.

According to theory, MBOC is expected to outperform BOC(1,1) for static scenarios, possibly bringing greater improvement relative to BOC(1,1) than the improvement of the BOC(1,1) relative to BPSK(1). This is to be verified after actual implementation of MBOC.

8. PHASE MULTIPATH

Simultaneous availability of 3 frequencies allows direct evaluation of phase multipath from triple-frequency iono-free geometry-free combinations of phase measurements [1, 9]:

$$M_{\Phi 123} = \lambda_3^2(\Phi_1 - \Phi_2) + \lambda_2^2(\Phi_3 - \Phi_1) + \lambda_1^2(\Phi_2 - \Phi_3). \quad (2)$$

TABLE 6: Multipath statistic for car tests (m).

	Rural static	Rural movement	Urban static	Urban movement
GPS-CA			1.19	0.23
L1BC	0.27	0.15	0.40	0.18
E6BC			0.50	0.22
E5a	0.20	0.16		
E5b	0.26	0.15		
E5AltBOC	0.10	0.11		

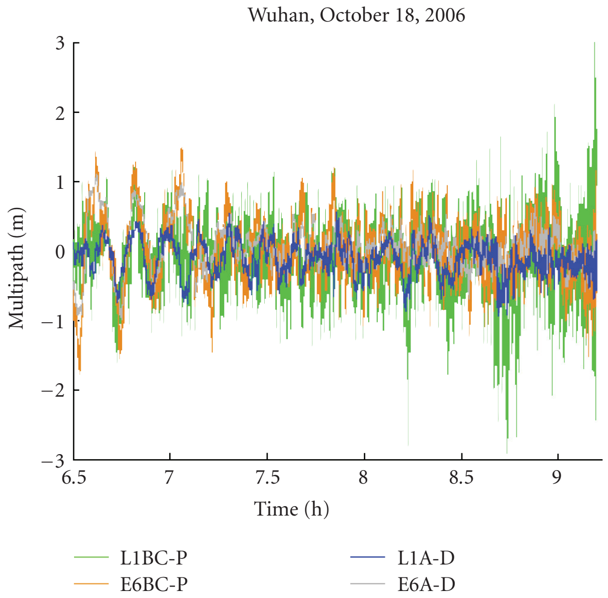

FIGURE 19: Time series of code multipath for Wuhan, October 18, 2006.

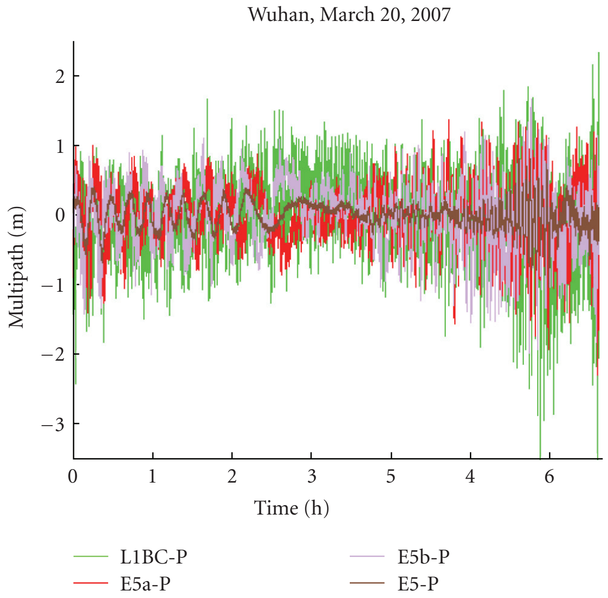

FIGURE 20: Time series of code multipath for Wuhan, March 20, 2007.

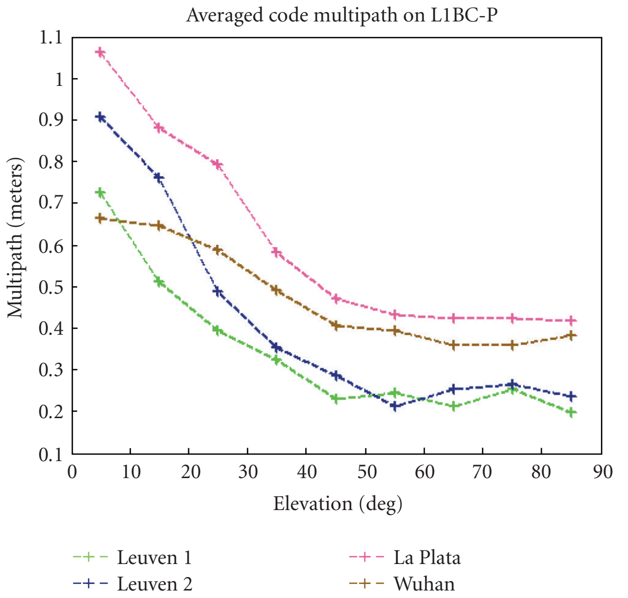

FIGURE 21: Code multipath on L1BC at 4 locations. Here "Leuven-1" is our main open-sky antenna site (Figure 2). "Leuven-2" is more multipath-rich site located between the ventilation outlets (see Section 5).

This formula is a linear combination of three geometry-free observables($\Phi_i - \Phi_j$), which all contain ionosphere delays. As it has been shown in [9], in (2) ionosphere delays cancel out. M_{123} contains a mix of phase multipath and tracking errors for the same satellite on 3 different frequencies and can be used as a global indicator of phase multipath severity. It can be used in particular to study elevation dependence and site dependence of phase multipath.

In this paper, we used one particular combination (E5a − 1.128*E5b + 0.128*L1BC) as an indicator of phase multipath. Figure 30 contains elevation dependence of this phase multipath indicator for all the static sites covered in this paper. The elevation dependence shows significant variability and does not indicate with certainty any differences between the sites.

The nature of phase multipath is in general quite different from code multipath. In particular, phase multipath for different signals is not expected to show significant differences. It has already been demonstrated in [1] that the phase tracking noise is identical for all the GIOVE-A signals.

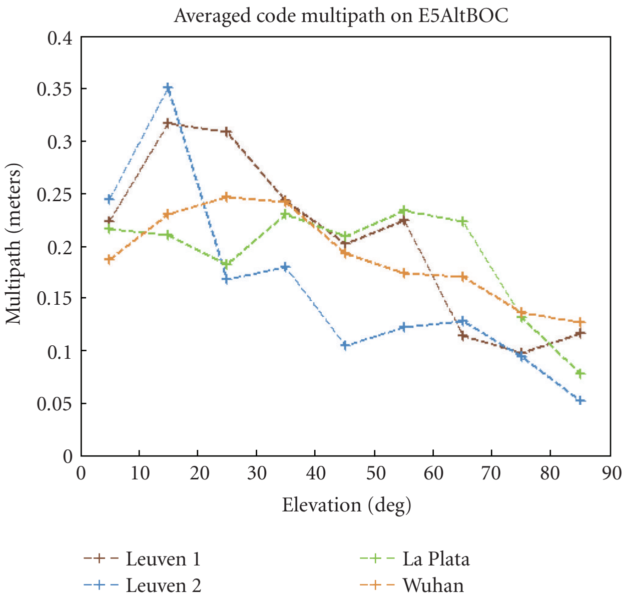

Figure 22: Code multipath on E5AltBOC at 4 locations. Here “Leuven-1” is our main open-sky antenna site (Figure 2). “Leuven-2” is more multipath-rich site located between the ventilation outlets (see Section 5).

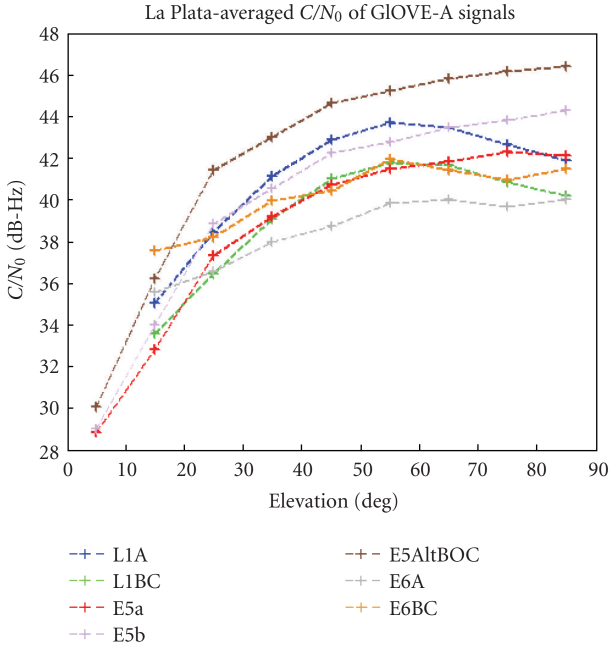

Figure 23: Signal power at La Plata station. It is systematically lower as compared to Leuven (Figure 3) and Wuhan (Figure 24).

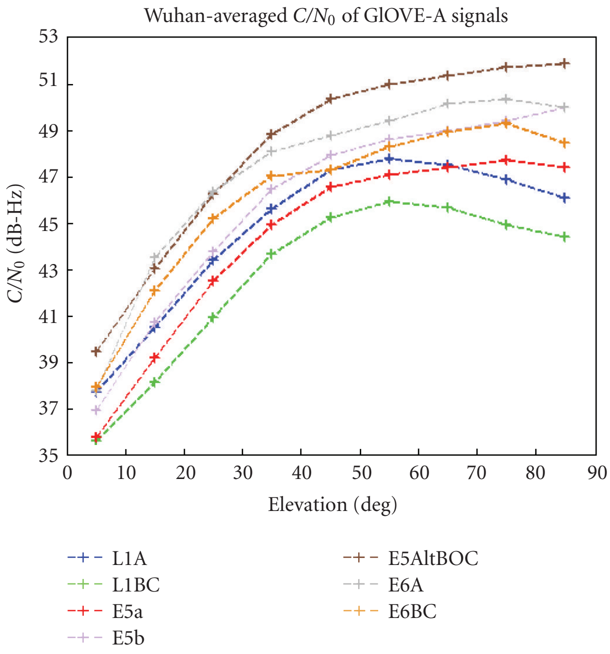

Figure 24: Signal power at Wuhan station.

Figure 25: Environment at the La Plata antenna site.

Figure 26: Environment at the Wuhan antenna site.

Phase multipath is generally much less studied than code multipath, so it is difficult to predict what the behavior of phase multipath should be. The time series of our phase multipath indicator is presented in Figure 31.

The elevation dependence of phase multipath is generally flatter and more variable that with the code multipath. There exist significant long-term variations which have impact on the statistics in a way of making it less stable. The pattern of phase multipath is quite different between the sites (cf. Figures 31 and 32).

9. CONCLUSIONS

Field experience with GIOVE-A signals has demonstrated stable reception in a variety of external conditions and

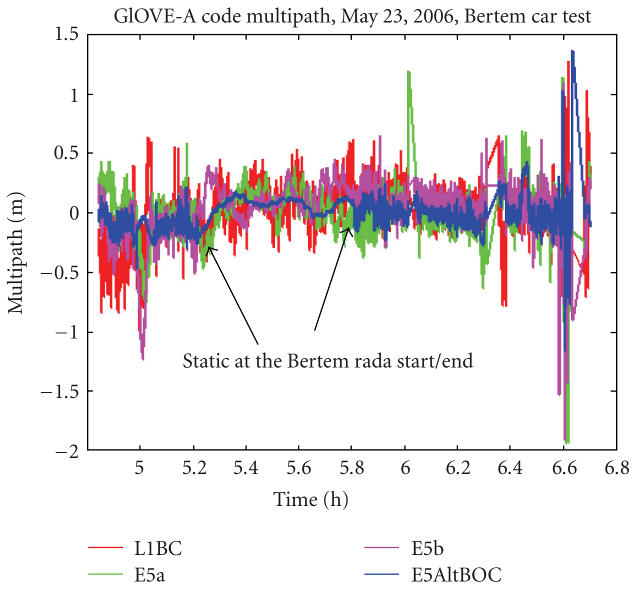

Figure 27: Code multipath during the rural car test.

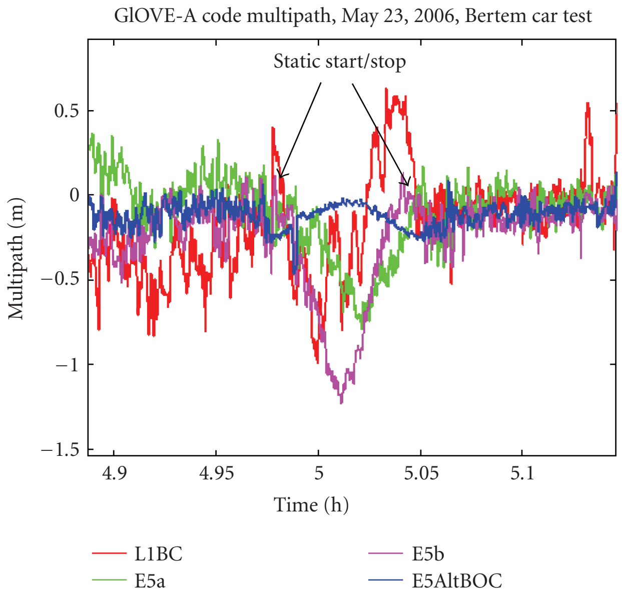

Figure 28: Zoom into one of the static portions of the rural test.

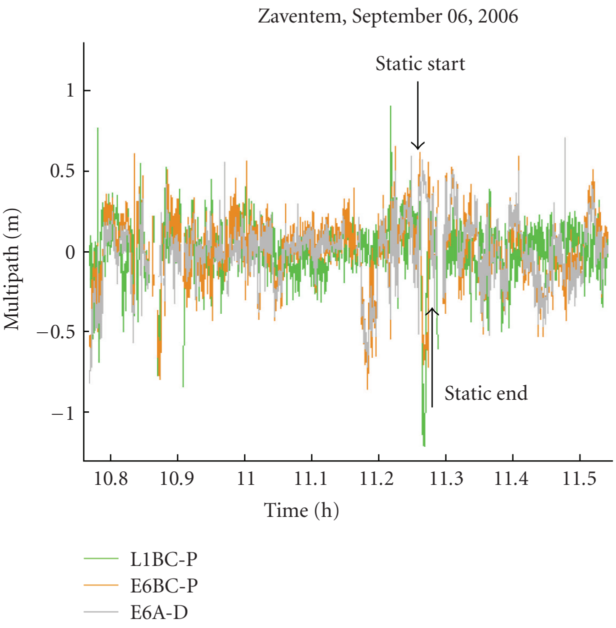

Figure 29: Code multipath during the urban test.

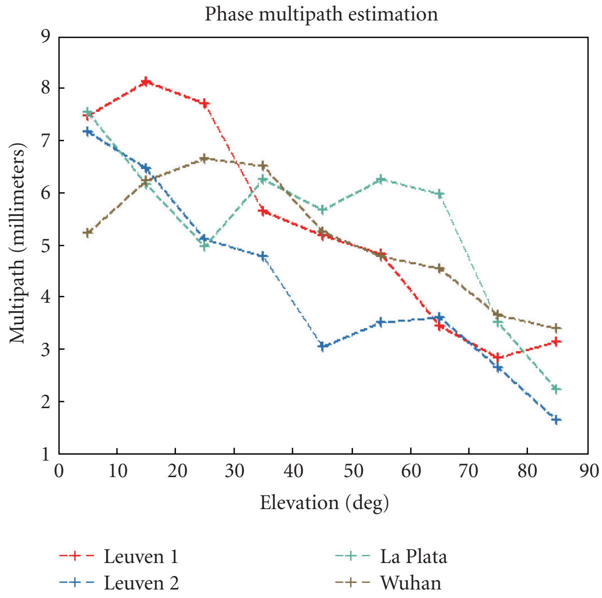

Figure 30: Phase multipath at 4 locations. Here "Leuven-1" is our main open-sky antenna site (Figure 2). "Leuven-2" is a more multipath-rich site located between the ventilation outlets (see Section 7).

confirmed the theoretical expectations as to superior multipath rejection of wide-band Galileo modulations. Multipath performance results for static and kinematic tests have been reported.

Comparison of the static data from different sites shows significant variability of the multipath performance for most of the Galileo signals. It seems that only the behavior of E5AltBOC is truly stable and repeatable for all the tests; in all the tests, the E5AltBOC demonstrates the highest multipath suppression as compared to other signals and very low magnitude of average multipath errors, down to the values about 0.2 m.

For all the other signals, we can talk about the tendencies which manifest themselves on average, but with significant site-dependent variations. The most important of these tendencies is the classification of all the modulations in groups shown in Table 2. According to this classification, E6A+L1A+E5AltBOC form the group of high-performance

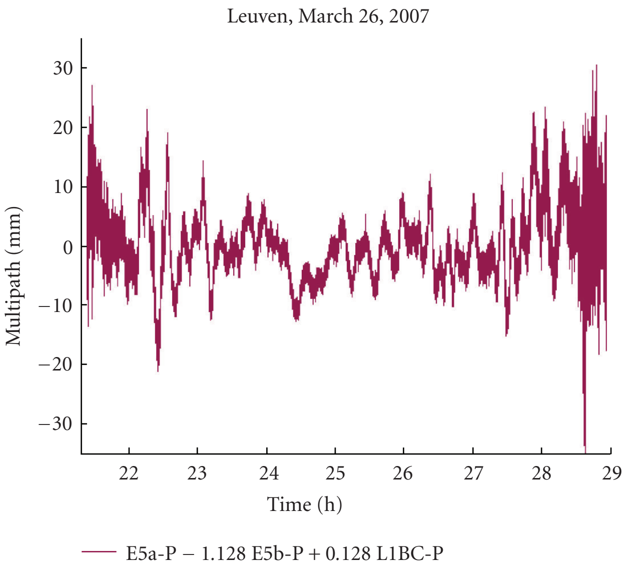

FIGURE 31: Phase multipath indicator (triple-frequency phase combination of L1BC, E5a, and E5b) at Leuven site.

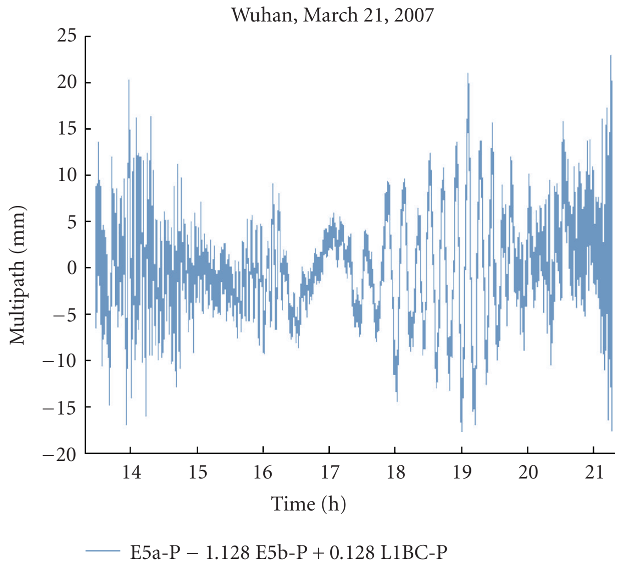

FIGURE 32: Phase multipath indicator (triple-frequency phase combination of L1BC, E5a, and E5b) at Wuhan.

signals, while the E5a, E5b, and E6BC signals belong to the medium group, the performance of L1BC is the lowest.

This classification, which agrees with theoretical predictions and computer simulations, can be accepted as a general rule, although in some tests E6BC and E5a,b show practically the same performance as L1BC, and E6A in the others shows performance more typical to the medium group.

The relationship between the signals for individual sites depends upon the spectra of multipath delays. For the Leuven site where the long-range multipath with a delay of about 200 m is clearly dominant, the wide-band signals with essential suppression of long-range multipath component show clearly superior performance. In other cases, when short-range multipath is dominant, the advantage of more advanced codes will be less pronounced.

The future research may take an approach of looking in more detail into specific multipath conditions and types of reflectors at different sites. Accumulation of much greater statistic may help to formulate the trends in a more reliable and detailed manner and make a classification of sites in accordance with the multipath behavior.

The kinematic tests have demonstrated a lot of smaller values of multipath errors and a much less significant dependence of multipath upon code modulations. This means in particular that any further changes in the signal definition of Galileo signals are not likely to bring any significant improvement to dynamic applications, such as automotive, although modulation changes may have impact on static applications.

In this paper, the phase multipath statistics for GIOVE-A signals is presented for the first time.

ACKNOWLEDGMENT

The authors would like to thank M. Falcone for his support of GIOVE signal experimentation activity.

REFERENCES

[1] A. Simsky, J.-M. Sleewaegen, M. Hollreiser, and M. Crisci, "Performance assessment of Galileo ranging signals transmitted by GSTB-V2 satellites," in *Proceedings of the 19th International Technical Meeting of the Satellite Division of the Institute of Navigation (ION GNSS '06)*, vol. 3, pp. 1547–1559, Fort Worth, Tex, USA, September 2006.

[2] M. Hollreiser, M. Crisci, J.-M. Sleewaegen, et al., "Galileo signal experimentation," *GPS World*, vol. 18, no. 5, pp. 44–50, 2007.

[3] M. Spelat, M. Crisci, M. Falcone, and M. Hollreiser, "GIOVE-A signal in space test activity at ESTEC," in *Proceedings of the 19th International Technical Meeting of the Satellite Division of the Institute of Navigation (ION GNSS '06)*, vol. 2, pp. 981–983, Fort Worth, Tex, USA, September 2006.

[4] M. Falcone, M. Lugert, M. Malik, et al., "GIOVE-A in orbit testing results," in *Proceedings of the 19th International Technical Meeting of the Satellite Division of the Institute of Navigation (ION GNSS '06)*, vol. 3, pp. 1535–1546, Fort Worth, Tex, USA, September 2006.

[5] M. Hollreiser, J.-M. Sleewaegen, W. de Wilde, M. Falcone, and F. Wilms, "Galileo test user segment," *GPS World*, vol. 16, no. 7, pp. 23–29, 2005.

[6] W. de Wilde, J.-M. Sleewaegen, A. Simsky, et al., "New fast signal acquisition unit for GPS/Galileo receivers," in *Proceedings of the European Navigation Conference (ENC GNSS '06)*, Manchester, UK, May 2006.

[7] J.-M. Sleewaegen, W. de Wilde, and M. Hollreiser, "Galileo Alt-BOC receiver," in *Proceedings of the European Navigation Conference (GNSS '04)*, Rotterdam, The Netherlands, May 2004.

[8] A. Fernandez, J. Diez, C. Griffin, et al., "UERE budget results for the Galileo test user receiver," in *Proceedings of the 19th International Technical Meeting of the Satellite Division of the Institute of Navigation (ION GNSS '06)*, vol. 2, pp. 1048–1059, Fort Worth, Tex, USA, September 2006.

[9] A. Simsky, "Three's the charm: triple-frequency combinations in future GNSS," *Inside GNSS*, vol. 1, no. 5, pp. 38–41, 2006.

Hindawi Publishing Corporation
International Journal of Navigation and Observation
Volume 2008, Article ID 785695, 17 pages
doi:10.1155/2008/785695

Research Article

Multiple Gate Delay Tracking Structures for GNSS Signals and Their Evaluation with Simulink, SystemC, and VHDL

Heikki Hurskainen,[1] Elena Simona Lohan,[2] Xuan Hu,[2] Jussi Raasakka,[1] and Jari Nurmi[1]

[1] *Department of Computer Systems, Tampere University of Technology, P.O. Box 553, 33101 Tampere, Finland*
[2] *Department of Communications Engineering, Tampere University of Technology, P.O. Box 553, 33101 Tampere, Finland*

Correspondence should be addressed to Heikki Hurskainen, heikki.hurskainen@tut.fi

Received 13 July 2007; Revised 11 December 2007; Accepted 29 February 2008

Recommended by Letizia Presti

Accurate delay tracking in multipath environments is one of the prerequisites of modern GNSS receivers. Several solutions have been proposed in the literature, both feedback and feedforward. However, this topic is still under active research focus, especially for mass-market receivers, where selection of lowcomplexity, nonpatented methods is preferred. Among the most encountered delay tracking structures implemented in today's receivers, we have the narrow correlator and the double-delta correlators. Both are heavily covered by various patents. The purpose of this paper is to introduce a new, generic structure, called multiple gate delay (MGD) structure, which covers also the patented correlators but offers much more flexibility in the design process. We show how the design parameters of such a structure can be optimized, we argue the performance of this structure via detailed simulation results based on various simulators, such as Matlab/Simulink-based tool, GRANADA, and we test the implementation feasibility of MGD structures on actual devices, via SystemC and FPGA prototyping. One of the main advantages of the proposed structure is its high degree of flexibility, which allows the designer to choose among, to the authors' knowledge, nonpatented solutions with delay tracking accuracy comparable with that of the current state-of-art trackers.

1. BACKGROUND AND MOTIVATION

The main algorithms used nowadays for GPS and Galileo code tracking are based on what is typically called a feedback delay estimator, and they are implemented based on a feedback loop. The most known feedback delay estimators are the delay locked loops (DLLs) and the today's GNSS receiver that typically use a particular DLL structure, called the narrow correlator or narrow early-minus-late (NEML) delay tracker, which proved to give good results in multipath environments [1–3]. Another class of enhanced DLL structures is the so-called double-delta correlator class [4], which started to gain more and more attention during last years. Examples belonging to this class are: the high resolution correlator (HRC) [3, 5], the strobe correlator [2, 4, 6], the pulse aperture correlator (PAC) [7], the multipath mitigation correlator [8], and the modified correlator reference waveform [2, 9]. Most of the double-delta correlators as well as the narrow correlator are patented or under patent applications [4, 5, 7, 10, 11].

An alternative to the above-mentioned feedback loop solutions is based on the open-loop (or feedforward) solutions, which refer to the solutions which make the delay estimation in a single step, without requiring a feedback loop. A general classification of open-loop solutions for CDMA communication applications can be found in [12, 13] and for GNSS applications in [14]. However, for the purpose of low-cost mass-market receiver implementation, feedback delay tracking structures are still the preferred ones, and they will be the focus of our paper.

We introduce here the flexible multiple gate delay (MGD) structure with adjustable parameters, and we present a method to optimize these parameters. We show the performance of MGD structures in multipath channels, with a particular attention to the situations with more than 2 paths (which are typically neglected in the literature, when analyzing the multipath error envelopes of delay tracking units). We also present, for the first time to the authors' knowledge, a comparison between using squared-envelopes versus envelopes before noncoherent integration stage as well as a comparison between using uniform versus nonuniform gate spacings in delay tracking units.

We then validate the MGD structures via implementation in a Simulink-based navigation tool, GRANADA. Based on the presented MGD structures, we also develop a flexible delay tracking prototype receiver (in SystemC and VHDL) for Galileo and GPS signals. The main focus is on sine-BOC and BPSK-modulated signals, but the design steps shown here can be extended in a straightforward manner to other BOC modulations (cosine BOC, multiplexed BOC, alternate BOC, etc.).

In the delay tracking receiver prototyping, we focus on the implementability, complexity, and flexibility of the proposed MGD structures. First, we present the implementations and discuss about the flexibility and the restrictions caused mostly by the digital hardware characteristics. Then, we verify the implementability of the chosen algorithms with a SystemC model. After that, the complexity of the implemented prototype hardware is evaluated as VHDL synthesis results.

2. COMMON DELAY TRACKING STRUCTURES FOR GNSS SIGNALS

The most common delay tracking loops for GNSS signals are based on feedback delay locked loop (DLL)-like structures. The state-of-art delay trackers, which are widely used in GNSS industry nowadays, include: the narrow early-minus-late (NEML) correlator [1–3, 10, 11] and the double-delta correlators [2, 15–17], also known under the names of pulse aperture correlator (PAC) [7], strobe correlator [2, 6, 18], or high resolution correlator (HRC) [3, 5, 19].

All the above-mentioned methods have a common underlying structure, in the sense that they are based on different weighted combinations of early and late samples of the correlation function with different chip-spacings between these samples. In what follows, we will first introduce the signal model for Galileo and GPS signals, then, we present the above-mentioned methods in more detail. We will then show that most of the currently used delay tracking structures (i.e., those mentioned above) can be unified under a generic structure, namely the multiple gate delay (MGD) structure, whose parameters are to be optimized in Section 3.

Typical satellite positioning signals, such as those used for GPS and Galileo, employ the direct-sequence code division multiple access (DS-CDMA) technique, where a PRN code is spreading the navigation data over S_F chips (or over a code epoch length) [20, 21]. In what follows, we adopt, for clarity reasons, a baseband model. Also, the delay tracking estimation in nowadays receivers is typically done in digital domain (using the baseband correlation samples). The time notation t stands for discrete time. The transmitted signal $x(t)$ can be written as the convolution between the modulating waveform $s_{\text{mod}}(t)$, the PRN code, including data modulation, and the pulse shaping filter $p_{T_B}(t)$ [22]:

$$x(t) = \sqrt{E_b}s_{\text{mod}}(t) \circledast \sum_{n=-\infty}^{+\infty}\sum_{k=1}^{S_F} b_n c_{k,n}\delta(t - nT_{\text{sym}} - kT_c) \circledast p_{T_B}(t), \qquad (1)$$

where E_b is the data bit energy, $\circledast$ is the convolution operator, b_n is the nth complex data symbol, $T_c = 1/f_c$ is the chip period, S_F is the spreading factor, T_{sym} is the symbol period ($T_{\text{sym}} = S_F T_c$), $c_{k,n}$ is the kth chip corresponding to the nth symbol, $\delta(t)$ is the Dirac pulse, and $p_{T_B}(t)$ is the pulse shaping filter applied to pulses of duration $T_B = T_c/N_B$. Here, N_B is a modulation-related parameter that is detailed in what follows. For example, if infinite bandwidth is assumed, $p_{T_B}(t)$ is a rectangular pulse of unit amplitude if $0 \le t \le T_B$ and 0 otherwise.

The signal $x(t)$ is typically transmitted over a multipath static or fading channel, where all interference sources (except the multipaths) are lumped into a single additive Gaussian noise term $\eta(t)$:

$$r(t) = \sum_{l=1}^{L}\alpha_l e^{-j\theta_l}x(t-\tau_l)e^{-j2\pi f_D t} + \eta(t), \qquad (2)$$

where $r(t)$ is the received signal, L is the number of channel paths, α_l is the amplitude coefficient of the lth path, θ_l is the phase of the lth path, τ_l is the channel delay introduced by the lth path, f_D is the Doppler shift introduced by the channel, and $\eta(t)$ is the complex additive Gaussian noise of zero mean and double-sided power spectral density N_0.

Typically, the signal-to-noise ratios for GNSS signals are expressed with respect to the code epoch bandwidth B_w, under the name of carrier-to-noise ratio (CNR). The relationship between CNR and bit-energy-to-noise ratio is [23]

$$\text{CNR[dB-Hz]} = \frac{E_b}{N_0} + 10\log_{10}(B_w). \qquad (3)$$

The delay tracking is typically based on the code epoch-by-code epoch correlation $\mathcal{R}(\cdot)$ between the incoming signal and the reference $x_{\text{ref}}(\cdot)$ modulated PRN code, with a certain candidate Doppler frequency $\hat{f}_D$ and delay $\hat{\tau}$:

$$\mathcal{R}(\hat{\tau}, \hat{f}_D, m) = \mathbf{E}\left(\frac{1}{T_{\text{sym}}}\int_{(m-1)T_{\text{sym}}}^{mT_{\text{sym}}} r(t)x_{\text{ref}}(\hat{\tau}, \hat{f}_D)dt\right), \qquad (4)$$

where m is the code epoch index, and $\mathbf{E}(\cdot)$ is the expectation operation, with respect to the PRN code, and

$$\begin{aligned} x_{\text{ref}}(\hat{\tau}, \hat{f}_D) &= \left(s_{\text{mod}}(t) \circledast \sum_{n=-\infty}^{+\infty}\sum_{k=1}^{S_F}\hat{b}_n c_{k,n}\delta(t - nT_{\text{sym}} - kT_c) \circledast p_{T_B}(t)\right) \\ &\quad \times e^{+j2\pi\hat{f}_D t}, \end{aligned} \qquad (5)$$

where $\hat{b}_n$ are the estimated data bits. For Galileo signals, a separate pilot channel is transmitted, thus the data bits are known at the receiver [21]. In order to reduce the noise level, we can use coherent and/or noncoherent integration. The averaged coherent correlation function $\overline{\mathcal{R}}_c(\hat{\tau}, \hat{f}_D)$ can be written as

$$\overline{\mathcal{R}}_c(\hat{\tau}, \hat{f}_D) = \frac{1}{N_c}\sum_{m=1}^{N_c}\mathcal{R}(\hat{\tau}, \hat{f}_D, m), \qquad (6)$$

where N_c is the coherent integration time (expressed in code epochs or milliseconds for GPS/Galileo signals), and the averaged noncoherent correlation function $\overline{\mathcal{R}}_{nc}(\hat{\tau}, \hat{f}_D)$ can be written as

$$\overline{\mathcal{R}}_{nc}(\hat{\tau}, \hat{f}_D) = \frac{1}{N_{nc}} \sum_{N_{nc}} \left| \frac{1}{N_c} \sum_{m=1}^{N_c} \mathcal{R}(\hat{\tau}, \hat{f}_D, m) \right|^{\text{pow}_{nc}}, \qquad (7)$$

where N_{nc} is the noncoherent integration time, expressed in blocks of length N_c milliseconds (for clarity of presentation, we dropped the block indexes used in the noncoherent summation), and pow_{nc} is a power index used for noncoherent summation. The most encountered variants are: $\text{pow}_{nc} = 1$ (i.e., sum of absolute values) and $\text{pow}_{nc} = 2$ (i.e., sum of squared-absolute values).

The DLL-like structures form a discriminator function $D(\hat{\tau})$ based on the early and late correlations, and they estimate the channel first path delay from the zero crossings of this discriminator function. The discriminator functions for NEML [1–3, 10, 11] and HRC [3, 5, 19] are well defined in literature and their expressions as equations are, for NEML:

$$D(\hat{\tau}) = \overline{\mathcal{R}}_{c/nc}\left(\hat{\tau} + \frac{\Delta_1}{2}, \hat{f}_D\right) - \overline{\mathcal{R}}_{c/nc}\left(\hat{\tau} - \frac{\Delta_1}{2}, \hat{f}_D\right), \qquad (8)$$

and for HRC:

$$\begin{aligned} D(\hat{\tau}) = {} & a_1\left(\overline{\mathcal{R}}_{c/nc}\left(\hat{\tau} + \frac{\Delta_1}{2}, \hat{f}_D\right) - \overline{\mathcal{R}}_{c/nc}\left(\hat{\tau} - \frac{\Delta_1}{2}, \hat{f}_D\right)\right) \\ & + a_2\left(\overline{\mathcal{R}}_{c/nc}\left(\hat{\tau} + \frac{\Delta_2}{2}, \hat{f}_D\right) - \overline{\mathcal{R}}_{c/nc}\left(\hat{\tau} - \frac{\Delta_2}{2}, \hat{f}_D\right)\right). \end{aligned} \qquad (9)$$

In single-path channels ($L = 1$), the mentioned discriminator functions cross the zero level when $\hat{\tau} = \tau_1$. That is, the zero-crossings show the presence of a channel path. However, due to BOC modulation, we might have more zero-crossings present, and the search range should be restricted to the linear range of the discriminator function (for SinBOC(1,1)), this linear range goes from about −0.05 till about 0.05 chip error. In multipath channels, we also want to have $D(\tau_1) = 0$, τ_1 being the true line-of-sight (LOS) delay, in order to estimate correctly the first path delay. However, this is not always possible, and an estimation error might happen due to multipath presence, that is, $D(\tau_1 + e_{\text{me}}) = 0$. The term e_{me} is the multipath error. An example is shown in Figure 1 for two in-phase paths of amplitudes 0 and −1 dB and path spacing of 0.2 chips. In this example, $e_{\text{me}} = 0.01$ chips for HRC, and $e_{\text{me}} = 0.04$ chips for NEML (in single-path channel, we had $e_{\text{me}} = 0$ chips for both structures). The maximum and minimum multipath errors define the multipath error envelopes (MEEs), as it will be discussed in more detail in Section 3.

While it is generally known that the performance of coherent correlators outperforms that of the noncoherent correlators in ideal conditions (e.g., absence of fading or clock synchronization errors, perfect data bit estimation, etc.), the nonidealities of practical channels make that the structures of choice in most nowadays receivers are the noncoherent ones. This motivates our choice of noncoherent correlator gates in what follows.

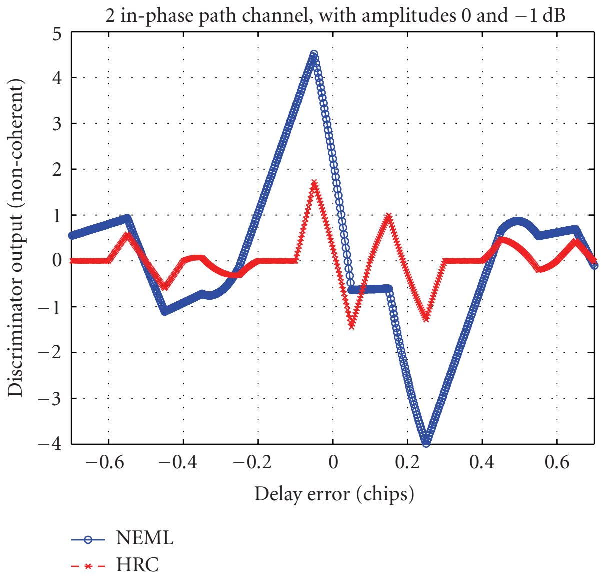

Figure 1: Examples of noncoherent discriminator outputs ($\text{pow}_{nc} = 2$) for two-path channels, for NEML and HRC correlators. SinBOC(1,1) signal, early-late spacing $\Delta_1 = 0.1$ chips.

3. MULTIPLE GATE DELAY (MGD) STRUCTURES

3.1. *Proposed architecture*

The proposed generalization of the NEML and double-delta structures (which cover most of the state-of-art delay tracking techniques used nowadays in industrial implementations) follows in a straightforward manner:

$$D(\hat{\tau}) = \sum_{i=1}^{N_g} a_i\left(\overline{\mathcal{R}}_{c/nc}\left(\hat{\tau} + \frac{\Delta_i}{2}, \hat{f}_D\right) - \overline{\mathcal{R}}_{c/nc}\left(\hat{\tau} - \frac{\Delta_i}{2}, \hat{f}_D\right)\right). \qquad (10)$$

Above, we have a weighted sum of N_g correlation pairs (or gates), with weighting factors a_i, $i = 1, \ldots, N_g$, and spacings between the ith early and the ith late gate equal to Δ_i. Uniform spacing between the gates (as that one used in NEML and double-delta correlators) means that $\Delta_i = i\Delta_1$, $i = 2, \ldots, N_g$. However, we need not to restrict our structure to uniform spacing alone. The above discriminator function characterizes the proposed multiple gate delays (MGDs). The first coefficient a_1 is normalized, in what follows, to 1 without loss of generality. An example of the discriminator function for MGD with uniform and nonuniform spacings is shown in Figure 2. For 2-path channel, the same channel profile as in Figure 1 was used. The multipath errors in these cases are: $e_{\text{me}} = -0.0025$ chips for MGD with uniform spacing and $e_{\text{me}} = 0.0150$ chips for MGD with nonuniform spacing.

The block diagram of the generic MGD structures is shown in Figure 3. The incoming signal is correlated with the reference, BOC or BPSK-modulated PRN code, via N_g gates or correlator pairs, and, then, it is coherently and noncoherently integrated. The coherent and noncoherent integration blocks are optional, but they usually should be

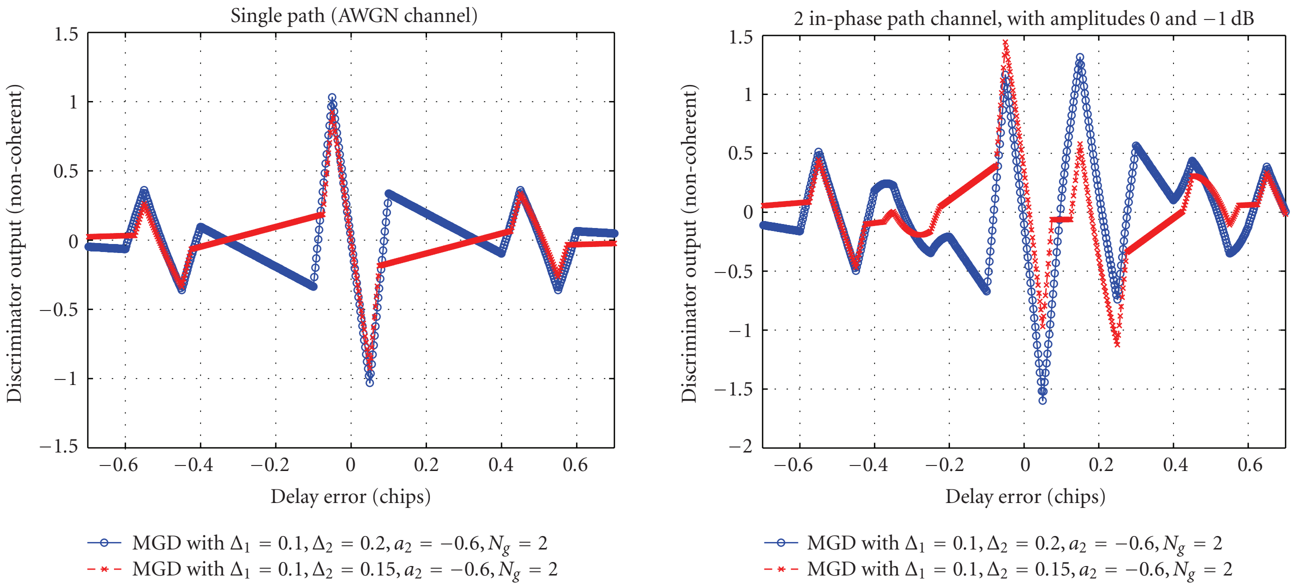

(a)

(b)

Figure 2: Examples of noncoherent discriminator outputs ($\text{pow}_{nc} = 2$) for single-path and two-path channels, for 2 types of MGD correlators, each with $N_g = 2$ gate pairs: uniform spacing ($\Delta_2 = 2\Delta_1$) versus decreasing spacing ($\Delta_2 = 1.5\Delta_1$). SinBOC(1,1) signal, early-late spacing $\Delta_1 = 0.1$ chips. $a_1 = 1$ for both structures.

employed for a better robustness against noise. The type of nonlinearity that can be used in the implementation is determined by the factor pow_{nc}, with typical values: $\text{pow}_{nc} = 1$ (envelope) or $\text{pow}_{nc} = 2$ (squared envelope). The choice of nonlinearity type is usually motivated by the design constraints (e.g., complexity of squaring versus taking absolute value, possible need for analytical models, which are easier to derive in the case of squared envelopes, via chi-squared statistics, etc.), therefore we will analyze both cases ($\text{pow}_{nc} = 1, 2$) in what follows. To the authors' knowledge, a comparison between squared envelopes and envelopes used in noncoherent integration is not yet available in the GNSS literature.

We remark that the structure shown in Figure 3 is not the only one possible; we might, in fact, combine the early-late gates after the discriminator function. Such structures have been analyzed in [24] and were shown to give worse results than the MGD structure selected here.

We also notice that the term of MGD has been used before in [15, 16]. We kept the same MGD nomination, since it is quite a generic one, but, by difference with our proposed MGDs, the discriminator formed in [15, 16] is a normalized discriminator, and the choice of the weighting parameters is not optimized. It is not surprising then, that, while getting rid of the false lock point problem, the MGD structures proposed in [15, 16] have even poorer code tracking performance than the narrow correlator [16].

We also remark that the linear combination of weighted correlation in order to shape the discriminator function has been also considered in [25]. There, the coefficients are optimized reducing the value of the correlation function outside the region ± 1 chip therefore consequently reducing the multipath error envelope area. However, the approach presented in [25] has been tested only for 2-path channels, with second path weaker than LOS path, and the optimization steps for other multipath scenarios seem to depend on previous knowledge about multipath profiles, which is not usually available. Our approach is different in the sense that we do not try to reach an optimal discriminator shape, but the optimization is done according to the estimated multipath errors, in such a way to minimize them, on average (i.e., under the assumption of various statistical distributions of channel paths, this optimization is performed, and the MGD parameters are found).

The next step is to choose the MGD parameters, namely the number of gating pairs N_g, the weighting coefficients a_i, and the gate spacings Δ_i. This choice is done according to an optimization criterion defined in the presence of multipath channels, as given in Section 3.2.

3.2. Optimization criterion

The typical criterion to evaluate the performance of a delay tracking unit in the presence of multipaths is the multipath error envelope (MEE) [1]. Typically, two paths, either in-phase or out-of-phase, are assumed to be present, and the multipath error is computed versus the path spacing. The upper error envelope is obtained when the paths are in-phase and the lower error envelope when the paths have 180° phase difference. The MEEs depend on the type and length of the PRN codes, on the additive white Gaussian noise (AWGN) level, and on the residual Doppler shift errors coming from the acquisition stage. However, in order to distinguish the performance deterioration due to multipath

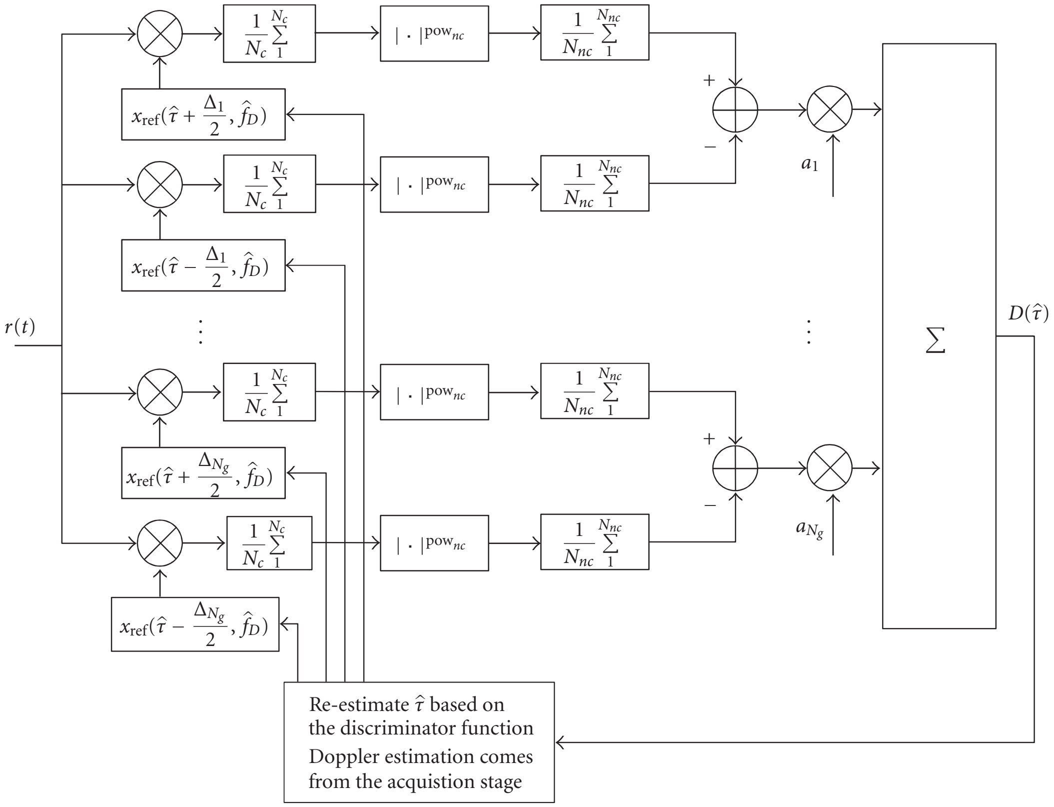

Figure 3: Block diagram of MGD delay tracking structures.

errors only, several simplifying assumptions can be made, such as: zero AWGN, ideal infinite-length PRN codes, and zero residual Doppler ($f_D = \hat{f}_D$). Under these assumptions, after straightforward manipulations of (1), (2), (4), (5), (6), and (7), for noncoherent integration we obtain the following:

$$\overline{\mathcal{R}}_{nc}(\hat{\tau},\hat{f}_D) = \left|\sqrt{E_b}\sum_{l=1}^{L}\alpha_l e^{-j\theta_l}\mathcal{R}_{\mathrm{mod}}(\hat{\tau}-\tau_l)\right|^{\mathrm{pow}_{nc}}, \tag{11}$$

where $\mathcal{R}_{\mathrm{mod}}(\tau)$ is the autocorrelation function of the modulated PRN code, given by [22]

$$\mathcal{R}_{\mathrm{mod}}(\tau) = \Lambda_{T_B}(t) \circledast \sum_{k=0}^{N_{B_2}-1}\sum_{k_1=0}^{N_{B_2}-1}\sum_{i=0}^{N_{B_1}-1}\sum_{i_1=0}^{N_{B_1}-1}(-1)^{k+k_1+i+i_1} \times \delta(t - iT_{B_1} + i_1T_{B_1} - kT_B + k_1T_B), \tag{12}$$

where $\Lambda_{T_B}(t) = p_{T_B} \circledast p_{T_B}$ is the triangular pulse of support $2T_B$, shown in Figure 4.

The MEEs can be then computed straightforwardly, under these ideal conditions, from (10), (11), and (12) (noncoherent structures), by considering two-paths in-phase and out-of-phase channels. However, since the multipath profiles cannot be known in advance, we can compute some averaged MEEs, when the second-path amplitude varies. The approach selected by us was to consider that the first channel path has a unit amplitude, and the second-path amplitude varies uniformly between 0.3 and 1.0. The final MEEs will be obtained as an average of all MEEs for each channel profile.

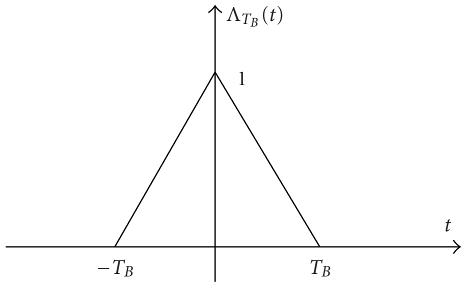

Figure 4: Illustration of a triangular pulse $\Lambda_{T_B}(t)$ of support $2T_B$.

A good delay tracking structure should furnish small average errors, small worst errors, and small maximum multipath spacing after which MEE becomes 0. The proposed optimization criterion, derived by intuitive reasoning is the area enclosed by the absolute value of the upper MEE and the absolute value with minus sign of the lower MEE. The illustration of this "enclosed area" principle is shown in Figure 5 for a MGD structure with 3 gate pairs, squared absolute value ($\mathrm{pow}_{nc} = 2$), and delta spacings and weighting coefficients shown in the figure's caption. The "enclosed area" is shown in dashed lines. We remark that the units

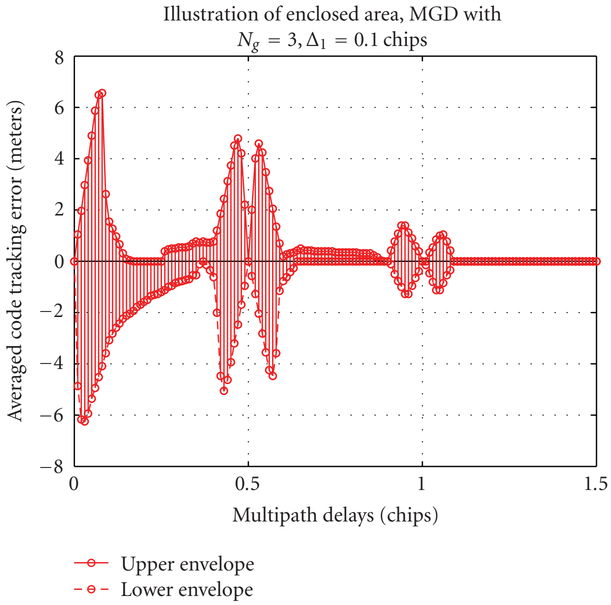

Figure 5: Illustration of the "enclosed area" principle for 2 path channel. Noncoherent MGD structure with $\text{pow}_{nc} = 2$, $N_g = 3$, $a_1 = 1$, $a_2 = -0.7$, $a_3 = 0.1$, and $\Delta_1 = 0.1$ chips, $\Delta_2 = 0.2$ chips, $\Delta_3 = 0.3$ chips.

to measure this area are the units of MEEs (e.g., chips or meters); here the errors are shown in meters, knowing that one chip error corresponds to 293.25 m (if the chip rate is 1.023 MHz).

3.3. *Tables with optimized parameters and interpretation of results*

As mentioned before, the parameters to be optimized are: the number of gate pairs N_g, the delta (or early-late) spacings Δ_i, the weighting coefficients $a = \{a_i\}_{i=1,\ldots,N_g}$, and the type of nonlinearity pow_{nc}. Three types of delta spacings have been studied here.

(1) Uniform spacing: $\Delta_i = i\Delta_1,\ i = 2,\ldots,N_g$.

(2) Decreasing spacing: $\Delta_i = ((2^i - 1)/2^{i-1})\Delta_1,\ i = 2,\ldots,N_g$.

(3) Increasing spacing: $\Delta_i = ((2^i + 1)/2)\Delta_1,\ i = 2,\ldots,N_g$.

The target was to minimize the area enclosed by the averaged MEEs, when the amplitude of the second channel path varied between 0.3 and 1.0 (linear scale), and the multipath spacing varied between 0 and 1.5 chips (with a step of 0.01). For convenience and without loss of generality, we normalized the weighting coefficients with respect to the first one. Thus, $a_1 = 1$, and the search ranges for a_i were between -1 and $+1$, with a step of 0.1.

First, we had a look at the minimum enclosed areas for $N_g = 2$ and $N_g = 3$ (in order to see the effect of increasing the number of gating pairs), and for the two types of nonlinearities $\text{pow}_{nc} = 1$ and $\text{pow}_{nc} = 2$. For SinBOC(1,1) modulation, the minimum enclosed areas are shown in Tables 1 and 2, and they correspond to the optimum coefficients given (partly) in Table 3 (only the most illustrative cases, i.e., uniform and decreasing spacings, are shown in this last referenced table).

Two well-known reference structures are also shown here for comparison purposes: the narrow correlator NEML and the high resolution correlator (HRC), both with $\text{pow}_{nc} = 1$ (which proved better than $\text{pow}_{nc} = 2$). In fact, both these structures are particular cases of the proposed MGDs: NEML has $a = [1, 0, 0]$, as shown in (8), HRC has $a = [1, -0.5, 0]$, and $\Delta_2 = 2\Delta_1$ (uniform spacing), according to (9).

If we compare Table 1 ($N_g = 2$) with Table 2 ($N_g = 3$), we remark that, by increasing the number of gate pairs, we may decrease the enclosed MEE area, and, thus, we may increase the multipath robustness. In the worst case, the areas remain the same when going from $N_g = 2$ to $N_g = 3$ gate pairs, which means that the optimum is already achieved with a double-delta correlator-like structure. In this situation, the optimum is typically given by HRC (see the last column of Tables 1 and 2). We also remark that the reduction of the enclosed area is not very large when we increase the number of gate pairs, which might justify the fact that we limit our structures to a maximum of $N_g = 3$ gate pairs (further increase in the number of gate pairs will boost the complexity, while providing only marginal benefit in terms of robustness against multipaths).

It is also seen from Tables 1 and 2 that using envelopes ($\text{pow}_{nc} = 1$) instead of squaring envelopes ($\text{pow}_{nc} = 2$) gives better results. Also, using a decreasing delta spacing instead of uniform delta spacing is generally better. Similar conclusions have been achieved also for GPS BPSK-modulated signals.

The optimum pairs of coefficients for the two nonlinearity types are shown in Table 3, for SinBOC(1,1) modulation, and in Table 4 for BPSK modulation. Only uniform and decreasing delta spacings are considered here, since the increasing delta spacing was clearly much worse than the other two types of spacing (as seen in Tables 1 and 2).

An illustration of the averaged MEEs for the narrow correlator, high resolution correlator, MGD with uniform spacing ($a_1 = 1$, $a_2 = -0.7$, $a_3 = -0.2$), and MGD with decreasing spacing ($a_1 = 1$, $a_2 = -0.9$, $a_3 = 0.2$) is shown in Figure 6, for SinBOC(1,1) signal, envelope-based nonlinearity ($\text{pow}_{nc} = 1$), and 0.25 chips minimum early-late spacing. The average is done with respect to the second channel path amplitude, which varies uniformly between 0.3 and 1.0 (when first channel path has unit amplitude). As discussed before, the best results among these 4 algorithms are obtained with the decreasing spacing, but the differences between the 4 considered tracking structures are not very large.

The values shown in Tables 3 and 4 give the designer the possibility of a wide choice of MGD parameters, according to the desired nonlinearity type (imposed, for example, by hardware restrictions) and to the desired minimum early-late spacing Δ_1. As seen in Tables 1 and 2, the smaller the minimum early-late spacing, the better the multipath performance. However, as mentioned in [23], the delay tracking error decreases with the early-late spacing only if we

Table 1: Minimum enclosed areas [chips] (i.e., for optimum coefficient pairs), $N_g = 2$, SinBOC(1,1) signal. Minimum early-late spacing Δ_1 is given in chips.

	$\text{pow}_{nc} = 1$			$\text{pow}_{nc} = 2$			Reference NEML $\text{pow}_{nc} = 1$	Reference HRC $\text{pow}_{nc} = 1$
	unif. spacing	decr. spacing	incr. spacing	unif. spacing	decr. spacing	incr. spacing		
$\Delta_1 = 0.1$	0.36	0.45	0.46	0.45	0.41	0.59	1.72	0.36
$\Delta_1 = 0.2$	1.49	1.24	1.79	1.61	1.27	1.94	3.15	1.49
$\Delta_1 = 0.3$	3.14	2.37	4.14	3.51	2.36	4.14	4.31	3.57

Table 2: Minimum enclosed areas [chips] (i.e., for optimum coefficient pairs), $N_g = 3$, SinBOC(1,1) signal. Minimum early-late spacing Δ_1 is given in chips.

	$\text{pow}_{nc} = 1$			$\text{pow}_{nc} = 2$			Reference NEML $\text{pow}_{nc} = 1$	Reference HRC $\text{pow}_{nc} = 1$
	unif. spacing	decr. spacing	incr. spacing	unif. spacing	decr. spacing	incr. spacing		
$\Delta_1 = 0.05$	0.08	0.06	0.11	0.11	0.07	0.11	0.88	0.08
$\Delta_1 = 0.1$	0.36	0.24	0.46	0.43	0.34	0.55	1.72	0.36
$\Delta_1 = 0.15$	0.82	0.57	1.04	0.94	0.70	1.18	2.46	0.82
$\Delta_1 = 0.2$	1.49	1.02	1.58	1.59	1.24	1.92	3.15	1.49
$\Delta_1 = 0.25$	2.04	1.68	2.95	2.33	1.77	3.07	3.77	2.46
$\Delta_1 = 0.3$	2.72	2.30	3.91	3.51	2.36	4.10	4.31	3.57
$\Delta_1 = 0.35$	3.57	3.19	4.63	3.95	3.31	4.59	4.64	4.48

Table 3: Optimum coefficient pairs a_i. $N_g = 3$. SinBOC(1,1) signal (Galileo). Minimum early-late spacing Δ_1 is given in chips.

	$\text{pow}_{nc} = 1$					
	unif. spacing			decr. spacing		
	a_1	a_2	a_3	a_1	a_2	a_3
$\Delta_1 = 0.05$	1	−0.5	0.0	1	−0.9	0.2
$\Delta_1 = 0.1$	1	−0.5	0.0	1	−0.9	0.2
$\Delta_1 = 0.15$	1	−0.5	0.0	1	−0.9	0.2
$\Delta_1 = 0.2$	1	−0.5	0.0	1	−0.9	0.2
$\Delta_1 = 0.25$	1	−0.7	−0.2	1	−0.9	0.2
$\Delta_1 = 0.3$	1	−1.0	−0.4	1	−0.8	0.1
$\Delta_1 = 0.35$	1	−1.0	0.5	1	−0.7	−0.1
	$\text{pow}_{nc} = 2$					
	unif. spacing			decr. spacing		
	a_1	a_2	a_3	a_1	a_2	a_3
$\Delta_1 = 0.05$	1	−0.8	0.2	1	−0.8	0.1
$\Delta_1 = 0.1$	1	−0.7	0.1	1	−0.5	−0.2
$\Delta_1 = 0.15$	1	−0.8	0.1	1	−1.0	0.2
$\Delta_1 = 0.2$	1	−0.9	0.1	1	−1.0	0.2
$\Delta_1 = 0.25$	1	−1.0	0.0	1	−1.0	0.1
$\Delta_1 = 0.3$	1	−1.0	0.0	1	−1.0	0.0
$\Delta_1 = 0.35$	1	−1.0	0.5	1	−1.0	−0.1

Table 4: Optimum coefficient pairs a_i. $N_g = 3$. BPSK signal (GPS). Minimum early-late spacing Δ_1 is given in chips.

	$\text{pow}_{nc} = 1$					
	unif. spacing			decr. spacing		
	a_1	a_2	a_3	a_1	a_2	a_3
$\Delta_1 = 0.05$	1	−0.5	0.0	1	−0.4	−0.2
$\Delta_1 = 0.1$	1	−0.5	0.0	1	−0.9	0.2
$\Delta_1 = 0.15$	1	−0.5	0.0	1	−0.2	−0.4
$\Delta_1 = 0.2$	1	−0.5	0.0	1	−0.9	0.2
$\Delta_1 = 0.25$	1	−0.5	0.0	1	−1.0	0.3
$\Delta_1 = 0.3$	1	−0.5	0.0	1	−0.9	0.2
$\Delta_1 = 0.35$	1	−0.5	0.0	1	−1.0	0.3
	$\text{pow}_{nc} = 2$					
	unif. spacing			decr. spacing		
	a_1	a_2	a_3	a_1	a_2	a_3
$\Delta_1 = 0.05$	1	−0.5	0.0	1	−0.2	−0.4
$\Delta_1 = 0.1$	1	−0.8	0.2	1	−0.8	0.1
$\Delta_1 = 0.15$	1	−0.4	−0.1	1	−0.9	0.2
$\Delta_1 = 0.2$	1	−0.8	0.2	1	−0.7	0.0
$\Delta_1 = 0.25$	1	−0.7	0.1	1	−0.7	0.0
$\Delta_1 = 0.3$	1	−0.7	0.1	1	−0.6	−0.1
$\Delta_1 = 0.35$	1	−0.7	0.1	1	−0.5	−0.2

assume infinite bandwidth. If the bandwidth is limited, there is a lower bound limit on the minimum early-late spacing. Although closed form expressions for this limit do not exist, a coarse limitation of the order of $\Delta_1 = 1/B_{rx}$ has been derived in [26], where B_{rx} is the receiver front-end bandwidth. For example, if the receiver bandwidth is limited to 20 MHz, the minimum early-late spacing that we can use will be around $\Delta_1 = 0.05$ chips. Decreasing the early-late spacing below this limit will not provide any additional benefit in terms of code tracking error, it will only decrease the linear range of the discriminator. A large linear range of the discriminator curve is also important, since it is directly related to the ability of the loop to keep the lock. The linear range is directly proportional with half of the early-late spacing $\Delta_1/2$, as illustrated in Figure 7 (there, the linear range for $\Delta_1 = 0.1$ chips goes from -0.05 till 0.05 chips, and the linear range for $\Delta_1 = 0.3$ chips goes from -0.1 till 0.1 chips, with high likelihood that the loop will not lose lock as long as the error is below 0.15 chips in absolute value, due to the piecewise linear and monotonic shape of the discriminator in the region -0.15 to 0.15 chips). An approximation of the linear range of the discriminator is therefore given by $\Delta_1/2$. Thus, when choosing Δ_1, the designer should take into account the multipath performance, on one hand, and the bandwidth limitations and linear range constraints, on the other hand.

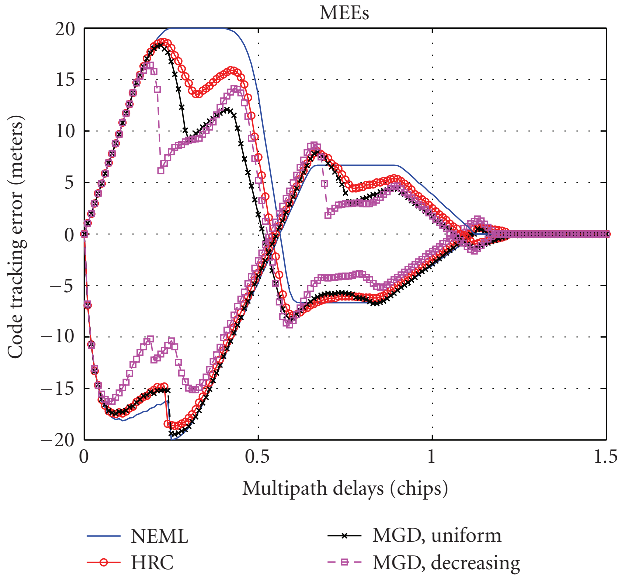

FIGURE 6: Illustration of the averaged MEEs for NEML, HRC, and two MGDs with optimal parameters as given in Table 3 (for uniform and decreasing spacings). $\text{pow}_{nc} = 1$, $\Delta_1 = 0.25$ chips, and SinBOC(1,1) signals.

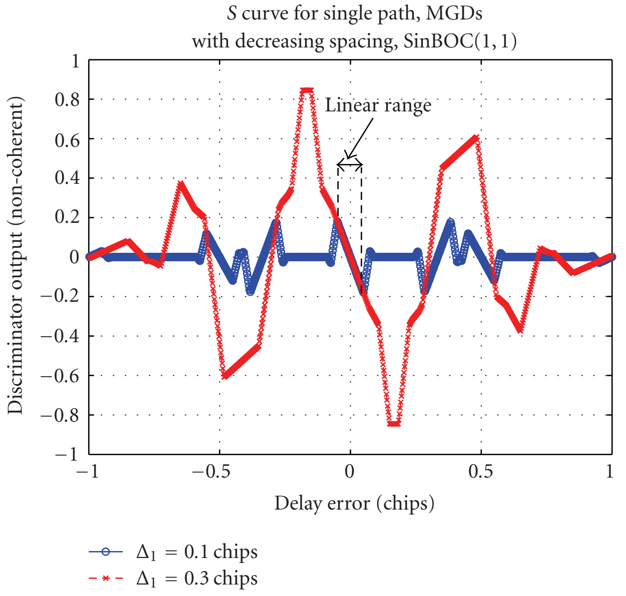

FIGURE 7: Illustration of the linear range of the discriminator, when we increase the minimum early-late spacing. MGDs with $N_g = 3$, decreasing spacings, $\text{pow}_{nc} = 1$, and optimal parameters as given in Table 3.

3.4. *MEEs for more than 2 paths*

When we want to analyze the MEEs in channels with more than 2 paths, there are no analytical expressions to compute them, due to the complexity of channel interactions. Thus, we cannot know if the “worst” case errors happen when all the paths are in phase or when they have alternate phases, and so forth. The solution we propose here in order to compute MEEs for multiple-paths channels is based on Monte-Carlo simulations: we generate a sufficient number of random channel realizations N_{random}, and we look at the highest positive and negative multipath errors over the N_{random} points. The goal is to study the MGD performance in multipath channels with more than 2 channel paths (which may occur especially in and urban indoor scenarios). For this purpose, we consider that the channel impulse response $h(t)$ is given by (same notations from (2) are used here)

$$h(t) = \sum_{l=1}^{L} \alpha_l e^{-j\theta_l} \delta(t - \tau_l). \tag{13}$$

We made the following assumptions during the following simulations: that the channel has a decaying power delay profile (PDP), meaning that $\alpha_l = \alpha_1 e^{-\mu(\tau_l - \tau_1)}$, where μ is the PDP coefficient (assumed in the simulations to be uniformly distributed in the interval [0.5; 1] when the path delays are expressed in samples), that the channel path phases θ_l are uniformly distributed in the interval $[0;\ 2\pi]$, that the number of channel paths L is uniformly distributed between 2 and $L_{\max}$ (with $L_{\max} = 3, 4, \ldots, n$), and that the successive path spacing $\tau_l - \tau_{l-1}$ is uniformly distributed in the interval $[1/N_s N_B;\ x_{\max}]$, where N_s is the oversampling factor or number of samples per BOC interval (a parameter which defines the resolution of the delay estimates), and $x_{\max}$ is the maximum value of the successive path spacing (which will define the multipath delay axis in the MEE curves). It follows that, for each channel realization (meaning a combination of amplitudes $\underline{\alpha} = \alpha_1, \ldots, \alpha_L$, phases $\underline{\theta} = \theta_1, \ldots, \theta_L$, path spacings, and number of channel paths L), a certain LOS delay is estimated $\hat{\tau}_1(\underline{\alpha}, \underline{\theta}, L)$ from the zero crossing of the discriminator function $(D(\tau)|_{\hat{\tau}_1(\underline{\alpha},\underline{\theta},L)} = 0)$, searched in the linear region of $D(\cdot)$. The LOS estimation error is thus $\hat{\tau}_1(\underline{\alpha}, \underline{\theta}, L) - \tau_1$, where τ_1 is the true LOS path delay. The multipath error envelopes (upper and lower) for a particular path spacing $x_{\max}$ can be therefore computed as

$$\begin{aligned} \text{MEE}_{\text{upper}}(x_{\max}) &= \max_{\underline{\alpha},\underline{\theta},L}\left(\hat{\tau}_1(\underline{\alpha}, \underline{\theta}, L) - \tau_1\right), \\ \text{MEE}_{\text{lower}}(x_{\max}) &= \min_{\underline{\alpha},\underline{\theta},L}\left(\hat{\tau}_1(\underline{\alpha}, \underline{\theta}, L) - \tau_1\right). \end{aligned} \tag{14}$$

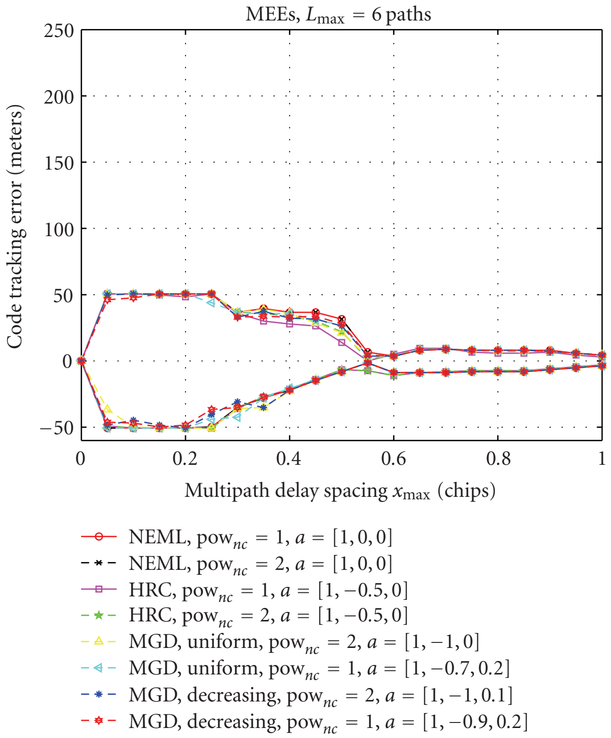

FIGURE 8: Multipath error envelopes for channels with more than 2 paths ($L_{\max} = 6$ paths), minimum early-late spacing $\Delta_1 = 0.25$ chips, SinBOC(1,1) signal.

The results based on the above rule are shown in Figure 8 for $L_{\max} = 6$ maximum channel paths. Similar results have been achieved also for $L_{\max}$ between 3 and 5 paths, with the only difference that the MEE levels are increasing when the number of path increases (this can be noticed also if we compare Figure 8 with Figure 6). Several structures with optimized parameters as given in Table 3 and different nonlinearity types were used here. The surprising result is that the higher the number of channel paths is, the more the performance of various MGD structures becomes similar for all the considered algorithms (and they all reach the performance of the narrow correlator). It follows that the main advantage of the proposed MGD structures comes from the fact that they offer patent-free alternatives to the current narrow and double-delta correlators, by preserving the same performance in realistic multipath channels.

4. SIMULINK/GRANADA-BASED IMPLEMENTATION

4.1. *Model description*

The Galileo receiver analysis and design application (GRANADA), developed by Deimos Space within GARDA project, is one of the popular GNSS simulation tools nowadays. It consists of two parts: Bit-true GNSS SW receiver simulator and GNSS Environment and Navigation simulator. Since the Bit-true GNSS SW receiver simulator is created based on the Simulink/Matlab, it is easy to be modified for new receiver technologies. This simulator is currently used by several universities and researchers [16, 27–29].

The GRANADA Bit-true GNSS SW receiver simulator is made up by three parts: the transmitter block, the propagation channel block, and receiver block, as shown in Figure 9. The transmitter block includes the code generation, BOC modulation, and channel multiplexing. The propagation channel model takes into consideration the multipaths, the AWGN noise, and a few other possible sources of interference, such as the wideband interference from other satellites. The receiver block contains basically receiver front end, acquisition, and code tracking blocks. The general architecture of receiver is shown in Figure 10. After some modification in GRANADA version 2.02, which is distributed under Galileo supervisory authority (GSA) licenses, it can be used for testing the performance of MGD structure. The modifications made to GRANADA tool are explained with details in [29, 30].

4.2. *Results in AWGN and multipath static and fading channels*

In order to evaluate the performance of the new structures, root mean square error (RMSE) between the estimated delay and the true LOS delay is calculated. In order to test the DLL performance in the noise presence, we chose three kinds of channel profiles: single-path static channel, two-path static channel, and four-path fading channel, as shown in Table 5.

Figures 11, 12, and 13 show the RMSE values of different algorithms in the different channel settings. Since the received signal cannot get synchronized in the acquisition stage of GRANADA when CNR is below 35 dB-Hz, we calculate the RMSE values from 35 dB-Hz to 50 dB-Hz. Structures with early-late spacing $\Delta_1 = 0.1$ chips have been selected for comparison purpose, but similar results (which are in accordance with the models given in Section 3) were obtained for other early-late spacings as well.

Besides the MGD structures described in Section 3, we also considered here a normalized MGD structure, where the discriminator function is normalized by the weighted sum of early and late correlations, similar with [15, 16]:

$$D_{\text{norm}}(\hat{\tau}) = \frac{D(\hat{\tau})}{\sum_{i=1}^{N_g} a_i\left(\overline{\mathcal{R}}_{c/nc}(\hat{\tau}+\Delta_i/2,\hat{f}_D)+\overline{\mathcal{R}}_{c/nc}(\hat{\tau}-\Delta_i/2,\hat{f}_D)\right)}. \tag{15}$$

The purpose of including the normalized MGD in the comparison was to show that the normalized MGD structures of [15, 16] have worse performance than the un-normalized structures proposed by us.

The delay error between the initial code replica in the receiver and the received signal has not been taken into account. The estimated delay values used for calculating RMSE are taken after the transient stage in the beginning of the tracking stage. From Figures 11 and 12, the simulation results in the static channel show that as CNR increases, the estimation delay errors converge to the corresponding value in the MEEs.

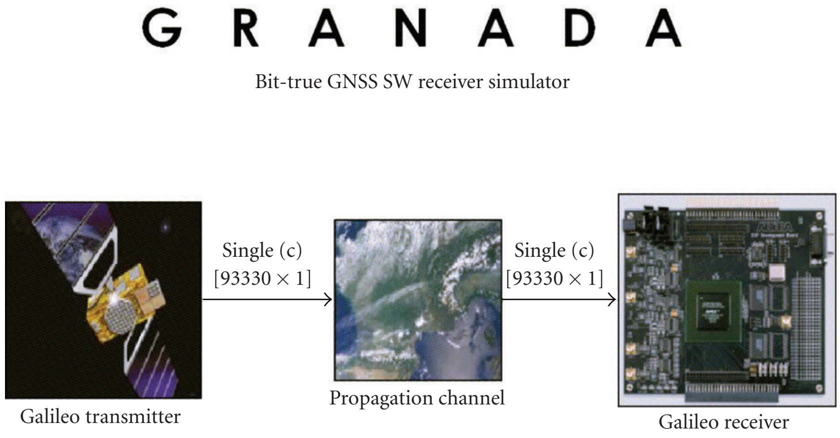

Figure 9: The basic diagram of GRANADA Bit-true software receiver simulator.

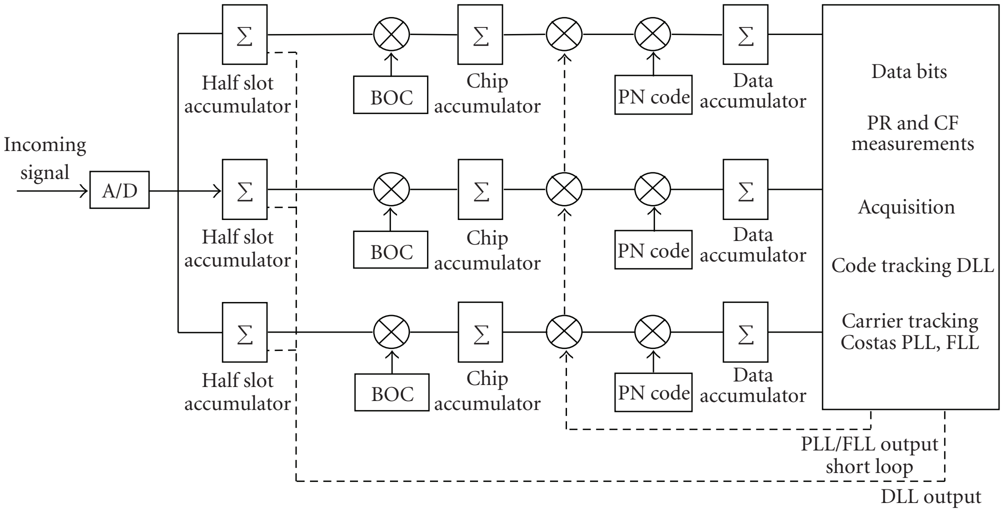

Figure 10: The simplified baseband receiver diagram in GRANADA (NEML).

For scenario 1, the estimated delay errors are caused by the noise only, since there is only LOS signal in the propagation channel. As the CNR increases, the RMSE value of each algorithm gets close to 0. When CNR is equal to 50 dB-Hz, the RMSE values are below 0.5 meters. From the single path simulation results, we notice that all these algorithms have similar performance in the AWGN channel, as desired.

For scenario 2, as the CNR increases, the RMSE value of each algorithm converge to different values. This is because the RMSE value takes both bias and variance into account. The variance is caused by the noise and decreases when CNR increases. However, the bias is caused by the multipath in the channel and is equal to the corresponding point in the MEEs. For instance, as the CNR increases, the RMSE values of NEML algorithm converge to 11 meters, which is the same value in the MEEs according to the channel profile of scenario 2. The normalized MGD has worse behavior than an un-normalized MGD with the same parameters.

From Figure 12, it is clear that the HRC algorithm and MGD algorithm with weighting factors $a = (1, -0.6, 0)$ show better performance than NEML algorithm, and MGD algorithm with $a = (1, -0.7, 0.1)$ (i.e., optimum parameters) shows the best performance among all considered algorithms (which is in accordance with the theoretical derivations in Section 3.2).

In the multipath fading channel, the LOS signal follows Rician distribution, and the NLOS signals follow Rayleigh distribution. The mean power and delay of each ray are described in Table 5. Figure 13 shows that the RMSE value of NEML is much higher than other algorithms, especially when CNR is 35 dB-Hz, it gets till 172 meters (not shown in the figure in order to get a better scale). An MGD structure with weighting factor $a = (1, -0.7, 0.1)$ shows again the best performance among the algorithms, as expected, according to the optimization results given in Section 3. The RMSE performance of normalized MGD algorithm is quite poor in fading channels.

Table 5: Simulation scenarios for Simulink/GRANADA-based simulations.

Scenario	Multipath model	Path delay (chip)	Relative path gain (dB)
Scenario 1	single-path static channel	0	0
Scenario 2	two-path static channel	[0 0.2]	[0 −3]
Scenario 3	four-path fading channel	[0 0.2 0.4 0.6]	[0 −1 −2 −3]

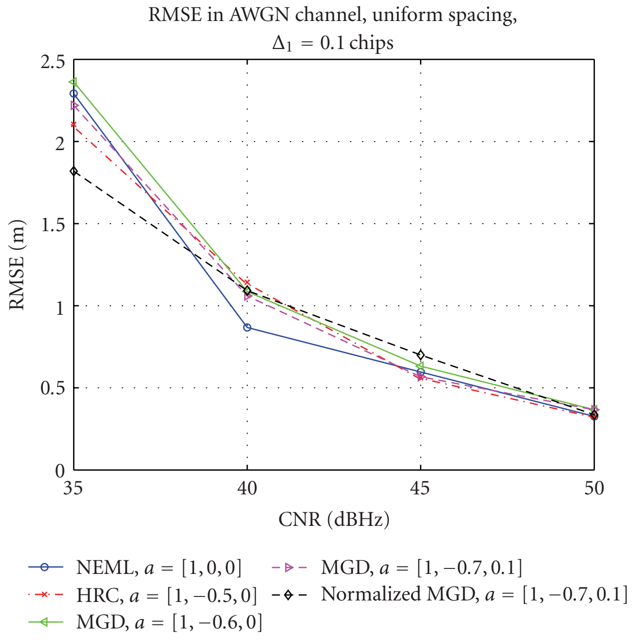

Figure 11: The RMSE simulation results in single-path static channel, $\Delta_1 = 0.1$ chips, $\text{pow}_{nc} = 2$.

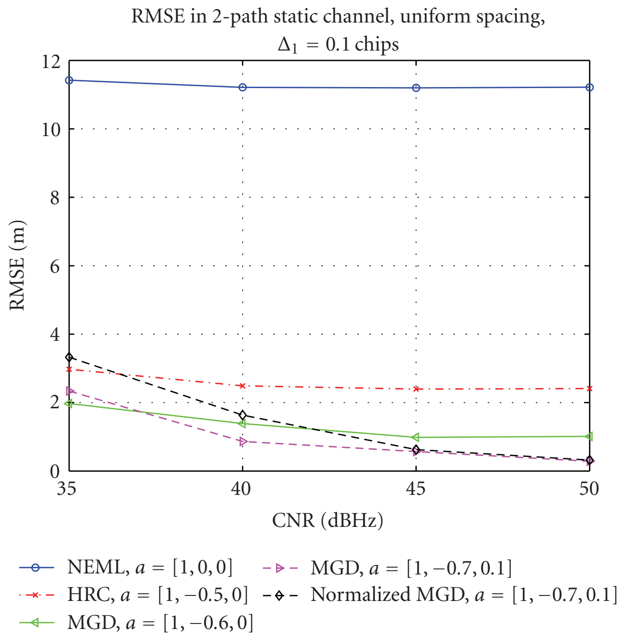

Figure 12: The RMSE simulation results in two-path static channel, $\Delta_1 = 0.1$ chips, $\text{pow}_{nc} = 2$.

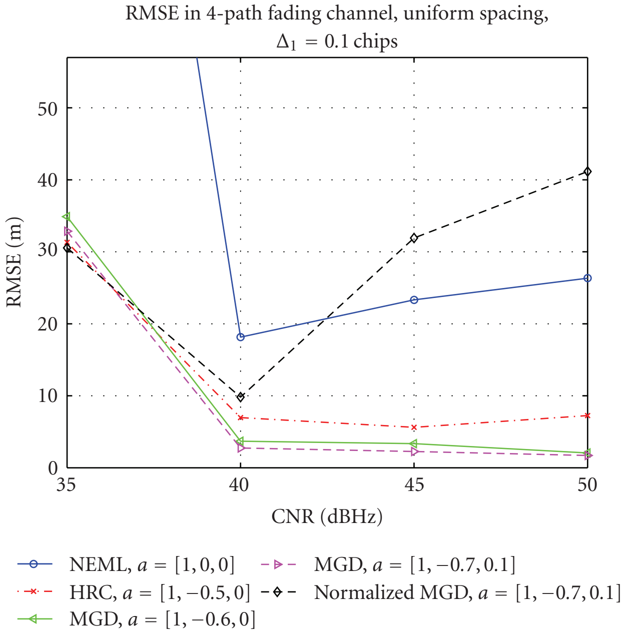

Figure 13: RMSE simulation results in 4-path fading channel, $\Delta_1 = 0.1$ chips, $\text{pow}_{nc} = 2$.

5. ALGORITHM TESTING/PROTOTYPING

From the MGD structure optimization results (Tables 2 and 3), we chose the MGD algorithm with $N_g = 3$ to be investigated further in prototype stage. Both uniform and decreasing spacings with the $\Delta_1 = 0.1$ and $\Delta_1 = 0.25$ chips were chosen to be studied.

The purpose here is to show that the chosen tracking algorithms are feasible to be implemented on actual devices. One of the targets of this study was to see if the behavior of the proposed algorithms does change due to the restrictions given by the hardware implementation. These restrictions include finite computation accuracy, and the effect of quantization due to the bit-width of the signals and the limitation caused by the operation frequency of the synchronous digital system.

We also focus on the design complexity issue, which characterizes the algorithm development especially in the low cost receivers. Since the trend in price of the satellite navigation receivers is currently descending [31], the manufacturers of these low cost, mass market, receivers will most likely reject the algorithms with high implementation complexity and cost.

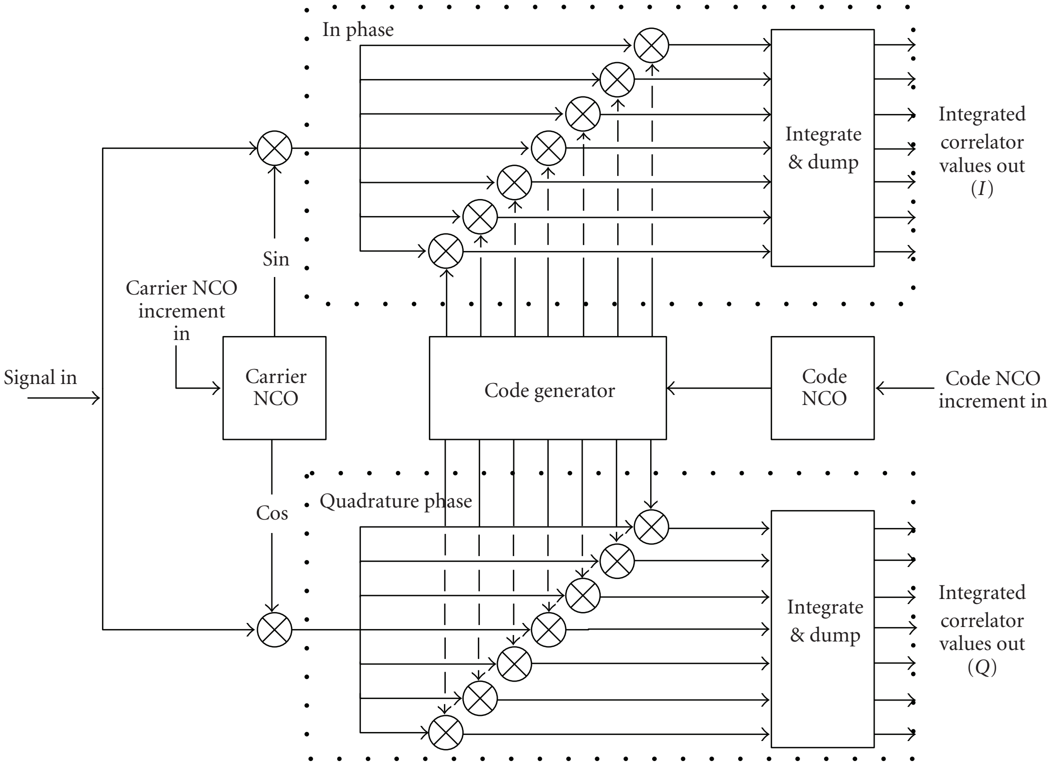

FIGURE 14: Implemented hardware tracking architecture with seven correlators.

In the satellite navigation receiver, the signal tracking is performed by hardware and software signal processing [23]. On the evolving field of satellite navigation systems, the issue of flexility has become more and more important. Flexible designs allow algorithm updates if the specifications of upcoming systems (like Galileo) change suddenly. Flexible designs are usually relying on software-based implementation [32]. For receivers, the software-based implementation is declared to be minimizing the area and cost. On the other hand, the computation burden of the real-time tracking algorithms is too high for most of the handheld device processors, and thus hardware-based computation acceleration is also required. The division between hardware and software implementation may vary in different cases and from the cost perspective it has quite an important role. For this software versus hardware division, one approach in the literature has been the division where the correlation of incoming signal and the reference code are implemented as a specific hardware accelerator, and the computation of discriminators for the feedback loop is done by software running on a digital signal processor (DSP) or some specific processor [20, 33]. In the commercial receiver chip sets, this division is usually implemented as a specific hardware GPS accelerator, engine or core, which is connected to an embedded processor [34, 35].

We chose this approach with the focus on the hardware complexity for our algorithm prototyping implementation. We used the hardware synthesis results (i.e., resource consumption on target FPGA) to estimate the relative complexity of the implemented algorithms.

5.1. Implemented architecture

We implemented the chosen MGD algorithm in both SystemC and VHDL hardware description languages. The hardware was implemented as a Galileo/GPS tracking structure with processes of carrier wipe-off, code tracking correlation, and result integration. The architecture of the implemented hardware delay tracking channel is illustrated in Figure 14. The number of correlators is related to the algorithm used. For the chosen MGD structure with $N_g = 3$, seven correlators are needed to form three correlator pairs and the prompt correlator.

The implemented tracking architecture contains the following functional units: numerically controlled oscillators (NCOs) are used to create the desired frequencies inside the system for the replica code and carrier generation. The code generator is used to generate the replica PRN code for tracking. The carrier NCO outputs sine and cosine waves, which are used to strip the intermediate frequency (IF) carrier from the incoming signal. The sine and cosine multiplications make also the division between in-phase and quadrature phase channels. Seven correlators in both channels are used to correlate the incoming signal with the delayed versions of locally generated code. The amount of delay between the code generation outputs defines the spacings (Δ_1, Δ_2, and Δ_3)

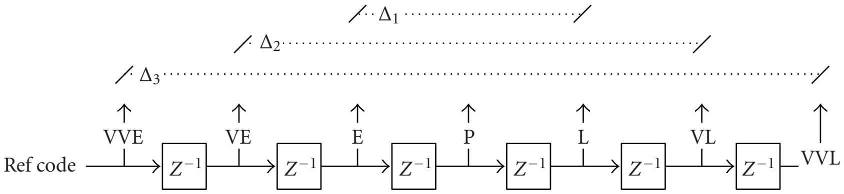

(a) Delay registers with uniform spacing

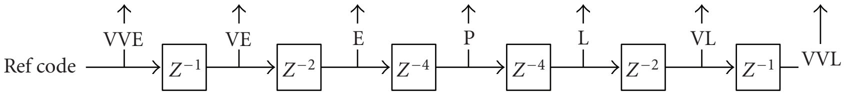

(b) Delay registers with decreasing spacing

FIGURE 15: Implemented delay registers: (a) uniform delay spacing, (b) decreasing delay spacing. *Ref code* is reference code chip value from code generator, *VVE, VE, E* are early, *P* is prompt, and *L, VL, VVL* late outputs of the delay register. The relative correlator spacings (Δ_1, Δ_2, Δ_3) are illustrated on top. Z^{-1} is the smallest uniform delay.

between the correlators. Discriminator function is computed from the accumulated (integrated) correlator outputs.

Since we decided to implement both uniform and decreasing spacing algorithms, two versions of the delay line in the code generator output was constructed. The main difference between these delay lines is illustrated in Figure 15. The uniform delay spacing is created simply by feeding the reference code chip value from the code generator through a delay shift register, where all delays are equal (e.g., for $\Delta_1 = 0.25$ chips, we have: $Z^{-1} = 0.125$ chips). The decreasing delay spacing implementation needs additional registers between the very-very-early (VVE) and very-very-late (VVL) outputs to align the delays correctly (e.g., for $\Delta_1 = 0.25$ chips, we have: $Z^{-1} = 0.03125$ chips, $Z^{-2} = 2Z^{-1} = 0.0625$ chips, and $Z^{-4} = 4Z^{-1} = 0.125$ chips). One may notice that the decreasing delay spaced register implementation needs much smaller uniform delay Z^{-1}. The relationship of smallest uniform delay Z^{-1} in cases of uniform and decreasing delay spacings is

$$Z^{-1}_{\text{uniform}} = 2^{N_g-1} Z^{-1}_{\text{decreasing}}. \qquad (16)$$

5.2. SystemC verification of the architecture

We started the prototyping task by creating a high-level SystemC model of the hardware tracking channel. SystemC is a C++ library extension which can be used, for example, to cycle accurate hardware architecture modeling [36]. The similarity of the syntax of the hardware description language with C++ allowed fast prototype generation. Another benefit of using SystemC is that it contains the simulator itself, thus a stand-alone executable can be created for the simulations. The developed model was based on the one published previously in [37]. In [37], the SystemC hardware description language was used to model an inter-operative GPS/Galileo code correlator channel. For the MGD tracking algorithm testing, a carrier wipe-off process was included to this newer version of model. We developed a Matlab code to represent the software part of the proposed MGD tracking algorithms. Matlab was also used for generation of the input signals for the test simulations. The division of resources between SystemC model and Matlab software environment is illustrated in Figure 16. The implemented SystemC model contains the same functional blocks as are illustrated in Figure 14 and, together with the surrounding Matlab environment, principally the same functionality as in Figure 3.

We used this SystemC model to see how the MEE curves of the proposed MGD algorithms behave when the hardware model is used. HRC and NEML algorithms were implemented for reference purposes. At first stage of MEE testing, we noticed that the envelopes ($\text{pow}_{nc} = 1$) generated with the SystemC model did have a constant negative offset. This can be seen clearly in Figure 17, where the blue-squared curve illustrating the SystemC hardware-based MEE of NEML ($\Delta_1 = 0.1$ chips) has a negative offset when comparing to the black-star, plain Matlab based, and reference curve. On the other hand, the hardware model's MEE shares the same shape with the ideal reference one.

The reason for this behavior was found to be the imperfect frequency generation inside the hardware tracking channel. When both code generating and sampling frequency are generated with the NCO, there is a possibility to a sample slip if the NCO's frequency resolution is too low. With no noise condition (as MEEs are generated), this has an effect on the shape of ideal autocorrelation function curve, making it not to have identical sides. We improved the output accuracy of NCOs by increasing the accumulation register size from 24 to 32 bits. This removed the offset from the discriminator output as can be seen from Figure 18, where red-diamond curve presents the MEE result with the new NCO size of 32 bits and blue-squared with NCO size of 24 bits.

After the issue of the NCO size was dealt with, we made a conclusion that the proposed MGD algorithms are implementable, and the implemented hardware architecture is solid for this purpose. An example curve for the uniformly spaced ($\Delta_1 = 0.1$, $\Delta_2 = 0.2$, $\Delta_3 = 0.3$ chips) MGD

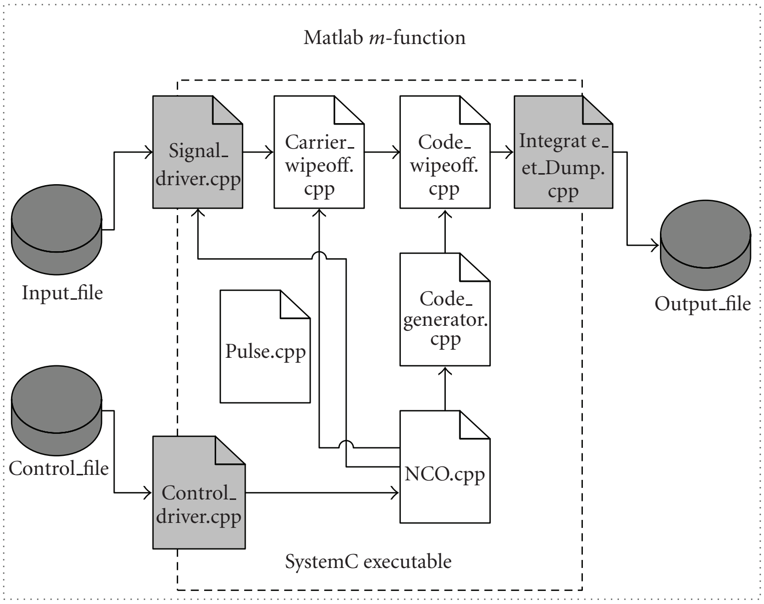

FIGURE 16: Block diagram of the implemented high-level SystemC hardware model inside the Matlab software.

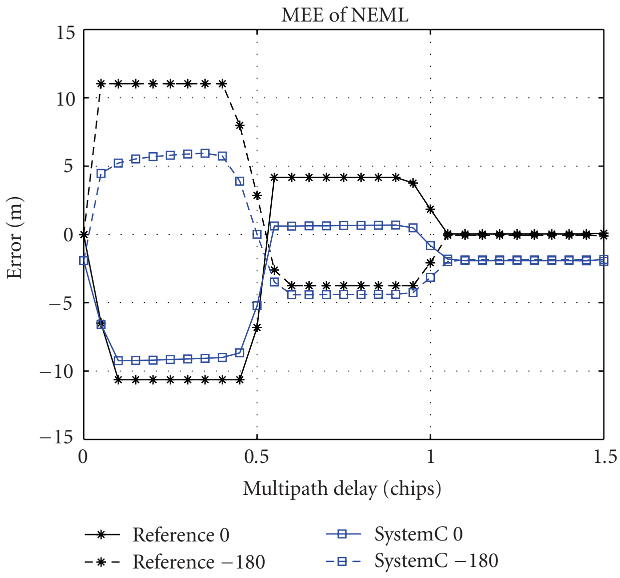

FIGURE 17: Difference between the hardware model and Matlab-based MEE curves of NEML discriminator ($\Delta_1 = 0.1$). The black line presents the behavior of reference Matlab simulation, and the blue curve illustrates the behavior of the SystemC model.

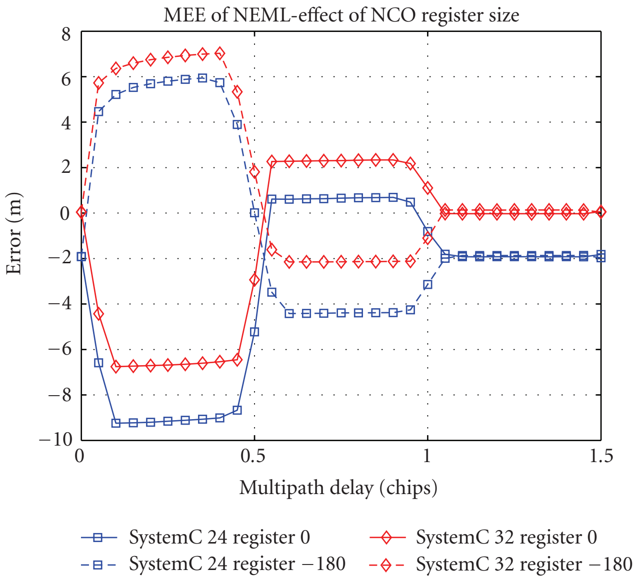

FIGURE 18: Effect of the NCO register length to the MEE curves of NEML discriminator ($\Delta_1 = 0.1$ chips) created by the SystemC model. The blue-squared curve presents the case when NCO register size was 24 bits; the red-diamond line is for the case of 32 bits.

structure ($N_g = 3$, $\text{pow}_{nc} = 1$) is illustrated in Figure 19. This figure shows how the shape of the hardware-based multipath envelope is similar to the one generated purely in Matlab in Figure 5. Figures 19 and 5 also show the difference in envelope area when alternating between $\text{pow}_{nc} = 1$ and $\text{pow}_{nc} = 2$.

5.3. VHDL implementation and synthesis

After the architecture of the hardware tracking channel and its functionality with the proposed MGD structure were verified with the SystemC hardware model, we build a VHDL model of the tracking channel. VHSIC hardware description

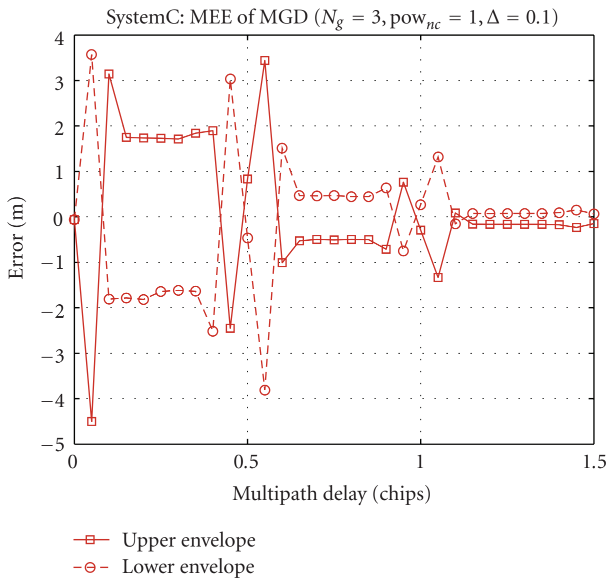

FIGURE 19: Example of the SystemC hardware-based MEE of the MGD ($N_g = 3$, $\text{pow}_{nc} = 1$, $\Delta_1 = 0.1$ chips, uniform spacing) with SinBOC(1,1) signal.

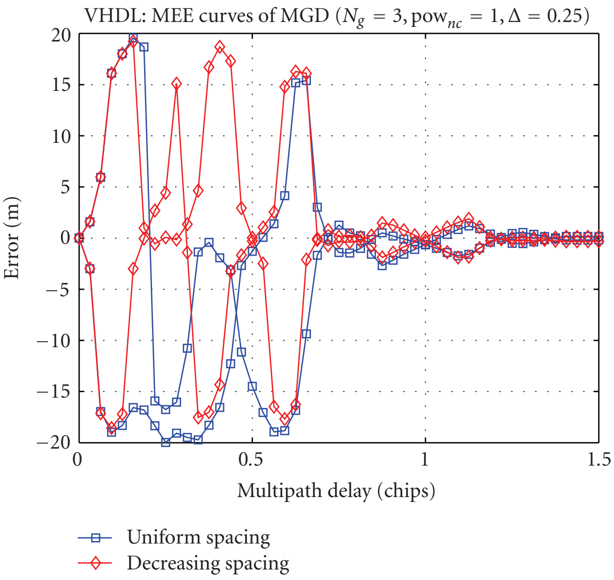

FIGURE 20: Example of VHDL hardware-based MEEs. MGD with uniform spacing ($a = [1, -0.7, -0.2]$) is illustrated in blue-squared curve and MGD with decreasing spacing is illustrated ($a = [1, -0.9, 0.2]$) in red-circled. ($N_g = 3$, $\text{pow}_{nc} = 1$, $\Delta_1 = 0.25$).

language (VHDL) is a language designed and optimized for describing the behavior of the digital systems, and it is one of the standard languages among the electronic engineers [16]. Since the VHDL needs a simulator software for simulation, we used ModelSim software and tool command language (TCL) scripts to run the simulations for MEE generation. The VHDL hardware-based MEE curve of the proposed MGD with both uniform ($a = [1, -0.7, -0.2]$) and decreasing ($a = [1, -0.9, 0.2]$) spacing implementations are illustrated in Figure 20. The blue-squared curve presents the uniform spaced MGD and the red-circled the decreasing spaced MGD, for both curves the common parameters were $N_g = 3$, $\text{pow}_{nc} = 1$, and $\Delta_1 = 0.25$ chips. From the figure, we can see that the MEE curves of the hardware implemented MGDs are active in the limits set by the theoretical ones, illustrated in Figure 6.

We used the synthesis results of the VHDL model to evaluate the implementation complexity of the proposed algorithms. The synthesis was done by using the Xilinx ISE software. We varied the number of correlators, since it is the characterizing quantity when choosing the MGD algorithm to be implemented (N_g). Our target device was the Xilinx Virtex II PRO field programmable gate array (FPGA). FPGAs are reprogrammable digital devices which can be used in tasks requiring a high processing speed, like tracking process [32].

The synthesis results are subjected to the target platform and, therefore, they can not be generalized. Because of this, we focused on the comparison between the complexity of uniform and decreasing delay spaced implementations, with a varying number of correlators. We synthesized only the delay register part of the hardware architecture since it is the only part that differs. The results are illustrated in Figure 21 and in Table 6. These results indicate that the hardware complexity, measured as usage of target FPGA resources (equivalent logic gate count, logic slices, flip flops, and lookup tables), increases linearly with respect to amount of correlators (N_g) in uniform delay spaced implementations. In cases of decreasing delay spaced implementations,. the complexity increase is much faster. One must note that the left out part of the system adds a constant positive offset to the synthesis results.

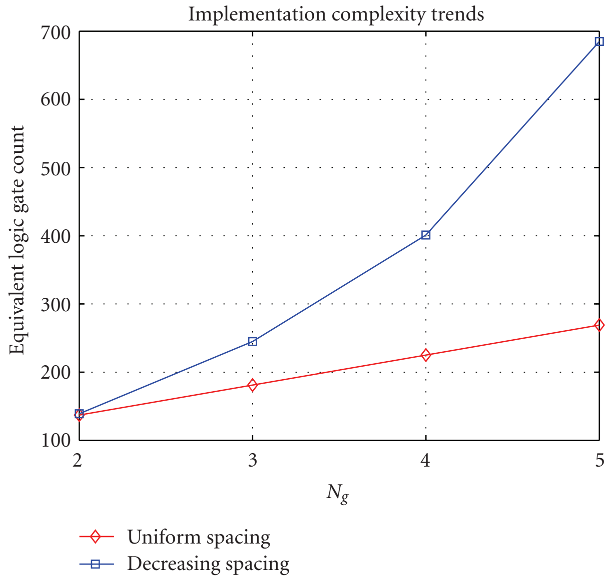

FIGURE 21: Synthesis of the architecture to the target device: effect of the number of correlators.

Another difference between the implementations of uniform and decreasing delay spacings is in the increase of the

Table 6: Xilinx resource usage.

	Resource usage in target device					
	unif. spacing			decr. spacing		
	Slices	FF	LUT	Slices	FF	LUT
$N_g = 2$	5	4	5	5	6	4
$N_g = 3$	7	6	7	11	14	7
$N_g = 4$	9	8	9	20	30	9
$N_g = 5$	11	10	11	37	62	11

generated frequencies when using the decreasing one. The proposed decreasing spacing structure with $N_g = 3$ requires approximately four times higher frequency to be generated than uniformly spaced MGD structure with equivalent N_g. This is because the smallest common uniform delay factor with the uniform spacing of $\Delta_1 = 0.25$ chips is $\Delta_1/2 = 0.125$, but for the proposed decreasing spacing structure of $\Delta_1 = 0.25$ chips it is $\Delta_1/8 = 0.03125$. This equals to the reference code delay register frequency increase from 8.184 MHz up to 32.736 MHz with Galileo E1 and GPS C/A signals, when their fundamental frequency is 1.023 MHz. Also the limitation caused by the RF front-end bandwidth is met much faster when using the decreasing spacing, compared with uniform spacing.

6. CONCLUSIONS

In this paper, a comprehensive description of Multiple Gate Delay tracking structures for GNSS signals in multipath environments has been introduced, covering all the steps from theoretical derivation and choice of design parameters till the final stage of prototyping. We showed that the proposed structures are implementable and that they have a high flexibility. We also explained in detail the design steps that should be taken in order to derive easily new MGD structures according to the target constraints (e.g., desired number of gate pairs, sampling frequencies, available bandwidths, etc.). We have discussed as well some aspects not taken into account in previous research papers, such as the effect of the nonlinearity type on the system performance, the design of gate spacings in multiple gate structures, and the effect of realistic PRN code lengths on the multipath error envelope analysis. We compared the MGD structures with uniform and decreasing spacings in terms of complexity, and we showed that the slightly better performance of MGDs with decreasing spacings is counter-balanced by a higher complexity, especially when the number of gate pairs increases. We showed that the state-of-art delay trackers, such as narrow correlator and double-delta correlators, can be seen as particular cases of MGD structures.

We saw that the best choices in terms of two-path error envelopes are the MGDs with decreasing gate spacings and envelope nonlinearity. However, we also showed that, when the number of channel path increases, various MGD structures start to have equal performance, and the performance gap between narrow correlator and MGD structures disappears. Nevertheless, the main advantage of the proposed MGD structures is that they offer a large set of unpatented choices (at least according to the very best of authors' knowledge) that can be used for the design of multipath delay trackers for mass-market GPS and Galileo receivers.

ACKNOWLEDGMENTS

This work has been carried out in the project "Galileo Receivers for the mAss market" (GREAT), co-funded by the European GNSS Supervisory Authority (EGSA) with funding from the 6th Framework Programme of the European Community for research and technological development. This work has also been supported by the Academy of Finland. The authors also want to express their thanks to Clemens Buergi and Bernhard Aumayer from u-blox AG for their useful comments regarding MGD algorithm.

REFERENCES

[1] A. J. van Dierendonck, P. Fenton, and T. Ford, "Theory and performance of narrow correlator spacing in a GPS receiver," *Journal of the Institute of Navigation*, vol. 39, no. 3, pp. 265–283, 1992.

[2] M. Irsigler and B. Eissfeller, "Comparison of multipath mitigation techniques with consideration of future signal structures," in *Proceedings of the 16th International Technical Meeting of the Satellite Division of the Institute of Navigation (ION GPS/GNSS '03)*, pp. 2584–2592, Portland, Ore, USA, September 2003.

[3] G. A. McGraw and M. S. Braasch, "GNSS multipath mitigation using gated and high resolution correlator concepts," in *Proceedings of the ION National Technical Meeting*, pp. 333–342, San Diego, Calif, USA, January 1999.

[4] T. Stansell, P. Fenton, L. Garin, et al., "BOC or MBOC: the common GPS/Galileo civil signal design," *Inside GNSS*, pp. 30–37, July/August 2006.

[5] G. A. McGraw, "High resolution correlator technique for spread spectrum ranging system code and carrier multipath mitigation," February 2004, Cedar Rapids Patent, US 6687316.

[6] L. Garin and J.-M. Rousseau, "Enhanced strobe correlator multipath rejection for code and carrier," in *Proceedings of the 9th International Technical Meeting of the Satellite Division of the Institute of Navigation (ION GPS '97)*, pp. 559–568, Kansas City, Mo, USA, September 1997.

[7] P. Fenton, B. Smith, and J. Jones, "Theory and performance of the pulse aperture correlator," Tech. Rep., NovAtel, Calgary, Alberta, Canada, September 2004, http://www.novatel.com/customer_support/alltechpapers.html.

[8] P. Jackson, "A high-performance, easy-to-use GPS surveying system," Leica Geosystems AG, September 1999, http://www.leicaadvantage.com/support/GPS1200/500TechnicalPapers/Sys500Summary.pdf.

[9] L. R. Weill, "Multipath mitigation—how good can it get with new signals?" *GPS World*, vol. 14, no. 6, pp. 106–113, 2003.

[10] P. Fenton, "Pseudorandom noise ranging receiver which compensates for multipath distortion by making use of multiple correlator time delay spacing," May 1995, NovAtel Patent, US 5 414 729.

[11] P. Fenton and A. J. van Dierendonck, "Pseudorandom noise ranging receiver which compensates for multipath distortion by dynamically adjusting the time delay spacing between early

and late correlators," February 1996, NovAtel Patent, US 5 495 499.

[12] E. S. Lohan, *Multipath delay estimators for fading channels with applications in CDMA receivers and mobile positioning*, Ph.D. thesis, Tampere University of Technology, Tampere, Finland, October 2003.

[13] E. S. Lohan, R. Hamila, A. Lakhzouri, and M. Renfors, "Highly efficient techniques for mitigating the effects of multipath propagation in DS-CDMA delay estimation," *IEEE Transactions on Wireless Communications*, vol. 4, no. 1, pp. 149–162, 2005.

[14] E. S. Lohan, A. Lakhzouri, and M. Renfors, "Feedforward delay estimators in adverse multipath propagation for Galileo and modernized GPS signals," *EURASIP Journal on Applied Signal Processing*, vol. 2006, Article ID 50971, 19 pages, 2006.

[15] P. A. Bello and R. L. Fante, "Code tracking performance for novel unambiguous m-code time discriminators," *MITRE Technical Report*, MITRE, Bedford, Mass, USA, 2006.

[16] D. de Castro, J. Diez, A. Fernández, and J.-M. Sleewaegen, "A new unambiguous low-complexity BOC tracking technique," in *Proceedings of the 19th International Technical Meeting of the Satellite Division of the Institute of Navigation (ION GNSS '06)*, pp. 1830–1835, Fort Worth, Tex, USA, September 2006.

[17] L. R. Weill, "Achieving theoretical bounds for receiver-based multipath mitigation using Galileo OS signals," in *Proceedings of the 19th International Technical Meeting of the Satellite Division of the Institute of Navigation (ION GNSS '06)*, pp. 1035–1047, Fort Worth, Tex, USA, September 2006.

[18] V. A. Veitsel, A. Zhdanov, and M. I. Zhodzishsky, "The mitigation of multipath errors by strobe correlators in GPS/GLONASS receivers," *GPS Solutions*, vol. 2, no. 2, pp. 38–45, 1998.

[19] G. A. McGraw, "Practical GPS carrier phase multipath mitigation using high resolution correlator techniques," in *Proceedings of the IAIN World Congress and the 56th Annual Meeting of the Institute of Navigation*, pp. 373–381, San Diego, Calif, USA, June 2000.

[20] E. D. Kaplan and C. J. Hegarty, Eds., *Understanding GPS, Principles and Applications*, Artech House, Boston, Mass, USA, 2nd edition, 2006.

[21] Galileo Joint Undertaking, "Galileo open service, signal in space interface control document (OS SIS ICD)," May 2006, http://www.galileoju.com/.

[22] E. S. Lohan, A. Lakhzouri, and M. Renfors, "Binary-offset-carrier modulation techniques with applications in satellite navigation systems," *Wireless Communications and Mobile Computing*, vol. 7, no. 6, pp. 767–779, 2007.

[23] M. S. Braasch and A. J. van Dierendonck, "GPS receiver architectures and measurements," *Proceedings of the IEEE*, vol. 87, no. 1, pp. 48–64, 1999.

[24] D. Skournetou and E. S. Lohan, "Non-coherent multiple correlator delay structures and their tracking performance for Galileo signals," in *Proceedings of the European Navigation Conference (ENC-GNSS '07)*, Geneva, Switzerland, May-June 2007.

[25] T. Pany, M. Irsigler, and B. Eissfeller, "S-curve shaping: a new method for optimum discriminator based code multipath mitigation," in *Proceedings of the 18th International Technical Meeting of the Satellite Division of the Institute of Navigation (ION GNSS '05)*, Long Beach, Calif, USA, September 2005.

[26] R. van Nee, *Multipath and multi-transmitter interference in spread-spectrum communication and navigation systems*, Ph.D. thesis, Delft University of Technology, Delft, The Netherlands, 1995.

[27] J. Diez, A. Fernández, J. S. Silva, L. Marradi, and V. Gabaglio, "Characterization of the pseudorange error due to code doppler shift in Galileo E5 and L1 receivers using the GRANADA bit-true simulator," in *Proceedings of the 18th International Technical Meeting of the Satellite Division of the Institute of Navigation (ION GNSS '05)*, Long Beach, Calif, USA, September 2005.

[28] J. Won, T. Pany, and G. Hein, "GNSS software defined radio: real receiver or just a tool for experts," *Inside GNSS*, vol. 1, no. 5, pp. 48–56, July/August 2006.

[29] X. Hu and E. S. Lohan, "GRANADA validation of optimized multiple gate delay structures for Galileo SinBOC(1,1) signal tracking," in *Proceedings of the 7th International Conference on ITS Telecommunications (ITST '07)*, pp. 1–5, Sophia Antipolis, France, June 2007.

[30] H. Hurskainen, X. Hu, S. Ancha, G. Bell, J. Raasakka, and J. Nurmi, "Enhancing usability of the GRANADA bit-true receiver simulation on Galileo L1," in *Proceedings of the 20th International Technical Meeting of the Satellite Division of The Institute of Navigation (ION GNSS '07)*, Fort Worth, Tex, USA, September 2007.

[31] S. Colwell, "The price is right! GPS prices drop for consumers," *GPS World*, vol. 18, no. 5, pp. 31–32, 2007.

[32] F. Dovis, A. Gramazio, and P. Mulassano, "SDR technology applied to Galileo receivers," in *Proceedings of the 15th International Technical Meeting of the Satellite Division of the Institute of Navigation (ION GPS '02)*, Portland, Ore, USA, September 2002.

[33] D. Benson, "The design and implementation of a GPS receiver channel," *Xilinx: DSP Magazine*, pp. 50–53, October 2005.

[34] u Blox, "UBX-G5010 product summary sheet," April 2007, http://www.u-blox.com/products/Product_Summaries/UBX-G5010_Prod_Summary(GPS.G5-X-06042).pdf.

[35] Sirf, "SiRFstarIII GSC3LP Product Insert," http://www.sirf.com/products/GSC3LPProductInsert.pdf.

[36] SystemC Version 2.0 User's Guide.

[37] H. Hurskainen and J. Nurmi, "SystemC model of an interoperative GPS/Galileo code correlator channel," in *Proceedings of the IEEE Workshop on Signal Processing Systems Design and Implementation (SIPS '06)*, pp. 327–332, Banff, Alberta, Canada, October 2006.

Hindawi Publishing Corporation
International Journal of Navigation and Observation
Volume 2008, Article ID 738183, 12 pages
doi:10.1155/2008/738183

Research Article

Data and Pilot Combining for Composite GNSS Signal Acquisition

Daniele Borio and Letizia Lo Presti

Dipartimento di Elettronica, Politecnico di Torino, Corso Duca degli Abruzzi, 10129 Torino, Italy

Correspondence should be addressed to Daniele Borio, daniele.borio@polito.it

Received 1 August 2007; Revised 20 December 2007; Accepted 18 March 2008

Recommended by Olivier Julien

With the advent of new global navigation satellite systems (GNSS), such as the European Galileo, the Chinese Compass and the modernized GPS, the presence of new modulations allows the use of special techniques specifically tailored to acquire and track the new signals. Of particular interest are the new composite GNSS signals that will consist of two different components, the data and pilot channels. Two strategies for the joint acquisition of the data and pilot components are compared. The first technique, noncoherent combining, is from the literature and it is used as a comparison term, whereas the analysis of the second one, coherent combining with sign recovery, represents the innovative contribution of this paper. Although the analysis is developed with respect to the Galileo E1 Open Service (OS) modulation, the obtained results are general and can be applied to other GNSS signals.

1. INTRODUCTION

With the advent of the new global navigation satellite system (GNSS), such as the European Galileo and the Chinese Compass, new signals and new modulations have been introduced in order to guarantee the coexistence and interoperability with existent systems, like the American GPS, and to fully exploit the technologies currently available.

An example of those new signals is the coherent adaptive subcarrier modulation (CASM) that will be used for the transmission of the Galileo signal on the E1 frequency. CASM combines three different signals in a constant amplitude modulation that allows the use of efficient class C amplifiers [1, 2].

The three signals combined in the CASM are denoted as the *A*, *B*, and *C* channels. The first one is used for public-regulated service (PRS), whereas the latter two will provide the open service (OS). The *B* and *C* channels have two different roles: the first one, denoted data channel, will carry the navigation message whereas the second one, denoted pilot channel, will be used for determining the pseudoranges between the satellites and the receiver. The *B* and *C* signals will be transmitted at the same time, at the same frequency, and they will be separated only by different codes [3]. The A signal is not completely defined by the galileo interface control document [1] but will probably be separated in frequency as for the A signal emitted by Giove-A [4], the first experimental satellite of the Galileo constellation.

The presence of new modulations allows one to adopt special techniques specifically tailored to acquire and track new signals.

One solution, when acquiring composite GNSS signals such as the Galileo E1 OS modulation, consists in ignoring the data channel and processing only the pilot signal. In this way only half of the useful power is employed and the GNSS receiver could not be able to acquire and track signals that would be easily processed if all the useful power were used. Pilot and data channel combining allows recovering all the available power improving the acquisition performance and providing more reliable signal detection. For these reasons the design of signal combing techniques is critical for the efficient acquisition of the new GNSS signals.

In this paper, Galileo E1 OS signals are considered and in particular two acquisition strategies for the efficient combining of data and pilot channels are analyzed. In the first strategy, called noncoherent combining, the received signal is correlated separately with the pilot and data local replicas. The correlation outputs are then squared and summed. This strategy essentially exploits the principle of noncoherent integration [5–7] employed to extend the integration period over the bit duration. Its use for data and pilot combining is reported by [8], however its performance in terms of false alarm and detection probabilities has been only marginally investigated.

The second strategy consists in multiplying the received signal by two new signals, obtained by summing and subtracting the data and pilot local replicas, respectively. Then, the maximum of the two correlations is adopted as decision variable. This strategy can be seen as an extension of the *(b–c)* technique proposed by [9, 10] in which only the correlation with the difference between data and pilot codes was considered. This second strategy implements the Maximum Likelihood estimator for the code delay, the Doppler frequency, and the relative phase between data and pilot channels, and, to the best of our knowledge, has never been applied to the E1 OS signals. This strategy allows the coherent combining of data and pilot channels and it will be denoted as coherent channel combining with sign recovery. The proposed method is the adaptation of the acquisition strategy proposed in [11] to the Galileo E1 OS signal. In particular [11] considered the case of data and pilot components transmitted with a ±90 degree phase difference. Moreover, [11] only proposed the method without providing any analytical characterization of its performance.

Both strategies have been analyzed in terms of false alarm and detection probabilities and closed-form expressions for the probabilities of coherent channel combining with sign recovery have been derived. To the best of our knowledge these expressions have never been derived before and represent one of the innovative contributions of this paper. Moreover, these formulas are general and can be easily adapted to the case of other modulations, for example, for the GPS L5 case that has been analyzed only by simulations [11].

In the analysis the coherent integration time is limited to a single code period. In this way the acquisition block has not to deal with the problem of bit transitions that can occur every 4 milliseconds. Moreover, an integration time of 4 milliseconds should be sufficient to acquire GNSS signals in high to moderate C/N_0 conditions. The problem of bit transitions can be overcome by using noncoherent integrations. The integration time can be also increased by considering the pilot channel alone and exploiting the structure imposed by its secondary code [11]. These issues are however out of the scope of this paper.

Monte Carlo techniques have been used for supporting the theoretical analysis: simulations and analytical expressions agree well proving the effectiveness of the developed theory.

From the analysis it emerges that the coherent combining always outperforms noncoherent combining and thus it should be adopted for the joint acquisition of data and pilot channels.

This work is organized as follows: Section 2 introduces the CASM and provides a model for Galileo E1 OS signals. In Section 3 the noncoherent and coherent combining algorithms are described and the expressions for false alarm and detection probabilities are derived. In Section 4 the derived formulas are validated by Monte Carlo simulations. Finally, the conclusions are presented in Section 5.

2. SIGNAL AND SYSTEM MODEL

The signal at the input of a Galileo receiver, in one-path additive Gaussian noise environment, can be written as

$$r_{\mathrm{RF}}(t) = \sum_{i=1}^{L} \sqrt{2P_{R,i}}\, y_i(t) + \eta_{\mathrm{RF}}(t) \tag{1}$$

that is the sum of L useful signals, emitted by L different satellites and with power $P_{R,i}$, and of a noise term $\eta_{\mathrm{RF}}(t)$. Each signal $y_i(t)$, in the Galileo E1 band, is given by [1, 2]:

$$\begin{aligned} y_i(t) &= \frac{\sqrt{2}}{3}\left[e_{B,i}(t-\tau_{0,i}) - e_{C,i}(t-\tau_{0,i})\right]\cos\left(2\pi\left(f_{\mathrm{RF}} + f_{d,i}\right)t + \theta_i\right) \\ &\quad - \frac{1}{3}\left[2e_{A,i}(t-\tau_{0,i}) + e_{A,i}(t-\tau_{0,i})e_{B,i}(t-\tau_{0,i})e_{C,i}(t-\tau_{0,i})\right] \\ &\quad \times \sin\left(2\pi\left(f_{\mathrm{RF}} + f_{d,i}\right)t + \theta_i\right), \end{aligned} \tag{2}$$

where

(i) $e_{A,i}(t)$, $e_{B,i}(t)$ and $e_{C,i}(t)$ are the three useful signals emitted on the E1 frequencies and corresponding to the A, B, and C channels, respectively, and $e_{A,i}(t)$ is a restricted access signal for PRS whereas $e_{B,i}(t)$ and $e_{C,i}(t)$ are the data and pilot signals for OS;

(ii) $\tau_{0,i}$, $f_{d,i}$, and θ_i are the delay, the Doppler frequency, and the phase introduced by the transmission channel;

(iii) $f_{\mathrm{RF}} = 1575.42$ MHz is the E1 central frequency.

$e_{A,i}(t)$, $e_{B,i}(t)$, and $e_{C,i}(t)$ are real binary sequences that assume value in the set $\{-1, 1\}$. These three signals are combined according to the CASM in order to obtain a constant envelope signal $y_i(t)$. This result is achieved by introducing the term proportional to the three useful signals in (2).

The input signal (1) is recovered by the receiver antenna, downconverted, and filtered by the receiver front end. A low-IF receiver is assumed. In mass-market receivers the bandwidth of the front-end filter is generally limited to a few MHz and thus the components depending on the PRS signal in (2) can be considered eliminated by the filtering process. This is due to the fact that a BOC(15,2.5) modulation [2, 4] is employed for the PRS signal. This modulation splits the PRS signal power far from the E1 central frequency where the power spectral densities (PSD) of the OS signals are concentrated. In this way, the received signal, before the analog-to-digital (AD) conversion, is given by

$$\begin{aligned} r_{\mathrm{IF}}(t) &= \sum_{i=1}^{L} \sqrt{2P_{R,i}}\,\overline{y}_i(t) + \eta_{\mathrm{IF}}(t) \\ &= \sum_{i=1}^{L} \sqrt{2P_{R,i}}\,\frac{\sqrt{2}}{3}\left[e_{B,i}(t-\tau_{0,i}) - e_{C,i}(t-\tau_{0,i})\right] \\ &\quad \times \cos\left(2\pi\left(f_{\mathrm{IF}} + f_{d,i}\right)t + \theta_i\right) + \eta_{\mathrm{IF}}(t), \end{aligned} \tag{3}$$

where f_{IF} is the receiver intermediate frequency and $\eta_{\mathrm{IF}}(t)$ is the downconverted and filtered noise component. In (3) the effect of the front-end filtering on the OS components is considered negligible.

Finally, (3) is sampled and AD is converted, obtaining, by neglecting the quantization impact, the following signal model:

$$\begin{aligned} r_{\mathrm{IF}}(nT_s) &= \sum_{i=1}^{L}\sqrt{2P_{R,i}}\bar{y}_i(nT_s) + \eta_{\mathrm{IF}}(nT_s) \\ &= \sum_{i=1}^{L}\sqrt{2P_{R,i}}\frac{\sqrt{2}}{3}\left[e_{B,i}(nT_s-\tau_{0,i}) - e_{C,i}(nT_s-\tau_{0,i})\right] \\ &\quad\times \cos(2\pi(f_{\mathrm{IF}}+f_{d,i})nT_s+\theta_i) + \eta_{\mathrm{IF}}(nT_s). \end{aligned} \tag{4}$$

In the following, the notation $x[n] = x(nT_s)$ will indicate a discrete-time sequence $x[n]$, obtained by sampling a continuous-time signal $x(t)$ with a sampling frequency $f_s = 1/T_s$. For this reason (4) can be rewritten as

$$\begin{aligned} r_{\mathrm{IF}}[n] &= \sum_{i=1}^{L}\sqrt{C_i}\left(e_{B,i}\left[n-\frac{\tau_{0,i}}{T_s}\right] - e_{C,i}\left[n-\frac{\tau_{0,i}}{T_s}\right]\right) \\ &\quad\times \cos(2\pi F_{D,0}^{i}n+\theta_i) + \eta_{\mathrm{IF}}[n], \end{aligned} \tag{5}$$

where $C_i = (4/9)P_{R,i}$ and $F_{D,0}^{i} = (f_{\mathrm{IF}} + f_{d,i})T_s$. C_i represents the total power of the i th received signal since the term

$$\left(e_{B,i}\left[n-\frac{\tau_{0,i}}{T_s}\right] - e_{C,i}\left[n-\frac{\tau_{0,i}}{T_s}\right]\right)\cos(2\pi F_{D,0}^{i}n+\theta_i) \tag{6}$$

has unitary power. The spectral characteristics of $\eta_{\mathrm{IF}}[n]$ depend on the type of filtering along with the sampling and decimation strategy adopted in the front end. A convenient choice is to sample the IF signal with a sampling frequency $f_s = 2B_{\mathrm{IF}}$, where B_{IF} is the one-sided front-end bandwidth. In this case, it is easily shown that the noise variance becomes

$$\sigma_{\mathrm{IF}}^2 = E\{\eta_{\mathrm{IF}}^2(t)\} = E\{\eta_{\mathrm{IF}}^2(nT_s)\} = \frac{N_0 f_s}{2} = N_0 B_{\mathrm{IF}}, \tag{7}$$

where $N_0/2$ is the Power Spectral Density of the IF noise. The autocorrelation function

$$R_{\mathrm{IF}}[m] = E\{\eta_{\mathrm{IF}}[n]\eta_{\mathrm{IF}}[n+m]\} = \sigma_{\mathrm{IF}}^2\delta[m] \tag{8}$$

implies that the discrete-time random process $\eta_{\mathrm{IF}}[n]$ is a classical independent and identically distributed (iid) wide-sense stationary (WSS) random process, or a white sequence. $\delta[m]$ is the Kronecker delta. From now on, this signal model is adopted and the system performance is expressed in terms of Carrier-to-Noise Ratio C_i/N_0.

Both data and pilot signals in (5) can be represented as the product of three terms

$$e_{B/C,i}[n] = c_{B/C,i}[n]s_B[n]d_{B/C,i}[n], \tag{9}$$

where $c_{B/C,i}[n]$ is a spreading code of length $N_c = 4092$, $s_B[n]$ is the subcarrier signal that in the Galileo OS signal is the BOC(1,1), and $d_{B/C,i}[n]$ is the navigation message for the data signal and the secondary code in the pilot case. $d_{B/C,i}[n]$ is constant over one code period. Hereinafter the product between the code and the subcarrier will be denoted as

$$\bar{e}_{B/C,i}[n] = c_{B/C,i}[n]s_B[n]. \tag{10}$$

As a result of code orthogonality, the different Galileo codes are analyzed separately by the receiver, and thus hereinafter the case of a single satellite is considered and the index i is dropped. Thus the resulting signal is

$$\begin{aligned} &r_{\mathrm{IF}}[n] \\ &= \sqrt{C}\left(e_B\left[n-\frac{\tau_0}{T_s}\right] - e_C\left[n-\frac{\tau_0}{T_s}\right]\right)\cos(2\pi F_{D,0}n+\theta) + \eta_{\mathrm{IF}}[n]. \end{aligned} \tag{11}$$

3. OS SIGNALS ACQUISITION

In traditional GPS receivers the delay and the Doppler frequencies of received signals are estimated by using the correlation with local signal replicas opportunely delayed and modulated. In the acquisition stage, the code delay and Doppler frequency are estimated as the ones that make the correlation with the local replica pass a fixed threshold. In the Galileo E1 case however this strategy cannot be directly employed since two different signals are present. Moreover, due to the navigation message on the data channel and to the secondary code on the pilot channel, these two components can be either summed or subtracted.

In this Section, we analyze two possible strategies for signal acquisition for Galileo OS signals. The performance of the two algorithms is evaluated in terms of false alarm and detection probabilities that are the probabilities that the decision variable passes a fixed threshold under two different hypotheses:

(H_0) the signal is present and correctly aligned with the local replica;

(H_1) the signal is absent or not correctly aligned with local replica.

The plot of the detection probability versus the false alarm probability is called receiver operating characteristic (ROC) and it completely defines the system performance [12]. The ROCs are usually employed for comparative analysis, as effective metric for characterizing an acquisition system [5, 6]. For these reasons they are adopted in this work and used as basis for the analysis of the two acquisition algorithms considered in the paper.

3.1. Pilot and data noncoherent combining

The conceptual scheme for the acquisition of Galileo E1 signals, with the noncoherent combination of data and pilot channels, is depicted in Figure 1. The received signal is multiplied by two orthogonal sinusoids at the frequency F_D,

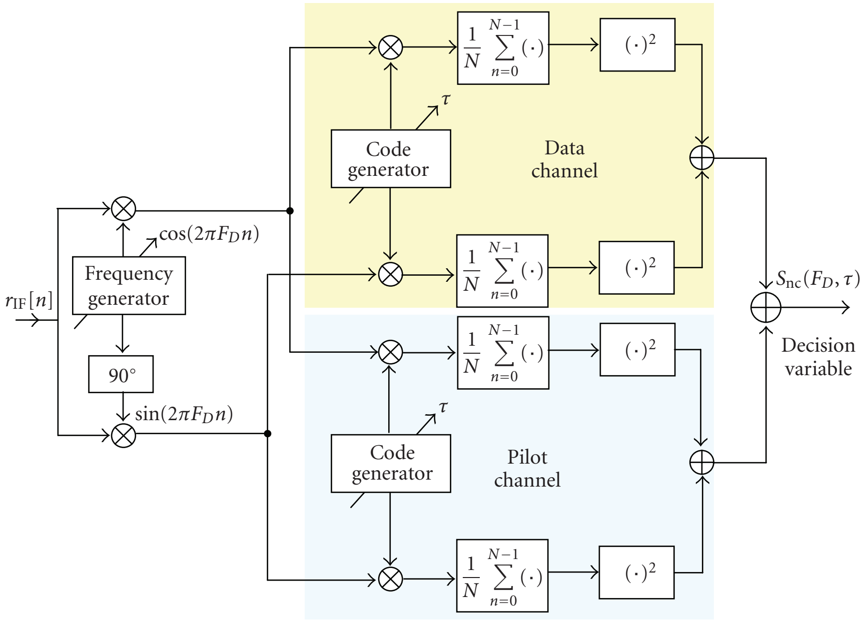

FIGURE 1: Conceptual scheme of the Galileo OS signals acquisition with noncoherent combining.

leading to the in-phase (I) and quadrature (Q) components. These signals are then split in two different branches where the correlations with the data and pilot codes are evaluated. The cross-correlations from the two branches are noncoherently combined leading to the decision variable

$$S_{\mathrm{nc}}(F_D,\tau) = \left|R_B(F_D,\tau)\right|^2 + \left|R_C(F_D,\tau)\right|^2, \tag{12}$$

where

$$\begin{aligned} R_B(F_D,\tau) &= \frac{1}{N}\sum_{n=0}^{N-1} r_{\mathrm{IF}}[n]\bar{e}_B\left[n-\frac{\tau}{T_s}\right]\exp\{j2\pi F_D n\}, \\ R_C(F_D,\tau) &= \frac{1}{N}\sum_{n=0}^{N-1} r_{\mathrm{IF}}[n]\bar{e}_C\left[n-\frac{\tau}{T_s}\right]\exp\{j2\pi F_D n\} \end{aligned} \tag{13}$$

are the cross-correlations of the received signal with the data and pilot replicas delayed by τ and modulated by F_D. In (13) N denotes the number of samples used to integrate the received signal over one-code period. More specifically, N is given by $\lfloor T_c \cdot f_s \rfloor$, where $T_c = 4$ milliseconds is the duration of one code period, f_s is the sampling frequency, and $\lfloor \cdot \rfloor$ denotes the floor operator. Since the cross-correlations $R_B(F_D,\tau)$ and $R_C(F_D,\tau)$ have been obtained from the input signal $r_{\mathrm{IF}}[n]$, they also depends on τ_0, $F_{D,0}$, and θ, the parameters that characterize $r_{\mathrm{IF}}[n]$. The dependence on these parameters has not been explicitly reported in (13) for the ease of notation.

The multiplication by the complex exponential in (13) is implemented in Figure (1) by the multiplication with the two orthogonal sinusoids.

In Appendix A it is shown that $R_B(F_D,\tau)$ and $R_C(F_D,\tau)$ are two complex Gaussian random variables that, due to the orthogonality properties of Galileo codes [3], are approximatively independent. Thus $|R_B(F_D,\tau)|^2$ and $|R_C(F_D,\tau)|^2$ are two χ^2 random variables with 2 degrees of freedom. From this consideration and (12), $S_{\mathrm{nc}}(F_D,\tau)$ is a χ^2 random variable with 4 degrees of freedom.

In order the determine the ROC, the two following probabilities have to be evaluated:

$$\begin{aligned} P_{\mathrm{fa}}^{\mathrm{nc}}(\beta) &= P(S_{\mathrm{nc}}(F_D,\tau) > \beta | H_1), \\ P_{d}^{\mathrm{nc}}(\beta) &= P(S_{\mathrm{nc}}(F_D,\tau) > \beta | H_0). \end{aligned} \tag{14}$$

When the signal is not present or not correctly aligned it is possible to assume [5, 6] that both $R_B(F_D,\tau)$ and $R_C(F_D,\tau)$ are zero mean. Thus $S_{\mathrm{nc}}(F_D,\tau)$ is a central χ^2 random variable, whose distribution is completely characterized by the variance of $R_B(F_D,\tau)$ and of $R_C(F_D,\tau)$. From (13) we have

$$\begin{aligned} &\mathrm{Var}\{R_B(F_D,\tau)\} \\ &= \mathrm{Var}\{R_C(F_D,\tau)\} \\ &= \mathrm{Var}\left\{\frac{1}{N}\sum_{i=0}^{N-1} r_{\mathrm{IF}}[n]\bar{e}_B\left[n-\frac{\tau}{T_s}\right]\exp\{j2\pi F_D n\}\right\} \\ &= \frac{1}{N^2}\sum_{i=0}^{N-1}\mathrm{Var}\{r_{\mathrm{IF}}[n]\} = \frac{1}{N^2}\sum_{i=0}^{N-1}\mathrm{Var}\{\eta_{\mathrm{IF}}[n]\} = \frac{N_0 f_s}{2N} = \frac{N_0 B_{\mathrm{IF}}}{N}. \end{aligned} \tag{15}$$

Equation (15) directly derives from the noise model reported in Section 2. In this case it is assumed that the input noise is a white sequence. In a real GNSS receivers the front end can introduce some correlation among the different noise samples. This correlation causes a correlation loss [13] that would affect both noise and signal components. This effect could be included in the analysis but it would introduce no further insight and thus, for the sake of clarity, it is not considered in this context.

Since both $R_B(F_D,\tau)$ and $R_C(F_D,\tau)$ are complex random variables with iid real and imaginary parts, the variance (15) is equally divided between the two components and thus we can define

$$\sigma_n^2 = \frac{N_0 f_s}{4N} = \frac{N_0 B_{\mathrm{IF}}}{2N}, \tag{16}$$

σ_n^2 is the variance of the real and of the imaginary parts of $R_B(F_D,\tau)$ and $R_C(F_D,\tau)$. Given these premises and exploiting the fact that $S_{\mathrm{nc}}(F_D,\tau)$ is a central χ^2 random variable it is possible to derive the false alarm probability [14]

$$P_{\mathrm{fa}}^{\mathrm{nc}}(\beta) = \exp\left\{-\frac{\beta}{2\sigma_n^2}\right\}\left(1+\frac{\beta}{2\sigma_n^2}\right). \tag{17}$$

When the signal is present and correctly aligned $S_{\mathrm{nc}}(F_D,\tau)$ is a noncentral χ^2 random variable with noncentrality parameter

$$\lambda = \left|E\{R_B(F_D,\tau)\}\right|^2 + \left|E\{R_C(F_D,\tau)\}\right|^2 = 2\left|E\{R_B(F_D,\tau)\}\right|^2 \tag{18}$$

that assumes the following expression [13, 15]:

$$\lambda = \frac{C}{2}\frac{\sin^2(\pi N\Delta F)}{(\pi N\Delta F)^2}K^2(\Delta\tau) \approx \frac{C}{2}, \tag{19}$$

where

(i) $\Delta F = F_{D,0} - F_D$ is the difference between the Doppler frequencies of the received signal and of the local replica;

(ii) $\Delta\tau = (\tau_0 - \tau)/T_s$ is the difference between the delays of the received signal and of the local replica, normalized with respect to the sampling interval;

(iii) $K(\cdot)$ is the correlation between the incoming code, filtered by the frontend, and the code generated at the receiver.

When the Doppler frequency and the delay of the local replica match the ones of the received signal, the loss $(\sin^2(\pi N\Delta F)/(\pi N\Delta F)^2)K^2(\Delta\tau)$ can be assumed negligible and $\lambda \approx C/2$.

From these considerations it is possible to evaluate the detection probability [14, 16]

$$P_d^{\mathrm{nc}}(\beta) = Q_2\left(\sqrt{\frac{\lambda}{\sigma_n^2}},\sqrt{\frac{\beta}{\sigma_n^2}}\right) \approx Q_2\left(\sqrt{\frac{2CN}{N_0 f_s}},\sqrt{4\frac{\beta N}{N_0 f_s}}\right), \tag{20}$$

where $Q_2(\cdot,\cdot)$ is the Generalized Marcum Q function of order 2 [16, 17], defined as

$$Q_K(a,b) = \frac{1}{a^{K-1}}\int_b^{+\infty} x^K \exp\left\{-\frac{x^2+a^2}{2}\right\} I_{K-1}(ax)\,dx \tag{21}$$

where $I_{K-1}(\cdot)$ is the modified Bessel function of first kind and order $K-1$ [18].

3.2. Pilot and data coherent combining with sign recovery

By considering (11) and by collecting the navigation message of the data channel, it is possible to rewrite the received signal $r_{\mathrm{IF}}[n]$ as

$$\begin{aligned} r_{\mathrm{IF}}[n] &= \sqrt{C}\,d_B\left[n-\frac{\tau_0}{T_s}\right] \\ &\quad\times\left(\bar{e}_B\left[\frac{\tau_0}{T_s}\right] - \frac{d_C[n-(\tau_0/T_s)]}{d_B[n-(\tau_0/T_s)]}\bar{e}_C\left[n-\frac{\tau_0}{T_s}\right]\right)\cos(2\pi F_{D,0}n+\theta) \\ &\quad+\eta_{\mathrm{IF}}[n]. \end{aligned} \tag{22}$$

Expressed in this form, (22) indicates that the navigation message $d_B[n]$ is spread by the equivalent pseudorandom sequence

$$e_{\mathrm{eq}}[n] = \bar{e}_B[n] - \frac{d_C[n]}{d_B[n]}\bar{e}_C[n]. \tag{23}$$

Since the navigation message $d_B[n]$ and the secondary code $d_C[n]$ are constant over one code period and since they can assume only two values, -1 and 1, only two equivalent spreading sequences are possible

$$e_{\mathrm{eq}}[n] = \begin{cases}\bar{e}_B[n] - \bar{e}_C[n], \\ \bar{e}_B[n] + \bar{e}_C[n].\end{cases} \tag{24}$$

In the coherent combining scheme, the received signal is correlated with both equivalent codes: the equivalent code that maximizes the cross-correlation is likely the correct one. Based on this principle the decision variable is given by

$$S_{\mathrm{ml}}(F_D,\tau) = \max\left\{\left|R^+(F_D,\tau)\right|^2, \left|R^-(F_D,\tau)\right|^2\right\}, \tag{25}$$

where

$$\begin{aligned} R^+(F_D,\tau) &= \frac{1}{N}\sum_{n=0}^{N-1} r_{\mathrm{IF}}[n]\left\{\bar{e}_B\left[n-\frac{\tau}{T_s}\right] + \bar{e}_C\left[n-\frac{\tau}{T_s}\right]\right\}\exp(j2\pi F_D n), \\ R^-(F_D,\tau) &= \frac{1}{N}\sum_{n=0}^{N-1} r_{\mathrm{IF}}[n]\left\{\bar{e}_B\left[n-\frac{\tau}{T_s}\right] - \bar{e}_C\left[n-\frac{\tau}{T_s}\right]\right\}\exp(j2\pi F_D n). \end{aligned} \tag{26}$$

This kind of algorithm is based on the Maximum Likelihood estimator for the code delay, Doppler frequency, and relative sign between data and pilot channels, since, as shown in Appendix B, the maximization of the correlation function, with respect to the delay τ, the frequency F_D, and the ratio $d_C[n]/d_B[n]$, corresponds to the maximization of the likelihood function evaluated for the received signal $r_{\mathrm{IF}}[n]$.

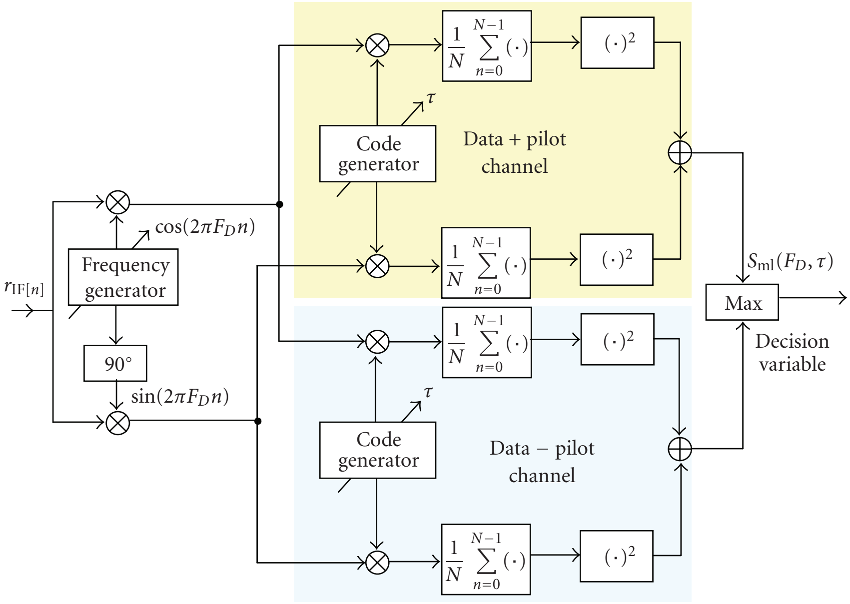

Figure 2: Conceptual scheme of the Galileo OS signals acquisition with coherent combining.

The acquisition scheme with coherent combining is reported in Figure 2: the received signal is correlated with the two equivalent codes and the decision variable is obtained by choosing the maximum of the two cross-correlations. It has to be noted that the variables $R^+(F_D,\tau)$ and $R^-(F_D,\tau)$ can be obtained by opportunely combining the cross-correlations with the data and the pilot codes

$$\begin{aligned}R^+(F_D,\tau) &= \frac{1}{N}\sum_{n=0}^{N-1} r_{\mathrm{IF}}[n]\bar{e}_B\left[n-\frac{\tau}{T_s}\right]\exp\left(j2\pi F_D n\right)\\ &\quad+\frac{1}{N}\sum_{n=0}^{N-1} r_{\mathrm{IF}}[n]\bar{e}_C\left[n-\frac{\tau}{T_s}\right]\exp\left(j2\pi F_D n\right)\\ &= R_B(F_D,\tau)+R_C(F_D,\tau),\end{aligned} \tag{27}$$

$$\begin{aligned}R^-(F_D,\tau) &= \frac{1}{N}\sum_{n=0}^{N-1} r_{\mathrm{IF}}[n]\bar{e}_B\left[n-\frac{\tau}{T_s}\right]\exp\left(j2\pi F_D n\right)\\ &\quad-\frac{1}{N}\sum_{n=0}^{N-1} r_{\mathrm{IF}}[n]\bar{e}_C\left[n-\frac{\tau}{T_s}\right]\exp\left(j2\pi F_D n\right)\\ &= R_B(F_D,\tau)-R_C(F_D,\tau).\end{aligned} \tag{28}$$

In this way the coherent combining algorithm can be implemented with a computational load similar to the one required by the noncoherent combining strategy.

From (28) and (27) it clearly emerges that $R^+(F_D,\tau)$ and $R^-(F_D,\tau)$ are linear combinations of $R_B(F_D,\tau)$ and $R_C(F_D,\tau)$. Thus, since $R_B(F_D,\tau)$ and $R_C(F_D,\tau)$ are complex Gaussian random variables, $R^+(F_D,\tau)$ and $R^-(F_D,\tau)$ are also complex and Gaussian.

The ROC for the coherent combining strategy can be easily obtained by determining the false alarm and detection probability of the variables $|R^+(F_D,\tau)|^2$ and $|R^-(F_D,\tau)|^2$. In fact it can be easily shown that the false alarm and the detection probabilities of the decision variable $S_{ml}(F_D,\tau)$ are given by

$$\begin{aligned}&P(S_{\mathrm{ml}}(F_D,\tau)>\beta)\\ &\quad= P\left(\max\left\{\left|R^+(F_D,\tau)\right|^2,\left|R^-(F_D,\tau)\right|^2\right\}>\beta\right)\\ &\quad= 1-P\left(\max\left\{\left|R^+(F_D,\tau)\right|^2,\left|R^-(F_D,\tau)\right|^2\right\}<\beta\right)\\ &\quad= 1-P\left(\left|R^+(F_D,\tau)\right|^2<\beta,\left|R^-(F_D,\tau)\right|^2<\beta\right)\\ &\quad= 1-P\left(\left|R^+(F_D,\tau)\right|^2<\beta\right)P\left(\left|R^-(F_D,\tau)\right|^2<\beta\right).\end{aligned} \tag{29}$$

The last line in (29) has been obtained by exploiting the independence between $|R^+(F_D,\tau)|^2$ and $|R^-(F_D,\tau)|^2$ that derives from the independence of $R^+(F_D,\tau)$ and $R^-(F_D,\tau)$. In fact we have

$$\begin{aligned}&E\{R^+(F_D,\tau)[R^-(F_D,\tau)]^*\}\\ &\quad= E\{[R_B(F_D,\tau)+R_C(F_D,\tau)][R_B(F_D,\tau)-R_C(F_D,\tau)]^*\}\\ &\quad= E\left[\left|R_B(F_D,\tau)\right|^2-\left|R_C(F_D,\tau)\right|^2\right]\\ &\quad= 0.\end{aligned} \tag{30}$$

Equation (30) is zero since $|R_B(F_D,\tau)|^2$ and $|R_C(F_D,\tau)|^2$ are equally distributed and the difference of their mean cancels out. From (30) $R^+(F_D,\tau)$ and $R^-(F_D,\tau)$ are uncorrelated and, since they are both Gaussian random variables, independent. For these reasons $|R^{+}(F_D,\tau)|^2$ and $|R^{-}(F_D,\tau)|^2$ are also independent.

Since $R^{+}(F_D,\tau)$ and $R^{-}(F_D,\tau)$ are Gaussian random variables, $|R^{+}(F_D,\tau)|^2$ and $|R^{-}(F_D,\tau)|^2$ are χ^2 distributed with two degrees of freedom. When the signal is absent, or the local replicas are not aligned with the received signal, then $|R^{+}(F_D,\tau)|^2$ and $|R^{-}(F_D,\tau)|^2$ are both central χ^2 random variables [14] and the false alarm probability of $S_{\mathrm{ml}}(F_D,\tau)$ is

$$P_{\mathrm{fa}}^{\mathrm{ml}}(\beta)=1-\left[1-\exp\left\{-\frac{\beta}{4\sigma_n^2}\right\}\right]^2. \tag{31}$$

Equation (31) has been obtained by substituting the cumulative density function (cdf) of central χ^2 random variables [14] into (29). It can be noted that the exponential in (31) depends on $4\sigma_n^2$ instead of $2\sigma_n^2$ as for (17). This is due to the fact that the equivalent code (24) has twice the power of the single pilot and data codes.

When the Galileo signal is present and correctly aligned with the local replica, $|R^{+}(F_D,\tau)|^2$ and $|R^{-}(F_D,\tau)|^2$ are no more central χ^2 random variables, and the noncentrality parameters λ_+ and λ_- have to be determined. λ_+ and λ_- can be obtained by determining the mean of $R^{+}(F_D,\tau)$ and $R^{-}(F_D,\tau)$ under the hypothesis that the local equivalent code matches or not the navigation bit. In particular we have

$$\begin{aligned}
&E[R^{+}(F_D,\tau)]\\
&=E\{R_B(F_D,\tau)+R_C(F_D,\tau)\}\\
&=\begin{cases}2E\{R_B(F_D,\tau)\}=\sqrt{C}\dfrac{\sin(\pi N\Delta F)}{(\pi N\Delta F)}K(\Delta\tau) & \\ \qquad\approx\sqrt{C} & \text{if } \dfrac{d_C[n]}{d_B[n]}=1,\\ 0 & \text{if } \dfrac{d_C[n]}{d_B[n]}=-1\end{cases}
\end{aligned} \tag{32}$$

and similarly

$$\begin{aligned}
&E[R^{-}(F_D,\tau)]\\
&=E\{R_B(F_D,\tau)-R_C(F_D,\tau)\}\\
&=\begin{cases}2E\{R_B(F_D,\tau)\}=\sqrt{C}\dfrac{\sin(\pi N\Delta F)}{(\pi N\Delta F)}K(\Delta\tau) & \\ \qquad\approx\sqrt{C} & \text{if } \dfrac{d_C[n]}{d_B[n]}=-1,\\ 0 & \text{if } \dfrac{d_C[n]}{d_B[n]}=1.\end{cases}
\end{aligned} \tag{33}$$

From these considerations it emerges that the decision variable $S_{\mathrm{ml}}(F_D,\tau)$, under the hypothesis of presence of signal and correct alignment, is given by the maximum between a central χ^2 and a noncentral χ^2 random variables with two degrees of freedom. The noncentrality parameter of the noncentral χ^2 random variable is given by

Table 1: Simulation parameters.

Parameter	Value
Sampling frequency	$f_s=4.092\,\mathrm{MHz}$
Intermediate frequency	$f_{\mathrm{IF}}=\dfrac{f_s}{4}=1.023\,\mathrm{MHz}$
Receiver bandwidth	$B_{\mathrm{IF}}=\dfrac{f_s}{2}=2.046\,\mathrm{MHz}$
Code rate	$1.023\cdot 10^6$ chip/s
Code length	4092 chip
Integration time	$NT_s=4\,\mathrm{ms}$

$$\lambda=C\frac{\sin^2(\pi N\Delta F)}{(\pi N\Delta F)^2}K^2(\Delta\tau)\approx C. \tag{34}$$

Given these premises it is finally possible to express the detection probability

$$\begin{aligned}
P_d^{\mathrm{ml}}(\beta)&=1-\left[1-\exp\left\{-\frac{\beta}{4\sigma_n^2}\right\}\right]\left[1-Q_1\left(\sqrt{\frac{\lambda}{2\sigma_n^2}},\sqrt{\frac{\beta}{2\sigma_n^2}}\right)\right]\\
&\approx 1-\left[1-\exp\left\{-\frac{\beta}{4\sigma_n^2}\right\}\right]\left[1-Q_1\left(\sqrt{\frac{2CN}{N_0 f_s}},\sqrt{\frac{2\beta N}{N_0 f_s}}\right)\right],
\end{aligned} \tag{35}$$

where $Q_1(\cdot,\cdot)$ is the Marcum Q function of order 1.

4. SIMULATION ANALYSIS

In order to validate the theoretical analysis developed in the previous sections, the Galileo E1 OS has been simulated according to the parameters reported in [1] and acquired according to the two methods considered in this work. The simulation parameters are reported in Table 1. More in detail a GNSS signal has been simulated according to model (11). The spreading codes from [1] has been used to generate the Galileo E1 OS signals, and the acquisition systems depicted in Figures 1 and 2 have been implemented in order to evaluate the decision statistics (12) and (25). The false alarm and detection probabilities have been estimated by verifying if the decision variables, under both (H_1) and (H_0) hypotheses, passed or not the decision threshold obtained by inverting (20) and (31). $2\cdot 10^5$ trials have been used for the estimation process. Frequency and delay errors have not been simulated and, for the evaluation of the detection probability, the incoming signal has been considered perfectly aligned with local replica. These errors were not considered in the theoretical model and thus they have not been considered in the simulation scheme as well. The impact of frequency and delay residual errors has been extensively studied in [15] and can be easily included in the models developed in previous sections. This topic is however out of the scope of this paper.

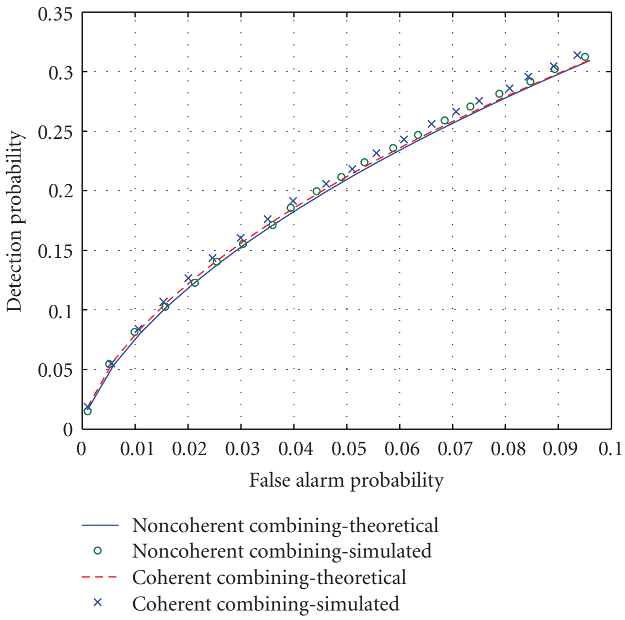

Figure 3: Simulated and theoretical ROCs for noncoherent and coherent acquisition systems. $C/N_0 = 25$ dB-Hz.

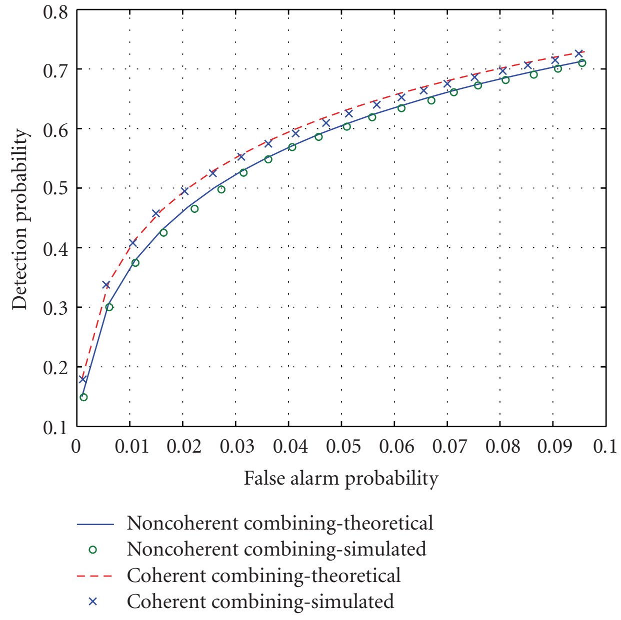

Figure 4: Simulated and theoretical ROCs for noncoherent and coherent acquisition systems. $C/N_0 = 30$ dB-Hz.

The simulations results are reported in Figures 3, 4, and 5, where the cases of $C/N_0 = 25, 30$, and 35 dB-Hz have been considered. These C/N_0 values have been chosen since they represent marginally strong and weak signal conditions. The probabilities evaluated by Monte Carlo simulations match the theoretical models developed in previous sections and the theoretical and simulated ROCs overlap in all the considered cases. Simulations effectively support the theoretical models proving the effectiveness of the analysis developed in Section 3.

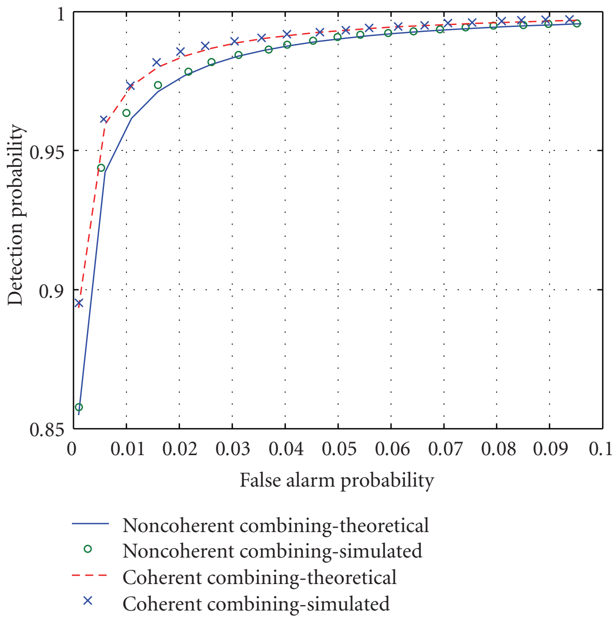

Figure 5: Simulated and theoretical ROCs for noncoherent and coherent acquisition systems. $C/N_0 = 35$ dB-Hz.

It can be noted, from Figures 3, 4, and 5, that the coherent acquisition algorithm always outperforms the noncoherent combining strategy. Moreover, it can be observed that the two methods tend to have similar performance for low C/N_0. This performance degradation of coherent combing with sign recovery is probably due to the fact that, for low C/N_0, the estimation of the relative phase between data and pilot becomes unreliable preventing an effective combination of the two channels transmitted for the Galileo E1 OS.

5. CONCLUSIONS

In this paper, two different acquisition strategies for the acquisition of the Galileo E1 OS signals have been considered and deeply analyzed. The first strategy, the noncoherent combining, is from the literature whereas the analysis of the second one, coherent combining with sign recovery, is new and represents the innovative contribution of this paper. An analytical model for the false alarm and detection probabilities of both algorithms has been derived and Monte Carlo simulations have been used for supporting the theoretical analysis. From the theoretical model and simulations it is shown that the coherent combining algorithm outperforms the noncoherent combing proving the effectiveness of the proposed method. Thus, provided that both algorithms require similar computational loads, the coherent combining acquisition algorithm results in preferable to noncoherent combining and should be adopted for the joint acquisition of the E1 OS data and pilot channels.

APPENDICES

A. INDEPENDENCE OF THE RANDOM VARIABLES AT THE OUTPUT OF THE DATA AND PILOT CORRELATORS

In this appendix we show that the random variables, obtained by correlating the input Galileo signal with the local replicas of the data and pilot channels, are approximatively independent. The proof is based on the correlation properties of Galileo memory codes [3].

From (11) the signal at the input of the Galileo receiver is the sum of a useful term and of white Gaussian noise. This input sequence is correlated with local replicas of the data and pilot primary codes, opportunely delayed and modulated, and for each satellite, a pair of random variables is obtained:

$$\begin{aligned} R_B(\tau,F_D) &= \frac{1}{N}\sum_{n=0}^{N-1} r_{\mathrm{IF}}[n]\bar{e}_B\left[n-\frac{\tau}{T_s}\right]\exp\{j2\pi F_D n\},\\ R_C(\tau,F_D) &= \frac{1}{N}\sum_{n=0}^{N-1} r_{\mathrm{IF}}[n]\bar{e}_C\left[n-\frac{\tau}{T_s}\right]\exp\{j2\pi F_D n\}. \end{aligned} \tag{A.1}$$

Since $r_{\mathrm{IF}}[n]$ is the sum of a deterministic component and white Gaussian noise and since both $R_B(\tau,F_D)$ and $R_C(\tau,F_D)$ are linear transformations of $r_{\mathrm{IF}}[n]$, then their independence can be proven by considering

$$\begin{aligned} X_B(\tau,F_D) &= \frac{1}{N}\sum_{n=0}^{N-1} \eta_{\mathrm{IF}}[n]\bar{e}_B\left[n-\frac{\tau}{T_s}\right]\exp\{j2\pi F_D n\},\\ X_C(\tau,F_D) &= \frac{1}{N}\sum_{n=0}^{N-1} \eta_{\mathrm{IF}}[n]\bar{e}_C\left[n-\frac{\tau}{T_s}\right]\exp\{j2\pi F_D n\} \end{aligned} \tag{A.2}$$

that are obtained from the noise component of r_{IF}. Since the input noise is assumed to be zero mean and since the useful signal component determines the mean of the correlation function, it is possible to write $X_B(\tau,F_D) = R_B(\tau,F_D) - E\{R_B(\tau,F_D)\}$ and $X_C(\tau,F_D) = R_C(\tau,F_D) - E\{R_C(\tau,F_D)\}$. Thus the independence of $X_B(\tau,F_D)$ and $X_C(\tau,F_D)$ implies the independence of $R_B(\tau,F_D)$ and $R_C(\tau,F_D)$. By defining

$$M = \begin{bmatrix} \eta_{\mathrm{IF}}[0]\\ \eta_{\mathrm{IF}}[1]\\ \cdots\\ \eta_{\mathrm{IF}}[N-1] \end{bmatrix};$$

$$E_x = \begin{bmatrix} 1 & 0 & \cdots & 0\\ 0 & \exp\{j2\pi F_D\} & \cdots & 0\\ \cdots & \cdots & \cdots & \cdots\\ 0 & 0 & \cdots & \exp\{j2\pi F_D(N-1)\} \end{bmatrix};$$

$$B = \begin{bmatrix} \bar{e}_B\left[-\frac{\tau}{T_s}\right]\\ \bar{e}_B\left[1-\frac{\tau}{T_s}\right]\\ \cdots\\ \bar{e}_B\left[N-1-\frac{\tau}{T_s}\right] \end{bmatrix};$$

$$C = \begin{bmatrix} \bar{e}_C\left[-\frac{\tau}{T_s}\right]\\ \bar{e}_C\left[1-\frac{\tau}{T_s}\right]\\ \cdots\\ \bar{e}_C\left[N-1-\frac{\tau}{T_s}\right] \end{bmatrix}; \tag{A.3}$$

it is then possible to rewrite (A.2) as

$$\begin{aligned} X_B(\tau,F_D) &= \frac{1}{N}M^T E_x B,\\ X_C(\tau,F_D) &= \frac{1}{N}M^T E_x C, \end{aligned} \tag{A.4}$$

and the covariance between X_B and X_C becomes

$$\begin{aligned} E[X_B(\tau,F_D)X_C^*(\tau,F_D)] &= E[X_C^H(\tau,F_D)X_B(\tau,F_D)]\\ &= E[\frac{1}{N^2}C^H E_x^H M^* M^T E_x B]\\ &= \frac{1}{N^2}C^H E_x^H E[M^* M^T]E_x B\\ &= \frac{\sigma_{\mathrm{IF}}^2}{N^2}C^H E_x^H E_x B = \frac{\sigma_{\mathrm{IF}}^2}{N^2}C^H B\\ &\approx 0. \end{aligned} \tag{A.5}$$

The covariance (A.5) is almost zero for the quasi-orthogonality of the Galileo memory codes. In (A.5) the fact that $E_x^H E_x = I_N$ and $E\{M^* M^T\} = \sigma_{\mathrm{IF}} I_N$ has been used. I_N is the $N \times N$ identity matrix.

From (A.5) $X_B(\tau,F_D)$ and $X_C(\tau,F_D)$ can be considered uncorrelated and thus, since they are Gaussian random variables, independent.

B. MAXIMUM LIKELIHOOD ESTIMATOR

In this appendix, the Maximum Likelihood estimator for the delay τ_0, the Doppler frequency $F_{D,0}$, and the relative phase between the Galileo E1 OS data and pilot channel is derived. Its connection with the coherent acquisition block with sign recovery is also shown.

In this context the signal presence is assumed and the signal parameters are treated as unknown constants. By considering (22) and by assuming $\eta_{\mathrm{IF}}[n]$ a white Gaussian sequence, it is possible to derive the joint probability density function of the set $\{r_{\mathrm{IF}}[n]\}_{n=0}^{N-1}$:

$$f(\vec{r}) = \frac{1}{\left(2\pi\sigma_{\mathrm{IF}}^2\right)^{N/2}} \exp\left\{\frac{-\sum_{i=0}^{N-1}\left[r_i - \mu_i(\tau, F_D, S)\right]^2}{2\sigma_{\mathrm{IF}}^2}\right\}, \tag{B.1}$$

where

(i)

$$\mu_i(\tau, F_D, S) = \sqrt{C} d_B\left[i - \frac{\tau}{T_s}\right]\left(\bar{e}_B\left[i - \frac{\tau}{T_s}\right] - S\bar{e}_C\left[i - \frac{\tau}{T_s}\right]\right)\cos(2\pi F_D i + \theta), \tag{B.2}$$

(ii) $S = d_C[i - \tau/T_s]/d_B[i - \tau/T_s]$ is the relative phase between the data and the pilot channels and can assume two values: -1 and 1,

(iii) r_i is the i th component of the vector $\vec{r}$.

The Likelihood function for the set (τ, F_D, S) is given by

$$\mathcal{L}(\tau, F_D, S) = \frac{1}{\left(2\pi\sigma_{\mathrm{IF}}^2\right)^{N/2}} \exp\left\{\frac{-\sum_{i=0}^{N-1}\left[r_{\mathrm{IF}}[i] - \mu_i(\tau, F_D, S)\right]^2}{2\sigma_{\mathrm{IF}}^2}\right\} \tag{B.3}$$

and its maximization is obtained by maximizing the argument of the exponential in (B.3). Thus the Maximum Likelihood estimator for (τ, F_D, S) is given by

$$\begin{aligned}
(\hat{\tau}, \hat{F}_D, \hat{S}) &= \arg\min_{\tau, F_D, S} \sum_{i=0}^{N-1}\left[r_{\mathrm{IF}}[i] - \mu_i(\tau, F_D, S)\right]^2 \\
&= \arg\min_{\tau, F_D, S}\left[\sum_{i=0}^{N-1} r_{\mathrm{IF}}^2[i] - 2\sum_{i=0}^{N-1}\mu_i(\tau, F_D, S) r_{\mathrm{IF}}[i] + \sum_{i=0}^{N-1}\mu_i(\tau, F_D, S)^2\right].
\end{aligned} \tag{B.4}$$

The term $\sum_{i=0}^{N-1} r_{\mathrm{IF}}^2[i]$ does not depend on $(\hat{\tau}, \hat{F}_D, \hat{S})$ and thus can be dropped. Moreover,

$$\begin{aligned}
&\sum_{i=0}^{N-1}\mu_i(\tau, F_D, S)^2 \\
&= \sum_{i=0}^{N-1} C\left(\bar{e}_B\left[i - \frac{\tau}{T_s}\right] - S\bar{e}_C\left[i - \frac{\tau}{T_s}\right]\right)^2 \cos^2(2\pi F_D i + \theta) \\
&= C\sum_{i=0}^{N-1}\left(2 - 2S\bar{e}_B\left[i - \frac{\tau}{T_s}\right]\bar{e}_C\left[i - \frac{\tau}{T_s}\right]\right)\left[\frac{1}{2} + \frac{1}{2}\cos(4\pi F_D i + 2\theta)\right] \\
&= 2C\sum_{i=0}^{N-1}\left[\frac{1}{2} + \frac{1}{2}\cos(4\pi F_D i + 2\theta)\right] \\
&\quad - 2SC\sum_{i=0}^{N-1}\bar{e}_B\left[i - \frac{\tau}{T_s}\right]\bar{e}_C\left[i - \frac{\tau}{T_s}\right]\left[\frac{1}{2} + \frac{1}{2}\cos(4\pi F_D i + \theta)\right] \\
&\approx CN,
\end{aligned} \tag{B.5}$$

where the orthogonality between $\bar{e}_B[i - \tau/T_s]$ and $\bar{e}_C[i - \tau/T_s]$ and the fact that the summation in (B.5) acts as a lowpass filter have been exploited. Equation (B.5) shows that also the term $\sum_{i=0}^{N-1}\mu_i(\tau, F_D, S)^2$ is approximatively independent from the parameters (τ, F_D, S) and thus (B.4) becomes

$$\begin{aligned}
(\hat{\tau}, \hat{F}_D, \hat{S}) &= \arg\max_{\tau, F_D, S}\sum_{i=0}^{N-1}\mu_i(\tau, F_D, S) r_{\mathrm{IF}}[i] \\
&= \arg\max_{\tau, F_D, S}\sum_{i=0}^{N-1} r_{\mathrm{IF}}[i] d_B\left[i - \frac{\tau}{T_s}\right] \\
&\quad \times\left(\bar{e}_B\left[i - \frac{\tau}{T_s}\right] - S\bar{e}_C\left[i - \frac{\tau}{T_s}\right]\right)\cos(2\pi F_D i + \theta) \\
&= \arg\max_{\tau, F_D, S} d_B\sum_{i=0}^{N-1} r_{\mathrm{IF}}[i] \\
&\quad \times\left(\bar{e}_B\left[i - \frac{\tau}{T_s}\right] - S\bar{e}_C\left[i - \frac{\tau}{T_s}\right]\right)\cos(2\pi F_D i + \theta).
\end{aligned} \tag{B.6}$$

Since the navigation bit d_B is supposed constant over one-code period it can be moved out the summation in (B.6). Equation (B.6) represents the expression for the maximum likelihood estimator for (τ, F_D, S), however it can be applied only under the hypothesis of knowing the bit d_B and the phase θ. In order to remove the dependence from those two parameters the cost function considered in (B.6) is usually modified according to the following methodology. Since all the terms in the last summation of (B.6) are real signals, it is possible to rewrite (B.6) as follows:

$$\begin{aligned}
(\hat{\tau}, \hat{F}_D, \hat{S}) &= \arg\max_{\tau, F_D, S}\mathbb{R}e\left\{d_B\sum_{i=0}^{N-1} r_{\mathrm{IF}}[i]\left(\bar{e}_B\left[i - \frac{\tau}{T_s}\right] - S\bar{e}_C\left[i - \frac{\tau}{T_s}\right]\right)\right. \\
&\qquad \left.\times\exp\left(j2\pi F_D i + j\theta\right)\right\},
\end{aligned} \tag{B.7}$$

that is, the real part of a complex scalar product. Equation (B.7) can be further expanded as

$$
\begin{aligned}
(\hat{\tau},\hat{F}_D,\hat{S}) &\\
&= \arg\max_{\tau,F_D,S} \Re e\Bigg\{\Bigg[\sum_{i=0}^{N-1} r_{\mathrm{IF}}[i]\left(\bar{e}_B\left[i-\frac{\tau}{T_s}\right]-S\,\bar{e}_C\left[i-\frac{\tau}{T_s}\right]\right)\\
&\qquad \times \exp\{j2\pi F_D i\}\Bigg]\cdot\exp\left\{j\theta+j(1-d_B)\frac{\pi}{2}\right\}\Bigg\},
\end{aligned}
\tag{B.8}
$$

where the terms in square brackets do not depend on the phase θ and on the sign d_B. Since d_B takes values in $\{-1,1\}$ it has been expressed as

$$
d_B = \exp\left\{j(1-d_B)\frac{\pi}{2}\right\}. \tag{B.9}
$$

The summation in (B.8) is a complex number that can be expressed in terms of phase and amplitude as

$$
\begin{aligned}
&\left[\sum_{i=0}^{N-1} r_{\mathrm{IF}}[i]\left(\bar{e}_B\left[i-\frac{\tau}{T_s}\right]-S\,\bar{e}_C\left[i-\frac{\tau}{T_s}\right]\right)\exp\{j2\pi F_D i\}\right]\\
&\qquad = A_S(\tau,F_D,S)\exp\{j\varphi_S(\tau,F_D,S)\}.
\end{aligned}
\tag{B.10}
$$

In this way (B.8) can be rewritten as

$$
\begin{aligned}
(\hat{\tau},\hat{F}_D,\hat{S}) &\\
&= \arg\max_{\tau,F_D,S} A_S(\tau,F_D,S)\\
&\qquad \times \Re e\left\{\exp\{j\varphi_S(\tau,F_D,S)\}\exp\left\{j\theta+j(1-d_B)\frac{\pi}{2}\right\}\right\}.
\end{aligned}
\tag{B.11}
$$

If the phase θ and the sign d_B are unknown, they can be estimated by maximizing (B.11) also with respect to these two parameters. Equation (B.11) is maximized with respect to θ and d_B when the condition

$$
\exp\{j\varphi_S(\tau,F_D,S)\}\exp\left\{j\theta+j(1-d_B)\frac{\pi}{2}\right\} = 1 \tag{B.12}
$$

is verified. By substituting (B.12) into (B.11), the joint estimator for the delay τ_0, the Doppler frequency $F_{D,0}$, and the relative phase S becomes

$$
\begin{aligned}
(\hat{\tau},\hat{F}_D,\hat{S}) &\\
&= \arg\max_{\tau,F_D,S} A_S(\tau,F_D,S)\\
&= \left|\sum_{i=0}^{N-1} r_{\mathrm{IF}}[i]\left(\bar{e}_B\left[i-\frac{\tau}{T_s}\right]-S\,\bar{e}_C\left[i-\frac{\tau}{T_s}\right]\right)\exp(j2\pi F_D i)\right|
\end{aligned}
\tag{B.13}
$$

that is a form of quadrature or incoherent matched filter [19]. The estimator (B.13) is equivalent to the coherent acquisition block with sign recovery

$$
\begin{aligned}
(\hat{\tau},\hat{F}_D,\hat{S}) &\\
&= \arg\max_{\tau,F_D,S} \left|\sum_{i=0}^{N-1} r_{\mathrm{IF}}[i]\left(\bar{e}_B\left[i-\frac{\tau}{T_s}\right]-S\,\bar{e}_C\left[i-\frac{\tau}{T_s}\right]\right)\exp(j2\pi F_D i)\right|^2.
\end{aligned}
\tag{B.14}
$$

ACKNOWLEDGMENT

The authors would like to thank Laura Camoriano for her support during the development of this work.

REFERENCES

[1] "Galileo open service signal in space interface control document," European Space Agency/Galileo Joint Undertaking, Draft GAL OS SIS ICD/D.0, May 2006.

[2] K. Borre, "The galileo signals with emphasis on L1 OS," in *Proceedings of the 12th International Power Electronics and Motion Control Conference (EPE-PEMC '06)*, pp. 2025–2030, Portoroz, Slovenia, August 2006.

[3] S. Wallner, J. Avila-Rodriguez, and G. W. Hein, "Galileo E1 OS and GPS L1C pseudo random codes requirements, generation, optimization and comparison," in *Proceedings of the 1st CNES Workshop on Galileo Signals and Signal Processing*, Toulouse, France, October 2006.

[4] "Giove-A open service signal in space interface control document," Galileo Project Office, First Issue ESA-DEUI-NGICD/02703, March 2007.

[5] E. D. Kaplan and C. J. Hegarty, Eds., *Understanding GPS: Principles and Applications*, Artech House, Norwood, Mass, USA, 2nd edition, 2005.

[6] P. Misra and P. Enge, *Global Positioning System: Signals, Measurements and Performance*, Ganga-Jamuna Press, Lincoln, Mass, USA, 2001.

[7] G. Lachapelle and M. Petovello, "Weak Signal Tracking and High-Sensitivity GPS for Indoors," Navtech GPS, vol. 3, September 2005.

[8] J. W. Betz, "Systems, Signals and Receiver Signal Processing," Navtech GPS, vol. 3, September 2006.

[9] P. G. Mattos, "Acquisition of the galileo OS L1b/c signal for the mass-market receiver," in *Proceedings of the 18th International Technical Meeting of the Satellite Division of the Institute of Navigation (ION GNSS '05)*, pp. 1143–1152, Long Beach, Calif, USA, September 2005.

[10] P. G. Mattos, "Galileo L1c—acquisition complexity: cross correlation benefits, sensitivity discussions on the choice of pure pilot, secondary code, or something different," in *Proceedings of IEEE/ION Position, Location, and Navigation Symposium (PLANS '06)*, pp. 845–852, San Diego, Calif, USA, April 2006.

[11] C. Yang, C. Hegarty, and M. Tran, "Acquisition of the GPS L5 signal using coherent combining of I5 and Q5," in *Proceedings of the 17th International Technical Meeting of the Satellite Division of the Institute of Navigation (ION GNSS '04)*, pp. 2184–2195, Long Beach, Calif, USA, September 2004.

[12] R. N. McDonough and A. D. Whalen, *Detection of Signals in Noise*, Academic Press, Boston, Mass, USA, 2nd edition, 1995.

[13] A. J. V. Dierendonck, "GPS receivers," in *GPS Theory and Applications*, B. W. Parkinson and J. J. Spilker Jr., Eds.,

vol. 1, American Institute of Aeronautics and Astronautics, Washington, DC, USA, 1st edition, 1996.

[14] J. Proakis, *Digital Communications*, McGraw-Hill, Boston, Mass, USA, 4th edition, 2000.

[15] D. Borio, M. Fantino, L. Lo Presti, and L. Camoriano, "Acquisition analysis for galileo BOC modulated signals: theory and simulation," in *Proceedings of the European Navigation Conference (ENC '06)*, Manchester, UK, May 2006.

[16] D. A. Shnidman, "The calculation of the probability of detection and the generalized Marcum Q-function," *IEEE Transactions on Information Theory*, vol. 35, no. 2, pp. 389–400, 1989.

[17] D. A. Marcum, "A statistical theory of target detection by pulsed radar," *IRE Transactions on Information Theory*, vol. 6, pp. 59–144, 1960.

[18] M. Abramowitz and I. A. Stegun, Eds., *Handbook of Mathematical Functions: with Formulas, Graphs, and Mathematical Tables*, Dover, New York, NY, USA, 1965.

[19] S. M. Kay, *Fundamentals of Statistical Signal Processing, Volume 2: Detection Theory*, Prentice Hall Signal Processing Series, Prentice Hall, Upper Saddle River, NJ, USA, 1st edition, 1998.

Hindawi Publishing Corporation
International Journal of Navigation and Observation
Volume 2008, Article ID 246703, 14 pages
doi:10.1155/2008/246703

Research Article

Design of Short Synchronization Codes for Use in Future GNSS System

Surendran K. Shanmugam,[1] Cécile Mongrédien,[1] John Nielsen,[2] and Gérard Lachapelle[1]

[1] *Department of Geomatics Engineering, University of Calgary, AB, Canada T2N 1N4*
[2] *Department of Electrical and Computer Engineering, University of Calgary, AB, Canada T2N 1N4*

Correspondence should be addressed to Surendran K. Shanmugam, suren@geomatics.ucalgary.ca

Received 4 August 2007; Accepted 7 February 2008

Recommended by Olivier Julien

The prolific growth in civilian GNSS market initiated the modernization of GPS and the GLONASS systems in addition to the potential deployment of Galileo and Compass GNSS system. The modernization efforts include numerous signal structure innovations to ensure better performances over legacy GNSS system. The adoption of secondary short synchronization codes is one among these innovations that play an important role in spectral separation, bit synchronization, and narrowband interference protection. In this paper, we present a short synchronization code design based on the optimization of judiciously selected performance criteria. The new synchronization codes were obtained for lengths up to 30 bits through exhaustive search and are characterized by optimal periodic correlation. More importantly, the presence of better synchronization codes over standardized GPS and Galileo codes corroborates the benefits and the need for short synchronization code design.

1. INTRODUCTION

The legacy global positioning system (GPS) has performed well beyond initial expectations in the past but faces stern impediments in the view point of new civilian GPS applications. Several initiatives were launched during the last decade to satisfy the demands of these new civilian applications. Consequently, these efforts led to the birth of second-generation global navigation satellite systems (GNSSs). These efforts include the modernization of legacy GPS and the restoration of Russian global navigation satellite system (GLONASS). The Galileo system, a major European initiative, is well positioned to benefit from the three decades of GPS and GLONASS experience [1]. More recently, the GNSS community has witnessed yet another highpoint with the launch of first medium earth orbit (MEO) satellite of Chinese Compass GNSS system [2].

A major milestone in the modernization initiative is the inclusion of new civilian signals that will provide the benefits of frequency diversity besides accuracy and availability improvements [3–5]. These new civilian signals include numerous structural innovations that will provide the foremost benefit to the civilian GNSS community. The modernized signals encompass key innovations such as dataless channel, improved navigation data message format, secondary spreading code structure, and new modulations schemes [6]. More specifically, both GPS and Galileo systems utilize secondary short synchronization codes to accomplish

(i) data symbol synchronization,
(ii) spectral separation,
(iii) narrowband interference protection.

For instance, the use of short 10-bit and 20-bit Neuman-Hofman (NH) codes, in GPS L5 signals, readily alleviates the issue of data symbol synchronization. Besides, the different code period of NH10 and NH20 codes in the data and pilot channels readily provides the necessary spectral separation. The secondary synchronization code further enhances the correlation suppression performance of the primary pseudorandom noise (PRN) code. Finally, it spreads the spectral lines of primary PRN I5/Q5 codes thereby reducing the effect of narrowband interference by another 13 dB [4]. The Galileo system also utilizes short secondary synchronization codes of various lengths to facilitate the aforementioned tasks [7].

Table 1: Secondary code assignment in GPS and Galileo systems.

GPS			Galileo		
Signal type	Code name	Code length	Signal type	code name	Code length
L5-Data	NH10	10	E5a-Data	CS20	20
L5-Pilot	NH20	20	E5a-Pilot	CS100$_{1-50}$	100
L1C-Pilot	OC1800$_{1-210}$	1800	E1c	CS25	25
			E5b-Data	CS4	4
			E5b-Pilot	CS100$_{51-1001}$	100
			E6c	CS100$_{1-50}$	100

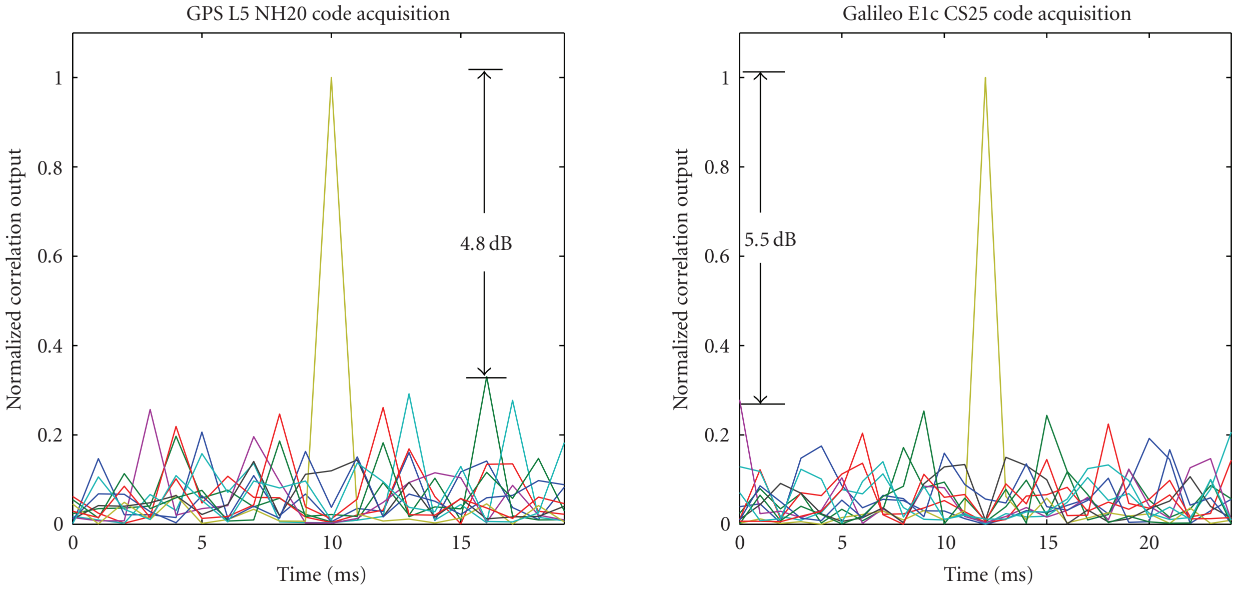

(a)

(b)

Figure 1: Superposition of secondary code correlation outputs for various Doppler offsets. (LHS) GPS L5 NH20 code (RHS) Galileo E1c CS25 code.

Table 1 lists the secondary code assignments and their lengths in GPS and Galileo systems.

The secondary synchronization codes are predominantly memory codes except for the L1C, wherein the overlay codes were obtained through truncated *m*-sequences (1–63) and gold sequences (64–210) [8]. There exists a trade-off between memory codes and codes that are obtained from linear feedback shift register (LFSR) implementation. While the LFSR-based codes are appealing in the view point of hardware implementation, they only exist for specific lengths. The use of truncation technique can alleviate this issue at the expense of inferior correlation properties. On the other hand, memory codes can be obtained for any specific lengths with optimal correlation characteristics. However, exhaustive search of optimal synchronization code becomes more difficult with increasing code lengths.

A limitation arising due to the usage of short synchronization codes is the degradation in correlation suppression especially in the presence of frequency errors. For instance, the vulnerability of NH20 code acquisition in the presence of Doppler uncertainties is discussed in [9]. The isolation of the main correlation peak to that of secondary peaks can degrade from the nominal 14 dB to 4.8 dB level under worst case Doppler scenarios [10]. Under these conditions, the NH code acquisition of weak GPS L5 signals becomes more difficult in the presence of other strong GPS L5 signals. The existence of better synchronization codes over standardized NH20 code was later reported in [10], which is based on the 20-bit synchronization code originally proposed in [11]. Under specific Doppler conditions, the new 20-bit code (known as the Merten's code) showed an improvement of around 2 dB over the standardized NH20 code in terms of correlation suppression [10]. However, the performance improvement achieved by the Merten's code corresponds to a specific Doppler scenario and thus does not reflect the actual performance improvement under Doppler uncertainty. Interestingly, the importance of spreading code selection for the Galileo GNSS system and the corresponding measures was identified in [12]. Besides, it is also desirable to develop optimal synchronization codes that offer better resistance to residual Doppler errors. In this paper, we introduce relative performance measures such as peak-to-side lobe ratio (PSLR) and integrated side lobe ratio (ISLR) related to the design of periodic binary codes that are utilized in GNSS system. More importantly, new optimal secondary synchronization codes were obtained using these performance measures through exhaustive search for lengths up to 30 bits. The merits of the proposed synchronization codes are also compared with standardized codes using the same performance measures. Besides, the association of the optimal synchronization codes with the systematic codes such as Golay complementary codes is also established. Numerical simulations were used to demonstrate the superior acquisition performance of the proposed short synchronization codes over standardized codes under Doppler uncertainties in terms of PSLR measure.

The remainder of this paper is organized as follows. In Section 2, the advantage of optimal synchronization codes is further established in the view point of GPS L5 NH code acquisition. More specifically, we show the inadequacy of NH20 code in comparison to Merten's 20-bit code under different Doppler conditions. The relevant performance measures pertaining to optimal binary periodic synchronization code are introduced in Section 3. The binary-code search strategy and the various code construction methods are detailed in Section 4. Besides, the merits of new synchronization codes are compared with the standardized codes. Acquisition performance analysis is then carried out in Section 5. The final concluding remarks are made in Section 6.

2. NEED FOR IMPROVED SYNCHRONIZATION CODES

An issue with short synchronization codes is limited correlation suppression performance due to their short code length. For instance, the correlation suppression performance of NH20 code can be degraded by as much as 8 dB from the nominal 14 dB in the presence of Doppler uncertainty [9]. In [10], the authors reported a degradation of 9.2 dB for NH20 code under specific Doppler scenarios. To further illustrate this, the GPS L5 NH20 code and Galileo E1c CS25 code correlation outputs for different Doppler bins are plotted in Figure 1. The acquisition criterion in Figure 1 was obtained following the analysis reported in [10]. For instance, the residual Doppler during the acquisition of NH20 and CS25 code was set to 12 Hz; and this residual Doppler was searched between 0 and 250 Hz in steps of 25 Hz.

In Figure 1, we can readily observe the degradation in correlation main peak isolation for NH20 from the nominal 14 dB to 4.8 dB as reported earlier in [10]. On the other hand, the Galileo E1c CS25 code degraded from the nominal 18.4 dB down to 5.5 dB. The additional 3 dB degradation in CS25 code acquisition can be attributed to the longer coherent integration time (i.e., 25 millie seconds rather than 20 millie seconds) and nonzero out-of-phase correlation in the original CS25 code. Accordingly, the acquisition of weak GPS L5 signals or Galileo E1c signals can be hindered in the presence of strong GPS L5 and Galileo E1c signals from other satellites. While the correlation suppression performance can be improved with longer length codes, judicial selection of synchronization codes can offer better correlation suppression for the same code length. For example, in [10], the authors reported a correlation suppression gain of around 2 dB for Merten's code over standard NH20 code under specific Doppler scenario. The LHS plot in Figure 2 shows the superposition of the Merten's 20-bit synchronization code (M20) correlation outputs for the same Doppler setting as in Figure 1. The RHS plot shows the correlation suppression performance for the standardized NH20 and the M20 code for various residual Doppler's. The Doppler was searched between 0 to 250 Hz in steps of 25 Hz.

The RHS plot in Figure 2 readily shows the 2 dB improvement accomplished by the M20 code over the standardized NH20 code for the residual Doppler of 12 Hz. In other words, the M20 code can tolerate another 10 Hz of residual Doppler for the same PSLR of 4.8 dB achieved by the NH20 code. The M20 code resulted in an average performance improvement of around 1.7 dB over the NH20 code for the range of residual Doppler's. The performance improvement in M20 code can readily be accredited to its better correlation characteristic. For instance, the periodic correlation of the different synchronization codes of length 20 (see Table 2) is summarized below

$$\begin{aligned}
R_{\mathrm{NH10}} &= \{10,-2,2,-2,-2,2,-2,-2,2,-2\},\\
R_{\mathrm{NH20}} &= \{20,0,0,0,0,0,-4,0,4,0,-4,0,4,0,-4,0,0,0,0,0\},\\
R_{\mathrm{CS20}} &= \{20,0,0,0,0,0,4,0,-4,0,-4,0,-4,0,4,0,0,0,0,0\},\\
R_{\mathrm{M20}} &= \{20,0,0,0,0,-4,0,-4,0,0,0,0,0,-4,0,-4,0,0,0,0\}.
\end{aligned} \tag{1}$$

The periodic correlation output of the M20 code, R_{M20}, has lesser number of out-of-phase correlation when compared to both NH20 and CS20 codes. Accordingly, one can expect its code acquisition performance to be superior even in the presence of residual Doppler. It is worth emphasizing here that the NH10 and NH20 codes were not obtained from exhaustive search, whereas the M20 code was obtained through exhaustive search [11]. The very existence of the NH20, M20, and CS20 corroborates the presence of multiple solutions for the code design problem. Besides, the search for periodic code is expected to yield multiple solutions due to the existence of equivalence classes [13]. Hence, it is necessary to obtain the binary codes that satisfy the optimal correlation characteristics and select the best possible code judiciously using relevant performance measures.

3. OPTIMAL SYNCHRONIZATION CODE—FIGURE OF MERITS

Better synchronization code can be obtained by optimizing the corresponding correlation characteristics of the individual codes. As we are dealing with binary codes of short period, the optimization of correlation characteristics can be achieved in an exhaustive fashion. It is however, necessary to derive performance measure or measures that readily embody the correlation characteristics of a binary code [12]. The two important performance measures pertaining

Table 2: Optimal binary synchronization code search result.

Code length	Number of codes	PSLR (dB)	ISLR (dB)	Code length	Number of codes	PSLR (dB)	ISLR (dB)
4	**8 (1)**	**∞**	**∞**	18	6,047 (168)	19.1	2.4
5	10 (1)	14	3.2	19	75 (2)	22.6	10
6	47 (8)	9.5	0.9	**20**	**5,079 (45)**	**14**	**3.1**
7	28 (2)	16.9	4.1	21	1,259 (30)	16.9	4.2
8	32 (2)	6	2	22	15,839 (360)	20.8	2.9
9	108 (8)	9.5	1.7	23	91 (2)	27.3	12
10	**360 (16)**	**14**	**1.4**	24	1,535 (32)	15.6	9
11	44 (4)	20.8	6.1	**25**	**7,000 (260)**	**18.4**	**4.3**
12	96 (4)	9.5	4.5	26	31,615 (608)	22.3	3.4
13	104 (4)	22.3	7.1	27	775 (144)	19.1	4.9
14	1,791 (128)	16.9	1.9	28	23,743 (424)	16.9	4.1
15	59 (4)	23.5	8	29	3,247 (56)	19.7	4.6
16	255 (16)	12	2.7	30	35,039 (584)	23.5	3.9
17	2,175 (64)	15.1	2.3				

to optimal synchronization codes are the peak-to-side lobe ratio (PSLR) [14] and the integrated side lobe ratio (ISLR) [15]. Besides, the synchronization codes are also expected to be *balanced* for desirable spectral characteristics. To define PSLR and ISLR, we first express the periodic auto-correlation of the binary code of length N (i.e., $\mathbf{x} = [x_0, x_1, \dots, x_{N-1}]$), at shift i, as

$$R(i) = \sum_{k=0}^{N-1} x(k)x(k - i \ \mathbf{mod}\ N), \quad i = 0, 1, 2, \dots, N-1, \tag{2}$$

where $x(k) \in \{+1, -1\}$ and **mod** is the modulo operation. The PSLR for the binary code $x(k)$ with the periodic auto-correlation, $R(i)$, is given by

$$\text{PSLR}(\mathbf{x}) = \frac{R(i=0)^2}{\mathbf{max}\left|R(i \neq 0)\right|^2}, \quad i = 0, 1, 2, \dots, N-1. \tag{3}$$

Maximizing the PSLR measure minimizes the out-of-phase correlation that eventually aids in reducing false acquisition. On the other side, ISLR measures the ratio of auto-correlation main lobe (or peak) energy to its side lobe energy [15]. The ISLR of a binary code is defined as

$$\text{ISLR}(\mathbf{x}) = \frac{N^2}{2\sum_{i=1}^{N-1}\left|R(i)\right|^2}, \quad i = 0, 1, 2, \dots, N-1. \tag{4}$$

Maximizing the ISLR measure readily limits the effect of out-of-phase correlation from all shifts. It will be emphasized here that the maximization of ISLR often maximizes the PSLR measure. Finally, the balanced property of a binary code is related to the mean value of the code and is given by

$$\mu(\mathbf{x}) = \frac{1}{N}\sum_{k=0}^{N-1} x(k). \tag{5}$$

For binary code sets design, as in the case of OC1800 in GPS and CS100 in Galileo, it is also desirable to minimize the mutual interference experienced by the individual codes from other codes. Minimizing the magnitude of cross-correlation readily limits the effect of mutual interference between any two codes. The *mean square correlation* (MSC) measure embodies this mutual correlation and can be utilized during multiobjective synchronization code optimization. For any two codes $x_p(k)$ and $x_q(k)$ of length N pertaining to the code set comprising of M unique codes, the mutual correlation or the MSC is given by

$$\text{MSC}(p, q) = 2\sum_{i=0}^{N-1}\left|R_{p,q}(i)\right|^2, \quad p \neq q, \tag{6}$$

where $R_{p,q}(i)$ is the periodic cross-correlation between the codes $x_p(k)$ and $x_q(k)$, and is given by

$$R_{p,q}(i) = \sum_{k=0}^{N-1} x_p(k)x_q(k - i \ \mathbf{mod}\ N), \quad i = 0, 1, 2, \dots, N-1. \tag{7}$$

The aforementioned mean square correlation is closely related to the well-known total squared correlation measure utilized in CDMA spread code optimization [16].

4. OPTIMUM CODE SEARCH RESULTS

For short code length, the synchronization code optimization can be accomplished through exhaustive search of binary codes with optimal correlation characteristics. The developed exhaustive search technique utilized fast Fourier transform (FFT)-based block processing and matrix manipulations to speed up the search process. Both PSLR and ISLR were utilized for the objective maximization. Optimal synchronization codes for lengths up to 30 were obtained through exhaustive search. Interestingly, the search process yielded large number of codes that were optimal based on the aforementioned performance measures. Table 2 lists the number of codes alongside the unique solutions within braces, the PSLR and ISLR values, respectively.

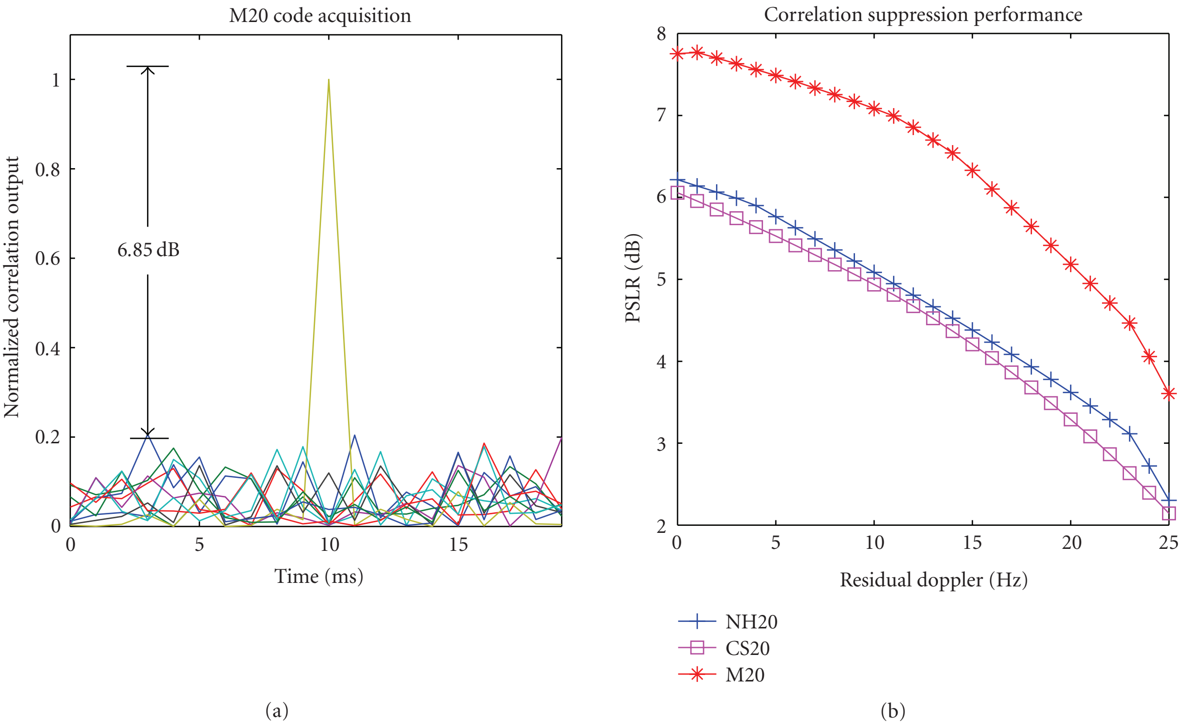

(a)

(b)

FIGURE 2: (LHS) superposition of secondary code correlation outputs for various Doppler offsets for M20 code (RHS) PSLR performance as a function of residual Doppler.

The large number of codes arise from existence of the equivalence classes due to the shift invariance property of the periodic codes [13]. For example, the code $x(k)$, its negated version, its time reversed, or its shifted version will be characterized by similar PSLR and ISLR measures. To obtain unique solutions, the search technique discarded codes if their maximum cross-correlation is equal to the code length. Accordingly, any two codes $x_p(k)$ and $x_q(k)$ satisfy the following cross-correlation constraint are considered unique:

$$\mathbf{max}\left|R_{p,q}(i)\right| < N, \quad i = 0, 1, 2, \ldots, N-1. \tag{8}$$

Besides, the codes are time-reversed and hence were tested for (8). While the balance property (i.e., $\mu(\mathbf{x})$) was not included during the code selection, its significance will be emphasized during the acquisition performance analysis. In Table 2, the binary codes whose lengths are similar to the standardized codes are highlighted in bold. In [17], the authors theoretically established the optimal periodic correlation of a *balanced* binary code as

$$R(i) = \begin{cases} 0 \text{ or } -4 & N \textbf{ mod } 4 = 0, \\ 2 \text{ or } -2 & N \textbf{ mod } 4 = 2, \end{cases} \quad i \neq 0. \tag{9}$$

The periodic correlation of optimal binary code for both odd and even lengths was further established in [18], and is expressed below

$$R(i) = \begin{cases} 0 \text{ or } 4 \text{ or } -4 & N \textbf{ mod } 4 = 0, \\ 1 \text{ or } -3 & N \textbf{ mod } 4 = 1, \\ 2 \text{ or } -2 & N \textbf{ mod } 4 = 2, \\ -1 \text{ or } 3 & N \textbf{ mod } 4 = 3, \end{cases} \quad i \neq 0. \tag{10}$$

From (1) and (9), we see that both NH10 and M20 possess optimal periodic correlation. Besides, the Galileo CS25 code was also optimal as it satisfied the periodic correlation expressed in (10). On the other hand, both NH20 and CS20 are not optimal in the view point of (9), but can be considered optimal in terms of PSLR measure. The inferior periodic correlation of NH20 does not come as a surprise as the original NH codes were not obtained by exhaustive search [19]. It should be noted here that all the secondary codes utilized in GPS and Galileo system are not balanced (i.e., sum of individual code phases is not equal to zero) and thus (9) cannot be applied in a strict sense, but indicates the conditions for optimality. Numerical analysis later confirmed the fact that even unbalanced binary code is characterized by periodic correlation as predicted in (9).

All the binary codes obtained through exhaustive search indeed satisfied the periodic correlation as expressed in (10) and thereby asserting the optimality of the developed binary codes. The optimal 10-bit and 25-bit code obtained through exhaustive search resulted in similar PSLR and ISLR performance measures to that of NH10 and CS25 codes in accordance to (10). On the other hand, the 20-bit code obtained via exhaustive search resulted in better

ISLR performance even as the PSLR performance was the same. Moreover, the new 20-bit code had similar correlation characteristics as that of M20 code introduced earlier. In Table 2, we can also observe that odd-length codes generally yielded better PSLR and ISLR performance. More specifically, the binary codes for lengths $N = 5, 7, 11, 13, 15$ showed similar PSLR and better ISLR, even when compared to twice their code lengths (i.e., $N = 10, 14, 22, 26, 30$). The high PSLR and ISLR values observed for code lengths $N = 5, 7, 11, 13, 15, 23$ can readily be attributed to their ideal correlation characteristics as expressed in (10). However, it is recognized that the choice of secondary code length in GNSS system can be influenced by other parameters besides correlation characteristics alone.

Further analysis of the optimal binary code of length 20 revealed the existence of close association of optimal binary codes to that of the well-known Golay complementary pairs [20]. The Golay complementary pairs have been extensively utilized in a number of applications ranging from radar signal processing [21] and communication [22] to multislit spectrometry [20]. Two binary codes $x_a(k)$ and $x_b(k)$ are said to be Golay complementary pair, if they satisfy the following constraint:

$$R_G(i) = R_a(i) + R_b(i) = \begin{cases} 2N, & i = 0, \\ 0, & i \neq 0, \end{cases} \tag{11}$$

where $R_a(i)$ and $R_b(i)$ are the periodic correlation of $x_a(k)$ and $x_b(k)$, respectively. $R_G(i)$ is the periodic correlation function of the Golay complementary pair. Besides, the individual codes in a Golay complementary pair are referred as Golay codes. The periodic correlation in (11) immediately asserts the advantage of Golay complementary codes in the view point of code design. For example, the NH10 code and the first-half of the NH20 code are Golay complementary pair as shown in Figure 3. Hence, there exists a possibility of utilizing this underlying structure to accomplish better acquisition abilities. Unfortunately, the NH10 code and second half of NH20 code are not Golay complementary pairs.

Motivated by this observation, the optimal binary codes of length 20 obtained via exhaustive search were tested for Golay complementary pair. Interestingly, many binary codes of length 20 obtained through exhaustive search (i.e., $\mathrm{S20}_2$ in Table 3) satisfied the Golay complementary condition. For example, the Golay complementary pairs $\mathrm{G10}_a$ and $\mathrm{G10}_b$ can be constructed from the even and odd samples of $\mathrm{S20}_2$ (hex value "05D39" and "FA2C6" also give rise to Golay pairs) listed in Table 3, and the corresponding Golay codes are given by

$$\begin{aligned} \mathrm{G10}_a &= [-1, 1, -1, 1, -1, -1, -1, -1, 1, 1], \\ \mathrm{G10}_b &= [1, -1, -1, 1, 1, -1, 1, 1, 1, 1]. \end{aligned} \tag{12}$$

More importantly, the individual Golay codes $\mathrm{G10}_a$ and $\mathrm{G10}_b$ were also optimal having periodic correlation in accordance to (9). Moreover, the Golay codes of length $N/2$ obtained from an optimal code of length N were also optimal. Consequently, the 45 optimal binary codes of length 20 (see Table 2) were tested for Golay complementary condition. Surprisingly, 75% (32 out of 45 codes) of the 20-bit optimal binary codes satisfied the Golay complementary condition. A corollary of this conjecture indicates the possibility of constructing optimal codes of length N from Golay complementary pairs of length $N/2$. The construction of binary codes by multiplexing Golay complementary pairs readily guarantees that every alternate shift will result in zero correlation due to the complementary correlation output of individual Golay codes. Interestingly, the aforementioned property of the Golay codes was utilized for signal acquisition in ultrasonic operations [23]. To further verify this corollary, we constructed a binary code from Golay complementary pairs of length 20 (hex values "CD87F" and "CE5AA"). The resulting binary code of length 40 (hex value "F0F6916EEE") demonstrated optimal periodic correlation as predicted by (9). Thus, it is possible to construct optimal binary codes of larger lengths by utilizing the aforementioned association between optimal codes and the Golay complementary codes. Besides, the highly regular structure of binary Golay complementary codes readily allows for an efficient construction [24].

Motivated by the aforementioned observation, we constructed synchronization codes of length $N = 100$ from optimal codes of lengths 10, 20, and 25. The specific choice of code length was dictated by the fact that the desired code length 100 was divisible by 10, 20, and 25. The final code length of 100 was obtained by manipulating the individual codes of length 10, 20, and 25 with the augmentation codes of length 10, 5 and 4. Let $x_p(k)$ and $x_s(k)$ be the primary and the augmentation code of length N_p and N_s. Thus, we have $N = N_s N_p$, where $N = 100$, $N_s = \{10, 5, 4\}$, and $N_p = \{10, 20, 25\}$ in our case. The final binary code, $x(k)$, of length N can be obtained as follows:

$$x(k) = \sum_{m=0}^{N_s-1} \sum_{n=0}^{N_p-1} x_s(m) x_p(n) g\left(k - m\frac{N}{N_s} - n\frac{N}{N_p}\right), \quad k = 0, 1, 2, \ldots, N-1, \tag{13}$$

where $g(k)$ is the rectangular pulse function and is given by

$$g(k + \Delta T) = \begin{cases} 1 & 0 \leq \Delta T < T_b, \\ 0 & \text{elsewhere}, \end{cases} \tag{14}$$

where T_b is the basic bit duration over which the x_k is constant. For example, the 100-bit code, $x(k)$ (hex value "C7F526E3FA9371FD49A7015B2"), was obtained from the primary code, $x_p(k)$ (hex value "380AD90"), and the augmentation code, $x_s(k)$ (hex value "1"). In Table 2, we saw that there exists 7,000 codes of length 25 with 260 unique solutions but we only need 100 unique codes. Thus, we utilized the following constraints on the PSLR and ISLR measures to limit the number of codes:

$$\begin{aligned} \mathrm{PSLR} &\geq 21.9\ \mathrm{dB}, \\ \mathrm{ISLR} &\geq 3\ \mathrm{dB}. \end{aligned} \tag{15}$$

The PSLR and ISLR thresholds in (15) were duly obtained from the average PSLR and ISLR measures of the Galileo

Table 3: Secondary synchronization code—performance measures ($\mu(\mathbf{x})$, PSLR, and ISLR are defined in (5), (3), and (4), resp.).

Secondary code performance									
Standard codes					Proposed codes				
Code identifier	Code length	$\lvert\mu(\mathbf{x})\rvert$	PSLR (dB)	ISLR (dB)	Code identifier	Code length	$\lvert\mu(\mathbf{x})\rvert$	PSLR (dB)	ISLR (dB)
CS4	4	0.5	∞	∞	S4	4	0.5	∞	∞
NH10	10	0.2	14	1.5	S10	10	0	14	1.5
NH20	20	0.2	14	4	$S20_1$	20	0	14	4
CS20	20	0.2	14	4	$S20_2$	20	0.1	14	4.9
CS25	25	0.2	18.4	6.3	$S20_3$	20	0.2	14	4
M4	4	0.5	∞	∞	$S25_1$	25	0.2	18.4	6.3
M10	10	0.4	14	1.5	$S25_2$	25	0.2	18.4	6.3
M20	20	0.1	14	4.9					
M25	25	0.2	18.4	6.3					

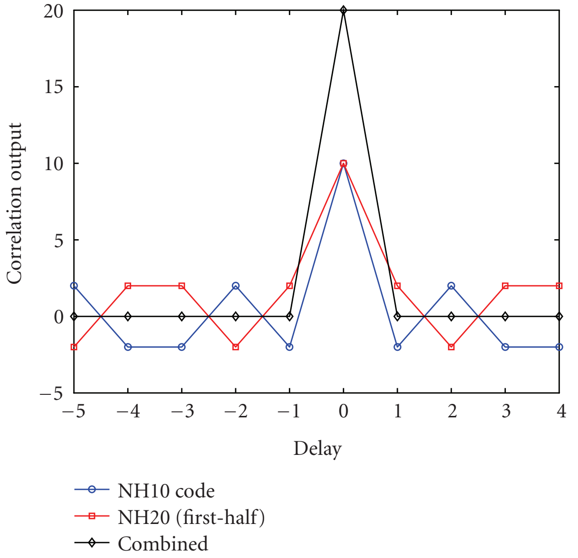

Figure 3: Correlation output of Golay complementary codes (NH10 and first half of NH20).

G100 code set [25]. Finally, the cross-correlation constraint expressed in (8) was also utilized to obtain unique solutions. Consequently, a total number of 105 unique codes were obtained in this fashion which satisfied the aforementioned conditions. The hexadecimal representations of the individual codes are listed in Table 6. It is worth noting here that not a single Galileo G100 code as well as the proposed 100-bit codes satisfied the optimal periodic correlation based on (9). The following section establishes the merits and limitations of the proposed binary synchronization codes in comparison to the standardized secondary synchronization codes.

5. ACQUISITION PERFORMANCE ANALYSIS

Having obtained the optimal binary codes of various lengths, we now turn our focus on the evaluation of the proposed codes in comparison to the standardized codes utilized in GPS and Galileo system. In this paper, the structure proposed in Tran and Hegarty [26] was adopted for the secondary code acquisition, wherein the primary code is assumed to be acquired within half chip duration alongside residual Doppler. The secondary code is acquired by correlating the primary code correlation outputs with the locally generated secondary code samples. The residual Doppler was assumed to be within ±250 Hz. During the secondary code acquisition, the residual Doppler was also searched within ±250 Hz in steps of 25 Hz.

The Galileo CS4 code is already established as the optimal code and will not be dealt during the acquisition performance analysis. Table 3 lists the $\mu(\mathbf{x})$, the PLSR, and the ISLR measures of the standardized Merten's and the proposed codes of various lengths. While the 20-bit synchronization codes achieved similar PSLR measure as that of 10-bit codes, their ISLR performances were much better than that of 10-bit codes. In Table 3, it can be noticed that there are 3 different sets of S20 code ($S20_1$, $S20_2$, and $S20_3$) and two sets of S25 code ($S25_1$ and $S25_2$). While these different codes are optimal in terms of correlation characteristics, their correlation characteristics differed in the presence of the residual Doppler with some outperforming the other codes. In Table 3, we see that the designed codes were not only optimal in terms of PSLR and ISLR measures, they were also more balanced. The advantage of the M20 and $S20_2$ over the NH20 and CS20 codes is readily asserted by the higher ISLR values. Interestingly, the other 20-bit codes $S20_1$ and $S20_3$ demonstrated better acquisition performance in comparison to M20 and $S20_2$ codes despite being inferior in ISLR measure. In the case of CS100 and S100 codes, the autocorrelation and cross-correlation protection were evaluated using a number of measures. The PSLR measure based on the auto-correlation was same for both CS100 and S100 codes despite being suboptimal in the view point of (9). The cross-correlation PSLR (CPSLR) measure was also obtained for CS100 and S100 codes. The CPSLR measures the ratio between the auto-correlation main peak of code ($R(i)$) to the maximum of the cross-correlation peak ($R_{p,q}(i)$) and it is given by

$$\text{CPSLR} = \frac{R(i=0)^2}{\mathbf{max}\left|R_{p,q}(i\neq 0)\right|^2}. \quad (16)$$

Table 4: Galileo CS100 and proposed S100 codes performance.

	Secondary code performance					
	CPSLR (dB)		ISLR (dB)		MSC (dB)	
	CS100	S100	CS100	S100	CS100	S100
Max	14.9	14	6.6	5.9	43.5	43.6
Min	6	2.9	3.7	5.1	42.6	42.8
Mean	11.2	9.1	4.9	5.6	43	43.1
Std. Dev	1.2	2.4	0.6	0.3	0.1	0.2

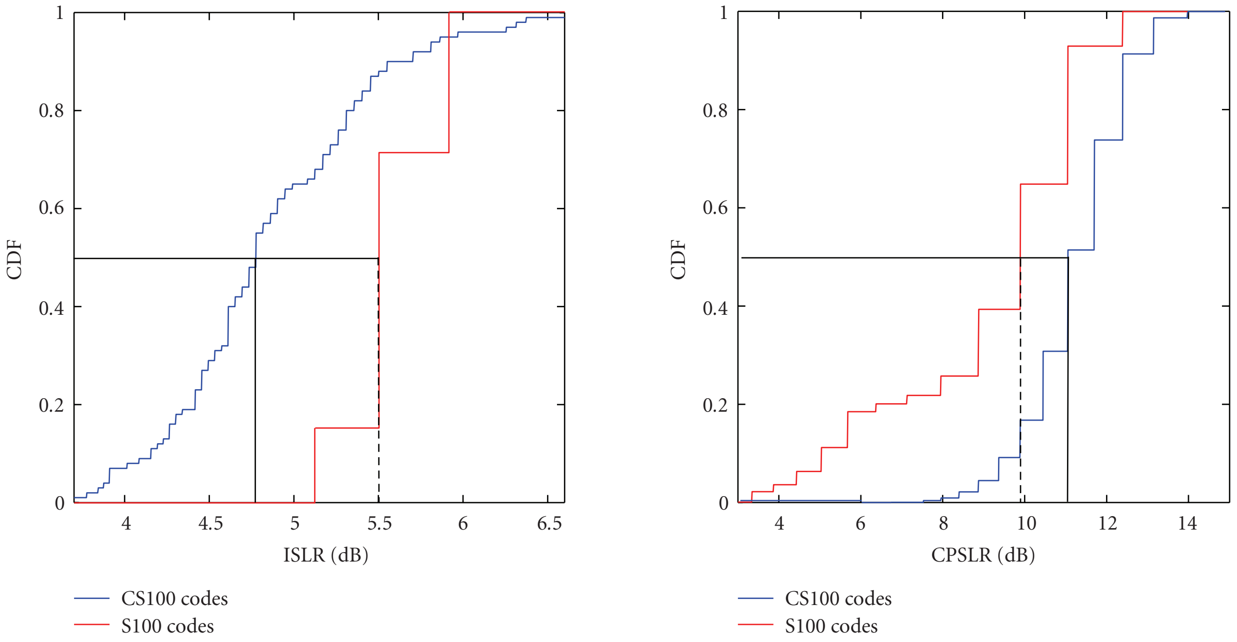

(a)

(b)

Figure 4: PSLR and ISLR performance of Galileo CS100 and the proposed S100 codes.

Table 5: Hexadecimal representation GPS/Galileo and proposed secondary codes (highlighted colour in bold represents equivalence).

Code identifier	Code length	Number of hex symbols	Number of zero padding	Hex value
CS4	4	1	0	**E**
NH10	10	3	2	F28
NH20	20	5	0	FB2B1
CS20	20	5	0	842E9
CS25	25	7	3	**380AD90**
M4	4	1	0	**D**
M10	10	3	2	CBC
M20	20	5	0	**FA2C6**
M25	25	7	3	**E3FA930**
S4	4	1	0	**B**
S10	10	3	2	3B0, 3C8
$S20_1$	20	5	0	14B37, 14B37
$S20_2$	20	5	0	**05D39**, 6345F
$S20_3$	20	5	0	315B0, 640E5
$S25_1$	25	7	3	21228F8, DFB45C0
$S25_2$	25	7	3	AD04C18

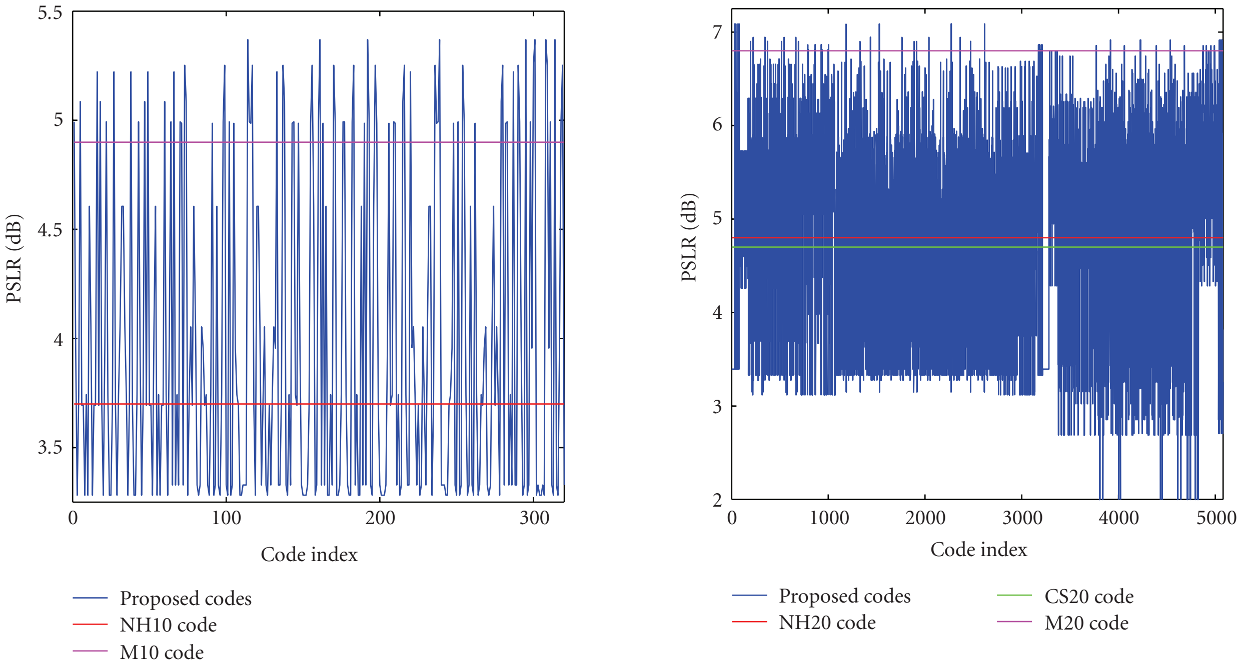

(a) (b)

Figure 5: PSLR performance in the presence of residual Doppler (LHS) 10-bit code (RHS) 20-bit code.

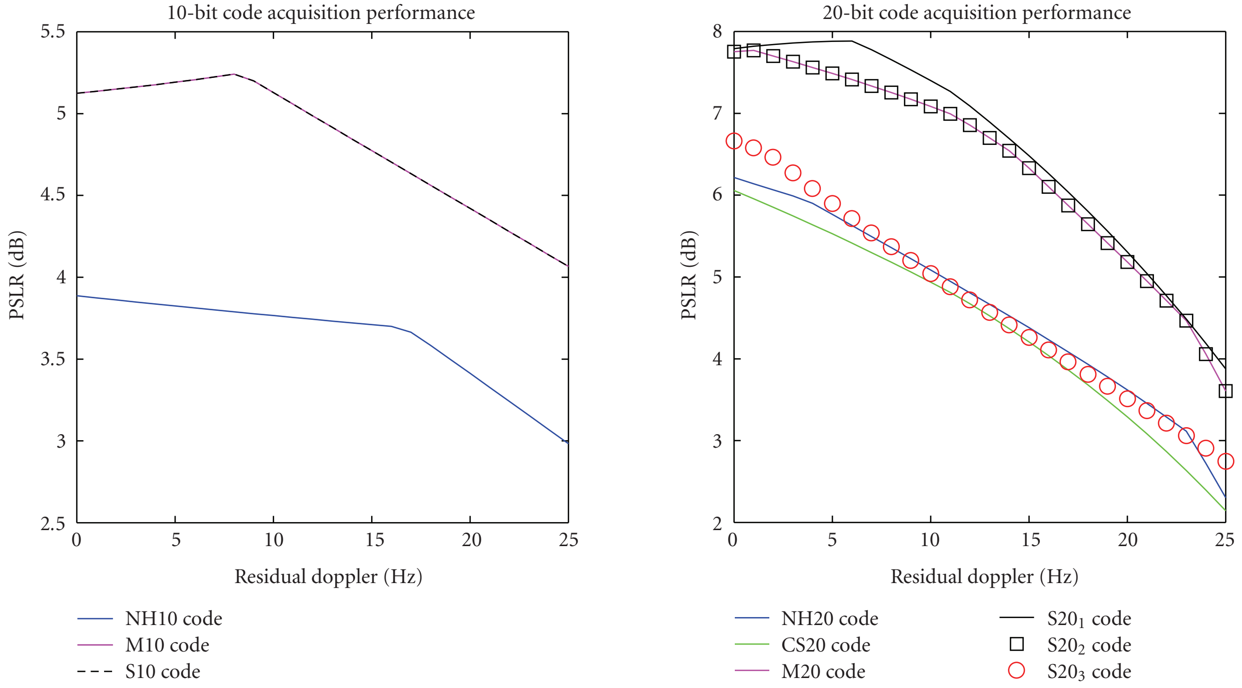

(a) (b)

Figure 6: Effect of residual Doppler on secondary code acquisition (LHS) 10-bit code (RHS) 20-bit code.

Table 4 lists the maximum, minimum, mean, and the standard deviation of CPSLR, ISLR, and MSC measures for the Galileo CS100 and the proposed S100 codes. While the standardized CS100 code is attractive in terms of CPSLR, the proposed S100 codes were appealing in the view point of ISLR. The MSC performance of both the codes was similar. The distribution of the CPSLR and ISLR measures of the CS100 and S100 codes is plotted in Figure 4 for better

Table 6: Hexadecimal representation of proposed S100 codes.

Hexadecimal values of S100 codes		
Code length = 100, no. of hex. symbols = 25, no. of zero padding = 0		
C7F526E3FA9371FD49A7015B2	CE054963FA9373815247015B2	CE05497E8B4E738152405D2C6
CE05494E5A2FF381524C69740	CE05497E39537381524071AB2	CE05496180DAB38152479FC95
CE0549549FCF3381524AD80C3	CE05497DD1CA738152408B8D6	9B501C63FA9366D40707015B2
9B501C7E8B4E66D407005D2C6	9B501C4E5A2FE6D4070C69740	9B501C7E395366D4070071AB2
9B501C6180DAA6D407079FC95	9B501C549FCF26D4070AD80C3	9B501C7DD1CA66D407008B8D6
C7F526E702A4B1FD49A63F56D	C7F526CDA80E31FD49AC95FC7	C7F526FE8B4E71FD49A05D2C6
C7F526CE5A2FF1FD49AC69740	C7F526FDD1CA71FD49A08B8D6	FD169CE702A4BF45A7263F56D
FD169CCDA80E3F45A72C95FC7	FD169CE3FA937F45A727015B2	FD169CFDD1CA7F45A7208B8D6
9CB45FE702A4A72D17E63F56D	9CB45FCDA80E272D17EC95FC7	9CB45FE3FA93672D17E7015B2
9CB45FFDD1CA672D17E08B8D6	FC72A6E702A4BF1CA9A63F56D	FC72A6CDA80E3F1CA9AC95FC7
C301B56702A4B0C06D463F56D	C301B54DA80E30C06D4C95FC7	A93F9E6702A4AA4FE7863F56D
A93F9E4DA80E2A4FE78C95FC7	FBA394E702A4BEE8E5263F56D	FBA394CDA80E3EE8E52C95FC7
FBA394E3FA937EE8E527015B2	FBA394FE8B4E7EE8E5205D2C6	FBA394CE5A2FFEE8E52C69740
CE0549592BF8F3815249B501C	CE054959538FF3815249AB1C0	CE05494A7177F381524D63A20
9B501C592BF8E6D40709B501C	9B501C59538FE6D40709AB1C0	9B501C4A7177E6D4070D63A20
9CB45F8E02B6672D17FC7F526	9CB45FD92BF8E72D17E9B501C	9CB45FCA7177E72D17ED63A20
FC72A6A4A81CFF1CA9B6D5F8C	FC72A68E02B67F1CA9BC7F526	C301B524A81CF0C06D56D5F8C
C301B50E02B670C06D5C7F526	A93F9E24A81CEA4FE796D5F8C	A93F9E0E02B66A4FE79C7F526
495039CA7177D2540E6D63A20	1C056CCE5A2FC7015B2C69740	1C056CFE8B4E47015B205D2C6
1C056CD9538FC7015B29AB1C0	1C056CAB6030C7015B3527F3C	1C056C9E7F2547015B386036A
1C056CCA7177C7015B2D63A20	B257F1A4A81CEC95FC76D5F8C	B257F1CE5A2FEC95FC6C69740
4DA80E1C056C936A0398FEA4D	B257F198FD5B6C95FC79C0A92	B2A71F98FD5B6CA9C7F9C0A92
94E2EF98FD5B6538BBF9C0A92	B257F1B257F1EC95FC736A038	B2A71FB257F1ECA9C7F36A038
94E2EFB257F1E538BBF36A038	4950399C056C92540E78FEA4D	1C056C9C056C87015B38FEA4D
94E2EF9C056CA538BBF8FEA4D	49503981C6AC92540E7F8E54D	1C056C81C6AC87015B3F8E54D
495039822E3592540E7F74729	1C056C822E3587015B3F74729	B257F1822E35AC95FC7F74729

comparison. In Figure 4, we see that the standard CS100 codes achieved 1 dB improvement over proposed S100 codes for 50% of the times in terms of CPSLR. On the other hand, the proposed codes showed an 0.9 dB improvement over standard CS100 codes for 50% of the times in terms of ISLR. The CPSLR degradation observed in proposed S100 codes is inherent to its construction. Alternatively, one can utilize evolutionary techniques for the multiple-objective code optimization encountered in CS100 code design [27].

In the preceding section, we inferred the existence of multiple solutions due to the code periodicity and Table 2 listed the number of codes that accomplished the optimal correlation characteristics as predicted by (10). To further arrange them, the individual codes were utilized for code acquisition and their corresponding PSLR measure was obtained in the presence of residual frequency error. For example, the PSLR of the 10-bit and the 20-bit codes in the presence of 12 Hz residual error is plotted in Figure 5. In the case of 20-bit synchronization code, the ISLR measure was relaxed to 4 dB so as to include the remaining synchronization codes. Accordingly, we evaluated the PSLR performance of all the 20-bit codes (5079 codes as listed in Table 2) obtained via exhaustive search. Figure 5 readily confirms the existence of optimal synchronization codes that are better then the standardized codes in terms of PSLR measure. However, a question may arise on the specific Doppler setting and whether that could influence the PSLR performance. Further analysis did confirm this conjecture due to the existence of codes that were superior for certain Doppler scenarios.

Thus, the average of the PSLR over a range of Doppler (namely from 0 Hz to 25 Hz) was utilized as the selection criterion for code selection. Under the new average PSLR measure, the codes that accomplished superior correlation suppression are listed in Table 5. The S10 and $S20_1$ codes achieved the overall best performance in terms of average PSLR taken over a range of Doppler's. It should be emphasized here that both these codes were balanced and thus asserting the significance of the balanced property introduced earlier. Figure 6 shows the PSLR performance of the standard, Merten's and the proposed 10-bit and 20-bit synchronization codes during two-dimensional acquisition in the absence of background noise. The residual Doppler was searched between 0 Hz and 250 Hz in steps of 25 Hz as reported in [10].

The LHS plot in Figure 6 readily affirms the limitation of standard NH10 code and the advantage of utilizing the M10 and the proposed S10 code. Later it will be shown that the

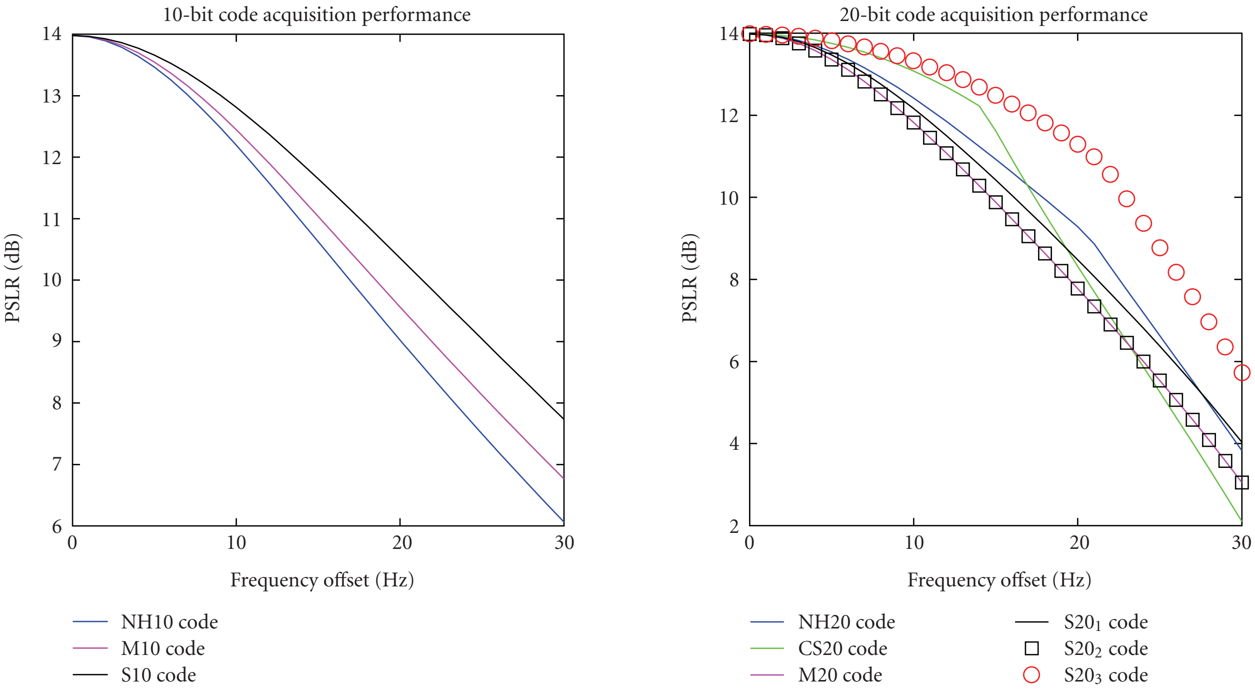

(a) (b)

Figure 7: PSLR performance in the presence of frequency offset (LHS) 10-bit code (RHS) 20-bit code.

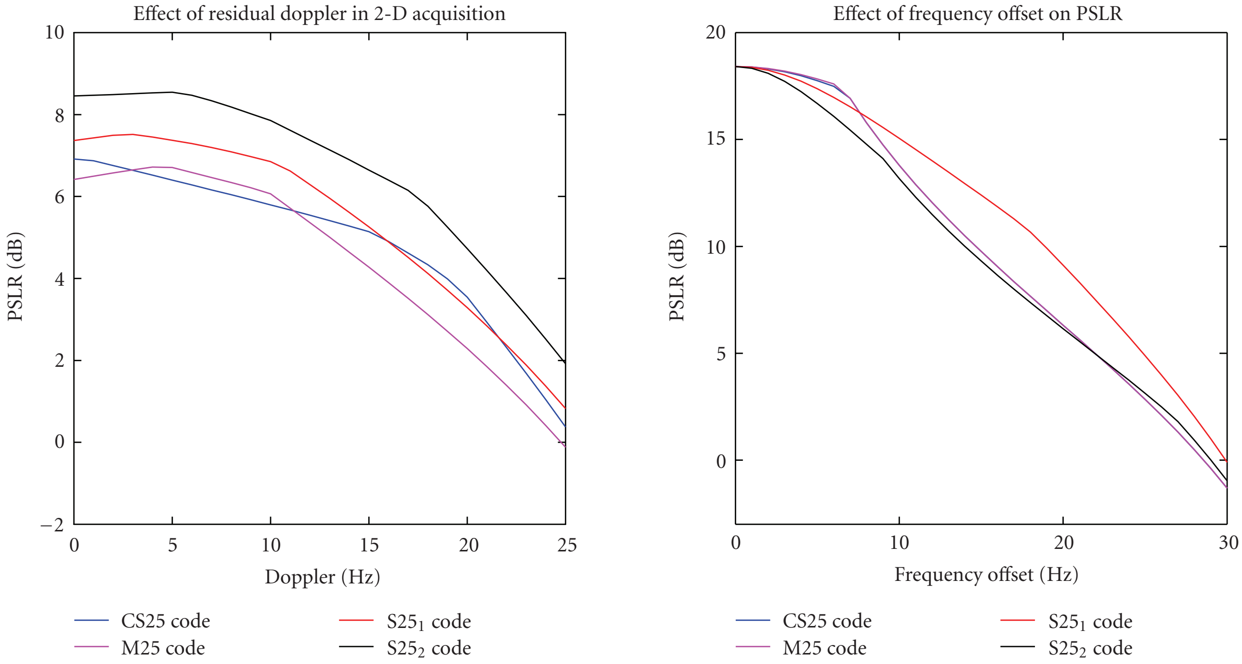

(a) (b)

Figure 8: 25-bit code performance. (LHS) effect of residual Doppler on secondary code acquisition (RHS) PSLR performance as a function of frequency offset.

proposed S10 code correlation can be better than that of M10 code in the presence of frequency offset. Amongst the 20-bit codes, the Galileo CS20 code had the worst performance in accordance to result shown in Figure 5. Both the M20 code and the proposed S20$_2$ code resulted in same performance as they belong to the same equivalence class. The S20$_3$ code demonstrated similar performance as that of the NH20 code. Finally, the proposed S20$_1$ code showed the best performance

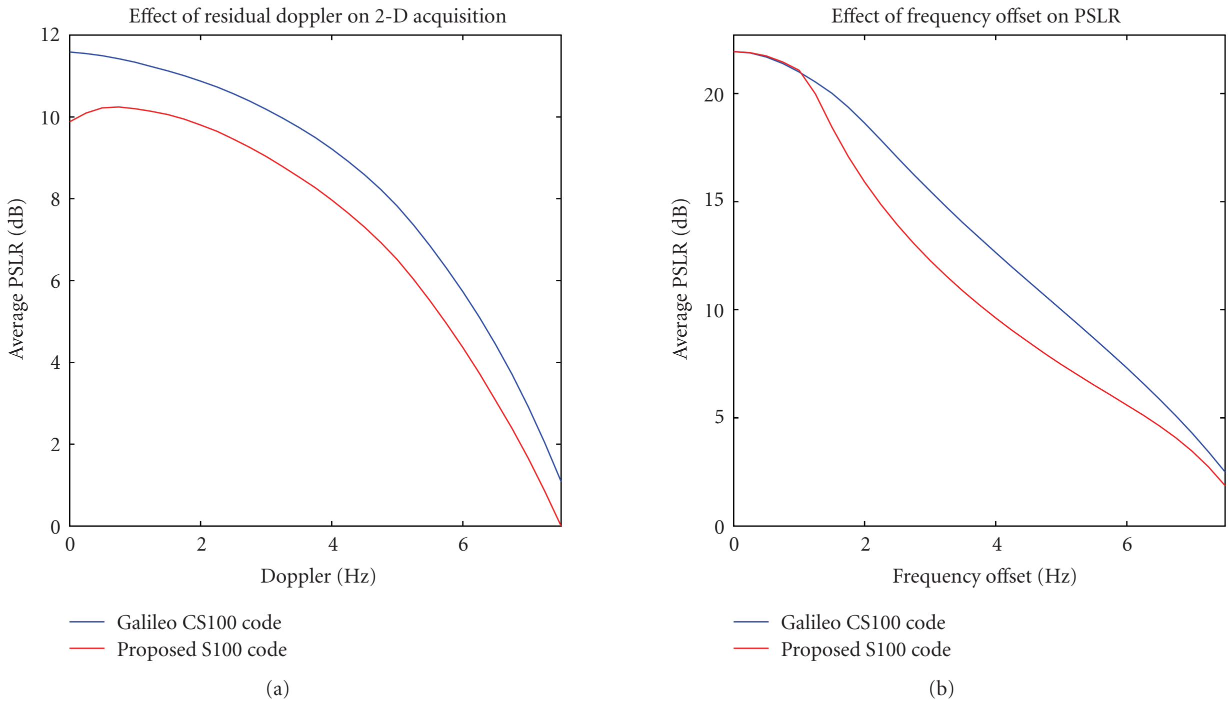

Figure 9: 100-bit code performance. (LHS) effect of residual Doppler on secondary code acquisition (RHS) PSLR performance as a function of frequency offset.

in terms of PSLR under Doppler conditions. The $S20_1$ code although suboptimal in terms of ISLR still performed better owing to its balanced property.

The correlation performance degradation in NH20 code as a function of frequency offset was analyzed in [10]. To further validate this initial observation and also to compare the correlation suppression performance of the proposed codes, numerical simulations were carried out. Figure 7 shows the PSLR performance for both 10-bit and 20-bit synchronization codes as a function of frequency offset. For the 10-bit code, one can readily notice the advantage of the proposed S10 code over the M10 and NH10 codes. In the case of 20-bit code, the standard NH20 and the CS20 codes performed better in comparison to the M20, $S20_1$, and $S20_2$ codes. On the other hand, the $S20_3$ resulted in the overall best performance and readily showed a PSLR gain of around 2.5 dB over standard NH20 and CS20 codes. However, the $S20_1$ is still attractive as it yielded the best PSLR performance as shown in Figures 6 and 7. The aforementioned analysis for a similar setting was carried out for the 25-bit code, which included the CS25, M25, and the proposed $S25_1$ and $S25_2$ codes. Note that the M25 and CS25 codes are essentially similar and are expected to perform similar. Figure 8 shows the effect of residual Doppler on secondary code acquisition and the PSLR performance as a function of frequency offset.

The standard CS25 code and that of M25 code were exactly same as far as frequency offset is concerned. However, the standard CS25 resulted in better PSLR performance as shown in LHS plot of Figure 8. On the other hand, both the proposed codes demonstrated superior PSLR performance. Interestingly, the codes $S25_1$ and $S25_2$ were complementary in their PSLR performance as shown in Figure 8. However, the code $S25_2$ can be considered optimal for not only achieving better PSLR performance (around 2 dB) in the presence of residual Doppler, it also retained similar PSLR performance to that of standard CS25 code for a wide range of frequency offsets.

Finally, the code acquisition performance of the standard CS100 and the proposed S100 codes was also evaluated in a similar manner. The residual Doppler range was reduced to 7.5 Hz so as to reflect the longer coherent integration utilized in acquiring these codes. Figure 9 shows the average PSLR performance of the standard and the proposed codes. The standard CS100 code demonstrated better performance in regards to the proposed S100 codes under both settings. The proposed code despite being characterized by better ISLR measure was still limited by its construction method from code of short length. Nevertheless, it readily corroborates the use of alternative solutions for the multiple code design problem.

6. CONCLUSIONS

The design of secondary synchronization code for GNSS system is important due to its role in acquisition and tracking. A limitation arising due to the usage of short secondary code is the apparent degradation in correlation isolation especially in the presence of residual frequency errors. This paper introduced the various performance measures that can be utilized for secondary synchronization code optimization. Consequently, these performance measures were utilized to obtain optimal codes of various lengths via exhaustive search. This paper also established the association between the optimal codes and the systematic codes such as Golay complementary codes. The proposed secondary synchronization codes of lengths 10, 20, and 25 obtained in this fashion readily demonstrated superior correlation isolation performance in the presence of residual frequency errors. The developed S100 codes although appealing in terms of ISLR measure demonstrated inferior acquisition performance over standardized CS100 codes. Truncation of LFSR codes or code design using genetic algorithms can produce code sets with better correlation characteristics. The significance of the correlation isolation improvement demonstrated by the new synchronization codes in terms of probability of false alarm and detection is currently being investigated. Finally, judicious design of short synchronization codes can offer optimal correlation suppression and efficient signal generation.

Example 1. The NH10 Code represented by the hexadecimal value “F28” is obtained as follows:

$$\begin{aligned} F &\longrightarrow 1\ 1\ 1\ 1, \\ 2 &\longrightarrow 0\ 0\ 1\ 0, \\ 8 &\longrightarrow 1\ 0\ 0\ 0. \end{aligned} \tag{17}$$

Hence, “F28”$\longrightarrow$ $1, 1, 1, 1, 0, 0, 1, 0, 1, 0, \mathbf{0}, \mathbf{0}$. The last two digits highlighted in bold are discarded, and the zero symbols are mapped in to -1. (i.e., $0 \rightarrow -1$).

REFERENCES

[1] G. W. Hein, J. Godet, J. L. Issler, et al., “Status of Galileo frequency and signal design,” in *Proceedings of the 15th International Technical Meeting of the Satellite Division of the Institute of Navigation (ION GPS ’02)*, pp. 266–277, Portland, Ore, USA, September 2002.

[2] T. Grelier, J. Dantepal, A. Delatour, A. Ghion, and L. Ries, “Initial observations and analysis of compass MEO satellite signals,” *Inside GNSS*, pp. 39–43, June 2007.

[3] R. D. Fontana, W. Cheung, and T. Stansell, “The modernized L2 civil signal,” *GPS World*, pp. 28–34, September 2001.

[4] A. J. van Dierendonck and C. Hegarty, “The new L5 civil GPS signal,” *GPS World*, vol. 11, no. 9, pp. 64–71, 2000.

[5] B. C. Barker, K. A. Rehborn, J. W. Betz, et al., “Overview of the GPS M code signal,” in *Proceedings of the National Technical Meeting of the Institute of Navigation (ION NTM ’00)*, pp. 542–549, Anaheim, Calif, USA, January 2000.

[6] S. Pullen and P. Enge, “A civil user perspective on near-term and long-term GPS modernization,” in *Proceedings of the GPS/GNSS Symposium*, p. 11, Tokyo, Japan, November 2004.

[7] Galileo SIS ICD, “Galileo Open Service: Signal In Space Interface Control Document,” August 2006.

[8] J. J. Rushanan, “The spreading and overlay codes for the L1C signal,” in *Proceedings of the National Technical Meeting of the Institute of Navigation (ION NTM ’07)*, pp. 539–547, San Diego, Calif, USA, January 2007.

[9] L. Ries, C. Macabiau, Q. Nouvel, et al., “A software receiver for GPS-IIF L5 signal,” in *Proceedings of the International Technical Meeting of the Satellite Division of the Institute of Navigation (ION GPS ’02)*, pp. 1540–1553, Portland, Ore, USA, September 2002.

[10] C. Macabiau, L. Ries, F. Bastide, and J.-L. Issler, “GPS L5 receiver implementation Issues,” in *Proceedings of the International Technical Meeting of the Institute of Navigation (ION GPS ’03)*, pp. 153–164, Portland, Ore, USA, September 2003.

[11] S. Mertens, “Exhaustive search for low-autocorrelation binary sequences,” *Journal of Physics A*, vol. 29, no. 18, pp. L473–L481, 1996.

[12] F. Soualle, M. Soellner, S. Wallner, et al., “Spreading code selection criteria for the future GNSS Galileo,” in *Proceedings of the European Navigation Conference (ENC GNSS ’05)*, p. 10, Munich, Germany, July 2005.

[13] C. Tellambura, M. G. Parker, Y. J. Guo, S. J. Shepherd, and S. K. Barton, “Optimal sequences for channel estimation using discrete Fourier transform techniques,” *IEEE Transactions on Communications*, vol. 47, no. 2, pp. 230–238, 1999.

[14] D. V. Sarwate and M. B. Pursley, “Crosscorrelation properties of pseudorandom and related sequences,” *Proceedings of the IEEE*, vol. 68, no. 5, pp. 593–619, 1980.

[15] M. Golay, “The merit factor of long low autocorrelation binary sequences (Corresp.),” *IEEE Transactions on Information Theory*, vol. 28, no. 3, pp. 543–549, 1982.

[16] M. Rupf and J. L. Massey, “Optimum sequence multisets for synchronous code-division multiple-access channels,” *IEEE Transactions on Information Theory*, vol. 40, no. 4, pp. 1261–1266, 1994.

[17] A. Lempel, M. Cohn, and W. L. Eastman, “A class of balanced binary sequences with optimal autocorrelation properties,” *IEEE Transactions on Information Theory*, vol. 23, no. 1, pp. 38–42, 1977.

[18] D. Jungnickel and A. Pott, “Perfect and almost perfect sequences,” *Discrete Applied Mathematics*, vol. 95, no. 1–3, pp. 331–359, 1999.

[19] F. Neuman and L. Hofman, “New pulse sequences with desirable correlation properties,” in *Proceedings of the IEEE National Telemetry Conference (NTC ’71)*, pp. 272–282, Washington, DC, USA, April 1971.

[20] M. Golay, “Complementary series,” *IEEE Transactions on Information Theory*, vol. 7, no. 2, pp. 82–87, 1961.

[21] H. Urkowitz, “Complementary-sequence pulse radar with matched filtering following doppler filtering,” US patent 5151702, September 1992.

[22] H. Minn, V. K. Bhargava, and K. B. Letaief, “A robust timing and frequency synchronization for OFDM systems,” *IEEE Transactions on Wireless Communications*, vol. 2, no. 4, pp. 822–839, 2003.

[23] V. Diaz, J. Urena, M. Mazo, J. J. Garcia, E. Bueno, and A. Hernandez, “Using Golay complementary sequences for multi-mode ultrasonicoperation,” in *Proceedings of the 7th IEEE International Conference on Emerging Technologies and Factory Automation (ETFA ’99)*, vol. 1, pp. 599–604, Barcelona, Spain, October 1999.

[24] S. Z. Budisin, “Efficient pulse compressor for Golay complementary sequences,” *Electronics Letters*, vol. 27, no. 3, pp. 219–220, 1991.

[25] European Space Agency, “Galileo Open Service: Signal In Space Interface Control Document,” Interface control document, European Union, May 2006, http://www.galileoic.org/la/files/Galileo%20OS%20SIS%20ICD%20230506.pdf.

[26] M. Tran and C. Hegarty, "Receiver algorithms for the new civil GPS signals," in *Proceedings of the National Technical Meeting of the Institute of Navigation (ION NTM '02)*, pp. 778–789, San Diego, Calif, USA, January 2002.

[27] S. K. Shanmugam and H. Leung, "Chaotic binary sequences for efficient wireless multipath channel estimation," in *Proceedings of the 60th IEEE Vehicular Technology Conference (VTC '04)*, vol. 60, pp. 1202–1205, Los Angeles, Calif, USA, September 2004.

Hindawi Publishing Corporation
International Journal of Navigation and Observation
Volume 2008, Article ID 651437, 8 pages
doi:10.1155/2008/651437

Research Article

Joint L-/C-Band Code and Carrier Phase Linear Combinations for Galileo

Patrick Henkel[1] **and Christoph Günther**[1, 2]

[1] *Institute of Communications and Navigation, Technische Universität München (TUM), Theresienstraße 90, 80333 München, Germany*
[2] *German Aerospace Center (DLR), Institute of Communications and Navigation (IKN), Münchner Straße 20, 82234 Weßling/Oberpfaffenhofen, Germany*

Correspondence should be addressed to Patrick Henkel, patrick.henkel@tum.de

Received 1 August 2007; Revised 27 November 2007; Accepted 15 January 2008

Recommended by Gerard Lachapelle

Linear code combinations have been considered for suppressing the ionospheric error. In the L-band, this leads to an increased noise floor. In a combined L- and C-band (5010–5030 MHz) approach, the ionosphere can be eliminated and the noise floor reduced at the same time. Furthermore, combinations that involve both code- and carrier-phase measurements are considered. A new L-band code-carrier combination with a wavelength of 3.215 meters and a noise level of 3.92 centimeters is found. The double difference integer ambiguities of this combination can be resolved by extending the system of equations with an ionosphere-free L-/C-band code combination. The probability of wrong fixing is reduced by several orders of magnitude when C-band measurements are included. Carrier smoothing can be used to further reduce the residual variance of the solution. The standard deviation is reduced by a factor 7.7 if C-band measurements are taken into account. These initial findings suggest that the combined use of L- and C-band measurements, as well as the combined code and phase processing are an attractive option for precise positioning.

1. INTRODUCTION

The integer ambiguity resolution of carrier-phase measurements has been simplified by the consideration of linear combinations of measurements at multiple frequencies. Early methods were the three-carrier ambiguity resolution (TCAR) method introduced by Forssell et al. [1], as well as the cascade integer resolution (CIR) developed by Jung et al. [2].The weighting coefficients of three-frequency phase combinations are designed either to eliminate the ionosphere at the price of a rather small wavelength or to reduce the ionosphere only by a certain amount with the advantage of a larger wavelength.

The systematic search of all possible GPS L1-L2 widelane combinations has been performed by Cocard and Geiger [3]. The L1-L2 linear combination of maximum wavelength (14.65 m) amplifies the ionospheric error by a factor 350. Collins gives an overview of reduced ionosphere L1-L2 combinations with wavelengths up to 86.2 cm $(+1, -1$ widelane) in [4].

The authors have extended this work to three-frequency (3F) Galileo combinations (E1-E5a-E5b) in [5]. A 3F widelane combination with a wavelength of 3.256 m and an ionospheric suppression of 16.4 dB was found. Furthermore, a 3F narrowlane combination with a wavelength of 5.43 cm could reduce the ionospheric error by as much as 36.7 dB. Sets of linear carrier-phase combinations that are robust against residual biases were studied in [6]. The integer ambiguities of the linear combinations can be estimated by the least-squares ambiguity decorrelation adjustment (LAMBDA) algorithm developed by Teunissen [7]. The method includes an integer transformation which can also be used to determine optimum sets of linear combinations [8].

In this paper, the authors used code- and carrier-phase measurements in the linear combinations for obtaining ionospheric elimination, large wavelengths, and a low noise level at the same time. The E5a and E5b code measurements are of special interest due to their large bandwidth (20 MHz) and their low associated Cramer-Rao bound of 5 cm [9]. The C-band phase measurements are particularly interesting due to their small wavelength and their thus reduced phase noise. The properties of code-carrier linear combinations are optimized by including both L- and C-band measurements. The cost function is defined as the ratio of half the wavelength and the noise level of the ionosphere-free code-carrier combination. It is called combination discrimination and it is a measure of the radius of the decision regions expressed in units given by the standard deviation of the noise. The L-Band signals of Galileo are defined in the Galileo-ICD [10]. The C-band signals are foreseen in a band between 5010 MHz to 5030 MHz [11]. The signal propagation and tracking characteristics in the C-band have been analyzed by Irsigler et al. [12]. The larger frequencies result in an additional free space loss of 10 dB that has to be compensated by a larger transmit power.

The paper is organized as follows: the next section introduces the design of code-carrier linear combinations. The underlying trade-off between a low noise level and strong ionospheric reduction turns out to be controlled by the weighting coefficients of E5a/E5b code measurements.

In Section 3, code-carrier linear combinations are computed in a way that include both L- and C-band measurements. An ionosphere-free code-only combination is determined that benefits from a 4.5 times lower noise level than a pure L-band combination. Furthermore, a pure L-band ionosphere-free code-carrier combination with a wavelength of 3.215 m and a noise standard deviation of 3.9 cm is found. The combined use of the two reduces the probability of wrong fixing of the latter solution by 9 orders of magnitude with respect to a pure L-band solution.

The use of C-band measurements for ionosphere-free carrier smoothing is discussed in Section 4: an ionosphere-free code-carrier combination of arbitrary wavelength is smoothed by a pure phase combination. The low noise level of C-band measurements provides a linear combination that benefits from an 8.9 dB lower noise level as compared to the equivalent L-band combination.

2. CODE-CARRIER LINEAR COMBINATIONS

Linear combinations of carrier-phase measurements are constructed to increase the wavelength (widelane), suppress the ionospheric error, and to simplify the integer ambiguity resolution. The properties of the linear combinations can be improved by including weighted code measurements into the pure phase combinations. Figure 1 shows a three frequency (3F) linear combination where the phase measurements are weighted by α, β, γ, and the code measurements are scaled by a, b, c. The weighting coefficients are generally restricted by a few conditions: first, the geometry should be preserved, that is

$$\alpha + \beta + \gamma + a + b + c \overset{!}{=} 1. \tag{1}$$

Moreover, the superposition of ambiguities should be an integer multiple of a common wavelength λ, that is

$$\alpha\lambda_1 N_1 + \beta\lambda_2 N_2 + \gamma\lambda_3 N_3 \overset{!}{=} \lambda N, \tag{2}$$

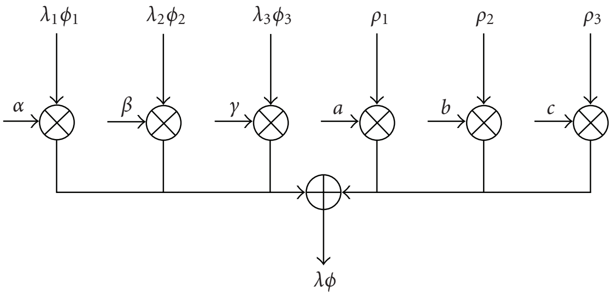

FIGURE 1: Linear combination of carrier-phase and code measurements.

which can be split into three sufficient conditions

$$i = \frac{\alpha\lambda_1}{\lambda} \in \mathbb{Z}, \qquad j = \frac{\beta\lambda_2}{\lambda} \in \mathbb{Z}, \qquad k = \frac{\gamma\lambda_3}{\lambda} \in \mathbb{Z}, \tag{3}$$

with $\mathbb{Z}$ denoting the space of integers. These integer constraints are rewritten to obtain the weighting coefficients

$$\alpha = \frac{i\lambda}{\lambda_1}, \qquad \beta = \frac{j\lambda}{\lambda_2}, \qquad \gamma = \frac{k\lambda}{\lambda_3}. \tag{4}$$

Mixed code-carrier combinations weight the phase part by τ and the code part by $1 - \tau$. The border cases are pure phase ($\tau = 1$) and pure code ($\tau = 0$) combinations. The parameter τ has a significant impact on the properties of the linear combination, and it is optimized later in this section. Replacing the weighting coefficients in $\tau = \alpha + \beta + \gamma$ by (4) yields the wavelength of the code-carrier combination

$$\lambda = \frac{\tau}{i/\lambda_1 + j/\lambda_2 + k/\lambda_3}. \tag{5}$$

The generalized widelane criterion is given for $\lambda_1 < \lambda_2 < \lambda_3$ by $\lambda > \lambda_3$. Equivalently, it can be expressed as a function of i, j, and k as

$$\tau > iq_{13} + jq_{23} + k > 0 \quad \text{with } q_{mn} = \frac{\lambda_n}{\lambda_m}. \tag{6}$$

The linear combination scales the ionospheric error by

$$A_I = \alpha + \beta q_{12}^2 + \gamma q_{13}^2 - a - bq_{12}^2 - cq_{13}^2. \tag{7}$$

The thermal noise of the elementary carrier phase measurements is assumed Gaussian with the standard deviation given by Kaplan and Hegarty [13]

$$\sigma_{\phi_i} = \frac{\lambda_i}{2\pi}\sqrt{\frac{B_L}{C/N_0}\left[1 + \frac{1}{2T \cdot C/N_0}\right]}, \tag{8}$$

where B_L denotes the loop bandwidth, C/N_0 the carrier-to-noise ratio, and T the predetection integration time. The overall noise contribution of the linear combination is

Table 1: Cramer-Rao bound for Galileo signals.

	Modulation	Bandwidth (MHz)	CRB (cm)
E1	BOC(1,1)	4	20
E5a	BPSK(10)	24	5
E5b	BPSK(10)	24	5
E5	BOC(15,10)	51	1

written as

$$N_m = \sqrt{(\alpha^2 + \beta^2 q_{12}^2 + \gamma^2 q_{13}^2) \cdot \sigma_{\phi_0}^2 + a^2\sigma_{\rho_1}^2 + b^2\sigma_{\rho_2}^2 + c^2\sigma_{\rho_3}^2} \tag{9}$$

with $\sigma_{\rho_1}^2, \ldots, \sigma_{\rho_3}^2$ being the noise variance of the code measurements. Table 1 shows the Cramer-Rao bound (CRB) for some Galileo signals as derived by Hein et al. [9]. A DLL bandwidth of 1 Hz has been assumed. The 4 MHz receiver bandwidth for E1 has been chosen to avoid sidelobe tracking.

For E1, E5a, E5b, E6 phase measurements, the wavelength scaling of σ_{ϕ_i} can be neglected due to the close vicinity of the frequency bands. However, it plays a major role when C-Band measurements are included.

Figure 2 shows the benefit of the code contribution to the $i = 1$ (E1), $j = -10$ (E5b), $k = 9$ (E5a) linear combination: a slight increase in noise level results in a considerable reduction of the ionospheric error. The phase weighting has been fixed to $\tau = 1$ so that α, β, γ, and λ are uniquely determined. The E5b and E5a code weights are adapted continuously and the ionosphere is eliminated in the border case

$$b = -c = \frac{\alpha + \beta q_{12}^2 + \gamma q_{13}^2}{q_{12}^2 - q_{13}^2}. \tag{10}$$

E1 code measurements have not been taken into account due to the increased noise level but might be included with a low weight.

The combination discrimination—measured by the ratio of half the wavelength and the noise level $\lambda/(2N_m)$—is proposed as a cost function to select linear combinations due to its independence of the geometry. It is shown for multiple ionosphere-free code-carrier combinations in Figure 3. The strong dependency on the phase weighting τ suggests an optimization with respect to this parameter. Note that the legend refers to the elementary wavelengths which have to be scaled by τ.

The computation of the optimum τ takes again only E5a/E5b code measurements into account as the benefit of the E1 code measurement is negligible ($a = 0$). The notation is simplified by

$$\begin{aligned} \lambda &= \tilde{\lambda} \cdot \tau, \\ A_I &= \tilde{\kappa} \cdot \tau - b q_{12}^2 - c q_{13}^2, \\ N_m &= \sqrt{\sigma_\phi^2 \cdot (\alpha^2 + \beta^2 q_{12}^2 + \gamma^2 q_{13}^2) + \sigma_\rho^2 \cdot (b^2 + c^2)} \\ &= \sqrt{\sigma_\phi^2 \cdot \tilde{\eta}^2 \tau^2 + \sigma_\rho^2 \cdot (b^2 + c^2)}, \end{aligned} \tag{11}$$

with $\tilde{\lambda}$, $\tilde{\kappa}$, and $\tilde{\eta}$ implicitly given by (5), (7), and (9). The E5a/E5b code weights are determined from the ionosphere-free and geometry-preserving conditions as

$$\begin{aligned} b &= 1 - c - \tau, \\ c &= \underbrace{\frac{\tilde{\kappa} + q_{12}^2}{q_{13}^2 - q_{12}^2}}_{w_1} \cdot \tau + \underbrace{\frac{-q_{12}^2}{q_{13}^2 - q_{12}^2}}_{w_2} = w_1 \cdot \tau + w_2. \end{aligned} \tag{12}$$

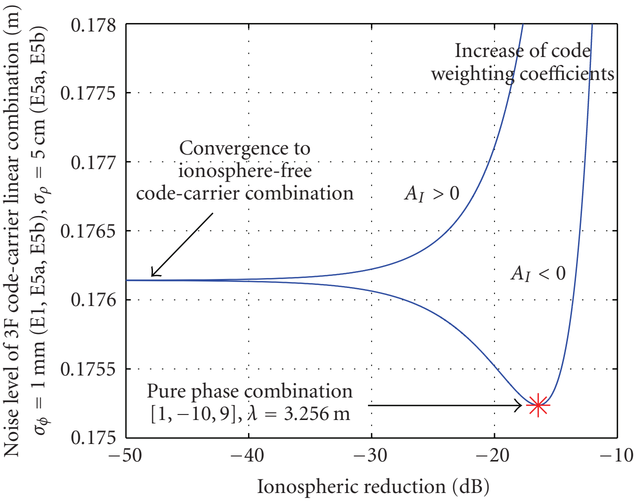

Figure 2: Adaptive code contribution to linear combinations: tradeoff between noise level and ionospheric reduction.

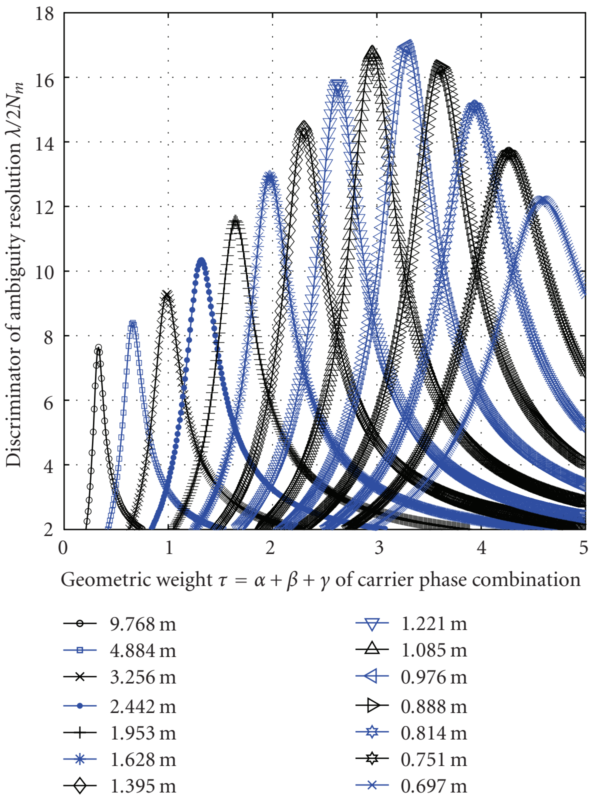

Figure 3: Optimal weighting of the phase combination part of ionosphere-free code-carrier combinations with $i = 1$, $k = -j - 1$, and $j \in \{-12, \ldots, 1\}$.

TABLE 2: Properties and weighting coefficients of ionosphere-free E1-E5b-E5a code-carrier combinations.

i	j	k	b	c	$\tilde{\lambda}$ (m)	λ (m)	N_m (m)	R
1	−12	11	0.327	0.344	9.768	3.217	0.28	5.81
1	−11	10	0.166	0.175	4.884	3.216	0.25	6.38
1	−10	9	0.006	0.007	3.256	3.214	0.23	7.05
1	−9	8	−0.154	−0.162	2.442	3.213	0.20	7.86
1	−8	7	−0.314	−0.330	1.954	3.212	0.18	8.84
1	−7	6	−0.474	−0.499	1.628	3.211	0.16	10.02
1	−6	5	−0.634	−0.667	1.396	3.210	0.14	11.42
1	−5	4	−0.793	−0.835	1.221	3.209	0.12	12.99
1	−4	3	−0.953	−1.003	1.085	3.208	0.11	14.54
1	−3	2	−1.112	−1.171	0.977	3.207	0.10	15.65
1	−2	1	−1.272	−1.339	0.888	3.206	0.10	15.85
1	−1	0	−1.431	−1.506	0.814	3.205	0.11	15.04
1	0	−1	−1.590	−1.674	0.751	3.204	0.12	13.59

The combination discrimination becomes from (5), (11), and (12):

$$R(\tau) = \frac{\lambda(\tau)/2}{N_m(\tau)} = \frac{\tilde{\lambda}\cdot\tau}{2\sqrt{\sigma_\phi^2\cdot\tilde{\eta}^2\tau^2+\sigma_\rho^2\cdot\left((w_1\tau+w_2)^2+(1-\tau-w_1\tau-w_2)^2\right)}}. \tag{13}$$

Setting the derivative to zero yields the optimum weighting

$$\tau_{\text{opt}} = \frac{1-2w_2+2w_2^2}{1+w_1-w_2-2w_1w_2}, \tag{14}$$

which is independent of both σ_ρ and σ_ϕ. Table 2 contains the weighting coefficients and characteristics of the code-carrier combinations shown in Figure 3.

Figure 4 shows the benefit of adaptive code and phase weighting for the code-carrier linear combination with $i = 0$ (E1), $j = 1$ (E5b), and $k = -1$ (E5a). Obviously, the wavelength increases linearly with τ and the ionosphere can be eliminated with any τ. The noise amplification depends on the level of ionospheric reduction: a linear increase can be observed near the pure phase combination, while the increase becomes negligible for the ionosphere-free combination. Thus, the combination discrimination of the ionosphere-free code-carrier combination is increased by almost the same factor as τ is risen.

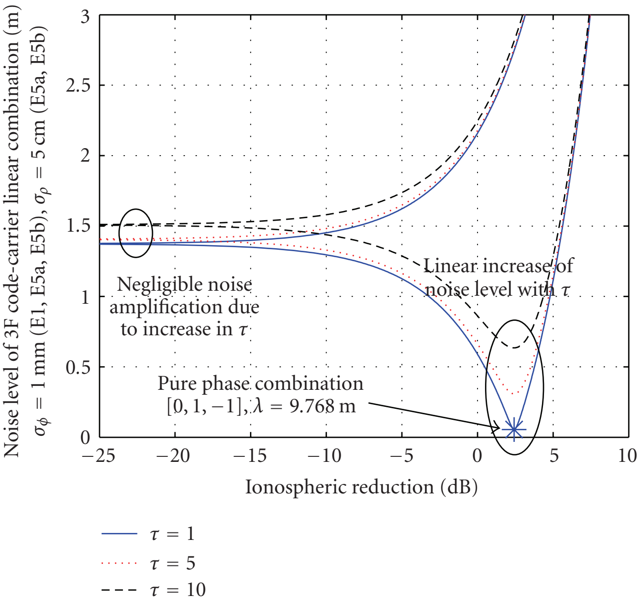

FIGURE 4: Benefit of adaptive code and phase weighting for linear combinations with $\lambda = \tau$ 9.768 m.

3. C-BAND AIDED CODE-CARRIER LINEAR COMBINATIONS

The 20 MHz wide C-Band (5010 · · · 5030 MHz = {489.736 · · · 491.691} · 10.23 MHz) has been reserved for Galileo. The higher frequency range has a multitude of advantages and drawbacks: an additional free space loss of 10 dB occurs which has to be compensated by a larger transmit power. The ionospheric delay is approximately 10 times lower than in the E1 band. The small wavelength of 5.9691 cm · · · 5.9839 cm complicates direct ambiguity resolution but results in an approximately 3.2 times lower standard deviation of phase noise. Moreover, the C-Band offers additional degrees of freedom for the design of linear combinations.

3.1. *Reduced noise ionosphere-free code-only combinations*

The design of three frequency code-only combinations that preserve geometry and eliminate ionospheric errors is characterized by one degree of freedom used for noise minimization. The weighting coefficients are derived from the geometry preserving and ionosphere-free constraints in (1), (7) as

$$a = 1-b-c,$$
$$b = \underbrace{-\frac{1}{q_{12}^2-1}}_{\nu_1}+\underbrace{\left(-\frac{q_{13}^2-1}{q_{12}^2-1}\right)}_{\nu_2}\cdot c = \nu_1+\nu_2\cdot c. \tag{15}$$

Minimization of $N_m^2 = a^2\sigma_{\rho_1}^2+b^2\sigma_{\rho_2}^2+c^2\sigma_{\rho_3}^2$ yields

$$c = \frac{(1-\nu_1+\nu_2-\nu_1\nu_2)\cdot\sigma_{\rho_1}^2-\nu_1\nu_2\cdot\sigma_{\rho_2}^2}{(1+2\nu_2+\nu_2^2)\cdot\sigma_{\rho_1}^2+\nu_2^2\cdot\sigma_{\rho_2}^2+\sigma_{\rho_3}^2}. \tag{16}$$

Ionosphere-free code-only combinations with more than three frequencies are obtained by a multidimensional derivative. Table 3 shows that the pure L-band E1-E5b-E5a combination is characterized by a noise level of 44.41 cm. If the E5 signal is received with full bandwidth, the CRB is reduced to 1 cm but the number of degrees of freedom is reduced by one so that the noise level of the E1-E5 combinations are lightly

Table 3: Ionosphere-free code-only combinations with minimum noise $\sigma_\rho(\mathrm{E1}) = \sigma_\rho(\mathrm{C1}) = \cdots = \sigma_\rho(\mathrm{C4}) = 20$ cm and $\sigma_\rho(\mathrm{E5a}, \mathrm{E5b}) = 5$ cm.

E1	E5b	E5a	C1	C2	C3	C4	N_m (cm)
2.090	1.500	−2.590	0	0	0	0	44.41
0.387	0.255	−0.506	0.863	0	0	0	19.14
0.213	0.128	−0.292	0.476	0.476	0	0	14.21
0.147	0.079	−0.211	0.328	0.328	0.329	0	11.80
0.112	0.054	−0.168	0.251	0.251	0.251	0.251	10.31

Table 4: Ionosphere-free code-only combinations with minimum noise $\sigma_\rho(\mathrm{E1}) = \sigma_\rho(\mathrm{C1}) = \cdots = \sigma_\rho(\mathrm{C4}) = 20$ cm and $\sigma_\rho(\mathrm{E5}) = 1$ cm.

E1	E5	C1	C2	C3	C4	N_m (cm)
2.338	−1.338	0	0	0	0	46.78
0.398	−0.278	0.879	0	0	0	19.31
0.217	−0.179	0.481	0.481	0	0	14.27
0.150	−0.142	0.331	0.331	0.331	0	11.84
0.114	−0.122	0.252	0.252	0.252	0.252	10.34

Table 5: Ionosphere-free code-carrier widelane combinations with $\sigma_\rho(\mathrm{E1}) = \sigma_\rho(\mathrm{C1}) = \cdots = \sigma_\rho(\mathrm{C4}) = 20$ cm and $\sigma_\rho(\mathrm{E5}) = 1$ cm.

i E1	j E5	k C1	l C2	m C3	n C4	a E1	b E5	λ (m)	N_m (cm)
1	−1	0	0	0	0	−4.4e−3	−3.11	3.21	3.92
1	−1	0	0	1	−1	−4.7e−3	−3.28	3.39	4.84
1	−1	0	1	−1	0	−4.7e−3	−3.28	3.39	4.84
1	−1	0	1	0	−1	−5.0e−3	−3.46	3.59	5.12
1	−1	1	−1	0	0	−4.7e−3	−3.28	3.39	4.84
1	−1	1	0	−1	0	−5.0e−3	−3.46	3.59	5.12
1	−1	1	0	0	−1	−5.3e−3	−3.67	3.81	5.43
0	0	−1	0	0	1	−8.5e−5	−6.0e−2	20.70	15.39

increased (Table 4). These combinations will play a role in conjunction with code-carrier combinations.

The C-band is split into 4 bands of 5 MHz bandwidth centered at $\{490, 490.5, 491, 491.5\} \cdot 10.23$ MHz and allows a significant reduction of the noise level. Note that the noise of any contributing elementary combination is reduced by a weighting coefficient smaller than one.

3.2. Joint L-/C-band widelane combinations

Code-carrier linear combinations can also include both L-band and C-band measurements. Therefore, (1)–(7) are extended to include the additional measurements. The weighting coefficients $\{\alpha, \beta, \gamma, \ldots\}$ and $\{a, b\}$ are computed such that the discriminator output of (13) is maximized for a given set of integer coefficients $\{i, j, k, \ldots\}$.

Table 5 contains ionosphere-free joint L-/C-band code-carrier widelane combinations ($\lambda > \max_i \lambda_i$). The E1-E5 pure L-band combination benefits from a noise level of only 3.92 cm which simplifies the resolution of the 3.215 m integer ambiguities. In contrast to the code-only combinations, the use of the full-bandwidth E5 signal is advantageous compared to separate E5a and E5b measurements. The C-band offers no benefit for these wavelengths. In the last row of Table 5, a linear combination with a pure L-band code and pure C-band phase part is described. The combination discrimination equals 67.25 but the noise level is also increased to 15.39 cm.

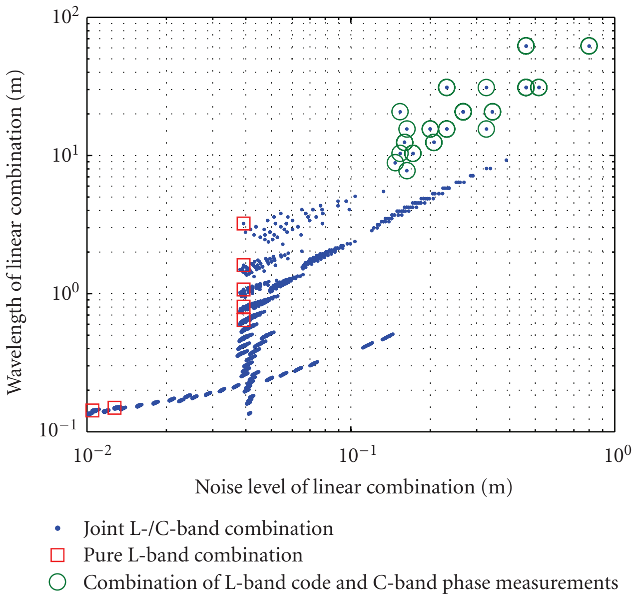

Figure 5: Comparison of joint L-/C-Band linear combinations for $\sigma_\rho(\mathrm{E1}) = 20$ cm, $\sigma_\rho(\mathrm{E5}) = 1$ cm and $\sigma_{\phi,i} = \lambda_i/\lambda_1 \cdot \sigma_{\phi_0}$ with $\sigma_{\phi_0} = 1$ mm.

Figure 5 shows the tradeoff between wavelength and noise level for joint L-/C-band ionosphere-free linear code-carrier combinations with $\{i, j\} \in [-5, +5]$ and $\{k, l, m, n\} \in [-2, +2]$. The E1-E5 combination is of special interest but the maximum combination discrimination is obtained for a joint L-/C-band combination.

3.3. Joint L-/C-band narrowlane combinations

There exists a large variety of joint code-carrier narrowlane combinations where C-band measurements help to reduce the noise substantially. Figure 6 shows the tradeoff between wavelength and noise level for $\{i, j\} \in [-5, +5]$ and $\{k, l, m, n\} \in [-2, +2]$. For $\lambda = 5.7$ cm, the consideration of C-band measurements reduces the noise level by a factor of 5 compared to a pure L-band combination (Table 6).

3.4. Reliability of ambiguity resolution

The integer ambiguity resolution is based on the linear combination of four different variable types: double-difference measurements for eliminating clock errors and satellite/receiver biases; multifrequency combinations for suppressing the ionosphere; code and carrier phase measurements for

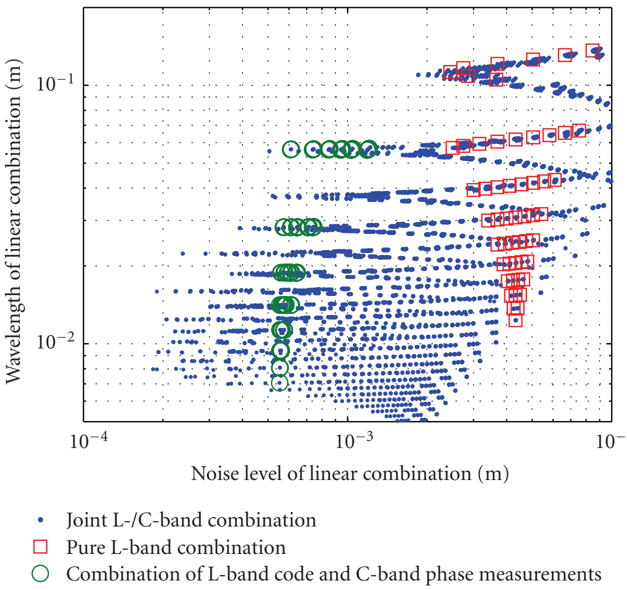

Figure 6: Comparison of joint L-/C-Band linear combinations for $\sigma_\rho(\text{E1}) = 20\,\text{cm}$, $\sigma_\rho(\text{E5}) = 1\,\text{cm}$ and $\sigma_{\phi,i} = \lambda_i/\lambda_1 \cdot \sigma_{\phi_0}$ with $\sigma_{\phi_0} = 1\,\text{mm}$.

Table 6: Ionosphere-free code-carrier narrowlane combinations with $\sigma_\rho(\text{E1}) = \sigma_\rho(\text{C1}) = \cdots = \sigma_\rho(\text{C4}) = 20\,\text{cm}$ and $\sigma_\rho(\text{E5}) = 1\,\text{cm}$.

i	E1	1	0	− 1	5
j	E5	− 1	0	1	− 3
k	C1	0	0	1	0
l	C2	0	0	0	0
m	C3	0	0	0	0
n	C4	1	1	0	0
a	E1	− 2.04e−6	7.60e−5	1.58e−4	2.55e−4
b	E5	− 1.43e−3	5.31e−2	0.110	0.178
λ	(cm)	5.55	5.65	5.76	5.73
N_m	(mm)	0.51	0.61	1.22	2.50
R		54.4	46.3	23.6	11.46

reducing the noise level; and finally, L-/C-band combinations for noise and discrimination characteristics.

Two joint L-/C-band code-carrier ionosphere-free combinations are chosen for real-time (single epoch) ambiguity resolution. The $\lambda = 3.215\,\text{m}$, $N_m = 3.92\,\text{cm}$ combination of Table 5 and one further combination of Table 4. The double difference (DD) ionosphere-free combinations are modeled as

$$\begin{bmatrix} y_{\rho\phi} \\ y_\rho \end{bmatrix} = \begin{bmatrix} G \\ G \end{bmatrix} \delta x + \begin{bmatrix} \lambda \cdot 1 \\ 0 \end{bmatrix} N + \varepsilon = X\beta + \varepsilon, \qquad (17)$$

with

$$X = \begin{bmatrix} \lambda \cdot 1 & G \\ 0 & G \end{bmatrix}, \qquad \beta = \begin{bmatrix} N \\ \delta x \end{bmatrix} \qquad (18)$$

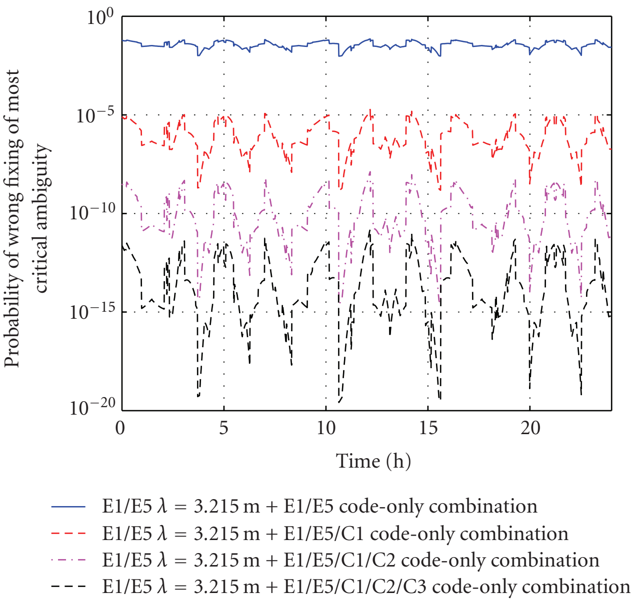

Figure 7: Reliability of $\lambda = 3.215\,\text{m}$ integer ambiguity resolution: impact of C-band measurements on the probability of wrong fixing of the most critical ambiguity.

and the DD geometry matrix G, the baseline δx and the integer ambiguities N. The double-differenced troposphere is assumed to be negligible or known a priori (e.g., from an accurate continued fraction model).

Note that the troposphere has the same impact on all geometry-preserving combinations and does not affect the optimization of the mixed code-carrier combinations. The noise vector is Gaussian distributed, that is,

$$\varepsilon \sim \mathcal{N}(0, \Sigma) \quad \text{with } \Sigma = \Sigma_{\text{LC}} \otimes \Sigma_{\text{DD}}, \qquad (19)$$

where ⊗ denotes the Kronecker product. Σ_{LC} models the linear combination induced correlation and Σ_{DD} includes the correlation due to double difference measurements from N_s visible satellites. The standard deviation of the most critical ambiguity estimate can be written as

$$\sigma_{\max} = \max_{i=\{1\cdots N_s-1\}} \sqrt{\Sigma_{\hat{\beta}}(i,i)}, \quad \Sigma_{\hat{\beta}} = \left(X^T \Sigma^{-1} X\right)^{-1}, \qquad (20)$$

and the probability of wrong fixing follows as

$$P_w^c = 1 - \int_{-0.5}^{+0.5} \frac{1}{\sqrt{2\pi\sigma_{\max}^2}} e^{-x^2/2\sigma_{\max}^2} dx. \qquad (21)$$

In the following analysis, the location of the reference station is at 48.1507° N, 11.5690° E with a baseline length of 10 km.

Figure 7 shows the benefit of C-band measurements for integer ambiguity fixing. If the E1-E5 pure L-band combination is used as second combination in (17), the failure rate varies between 0.01 and 0.07 due to its poor noise characteristics. The use of two additional C-band measurements reduces the maximum probability of wrong fixing to 10^{-5}. For three C-band frequencies, the failure rate is at most 10^{-11}

which corresponds to a gain of 9 to 17 orders of magnitude compared to the pure L-band combination.

The reliability of ambiguity resolution can be further improved by using the LAMBDA method of Teunissen [7]. The float ambiguity estimates are decorrelated by an integer transformation Z^T and the ambiguity covariance matrix is written as

$$\Sigma_{\hat{N}'} = Z^T \Sigma_{\hat{N}} Z = LDL^T, \tag{22}$$

with the decomposition into a lower triangular matrix L and a diagonal matrix D. The probability of wrong fixing of the sequential bootstrapping estimator is given by Teunissen [14] as

$$P_w = 1 - \prod_{i=1}^{N_s-1} \int_{-0.5}^{+0.5} \frac{1}{\sqrt{2\pi\sigma_c^2(i)}} e^{-x^2/2\sigma_c^2(i)} dx, \tag{23}$$

with $\sigma_c(i) = \sqrt{D(i,i)}$. It represents a lower bound for the success rate of the integer least-square estimator and is depicted in Figure 8. Obviously, the use of joint L-/C-band linear combinations reduces the probability of wrong fixing by several orders of magnitude compared to pure L-band combinations.

3.5. *Accuracy of baseline estimation*

After integer ambiguity fixing, the baseline is re-estimated from (17). The covariance matrix of the baseline estimate in local coordinates is given by

$$\Sigma_{\delta\hat{x}} = R_L \left(G^T \Sigma^{-1} G\right)^{-1} R_L^T \tag{24}$$

with the rotation matrix R_L. Figure 9 shows the achievable horizontal and vertical accuracies for the two optimized joint L-/C-band combinations.

The pure L-band combinations in the first row of Tables 4 and 5 have been again selected as reference scenario. It can be observed that the use of joint L-/C-band linear combinations enables a slight improvement in position estimates compared to the significant benefit for ambiguity resolution.

4. JOINT L-/C-BAND CARRIER SMOOTHED CARRIER

Ionosphere-free code-carrier linear combinations are characterized by a noise level that is one to two orders of magnitude larger than of the underlying carrier-phase measurements (Table 5). Both noise and multipath of the code-carrier combinations can be reduced by the smoothing filter of Hatch [15] which is shown in Figure 10. The upper input can be an ionosphere-free code-carrier combination of arbitrary wavelength. The lower input is a pure ionosphere-free phase combination that is determined by three conditions: the first ensures that the geometry is preserved, the second eliminates the ionosphere, and the third minimizes the noise, that is,

$$\begin{aligned} &\alpha + \beta + \gamma \overset{!}{=} 1, \\ &\alpha + \beta q_{12}^2 + \gamma q_{13}^2 \overset{!}{=} 0, \\ &\min_{\alpha,\beta,\gamma} N_m^2 = \min_{\alpha,\beta,\gamma} \left(\sigma_{\phi,0}^2 \cdot \left(\alpha^2 + \beta^2 q_{12}^2 + \gamma^2 q_{13}^2\right)\right). \end{aligned} \tag{25}$$

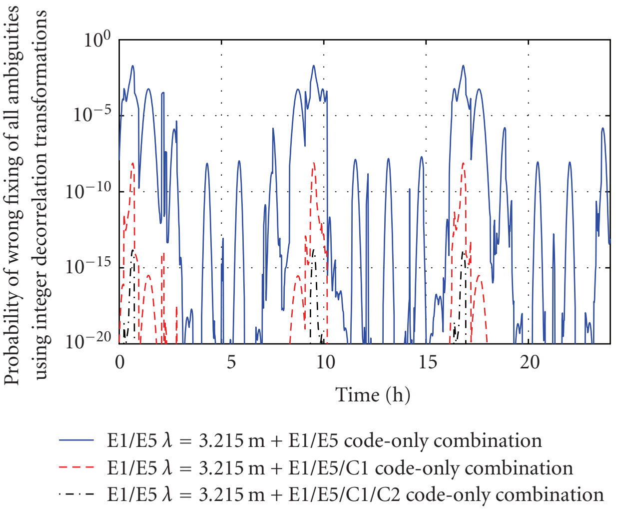

FIGURE 8: Reliability of $\lambda = 3.215$ m integer ambiguity resolution: impact of C-band measurements on the probability of wrong fixing based on sequential fixing with the integer decorrelation transformation.

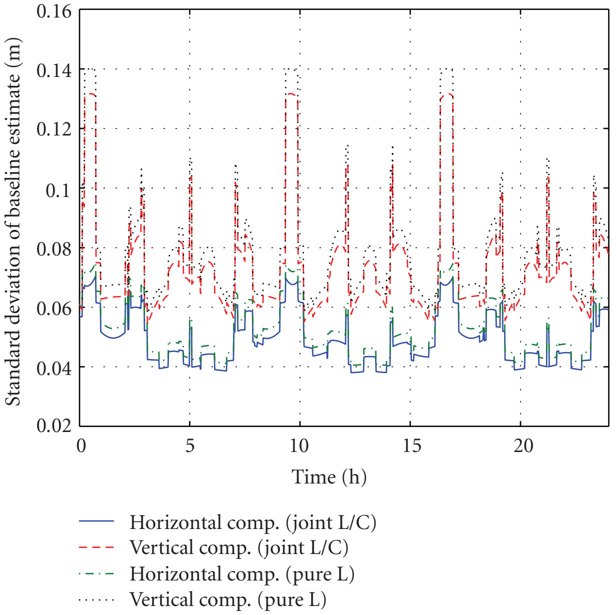

FIGURE 9: Standard deviation of baseline estimation using the $\lambda = 3.215$ m E1-E5 ionosphere-free code-carrier combination and the E1-E5-C1 · · · C4 ionosphere-free code-only combination.

Note that the superposition of ambiguities of the pure phase combination is not necessarily an integer number of a common wavelength. The respective ambiguities are not affected by the low pass filter and do not occur in the smoothed output $\lambda_A \overline{\phi}_A$ due to different signs in the addition to $\lambda_A \phi_A$ (Figure 10).

Table 7 shows an ionosphere-free E1-E5a-E5b phase combination that increases the noise level by a factor 2.64. However, the low noise level of C-band measurements suggests the use of the second combination with $f_3 = 491 \cdot 10.23$ MHz. In this case, the noise level is not only reduced

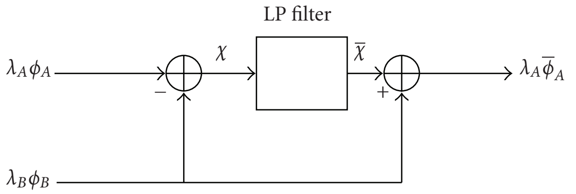

FIGURE 10: Ionosphere-free carrier smoothed code-carrier combinations.

TABLE 7: Weighting coefficients and properties of ionosphere-free carrier smoothed carrier phase combinations.

f_1	f_2	f_3	α	β	γ	N_m
E1	E5b	E5a	2.324	− 0.559	− 0.764	$2.64 \cdot \sigma_{\phi_0}$
E1	E5b	C	− 0.008	− 0.056	1.064	$0.34 \cdot \sigma_{\phi_0}$

by smoothing but also by the coefficients of the pure phase combination.

The variance of the smoothed combination is given by

$$\sigma_{\overline{A}}^2 = E\{(\overline{\varepsilon}_A(t) - \overline{\varepsilon}_B(t) + \varepsilon_B(t))^2\}, \tag{26}$$

with the low-pass filtered noise (e.g., Konno et al. [16])

$$\overline{\varepsilon}_A(t) = \frac{1}{\tau_s} \cdot \sum_{n=0}^{\infty} \left(1 - \frac{1}{\tau_s}\right)^n \varepsilon_A(t-n), \tag{27}$$

and the smoothing time τ_s. Setting (27) into (26), and using the definition of a geometric series yields

$$\sigma_{\overline{A}}^2 = \sigma_B^2 + \frac{1}{2\tau_s - 1} \cdot (\sigma_A^2 + \sigma_B^2 - 2\sigma_{AB}^2) + \frac{2}{\tau_s} \cdot (\sigma_{AB}^2 - \sigma_B^2). \tag{28}$$

For long smoothing times, only the low noise of the joint L/C pure carrier-phase combination $\lambda_B\phi_B$ remains (Table 7).

5. CONCLUSIONS

In this paper, new joint L-/C-band linear combinations that include both code- and carrier-phase measurements have been determined. The weighting coefficients are selected such that the ratio between wavelength and noise level is maximized. An ionosphere-free L-band combination (IFL) could be found at a wavelength of 3.215 m with a noise level of 3.92 cm.

The combination of L- and C-band measurements reduces the noise level of ionosphere-free code-only combinations by a factor 4.5 compared to pure L-band combinations. This increases the reliability of an ambiguity resolution option for the IFL combination by 9 orders of magnitude.

The residual variance of the noise can be further reduced by smoothing. An L-/C-band carrier combination can smooth the noise with a residual variance below the L-band phase noise variance. The smoothed solution can either be used directly or can be used to resolve the narrowlane ambiguities. The variance is basically the same in both cases. The resolved ambiguities, however, provide instantaneous independent solutions.

REFERENCES

[1] B. Forssell, M. Martin-Neira, and R. A. Harris, "Carrier phase ambiguity resolution in GNSS-2," in *Proceedings of the 10th International Technical Meeting of the Satellite Division of the Institute of Navigation (ION GPS '97)*, vol. 2, pp. 1727–1736, Kansas City, Mo, USA, September 1997.

[2] J. Jung, P. Enge, and B. Pervan, "Optimization of cascade integer resolution with three civil frequencies," in *Proceedings of the 13th International Technical Meeting of the Satellite Division of the Institute of Navigation (ION GPS '00)*, Salt Lake City, Utah, USA, September 2000.

[3] M. Cocard and A. Geiger, "Systematic search for all possible Widelanes," in *Proceedings of the 6th International Geodetic Symposium on Satellite Positioning*, Columbus, Ohio, USA, March 1992.

[4] P. Collins, "An overview of gps inter-frequency carrier phase combinations," Technical Memorandum, Geodetic Survey Division, University of New Brunswick, Ottawa, Ontario, Canada, 1999.

[5] P. Henkel and C. Günther, "Three frequency linear combinations for Galileo," in *Proceedings of the 4th Workshop on Positioning, Navigation and Communication (WPNC '07)*, pp. 239–245, Hannover, Germany, March 2007.

[6] P. Henkel and C. Günther, "Sets of robust full-rank linear combinations for wide-area differential ambiguity fixing," in *Proceedings of the 2nd ESA Workshop on GNSS Signals and Signal Processing*, Noordwijk, The Netherlands, April 2007.

[7] P. Teunissen, "Least-squares estimation of the integer ambiguities," Invited lecture, Section IV, Theory and Methodology, IAG General Meeting, Beijing, China, 1993.

[8] P. J. G. Teunissen, "On the GPS widelane and its decorrelating property," *Journal of Geodesy*, vol. 71, no. 9, pp. 577–587, 1997.

[9] G. Hein, J. Godet, J. Issler, et al., "Status of galileo frequency and signal design," in *Proceedings of the 15th International Technical Meeting of the Satellite Division of the Institute of Navigation (ION GPS '02)*, pp. 266–277, Portland, Ore, USA, September 2002.

[10] "Galileo Open Service Signal-in-Space ICD," http://www.galileoju.com.

[11] European Radiocommunications Office, "The European Table of Frequency Allocations and Utilisations in the Frequency Range 9 kHz to 1000 GHz," ERC Report 25, p. 132, 2007.

[12] M. Irsigler, G. Hein, B. Eissfeller, et al., "Aspects of C-band satellite navigation: signal propagation and satellite signal tracking," in *Proceedings of the European Navigation Conference (ENC GNSS '02)*, Kopenhagen, Denmark, May 2002.

[13] E. Kaplan and C. Hegarty, *Understanding GPS: Principles and Applications*, Artech House, London, UK, 2nd edition, 2006.

[14] P. J. G. Teunissen, "Success probability of integer GPS ambiguity rounding and bootstrapping," *Journal of Geodesy*, vol. 72, no. 10, pp. 606–612, 1998.

[15] R. R. Hatch, "A new three-frequency, geometry-free, technique for ambiguity resolution," in *Proceedings of the 19th International Technical Meeting of the Satellite Division of the Institute of Navigation (ION GNSS '06)*, vol. 1, pp. 309–316, Fort Worth, Tex, USA, September 2006.

[16] H. Konno, S. Pullen, J. Rife, and P. Enge, "Evaluation of two types of dual-frequency differential GPS techniques under anomalous ionosphere conditions," in *Proceedings of the National Technical Meeting of the Institute of Navigation (NTM '06)*, vol. 2, pp. 735–747, Monterey, Calif, USA, January 2006.

Hindawi Publishing Corporation
International Journal of Navigation and Observation
Volume 2008, Article ID 372651, 11 pages
doi:10.1155/2008/372651

Research Article

Bayesian Time Delay Estimation of GNSS Signals in Dynamic Multipath Environments

Michael Lentmaier,[1] Bernhard Krach,[2] and Patrick Robertson[2]

[1] *Vodafone Chair Communications Systems, Dresden University of Technology, TU Dresden, 01062 Dresden, Germany*
[2] *German Aerospace Center DLR, Institute of Communications and Navigation, Oberpfaffenhofen, 82234 Wessling, Germany*

Correspondence should be addressed to Michael Lentmaier, michael.lentmaier@ifn.et.tu-dresden.de

Received 1 August 2007; Revised 7 December 2007; Accepted 17 March 2008

Recommended by Letizia Presti

A sequential Bayesian estimation algorithm for multipath mitigation is presented, with an underlying movement model that is especially designed for dynamic channel scenarios. In order to facilitate efficient integration into receiver tracking loops, it builds upon complexity reduction concepts that previously have been applied within maximum likelihood (ML) estimators. To demonstrate its capabilities under different GNSS signal conditions, simulation results are presented for both BPSK-modulated and BOC-(1,1) modulated navigation signals.

1. INTRODUCTION

A major error source within global navigation satellite systems (GNSSs) comes from multipath, the reception of additional signal replica due to reflections, which introduce a bias into the estimate of the delay lock loop (DLL) of a conventional navigation receiver. For efficient removal of this bias, it is possible to formulate advanced maximum likelihood (ML) estimators that incorporate the echoes into the signal model and are capable of achieving the theoretical limits given by the Cramér Rao bound. The drawback of ML estimator techniques is that the parameters are assumed to be constant during the time of observation. Independent estimates are obtained for successive observation intervals, whose length has to be adapted to the dynamics of the channel.

In this paper, we consider the important practical case of dynamic channel scenarios and assess how the time-delay estimation can be improved if information is available about the temporal evolution of the channel parameters. Our approach is based on Bayesian filtering, the optimal and well-known framework to address such dynamic state estimation problems [1]. Sequential Monte Carlo (SMC) methods [2, 3] are used for computing the posterior probability density functions (PDFs) of the signal parameters.

2. A COMPARISON OF VARIOUS MULTIPATH MITIGATION APPROACHES

Figure 1 gives an overview of the relationships between different multipath mitigation and estimation approaches. In fact, we have chosen to discriminate approaches according to their primary objective. The left column represents the class of techniques that attempt to *mitigate* the effect of multipath in different ways. This can for example be achieved by modifications of the antenna response, either by means of hardware design or with signal processing techniques (e.g., beamforming). The majority of the remaining mitigation techniques are in some way aligning the more or less traditional receiver components (e.g., the early/late correlator) to the signal received in the multipath environment. The probably most simple technique is the adjustment of the correlator spacing applied in the Narrow Correlator [4]. Other well-known examples of this category are the Strobe Correlator [5], the Gated Correlator [6], or the Pulse Aperture Correlator [7]. To incorporate new signal forms (such as BOC), these methods need "tuning" in order to suffer as little as possible from multipath. On the other hand, multipath *estimation* techniques (right column) treat multipath (in particular the delay of the paths) as something to be estimated from the channel observations, so that its

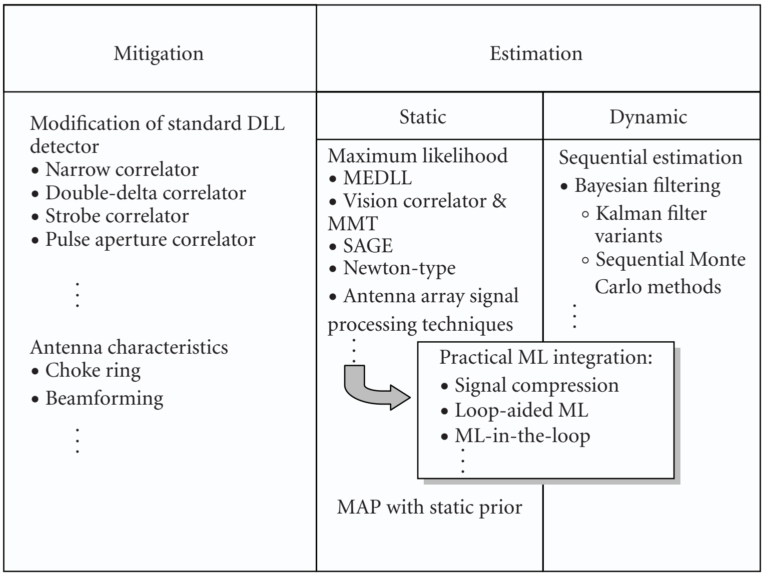

Figure 1: Classification of multipath mitigation approaches.

effects can be trivially removed at a later processing stage. For the estimation techniques, we have differentiated between *static* and *dynamic* approaches, according to the underlying assumption of the channel dynamics. Examples for static multipath estimation are those belonging to the family of ML estimators, often using different efficient maximization strategies over the likelihood function [8–13]. For static channels without availability of prior information, the ML approach is optimal and performs significantly better than other techniques, especially if the echoes have short delay. An estimator based on sequential importance sampling (SIS) methods (particle filtering) for static multipath scenarios has been considered in [14], which has the advantage that prior channel knowledge can be incorporated.

As a first step towards addressing dynamic channels, one can incorporate ML estimators in receiver loops or formulate quasisequential estimators [15, 16]. Finally, dynamic estimators that target the computation of the posterior PDF conditioned on the received channel output sequence at the receiver can be applied on a per single range basis or operate in the position domain. In this paper, we concentrate on dynamic estimators applied per each range. The sequential Monte Carlo approach has also been suggested in the communications field for estimation of time-varying channel responses in spread spectrum systems [17, 18].

3. SIGNAL MODEL

Assume that the complex valued baseband-equivalent received signal is equal to

$$z(t) = \sum_{i=1}^{N_m} e_i(t)\cdot a_i(t)\cdot\left[c(t)*g\left(t-\tau_i(t)\right)\right] + n(t), \quad (1)$$

where $c(t)$ is a delta-train code sequence that is modulated on a pulse $g(t)$, N_m is the maximum number of allowed paths reaching the receiver (to restrict the modeling complexity), $e_i(t)$ is a binary function that controls the activity of the i'th path, and $a_i(t)$ and $\tau_i(t)$ are their individual complex amplitudes and time delays, respectively. The signal is disturbed by additive white Gaussian noise $n(t)$. Grouping blocks of L samples at times $(m+kL)T_s$, $m = 0,\dots,L-1$, together into vectors $\mathbf{z}_k$, $k = 0,1,\dots,n$ whilst assuming the parameter functions $e_i(t)$, $a_i(t)$, and $\tau_i(t)$ being constant within the corresponding time interval and equal to $e_{i,k}$, $a_{i,k}$, and $\tau_{i,k}$, this can be rewritten as

$$\mathbf{z}_k = \mathbf{C}\mathbf{G}(\boldsymbol{\tau}_k)\mathbf{E}_k\mathbf{a}_k + \mathbf{n}_k \mathrel{\widehat{=}} \mathbf{s}_k + \mathbf{n}_k. \quad (2)$$

In the compact form on the right hand side, the samples of the delayed pulses $\mathbf{g}(\tau_{i,k})$ are stacked together as columns of the matrix $\mathbf{G}(\boldsymbol{\tau}_k) = [\mathbf{g}(\tau_{1,k}),\dots,\mathbf{g}(\tau_{N_m,k})]$, $\mathbf{C}$ is a matrix representing the convolution with the code, and the delays and amplitudes are collected in the vectors $\boldsymbol{\tau}_k = [\tau_{1,k},\dots,\tau_{N_m,k}]^T$ and $\mathbf{a}_k = [a_{1,k},\dots,a_{N_m,k}]^T$, respectively. Furthermore, for concise notation we use $\mathbf{E}_k = \operatorname{diag}[\mathbf{e}_k]$ whilst the elements of the vector $\mathbf{e}_k = [e_{1,k},\dots,e_{N_m,k}]^T$, $e_{i,k} \in [0,1]$, determine whether the i'th path is active or not by being either $e_{i,k} = 1$ corresponding to an active path or $e_{i,k} = 0$ for a path that is currently not active. The term $\mathbf{s}_k$ denotes the signal hypothesis and is completely determined by the channel parameters $\boldsymbol{\tau}_k$, $\mathbf{a}_k$, and $\mathbf{e}_k$. Using (2), we can write the associated *likelihood function* as

$$p(\mathbf{z}_k \mid \mathbf{s}_k) = \frac{1}{(2\pi)^L\sigma^{2L}}\cdot\exp\left[-\frac{1}{2\sigma^2}\left(\mathbf{z}_k-\mathbf{s}_k\right)^H\left(\mathbf{z}_k-\mathbf{s}_k\right)\right]. \quad (3)$$

The likelihood function will play a central role in the algorithms discussed in this paper; its purpose is to quantify the conditional probability of the received signal conditioned on the unknown signal (specifically the channel parameters).

3.1. Efficient likelihood computation

In [11], a general concept for the efficient representation of the likelihood (3) was presented, which is applicable to many of the existing ML multipath mitigation methods. The key idea of this concept is to formulate (3) through a vector $\mathbf{z}_{c,k}$ resulting from an orthonormal projection of the observed signal $\mathbf{z}_k$ onto a smaller vector space, so that $\mathbf{z}_{c,k}$ is a sufficient statistic according to the Neyman-Fisher factorization [19] and hence suitable for estimating $\mathbf{s}_k$. In other words, the reduced signal comprises the same information as the original signal itself. In practice, this concept becomes relevant as the projection can be achieved by processing the received signal (2) with a bank of correlators and a subsequent decorrelation of the correlator outputs. A variant of this very general concept, applied in [13], has also been referred to as the *Signal Compression Theorem* in [20] for a set of special projections that do not require the step of decorrelation due to the structure of the used correlators. For instance, unlike the correlation technique used in [8], the one suggested in [13] already projects onto an orthogonal and thus uncorrelated subspace, similar to the code matched correlator technique proposed in [11]. Due to complexity reasons, all practically relevant realizations of ML estimators [8, 13] operate in a projected space, namely after correlation. The corresponding mathematical background will be discussed below, including also interpolation of the likelihood and elimination of complex amplitudes as further methods for complexity reduction.

3.1.1. Data compression

As explained above, the large vector containing the received signal samples $\mathbf{z}_k$ is linearly transformed into a vector $\mathbf{z}_{c,k}$ of much smaller size. Following this approach, the likelihood according to (2) can be rewritten as

$$\begin{aligned} p(\mathbf{z}_k \mid \mathbf{s}_k) &= \frac{1}{(2\pi)^L \sigma^{2L}} \exp\left[-\frac{\mathbf{z}_k^H \mathbf{z}_k}{2\sigma^2}\right] \\ &\quad \cdot \exp\left[\frac{\Re\{\mathbf{z}_k^H \mathbf{Q}_c \mathbf{Q}_c^H \mathbf{s}_k\}}{\sigma^2} - \frac{\mathbf{s}_k^H \mathbf{Q}_c \mathbf{Q}_c^H \mathbf{s}_k}{2\sigma^2}\right] \\ &= \frac{1}{(2\pi)^L \sigma^{2L}} \exp\left[-\frac{\mathbf{z}_k^H \mathbf{z}_k}{2\sigma^2}\right] \\ &\quad \cdot \exp\left[\frac{\Re\{\mathbf{z}_{c,k}^H \mathbf{s}_{c,k}\}}{\sigma^2} - \frac{\mathbf{s}_{c,k}^H \mathbf{s}_{c,k}}{2\sigma^2}\right], \end{aligned} \tag{4}$$

with the compressed received vector $\mathbf{z}_{c,k}$ and the compressed signal hypothesis $\mathbf{s}_{c,k}$:

$$\mathbf{z}_{c,k} = \mathbf{Q}_c^H \mathbf{z}_k, \qquad \mathbf{s}_{c,k} = \mathbf{Q}_c^H \mathbf{s}_k, \tag{5}$$

and the orthonormal compression matrix $\mathbf{Q}_c$, which needs to fulfill

$$\mathbf{Q}_c \mathbf{Q}_c^H \approx \mathbf{I}, \qquad \mathbf{Q}_c^H \mathbf{Q}_c \approx \mathbf{I}, \tag{6}$$

to minimize the compression loss. According to [11], the compression can be two-fold so that we can factorize

$$\mathbf{Q}_c = \mathbf{Q}_{cc} \mathbf{Q}_{pc} \tag{7}$$

into a *canonical component decomposition*, given by an $L \times N_{cc}$ matrix $\mathbf{Q}_{cc}$, and a *principal component decomposition*, given by an $N_{cc} \times N_{pc}$ matrix $\mathbf{Q}_{pc}$. In [11], two choices for $\mathbf{Q}_{cc}$ are proposed

$$\mathbf{Q}_{cc} = \begin{cases} \mathbf{C}\mathbf{G}(\boldsymbol{\tau}^b)\mathbf{R}_{cc}^{-1} & \text{Signal matched,} \\ \mathbf{C}(\boldsymbol{\tau}^b)\mathbf{R}_{cc}^{-1} & \text{Code matched,} \end{cases} \tag{8}$$

where the elements of the vector $\boldsymbol{\tau}^b$ define the positions of the individual correlators. The noise-free outputs of the corresponding correlator banks are illustrated in Figure 2. To decorrelate the bank outputs $(\mathbf{C}\mathbf{G}(\boldsymbol{\tau}^b))^H\mathbf{y}$ and $\mathbf{C}(\boldsymbol{\tau}^b)^H\mathbf{y}$, as mentioned above, the whitening matrix $\mathbf{R}_{cc}$ can be obtained from a QR decomposition of $\mathbf{C}\mathbf{G}(\boldsymbol{\tau}^b)$ and $\mathbf{C}(\boldsymbol{\tau}^b)$, respectively. Apart from practical implementation issues, both correlation methods given by (8) are equivalent from a conceptual point of view. For details on the compression through $\mathbf{Q}_{pc,}$ the reader is referred to [11].

3.1.2. Interpolation

In order to compute (4) independently of the sampling grid, advantage can be made of interpolation techniques. Using the discrete Fourier transformation (DFT), with $\boldsymbol{\Psi}$ being the DFT matrix and $\boldsymbol{\Psi}^{-1}$ being its inverse counterpart (IDFT), we get

$$\begin{aligned} \mathbf{s}_{c,k} &= \mathbf{Q}_c^H \mathbf{C} \boldsymbol{\Psi}^{-1} \operatorname{diag}[\boldsymbol{\Psi}\mathbf{g}(0)] \boldsymbol{\Omega}(\boldsymbol{\tau}_k) \mathbf{E}_k \mathbf{a}_k \\ &\,\widehat{=}\, \mathbf{M}_{s_c} \boldsymbol{\Omega}(\boldsymbol{\tau}_k) \mathbf{E}_k \mathbf{a}_k, \end{aligned} \tag{9}$$

with $\boldsymbol{\Omega}(\boldsymbol{\tau}_k)$ being a matrix of column-wise stacked vectors with Vandermonde structure [10, 11], such that the element at row p and column q computes with

$$\begin{aligned} \Re\{[\boldsymbol{\Omega}(\boldsymbol{\tau}_k)]_{p,q}\} &= \cos\left(\frac{2\pi(p-1)\tau_{q,k}}{N_g T_s}\right), \\ \Im\{[\boldsymbol{\Omega}(\boldsymbol{\tau}_k)]_{p,q}\} &= -\sin\left(\frac{2\pi(p-1)\tau_{q,k}}{N_g T_s}\right). \end{aligned} \tag{10}$$

N_g is the length of the pulse $\mathbf{g}$ in samples. The advantage of the interpolation is that it can take place in the reduced space. The most costly computations in (9) can be carried out in precalculations as the matrix $\mathbf{M}_{s_c}$, whose row dimension corresponds to the dimension of the reduced space and whose column dimension is N_g, is constant.

3.1.3. Amplitude elimination

In a further step, we reduce the number of parameters by optimizing (4) for a given set of $\boldsymbol{\tau}_k$ and $\mathbf{e}_k$ with respect to the complex amplitudes $\mathbf{a}_k$, which can be achieved through a closed-form solution. Using

$$\mathbf{S}_{c,k} = \mathbf{M}_{s_c} \boldsymbol{\Omega}(\boldsymbol{\tau}_k) \mathbf{E}_k \tag{11}$$

and obtaining $\mathbf{S}_{c,k}^+$ by removing zero columns from $\mathbf{S}_{c,k,}$ one yields the corresponding amplitude values of the active paths:

$$\hat{\mathbf{a}}_k^+ = (\mathbf{S}_{c,k}^{+H} \mathbf{S}_{c,k}^+)^{-1} \mathbf{S}_{c,k}^{+H} \bar{\mathbf{z}}_{c,k}. \tag{12}$$

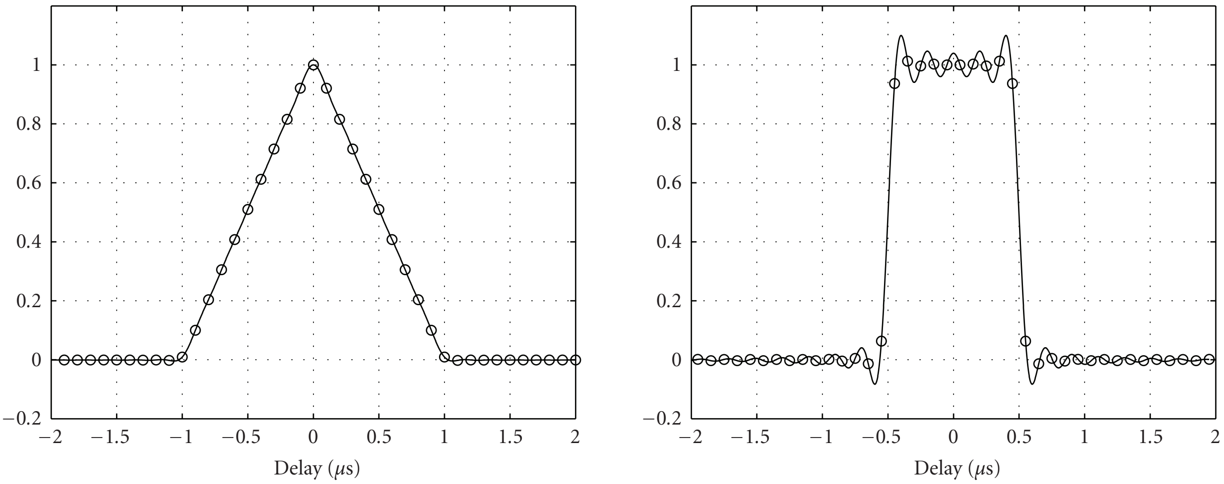

(a) BPSK signal matched

(b) BPSK code matched

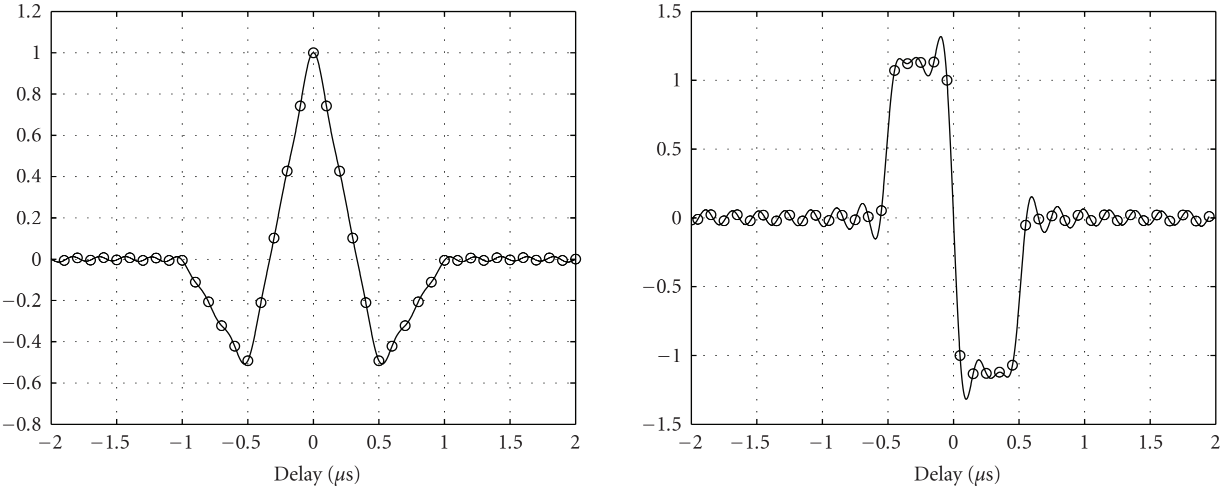

(c) BOC(1,1) signal matched

(d) BOC(1,1) code matched

Figure 2: Output of the canonical component type correlator banks $\mathbf{CG}(\boldsymbol{\tau}^b)$ and $\mathbf{C}(\boldsymbol{\tau}^b)$ for BPSK and BOC(1,1).

As we have introduced a potential source of performance loss by eliminating the amplitudes and thus practically are disregarding their temporal correlation, we propose to optimize (4) using

$$\bar{\mathbf{z}}_{c,k} = \frac{1}{Q} \cdot \sum_{l=0}^{Q-1} \mathbf{z}_{c,k-l}, \tag{13}$$

with the adjustable averaging coefficient Q. When evaluating (4), we substitute $\mathbf{s}_{c,k}$ by

$$\tilde{\mathbf{s}}_{c,k} = \mathbf{S}_{c,k}\hat{\mathbf{a}}_k, \tag{14}$$

where the elements of the vector $\hat{\mathbf{a}}_k$ that are indicated to have an active path $(a_{k,i} \; : \; i \rightarrow e_{k,i} = 1)$ are set equal to the corresponding elements of $\hat{\mathbf{a}}_k^+$. All other elements $(a_{k,i} \; : \; i \rightarrow e_{k,i} = 0)$ can be set arbitrarily as their influence is masked by the zero elements of $\mathbf{e}_k$.

3.2. Review of the ML Concept

The concept of ML multipath estimation has drawn substantial research interest since the first approach was proposed in [8]. Despite being treated differently in various publications, the objective is the same for all ML approaches, namely to find the signal parameters that maximize (3) for a given observation $\mathbf{z}_k$:

$$\hat{\mathbf{s}}_k = \arg\max_{\mathbf{s}_k} \{ p(\mathbf{z}_k \mid \mathbf{s}_k) \}. \tag{15}$$

The signal parameters are thereby assumed as being constant throughout the observation period k. Different maximization strategies exist, which basically characterize the different approaches. Despite offering great advantages for theoretical analysis, the practical advantage of the generic ML concept is questionable due to a number of serious drawbacks.

(i) The ML estimator assumes that the channel is static for the observation period and is not able to exploit its temporal correlation throughout the sequence $k = 1, \dots, n$. Measured channel scenarios have shown significant temporal correlation [21].

(ii) Despite being of great interest in practice, the estimation of the number of received paths is often not addressed. The crucial problem here is to correctly estimate the current number of paths to avoid over determination, since an overdetermined estimator will tend to use the additional degrees of freedom to match the noise by introducing erroneous paths. There exist various techniques based on model selection that can be employed to estimate the number of paths [22] but they suffer from the problem of having to dynamically adjust the decision thresholds. Typically, only a single hypothesis is tracked, which in practice causes error event propagation.

(iii) The ML estimator does only provide the most likely parameter set for the given observation. No reliability information about the estimates is provided. Consequently, ambiguities and multiple modes of the likelihood are not preserved by the estimator.

ML estimators require that the estimated parameters remain constant during the observation period. Due to data modulation and phase variations in practice, this period, which is often referred to as the coherent integration time, is limited to a range of 1 millisecond–20 milliseconds. To reach a sufficient noise performance with a ML estimator in practice, it is required to extend its observation interval approximately to the equivalent averaging time of a conventional tracking loop, which is commonly in the order of several hundred coherent integration periods. To overcome this problem, the observations are forced to be quasicoherent by aiding the ML estimator with a phase locked loop (PLL) and a data removal mechanism [8].

4. SEQUENTIAL ESTIMATION

4.1. *Optimal solution*

In Section 3, we have established the models of the underlying time-variant processes. The problem of multipath mitigation now becomes one of *sequential estimation of a hidden Markov process*. We want to estimate the unknown channel parameters based on an evolving sequence of received noisy channel outputs $\mathbf{z}_k$. The channel process for each range of a satellite navigation system can be modeled as a first-order Markov process if future channel parameters given the present state of the channel and all its past states depend only on the present channel state (and not on any past states). We also assume that the noise affecting successive channel outputs is independent of the past noise values; so *each channel observation depends only on the present channel state*.

Intuitively, we are exploiting not only the channel observations to estimate the hidden channel parameters (via the likelihood function), but we are also exploiting our prior knowledge about the statistical dependencies between successive sets of channel parameters. We know from channel measurements that channel parameters are time varying but not independent from one time instance to the next; for example, an echo usually experiences a "life-cycle" from its first occurrence, then a more or less gradual change in its delay and phase over time, until it disappears [21]. These measurements also show that the common channel models considered in communication systems [17, 18] are not adequately reflecting the properties that are crucial for high-resolution signal delay estimation as required in navigation systems.

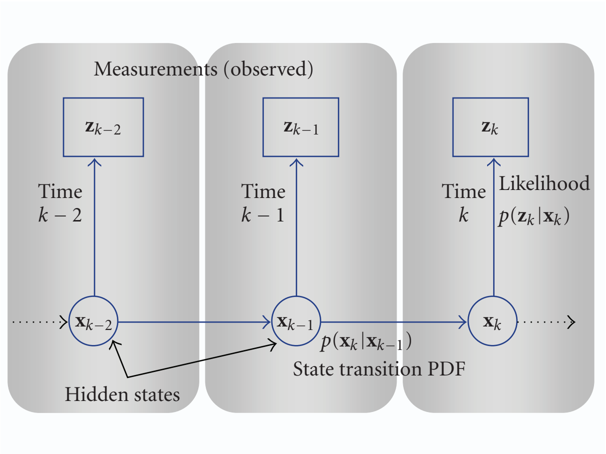

Figure 3: Illustration of the hidden Markov estimation process for three time instances. Our channel measurements are the sequence $\{\mathbf{z}_i,\ i = 1, \dots, k\}$, and the channel parameters to be estimated are $\{\mathbf{x}_i,\ i = 1, \dots, k\}$.

Now that our major assumptions have been established, we may apply the concept of *sequential Bayesian estimation*. The reader is referred to [23] which gives a derivation of the general framework for optimal estimation of temporally evolving (Markovian) parameters by means of inference, and we have chosen similar notation. The entire history of observations (over the temporal index k) can be written as

$$\mathbf{Z}_k \mathrel{\widehat{=}} \{\mathbf{z}_{k'},\ k' = 1, \dots, k\}. \tag{16}$$

Similarly, we denote the sequence of parameters of our hidden Markovian process by

$$\mathbf{X}_k \mathrel{\widehat{=}} \{\mathbf{x}_{k'},\ k' = 1, \dots, k\}. \tag{17}$$

Here, $\mathbf{x}_{k'}$ represents the characterization of the hidden channel state, including the parameters that specify the signal hypothesis $\mathbf{s}_{k'}$ given in (2). Our goal is to determine the posterior PDF of every possible channel characterization given all channel observations: $p(\mathbf{x}_k \mid \mathbf{Z}_k)$ (see Figure 3). Once we have evaluated this posterior PDF, we can either determine that channel configuration that maximizes it—the so-called maximum a posteriori (MAP) estimate; or we can choose the expectation—equivalent to the minimum mean square error (MMSE) estimate. In addition, the posterior distribution itself contains all uncertainty about the current range and is thus the optimal measure to perform sensor data fusion in an overall positioning system.

It can be shown that the sequential estimation algorithm is recursive, as it uses the posterior PDF computed for time instance $k-1$ to compute the posterior PDF for instance k (see Figure 4). For a given posterior PDF at time instance $k-1$, $p(\mathbf{x}_{k-1} \mid \mathbf{Z}_{k-1})$, the prior PDF $p(\mathbf{x}_k \mid \mathbf{Z}_{k-1})$ is calculated in the so-called *prediction step* by applying the Chapman-Kolmogorov equation:

$$p(\mathbf{x}_k \mid \mathbf{Z}_{k-1}) = \int p(\mathbf{x}_k \mid \mathbf{x}_{k-1})\, p(\mathbf{x}_{k-1} \mid \mathbf{Z}_{k-1})\, \mathrm{d}\mathbf{x}_{k-1}, \tag{18}$$

with $p(\mathbf{x}_k \mid \mathbf{x}_{k-1})$ being the state transition PDF of the Markov process. In the *update step,* the new posterior PDF for step k is obtained by applying Bayes' rule to $p(\mathbf{x}_k \mid \mathbf{z}_k, \mathbf{Z}_{k-1})$ yielding the normalized product of the likelihood $p(\mathbf{z}_k \mid \mathbf{x}_k)$ and the prior PDF:

$$\begin{aligned} p(\mathbf{x}_k \mid \mathbf{Z}_k) &= p(\mathbf{x}_k \mid \mathbf{z}_k, \mathbf{Z}_{k-1}) \\ &= \frac{p(\mathbf{z}_k \mid \mathbf{x}_k, \mathbf{Z}_{k-1})\, p(\mathbf{x}_k \mid \mathbf{Z}_{k-1})}{p(\mathbf{z}_k \mid \mathbf{Z}_{k-1})} \\ &= \frac{p(\mathbf{z}_k \mid \mathbf{x}_k)\, p(\mathbf{x}_k \mid \mathbf{Z}_{k-1})}{p(\mathbf{z}_k \mid \mathbf{Z}_{k-1})}. \end{aligned} \tag{19}$$

The term $p(\mathbf{z}_k \mid \mathbf{x}_k) = p(\mathbf{z}_k \mid \mathbf{s}_{c,k} = \widetilde{\mathbf{s}}_{c,k})$ follows from (4) and represents the probability of the measured channel output (often referred to as the likelihood value), conditioned on a certain configuration of channel parameters at the same time step k. The denominator of (19) does not depend on $\mathbf{x}_k$, and so it can be computed by integrating the numerator of (19) over the entire range of $\mathbf{x}_k$ (normalization).

To summarize so far, the entire process of prediction and update can be carried out recursively to calculate the posterior PDF (19) sequentially, based on an initial value of $p(\mathbf{x}_0 \mid \mathbf{z}_0) = p(\mathbf{x}_0)$. The evaluation of the likelihood function $p(\mathbf{z}_k \mid \mathbf{x}_k)$ is the essence of the update step. Similarly, maximizing this likelihood function (i.e., ML estimation) would be equivalent to maximizing $p(\mathbf{x}_k \mid \mathbf{Z}_k)$ only in the case that the prior PDF $p(\mathbf{x}_k \mid \mathbf{Z}_{k-1})$ does not depend on $\mathbf{Z}_{k-1,}$ and when all values of x_k are a priori equally likely. Since these conditions are not met, evaluation of $p(\mathbf{x}_k \mid \mathbf{Z}_k)$ entails all the above steps.

4.2. Sequential estimation using particle filters

The optimal estimation algorithm relies on evaluating the integral (18), which is usually a very difficult task, except for certain additional restrictions imposed on the model and the noise process. So, very often a suboptimal realization of a Bayesian estimator has to be chosen for implementation. In this paper, we use a sequential Monte Carlo (SMC) filter, in particular a sampling importance resampling particle filter (SIR-PF) according to [23]. In this algorithm, the posterior density at step k is represented as a sum and is specified by a set of N_p particles:

$$p(\mathbf{x}_k \mid \mathbf{Z}_k) \approx \sum_{j=1}^{N_p} w_k^j \cdot \delta(\mathbf{x}_k - \mathbf{x}_k^j), \tag{20}$$

where each particle with index j has a state $\mathbf{x}_k^j$ and has a *weight* w_k^j. The sum over all particles' weights is one. In SIR-PF, the weights are computed according to the principle of *importance sampling* where the so-called proposal density is chosen to be $p(\mathbf{x}_k \mid \mathbf{x}_{k-1} = \mathbf{x}_{k-1}^j)$, and with *resampling* at every time step. For $N_p \to \infty$, the approximate posterior approaches the true PDF.

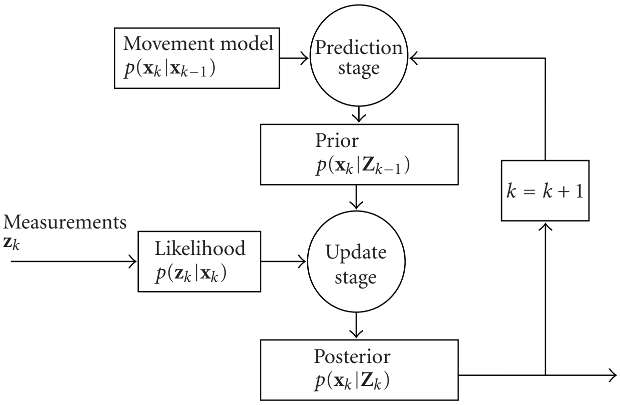

FIGURE 4: Illustration of the recursive Bayesian estimator.

The key step, in which the *measurement* for instance k is incorporated, is in the calculation of the weight w_k^j which for the SIR-PF can be shown to be the likelihood function: $p(\mathbf{z}_k \mid \mathbf{x}_k^j)$. The characterization of the *channel process* enters in the algorithm, when at each time instance k, the state of each particle $\mathbf{x}_k^i$ is drawn randomly from the proposal distribution, that is, from $p(\mathbf{x}_k \mid \mathbf{x}_{k-1}^j)$.

4.3. Exploiting linear substructures

If there exist linear substructures in the model, it is possible to reduce the computational complexity of the filter by means of marginalization over the linear state variables [24], also known as Rao-Blackwellization [25]. In a marginalized filter, particles are still used to estimate the nonlinear states, while for each of the particles the linear states can be estimated analytically. In our case, since the measurement $\mathbf{z}_k$ is a linear function of the complex amplitudes $\mathbf{a}_k$, the likelihood function can be factorized as

$$p(\mathbf{z}_k \mid \mathbf{s}_{c,k}) = p(\mathbf{z}_k \mid \boldsymbol{\tau}_k, \mathbf{e}_k, \mathbf{a}_k) = f(\mathbf{z}_k, \boldsymbol{\tau}_k, \mathbf{e}_k) \cdot g(\mathbf{z}_k, \boldsymbol{\tau}_k, \mathbf{e}_k, \mathbf{a}_k), \tag{21}$$

where the function $g(\mathbf{z}_k, \boldsymbol{\tau}_k, \mathbf{e}_k, \mathbf{a}_k)$ is Gaussian with respect to $\mathbf{a}_k$, and $f(\mathbf{z}_k, \boldsymbol{\tau}_k, \mathbf{e}_k)$ is proportional to $p(\mathbf{z}_k \mid \widetilde{\mathbf{s}}_{c,k})$. Marginalization of (21) over the linear state variables gives

$$\int_{\mathbf{a}_k} p(\mathbf{z}_k \mid \boldsymbol{\tau}_k, \mathbf{e}_k, \mathbf{a}_k)\, d\mathbf{a}_k = f(\mathbf{z}_k, \boldsymbol{\tau}_k, \mathbf{e}_k) \propto p(\mathbf{z}_k \mid \widetilde{\mathbf{s}}_{c,k}). \tag{22}$$

Assuming that the amplitudes are block-wise independent ($Q = 1$), it follows that the weights of the SIR particle filter are equal to $p(\mathbf{z}_k \mid \mathbf{x}_k^j) = p(\mathbf{z}_k \mid \mathbf{s}_{c,k} = \widetilde{\mathbf{s}}_{c,k}^j)$, which is given by (4).

If there exists a temporal correlation of the amplitudes, an optimal marginalized filter requires the implementation of a separate Kalman filter for each of the particles. As we do not want to increase the complexity per particle, we take the correlation into account by adjustment of Q in (13).

4.4. Choice of appropriate channel process

To exploit the advantages of sequential estimation for our task of multipath mitigation/estimation, we must be able to describe the actual channel characteristics (channel parameters) so that these are captured by $p(\mathbf{x}_k \mid \mathbf{x}_{k-1})$. In other words, the model must be a first-order Markov model, and all transition probabilities must be known. In our approach, we approximate the channel as follows.

(i) The channel is totally characterized by a direct path (index $i = 1$) and at most $N_m - 1$ echoes,

(ii) each path has complex amplitude $a_{i,k}$ and relative delay and $\Delta\tau_{i,k} = \tau_{i,k} - \tau_{1,k}$; where echoes are constrained to have delay $\tau_{i,k} \geq \tau_{1,k}$, that is, $\Delta\tau_{i,k} \geq 0$,

(iii) the different path delays follow the process:

$$\begin{aligned} \tau_{1,k} &= \tau_{1,k-1} + \alpha_{1,k-1} \cdot \Delta t + n_\tau, \\ \Delta\tau_{i,k} &= \Delta\tau_{i,k-1} + \alpha_{i,k-1} \cdot \Delta t + n_\tau, \end{aligned} \tag{23}$$

(iv) each parameter $\alpha_{i,k}$ that specifies the speed of the change of the path delay follows its own process:

$$\alpha_{i,k} = \left(1 - \frac{1}{K}\right) \cdot \alpha_{i,k-1} + n_\alpha, \tag{24}$$

(v) the magnitudes and phases of the individual paths, represented by the complex amplitudes $a_{i,k}$, are eliminated according to (12) and (14) for the computation of the likelihood (4),

(vi) each path is either “on” or “off,” as defined by channel parameter $e_{i,k} \in \{1 \equiv \text{“on,''}0 \equiv \text{“off}'\}$,

(vii) where $e_{i,k}$ follows a simple two-state Markov process with a-symmetric crossover and same-state probabilities:

$$p(e_{i,k} = 0 \mid e_{i,k-1} = 1) = p_{\text{onoff}}, \tag{25}$$

$$p(e_{i,k} = 1 \mid e_{i,k-1} = 0) = p_{\text{offon}}. \tag{26}$$

The model implicitly incorporates three i.i.d noise sources: Gaussian n_τ and n_α as well as the noise process driving the state changes for $e_{i,k}$. These sources provide the randomness of the model. The parameter K defines how quickly the speed of path delays can change (for a given variance of n_α). Finally, Δt is the time between instances $k-1$ and k. We assume all *model parameters* (i.e., K, Δt, noise variances, and the “on”/“off” Markov model) to be independent of k (see Figure 5). The hidden channel state vector $\mathbf{x}_k$ can therefore be represented as

$$\left[\tau_{1,k}, \Delta\tau_{2,k}, \ldots, \Delta\tau_{N_m,k}, \alpha_{1,k}, \ldots, \alpha_{N_m,k}, e_{i,k}, \ldots, e_{N_m,k}\right]^T. \tag{27}$$

Note that the model implicitly represents the number of paths

$$N_{m,k} \widehat{=} \sum_{i=1}^{N_m} e_{i,k} \tag{28}$$

as a time-variant parameter.

When applied to our particle filtering algorithm, drawing from the proposal density is simple. Each particle stores the above-channel parameters of the model, and then the new state of each particle is drawn randomly from $p(\mathbf{x}_k \mid \mathbf{x}_{k-1}^j)$ which corresponds to drawing values for n_α and n_τ as well as propagating the “on”/“off” Markov model, and then updating the channel parameters for k according to (23)–(26).

4.5. Practical issues

4.5.1. Model matching

It is important to point out that a sequential estimator is only as good as its state transition model matches the real world situation. The state model needs to capture *all* relevant hidden states with memory and needs to correctly model their dependencies, while adhering to the first order Markov condition. Furthermore, any memory of the measurement noise affecting the likelihood function $p(\mathbf{z}_k \mid \mathbf{x}_k)$ must be explicitly contained as additional states of the model $\mathbf{x}$, so that the measurement noise is i.i.d.

The channel state model is motivated by channel modeling work for multipath prone environments such as the urban satellite navigation channel [21, 26]. In fact, the process of constructing a channel model in order to characterize the channel for signal level simulations and receiver evaluation comes close to our task of building a first-order Markov process for sequential estimation. For particle filtering, the model needs to satisfy the condition that one can draw states with relatively low computational complexity. Adapting the model structure and the model parameters to the real channel environment is a task for current and future work. It may even be possible to envisage hierarchical models in which the selection of the current model itself follows a process. In this case, a sequential estimator will automatically choose the correct weighting of these models according to their ability to fit the received signal.

4.5.2. Integration into a receiver

For receiver integration, the computational complexity of the filtering algorithm is crucial. From a theoretical point of view, it is desirable to run the sequential filter clocked corresponding to the coherent integration period of the receiver and with a very large number of particles. From the practical point of view, however, it is desirable to reduce the sequential filter rate to the navigation rate and to minimize the number of particles. Existing ML approaches can help here to achieve a flexible complexity/performance tradeoff, as strategies already developed to extend the observation

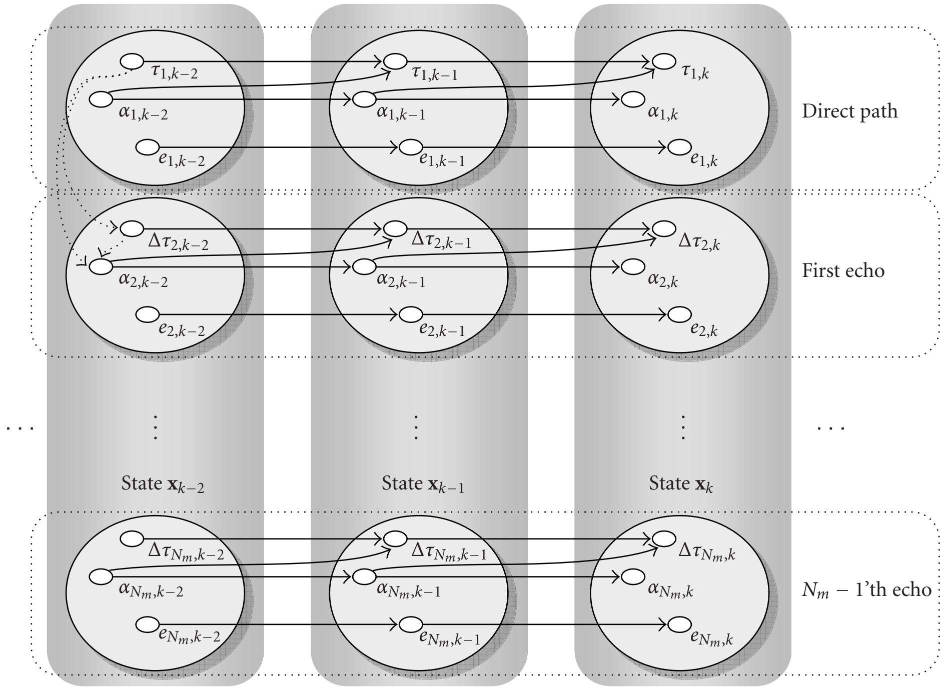

FIGURE 5: The Markov process chosen in this paper to model the channel with N_m paths. Dotted arrows—shown only for a small subset of the transitions—indicate the constraint that $\Delta\tau_{i,k} \geq 0$. For an explanation of the terms, see the text leading up to (27).

periods of ML estimators can be used directly to reduce the rate of the sequential filtering algorithm.

5. PERFORMANCE EVALUATION

To demonstrate the capabilities of the SMC-based Bayesian time delay estimator proposed in Section 4, we have carried out computer simulations for both static and dynamic channel environments. The signal-to-multipath ratio (SMR) was chosen constant and equal to 6 dB, while the relative phases are changing according to $\Delta\varphi_{i,k} = 2\pi\Delta\tau_{i,k} f_c$ with $f_c = 1575.42$ MHz being the frequency of the L1 carrier. The Bayesian estimator uses a time interval of $\Delta t = 1$ millisecond corresponding to the duration of a codeword. The amplitude averaging coefficient is set to $Q = 10$, and signal compression is applied with $N_{cc} = 41$ (code-matched correlators) $N_{pc} = 25$. The channel parameters $\sigma^2_{i,\tau}$, $\sigma^2_{i,\alpha}$, K, and $p(e_{i,k} \mid e_{i,k-1})$ are selected to fit the statistics of a real channel according to [21]. The SIR-PF uses the minimum mean square error (MMSE) criterion to estimate the parameters $\mathbf{x}_k$ from the posterior.

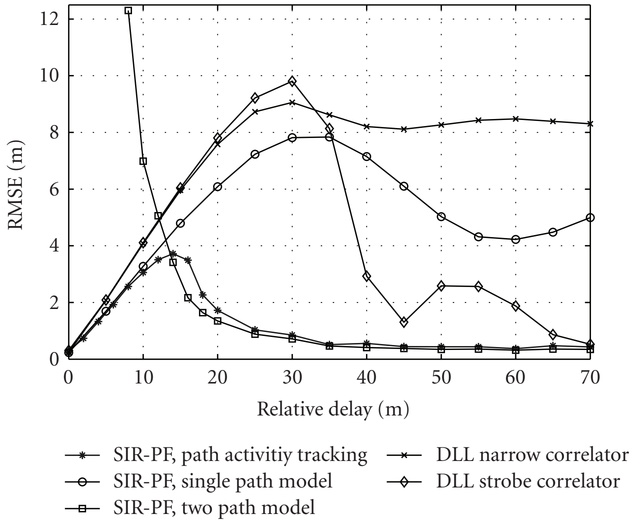

FIGURE 6: Static scenario: performance of SIR-PF for BPSK modulation as function of relative multipath delay for different path models.

5.1. Static multipath scenario

The capability of multipath mitigation techniques is commonly assessed by showing the systematic error due to a single multipath replica plotted as a function of the relative multipath delay in a static channel scenario. In Figure 6, the root mean square error (RMSE) is shown for the proposed sequential estimator, implemented as a SIR-PF with $N_s = 2000$ particles. For comparison, the performance of conventional DLLs with Narrow Correlator and with Strobe Correlator is also shown. The simulated signal corresponds to a GPS L1 signal with $c(t)$ being a Gold code of length 1023 that is modulated on a bandlimited rectangular pulse. The chip rate is 1.023 Mchips/s so that the duration of the codeword is 1millisecond. The one-sided bandwidth of the resulting navigation signal is 5 MHz. Estimators with fixed two-path model or fixed single path model are also shown for comparison with the implicit path

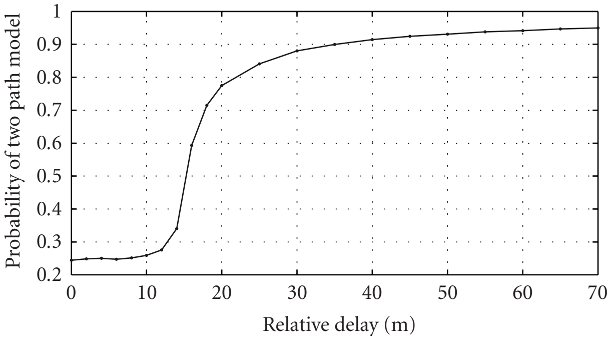

Figure 7: Static scenario: average probability of a two-path model for the estimator with path activity tracking.

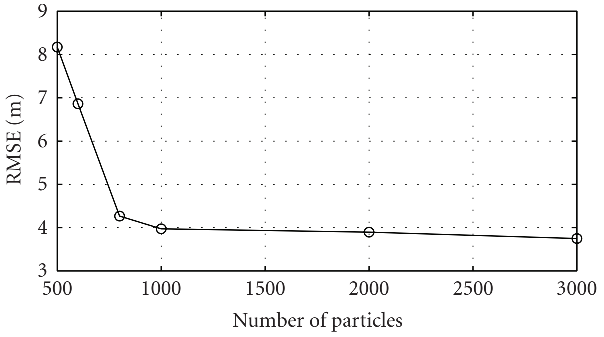

Figure 8: Static scenario: RMSE performance as function of number of particles N_s for BPSK modulation.

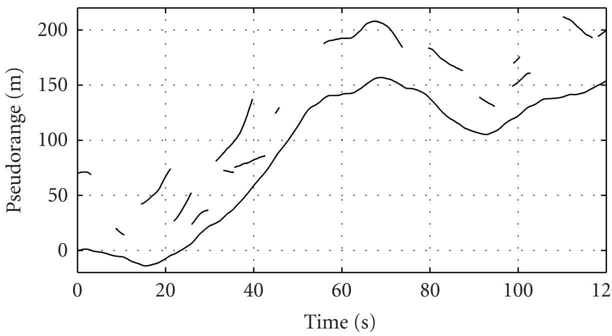

Figure 9: Considered dynamic multipath scenario: pseudoranges over time of the direct path (continuous line) and the temporarily present echoes.

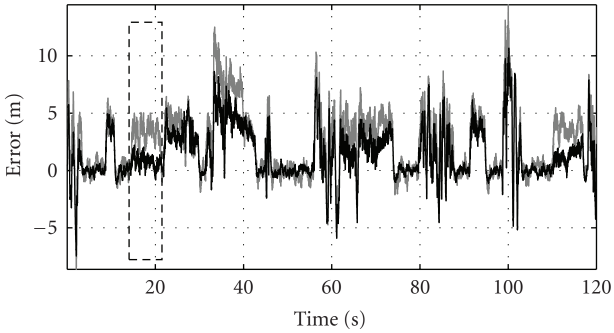

Figure 10: Dynamic scenario: performance of the DLL with narrow correlator for BPSK modulation (upper/grey) and BOC(1,1) modulation (lower/black). The segment marked with a dashed box shows a situation where BOC(1,1) is clearly superior to BPSK.

activity tracking. The performance of a single path estimator is comparable to that of a DLL with infinitesimal correlator spacing and shows a considerable bias over a large delay range. The estimator with fixed two-path model successfully mitigates the multipath bias for delays greater than 30 m. However, for smaller delays it shows an increasing variance and is outperformed by the single path estimator. The estimator with path activity tracking is capable of combining the advantages of both models. From the posterior, it is possible to calculate the estimated average probability $P(N_{m,k} = 2 \mid \mathbf{Z}_k)$ of a two-path model, which is shown in Figure 7, and indicates the transition between the models: for small delays the two paths essentially merge to a single one. Note that in these simulations, the model parameters of the sequential estimator are still the ones designed for the dynamic channel and not optimal for this static scenario. The RMSE as function of the number of particles N_s is shown in Figure 8 for a relative multipath delay of 14 m, which corresponds to the worst case in Figure 6.

5.2. *Dynamic scenario*

The dynamic multipath channel scenario with up to $N_m = 3$ paths, used in the following simulations and depicted in Figure 9, has been generated according to the movement model, whereby the parameters $K = 25000$, $\sigma_{n_\alpha} = 10^{-10}$, $\sigma_{n_\tau} = 10^{-8}$, and $p_{\text{onoff}} = p_{\text{offon}} = 0.0001$ were chosen to resemble a typical urban satellite navigation channel environment [26].

Figure 10 shows for this multipath scenario at a carrier-to-noise ratio of $C/N_0 = 45$ dB-Hz the BPSK and the BOC(1,1) performance of a DLL with a narrow correlator spacing of 10^{-7} seconds, corresponding to a tenth of a code chip. A DLL loop bandwidth of 1 Hz was selected, which appeared to deliver the best DLL performance for this channel. For a fair comparison of the different modulation techniques, both signals were generated with the same C/A code sequence of length 1023, the same receiver bandwidth of 5 MHz (one-sided), a sampling rate of $1/T_s = 10.23$ MHz, and a coherent integration time of $LT_s = 1$ millisecond. Although the results show an improvement for the BOC(1,1) modulation, there still remains a considerable error due to the multipath. This behavior is confirmed by a comparison with the multipath error envelope, depicted in Figure 11. While in some multipath delay regions, the error is reduced by the BOC(1,1) modulation (see, e.g, the segment marked by the dashed box in Figure 10), more sophisticated multipath mitigating techniques are required to reduce the errors due to short range multipath.

The simulation results for the particle filter-based estimator with $N_s = 20000$ particles are given in Figures 12(a) and

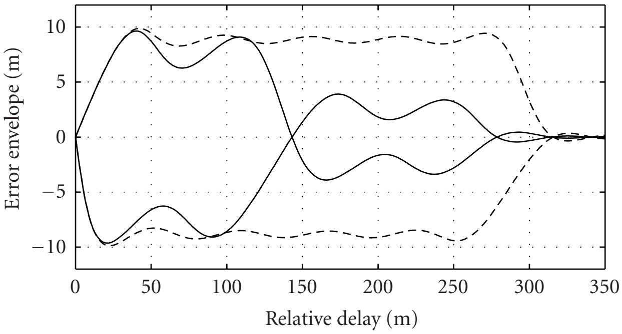

FIGURE 11: Multipath error envelope of the DLL with narrow correlator for BPSK modulation (dashed) and BOC(1,1) modulation (inner/solid).

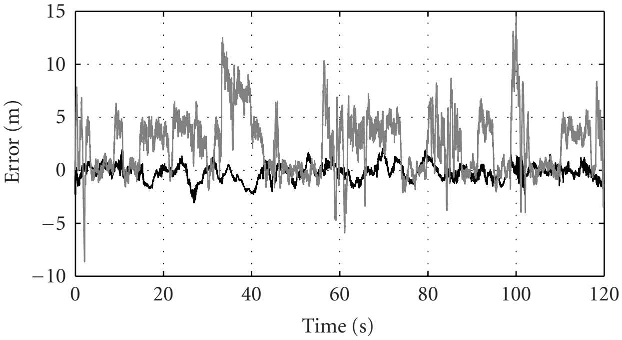

(a) BPSK modulation

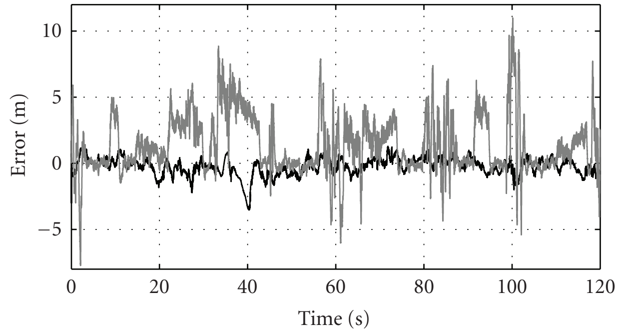

(b) BOC(1,1) modulation

FIGURE 12: Dynamic scenario: Performance of the sequential estimator with particle filtering (black) compared to the DLL (grey). The sequential estimator is clearly superior for multipath mitigation.

12(b) for the same channel as in Figure 10. They show that the performance could be improved substantially, resulting in a reduction of the root mean square (RMS) error from 3.77 m to 0.769 m for BPSK modulation and from 2.61 m to 0.694 m for BOC(1,1) modulation, respectively.

The RMSE as function of the number of particles N_s is shown in Figure 13.

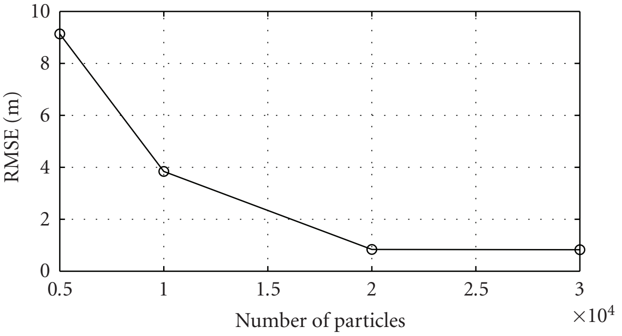

FIGURE 13: Dynamic scenario: RMSE performance as function of number of particles N_s for BPSK modulation.

6. CONCLUSIONS

We have demonstrated how sequential Bayesian estimation techniques can be applied to the multipath mitigation problem in a navigation receiver. The proposed approach is characterized by code-matched, correlator-based signal compression together with interpolation techniques for efficient likelihood computation in combination with a particle filter realization of the prediction and update recursion. The considered movement model has been adapted to dynamic multipath scenarios and incorporates the number of echoes as a time-variant hidden channel state variable that is tracked together with the other parameters in a probabilistic fashion. A further advantage compared to ML estimation is that the posterior PDF at the output of the estimator represents reliability information about the desired parameters and preserves the ambiguities and multiple modes that may occur within the likelihood function. Simulation results for BPSK- and BOC-(1,1) modulated signals show that in both cases significant improvements can be achieved compared to a DLL with narrow correlator. In this work, we have employed two methods to reduce complexity: the signal compression to facilitate the computation of the likelihood function as well as a simple form of Rao-Blackwellization to eliminate the complex amplitudes from the state space. Further work will concentrate on additional complexity reduction techniques such as more suitable proposal functions or particle filtering algorithms such as the auxiliary particle filter that are possibly more efficient with respect to the number of particles when applied to our problem domain.

REFERENCES

[1] A. H. Jazwinski, *Stochastic Processes and Filtering Theory*, Academic Press, New York, NY, USA, 1970.

[2] A. Doucet, N. de Freitas, and N. Gordon, Eds., *Sequential Monte Carlo Methods in Practice*, Springer, New York, NY, USA, 2001.

[3] B. Ristic, S. Arulampalam, and N. Gordon, *Beyond the Kalman Filter: Particle Filters for Tracking Applications*, Artech House, Boston, Mass, USA, 2004.

[4] A. J. Van Dierendonck, P. C. Fenton, and T. Ford, "Theory and performance of narrow correlator spacing in a GPS receiver,"

in *Proceedings of the ION National Technical Meeting*, San Diego, Calif, USA, January 1992.

[5] L. Garin, F. van Diggelen, and J.-M. Rousseau, "Strobe and edge correlator multipath mitigation for code," in *Proceedings of the 9th International Technical Meeting of the Satellite Division of the Institute of Navigation (ION GPS '96)*, pp. 657–664, Kansas City, Mo, USA, September 1996.

[6] G. MacGraw and M. Brasch, "GNSS multipath mitigation using gated and high resolution correlator concepts," in *Proceedings of the ION National Technical Meeting*, San Diego, Calif, USA, January 1999.

[7] J. Jones, P. C. Fenton, and B. Smith, "Theory and performance of the pulse aperture correlator," NovAtel Technical Report, NovAtel, Calgary, Alberta, Canada, 2004.

[8] R. D. J. van Nee, J. Siereveld, P. C. Fenton, and B. R. Townsend, "The Multipath estimating delay lock loop: approaching theoretical accuracy limits," in *Proceedings of the IEEE Position Location and Navigation Symposium (PLANS '94)*, pp. 246–251, Las Vegas, Nev, USA, April 1994.

[9] L. R. Weill, "Achieving theoretical accuracy limits for pseudoranging in the presence of multipath," in *Proceedings of the 8th International Technical Meeting of the Satellite Division of the Institute of Navigation (ION GPS '95)*, pp. 1521–1530, Palm Springs, Calif, USA, September 1995.

[10] J. Selva Vera, "Complexity reduction in the parametric estimation of superimposed signal replicas," *Signal Processing*, vol. 84, no. 12, pp. 2325–2343, 2004.

[11] J. Selva Vera, "Efficient multipath mitigation in navigation systems," Ph.D. dissertation, Universitat Politecnica de Catalunya, Barcelona, Spain, February 2004.

[12] F. Antreich, O. Esbrí-Rodríguez, J. A. Nossek, and W. Utchick, "Estimation of synchronization parameters using SAGE in a GNSS-receiver," in *Proceedings of the 18th International Technical Meeting of the Satellite Division of the Institute of Navigation (ION GNSS '05)*, pp. 2124–2131, Long Beach, Calif, USA, September 2005.

[13] P. C. Fenton and J. Jones, "The theory and performance of NovAtel Inc.'s vision correlator," in *Proceedings of the 18th International Technical Meeting of the Satellite Division of the Institute of Navigation (ION GNSS '05)*, pp. 2178–2186, Long Beach, Calif, USA, September 2005.

[14] P. Closas, C. Fernández-Prades, J. A. Fernández-Rubio, and A. Ramírez-González, "Multipath mitigation using particle filtering," in *Proceedings of the 19th International Technical Meeting of the Satellite Division of the Institute of Navigation (ION GNSS '06)*, pp. 1733–1740, Fort Worth, Tex, USA, September 2006.

[15] M. Lentmaier and B. Krach, "Maximum likelihood multipath estimation in comparison with conventional delay lock loops," in *Proceedings of the 19th International Technical Meeting of the Satellite Division of the Institute of Navigation (ION GNSS '06)*, pp. 1741–1751, Fort Worth, Tex, USA, September 2006.

[16] B. Krach and M. Lentmaier, "Efficient soft-output GNSS signal parameter estimation using signal compression techniques," in *Proceedings of the 3rd ESA Workshop on Satellite Navigation User Equipment Technologies (NAVITECH '06)*, Noordwijk, The Netherlands, December 2006.

[17] E. Punskaya, A. Doucet, and W. J. Fitzgerald, "Particle filtering for joint symbol and code delay estimation in DS spread spectrum systems in multipath environment," *EURASIP Journal on Applied Signal Processing*, vol. 2004, no. 15, pp. 2306–2314, 2004.

[18] T. Bertozzi, D. L. Ruyet, C. Panazio, and H. V. Thien, "Channel tracking using particle filtering in unresolvable multipath environments," *EURASIP Journal on Applied Signal Processing*, vol. 2004, no. 15, pp. 2328–2338, 2004.

[19] S. M. Kay, *Fundamentals of Statistical Signal Processing: Estimation Theory*, Prentice Hall, Upper Saddle River, NJ, USA, 1993.

[20] L. R. Weill, "Achieving theoretical bounds for receiver-based multipath mitigation using galileo OS signals," in *Proceedings of the 19th International Technical Meeting of the Satellite Division of the Institute of Navigation (ION GNSS '06)*, pp. 1035–1047, Fort Worth, Tex, USA, September 2006.

[21] A. Steingass and A. Lehner, "Measuring the navigation multipath channel—a statistical analysis," in *Proceedings of the 17th International Technical Meeting of the Satellite Division of the Institute of Navigation (ION GNSS '04)*, pp. 1157–1164, Long Beach, Calif, USA, September 2004.

[22] P. Stoica, Y. Selén, and J. Li, "On information criteria and the generalized likelihood ratio test of model order selection," *IEEE Signal Processing Letters*, vol. 11, no. 10, pp. 794–797, 2004.

[23] M. S. Arulampalam, S. Maskell, N. Gordon, and T. Clapp, "A tutorial on particle filters for online nonlinear/non-Gaussian Bayesian tracking," *IEEE Transactions on Signal Processing*, vol. 50, no. 2, pp. 174–188, 2002.

[24] T. Schön, F. Gustafsson, and P.-J. Nordlund, "Marginalized particle filters for mixed linear/nonlinear state-space models," *IEEE Transactions on Signal Processing*, vol. 53, no. 7, pp. 2279–2289, 2005.

[25] A. Doucet, N. de Freitas, K. Murphy, and S. Russell, "Rao-blackwellised particle filtering for dynamic Bayesian networks," in *Proceedings of the 16th Annual Conference on Uncertainty in Artificial Intelligence (UAI '00)*, pp. 176–183, San Francisco, Calif, USA, June-July 2000.

[26] A. Steingass and A. Lehner, "Land mobile satellite navigation—characteristics of the multipath channel," in *Proceedings of the 16th International Technical Meeting of the Satellite Division of the Institute of Navigation (ION GNSS '03)*, Portland, Ore, USA, September 2003.

Hindawi Publishing Corporation
International Journal of Navigation and Observation
Volume 2008, Article ID 793868, 9 pages
doi:10.1155/2008/793868

Research Article

Comparison between Galileo CBOC Candidates and BOC(1,1) in Terms of Detection Performance

Fabio Dovis,[1] Letizia Lo Presti,[1] Maurizio Fantino,[2] Paolo Mulassano,[2] and Jérémie Godet[3]

[1] *Dipartimento di Elettronica, Politecnico di Torino, Corso Duca degli Abruzzi 24, 10138 Torino, Italy*
[2] *Istituto Superiore Mario Boella, Corso Castelfidardo 30/A, 10138 Torino, Italy*
[3] *Galileo Unit, European Commission DG-Tren, 28 Rue de Mot, 1049 Brussels, Belgium*

Correspondence should be addressed to Maurizio Fantino, maurizio.fantino@ismb.it

Received 31 July 2007; Revised 30 December 2007; Accepted 25 February 2008

Recommended by Gerard Lachapelle

Many scientific activities within the navigation field have been focused on the analysis of innovative modulations for both GPS L1C and Galileo E1 OS, after the 2004 agreement between United States and European Commission on the development of GPS and Galileo. The joint effort by scientists of both parties has been focused on the multiplexed binary offset carrier (MBOC) which is defined on the basis of its spectrum, and in this sense different time waveforms can be selected as possible modulation candidates. The goal of this paper is to present the detection performance of the composite BOC implementation of an MBOC signal in terms of detection and false alarm probabilities. A comparison among the CBOC and BOC(1,1) modulations is also presented to show how the CBOC solution, designed to have excellent tracking performance and multipath rejection capabilities, does not limit the acquisition process.

1. INTRODUCTION

The agreement reached in 2004 by United States (US) and European Commission (EC) [1] focused on the Galileo and GPS coexistence clearly stated as central point to the selection of a common signal in space (SIS) baseline structure that is the BOC(1,1). In addition, the same agreement paved the way for common signal optimization with the goal to provide increased performance as well as considerable flexibility to receiver manufacturers.

Therefore, EC and US started to analyze possible innovative modulation strategies [2] in the view of Galileo E1 OS optimization and for the future L1C signals of the new generation GPS satellites.

Considering the recent activities carried out by the Galileo signal task force (STF) jointly to US experts in the Working Group A, it came out that the multiplexed binary offset carrier (MBOC) could be a good candidate for both GPS and Galileo satellites. In fact, on the 26th of July 2007 US and EC announced their decision to jointly implement the MBOC on the Galileo open service (OS) and the GPS IIIA civil signal as reported in [3].

The MBOC power spectral density (PSD) is a mixture of BOC(1,1) spectrum and BOC(6,1) spectrum; then different time waveforms can be combined to produce the MBOC-like spectral density. The contribution of the BOC(6,1) subcarrier brings in an increased amount of power on higher frequencies, which leads to signals with narrower correlation functions and then yielding better performance at the receiver level.

The European approach to the MBOC implementation consists in adding in time a BOC(1,1) and a BOC(6,1), defined as composite BOC (CBOC) modulation. At the time of writing, the US is likely to choose a time-multiplexed implementation, named TMBOC. Throughout the paper, the CBOC features will be described and clarified taking also into account different implementation options like, for example, the allocation of the power among the data and pilot channels of the E1 signal.

Regardless the kind of CBOC, such a signal structure allows the receivers to obtain high performance in terms of multipath rejection and tracking [4, 5]. This is mainly due to a higher transition rate brought by the BOC(6,1) on top of the BOC(1,1). However, the optimization process must also consider the signal candidates in terms of their acquisition performance. It is known that CBOC signals have sharper correlation functions [4, 5] than the BOC(1,1) solution and this characteristic, as described in [6, 7], makes the acquisition process more challenging. In this paper, the acquisition of a CBOC signal in terms of its detection and false alarm probabilities (more related to the modulation characteristics and less connected to the acquisition implementation) is investigated and compared to the performance of the pure BOC(1,1) modulation as well as the detection performance of a BOC(1,1) legacy receiver acquiring a CBOC signal. In this paper, the mean acquisition time is not investigated, since it is connected to the detection rate performance as well as the acquisition solution being implemented, so not only dependent on the signal modulation itself.

The results show that from the acquisition standpoint, thanks to the 10/11th of power located to a BOC(1,1) in the MBOC spectrum, the compatibility with the state-of-the-art BOC(1,1) receiver baseline is assured.

Moreover, it is assumed to use the Galileo acquisition engines presented in [8] which work on a pilot channel with a secondary code, that further modulates the primary pseudorandom sequences (any kind of BOC or MBOC).

The paper is organized as follows: Section 2 reports the main features of the MBOC approach while Section 3 presents the correlations properties as well as the possible CBOC candidates in terms of power allocation. Then, Section 4 is devoted to the description of the acquisition problem from a theoretical aspect, and Section 5 presents the related simulation results for the CBOCs and BOC(1,1) modulated signals. Finally, Section 6 draws some conclusions.

2. MBOC DEFINITION AND SPECTRUM CHARACTERISTICS

As reported in [9], the MBOC signal is obtained defining its power spectral density as a combination of the BOC(1,1) and BOC(6,1) power spectra (i.e., including both pilot and data channel components). The notation introduced in [9] is MBOC(6,1,1/11), where the term (6,1) refers to the BOC(6,1), and the ratio 1/11 represents the power split between the BOC(1,1) and BOC(6,1) spectrum components as given by

$$G_{\mathrm{MBOC}}(f) = \frac{10}{11} G_{\mathrm{BOC}(1,1)}(f) + \frac{1}{11} G_{\mathrm{BOC}(6,1)}(f), \qquad (1)$$

where $G_{\mathrm{BOC}(m,n)}(f)$ is the unit-power spectrum density of a sine-phased BOC modulation as defined in [10].

Figure 1 shows the comparison among the PSDs of the BOC(1,1) and the MBOC(6,1,1/11) foreseen for the Galileo E1 signal as well as for the future GPS L1C. In the picture, it is evident that the increased power at a frequency shifted about 6 MHz from the central frequency E1, deriving by the presence of the BOC(6,1) component.

It is important to remark that MBOC is defined starting from the power spectrum. In this sense, many possible time-domain implementations can result with the same approximation of the defined spectrum.

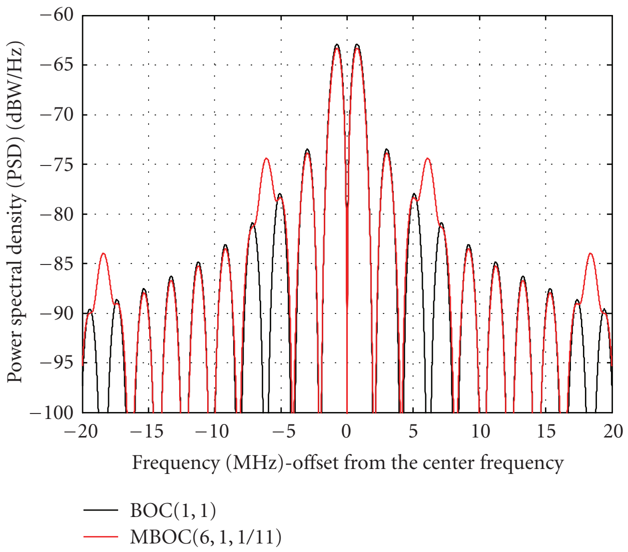

FIGURE 1: Unit power spectral densities comparison of BOC(1,1) and MBOC(6,1,1/11). (Equivalent baseband representation of the E1 carrier signals.)

3. CBOC FEATURES

In CBOC implementations, each ranging code is modulated by a weighted combination of a BOC(1,1) and a BOC(6,1) subcarriers:

$$s_{\mathrm{BOC}(1,1)}(t) = \begin{cases} \operatorname{sign}\left[\sin\left(\dfrac{2\pi t}{T_C}\right)\right], & 0 \le t \le T_C, \\ 0, & \text{elsewhere}, \end{cases}$$
$$s_{\mathrm{BOC}(6,1)}(t) = \begin{cases} \operatorname{sign}\left[\sin\left(\dfrac{12\pi t}{T_C}\right)\right], & 0 \le t \le T_C, \\ 0, & \text{elsewhere}, \end{cases} \qquad (2)$$

where $T_C = 1/(1.023 \cdot 10^6)$ [second] is the chip duration.

The notation usually reported for the composite BOC signal is CBOC(6,1,γ/ρ), where the parameters γ and ρ are related to the power splitting between the BOC(1,1) modulated signal and the BOC(6,1) contribution. However, such a notation does not take into account that the actual overall signal is obtained by combining data and pilot channels, then introducing a further degree of freedom. Furthermore, it is not mandatory that the BOC(6,1) contribution has to be present on both data and pilot channels, opening additional options to the implementation.

Therefore, the time-domain signal on the E1 data channel can be expressed as

$$s_{\mathrm{E1}}^{tx}(t) = x_{\mathrm{E1},d}(t) \cdot \alpha \left[\sqrt{\frac{\rho - \gamma}{\rho}} s_{\mathrm{BOC}(1,1)}(t) + k_d \sqrt{\frac{\gamma}{\rho}} s_{\mathrm{BOC}(6,1)}(t) \right], \qquad (3)$$

where $x_{\mathrm{E1},d}(t)$ is the product of the navigation message and the spreading code, and α is the fraction of power allocated

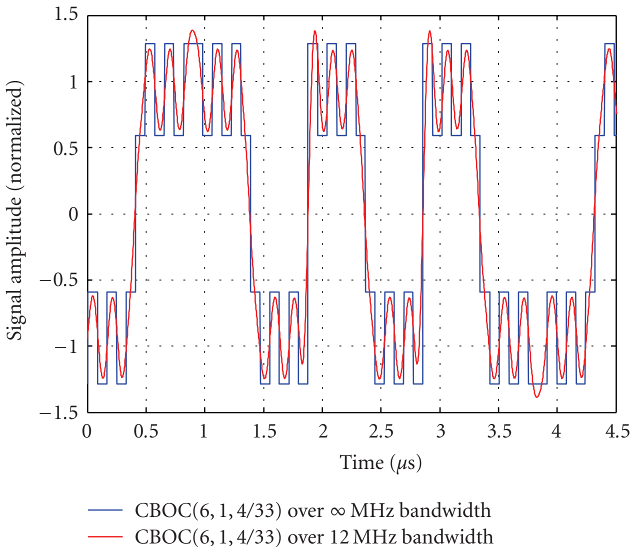

Figure 2: Example of a CBOC(6,1,1/11) over an infinite bandwidth (blue line) and shaped with a 12 MHz, 4 pole, Butterworth filter (red line).

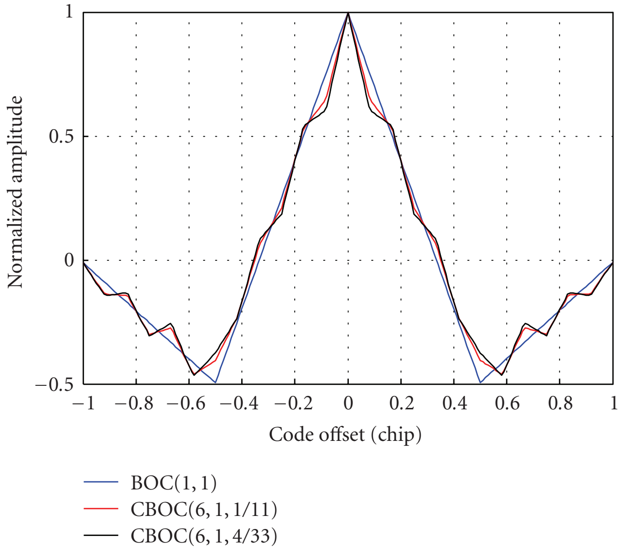

Figure 3: Normalized autocorrelation functions comparison of BOC(1,1), CBOC(6,1,1/11), and CBOC(6,1,4/33) computed over an infinite bandwidth.

Table 1: Possible options for the MBOC signal implementation by means of CBOC modulations.

Data channel modulation	Data channel power	Pilot channel modulation	Pilot channel power
CBOC(6,1,1/11)	25%	CBOC(6,1,1/11)	75%
CBOC(6,1,1/11)	50%	CBOC(6,1,1/11)	50%
BOC(1,1)	25%	CBOC(6,1,4/33)	75%

to the data channel. In the same way, the E1 pilot channel can be expressed as

$$s_{\mathrm{E1}}^{tx}(t) = x_{\mathrm{E1},p}(t)\cdot\beta\left[\sqrt{\frac{\rho-\gamma}{\rho}}s_{\mathrm{BOC}(1,1)}(t)+k_p\sqrt{\frac{\gamma}{\rho}}s_{\mathrm{BOC}(6,1)}(t)\right], \tag{4}$$

where $x_{\mathrm{E1},p}(t)$ is the spreading code sequence, and β is the fraction of power allocated to the pilot channel.

The parameters k_d and k_p can assume the values $(0, \pm 1)$, and they are used to model the presence or not of the BOC(6,1) subcarrier and its sign in the channels.

It is important to remark that, under the assumption that data and pilot channels use orthogonal spreading codes, the residual cross-correlation between the spreading sequences chosen for Galileo can be considered negligible, the overall spectrum on the E1 band is the summation of the power spectra of the pilot and data channels. Different combinations of the parameters α, β, k_d, k_p, γ, and ρ can be chosen in order to obtain signals, whose power spectral density resembles the spectral mask defined for the MBOC signal.

Table 1 shows some possible selection of the parameters associated to the power split between data and pilot channels.

As already remarked, it is not always the case that the CBOC is selected for both data and pilot channels (see third row of Table 1). Anyway, the most probable implementation selected by EC will fall on the CBOC(6,1,1/11) option (and both k_d and k_p positive) with 50% of power on both channels. This decision is due to the relatively high data rate on the E1 data channel, which is known also to carry integrity messages.

Regardless the power splitting, the CBOC in time-domain shows a four-level spreading sequence as depicted in Figure 2, where a CBOC(6,1,1/11) realization with positive contribution coming from the BOC(6,1) subcarrier has been reported.

The presence of higher transition rate (due to BOC(6,1) component) creates a sharper correlation function than the BOC(1,1) baseline. The normalized autocorrelation functions of the CBOC(6,1,1/11) and CBOC(6,1,4/33) are compared to the BOC(1,1) correlation in Figure 3.

The larger is the contribution of the BOC(6,1) subcarrier (as so the γ over ρ ratio) in the CBOC implementation, the sharper is the correlation function.

This characteristic will be deeply highlighted in the following sections considering its impact on the detection performance of the acquisition stage of the receiver.

To better highlight the sharper CBOC correlation functions, a zoom of Figure 3 around the main peak is reported in Figure 4.

The CBOC autocorrelation function can be written by means of the BOC(1,1) and BOC(6,1) autocorrelations and cross-correlations as

$$\begin{aligned} R_{\mathrm{CBOC}(6,1,\gamma/\rho)}(\tau) = {} & \frac{\rho-\gamma}{\rho}R_{\mathrm{BOC}(1,1)}(\tau) \\ & + \frac{\gamma}{\rho}R_{\mathrm{BOC}(6,1)}(\tau) \\ & + 2\frac{\gamma}{\rho}\sqrt{\frac{\rho}{\gamma}-1}\,R_{\mathrm{BOC}(1,1)\mathrm{BOC}(6,1)}(\tau), \end{aligned} \tag{5}$$

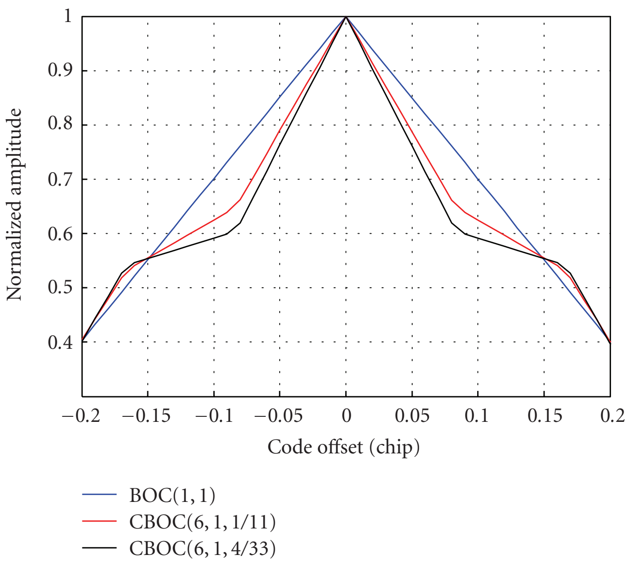

Figure 4: Zoom of the normalized autocorrelation functions comparison among BOC(1,1), CBOC(6,1,1/11), and CBOC(6,1,4/33) computed over an infinite bandwidth.

where the term $R_{\mathrm{BOC}(1,1)\mathrm{BOC}(6,1)}(\tau)$ is the cross-correlation term between the BOC(1,1) and BOC(6,1).

The presence of a cross-correlation factor in (5) results in creating little differences with respect to the MBOC spectrum as defined in (1). Therefore, on-going studies are in place with the goal to define implementation strategies to remove such cross factor. Among the others, the most promising is to alternate BOC(6,1) and BOC(1,1) phases on adjacent code chips (see as an example [11]).

4. ACQUISITION OF THE OPTIMIZED CBOC SIGNAL

The first operation performed by any GNSS receiver is the signal acquisition, in charge to understand which satellites are in the line of sight and to provide the tracking stages with a coarse estimation of the received code delay and a rough estimation of the Doppler frequency shift.

The declaration of the presence or absence of a satellite (determination of both code delay and Doppler shift) is obtained by evaluating a two-dimensional matrix called search space. Each item of such a matrix, that is, cell, corresponds to the value assumed by the bi-dimensional correlation for a specific couple code delay $\hat{\tau}$ and Doppler shift $\hat{f}_d$. This bi-dimensional correlation is also known as cross-ambiguity function.

As shown in [8], several are the solutions that can be found in literature for the signal acquisition: serial search, fast acquisition, and parallel acquisition in frequency domain, but they just differ in the way the search space is obtained and equivalent in terms of detection performance. Other acquisition techniques known with the name of differential acquisition strategies are nowadays used in GNSS fields [12], but since the mathematical details are different from the previous mentioned methodologies, they will not be considered in this paper.

Any acquisition technique can be characterized for a given C/N_0 by the false alarm and detection probabilities. Here, just the false alarm and detection cell probabilities will be considered, since as discussed in [13] the characteristics of the acquisition engine can always be related to these fundamental values.

Such probability functions are usually evaluated considering only the peak amplitude of the correlation function and the presence of noise. Such characterization does not take into account the fact that, for a given Doppler shift and code phase error, the correlation generally does not achieve the maximum possible value. This effect can be modeled as a correlation loss which depends on the shape of the cross ambiguity function and on its representation in terms of resolution (i.e., Doppler shift and code delay steps) in the search space [8].

In order to take into account also this effect in the comparison of BOC(1,1) and CBOC(6,1,γ/ρ) functions, the behavior around the peak in the search space has to be studied.

Once decided the acquisition threshold V_t, the cell false alarm probability can be easily evaluated as the integral of the tail of the distribution of the search matrix in a misalignment condition (or equivalently when the signal is absent). In formula is (see [14])

$$P_{fa}(V_t) = \int_{V_t}^{+\infty} f_{na}^{K}(x)dx. \tag{6}$$

The distribution of $f_{na}^{K}(r)$ can be shown to assume the expression [8]:

$$f_{na}^{K}(r) = \frac{1}{2^K(K-1)!\sigma^{2K}} r^{K-1} e^{-r/2\sigma^2} u(r), \tag{7}$$

where, when the local code spreading sequence has unitary power, and the signal is digitized respecting the Nyquist criterion, σ^2 is equal to $(N/2)\sigma_n^2$. N is the number of samples coherently integrated, and σ_n^2 is the variance of the Gaussian noise affecting the received signal.

Equation (7) holds for the case of noncoherent integration process applied to a serial or parallel acquisition technique. With this technique, the detection and decision can be taken over the summation of K correlation outputs before the envelope operation so to reduce the noise impact and to increase the acquisition detection rate [8].

The probability density function of the correlator output depends on two variables: the code displacement error $\Delta\tau = \tau - \hat{\tau}$ and the Doppler shift error $\Delta f_d = f_d - \hat{f}_d$, respectively. The conditional probability density function to the hypothesis of a perfect code and Doppler alignment $(\Delta\tau = 0, \Delta\tau = 0)$ is demonstrated in [8] to assume the expression:

$$f_a^K(r \mid \Delta\tau, \Delta f_d = 0) = \frac{\sqrt{K}\alpha}{\sigma^2}\left(\frac{r}{\sqrt{K}\alpha}\right)^K e^{-(1/2)((r^2+K\alpha^2)/\sigma^2)} I_{K-1}\left(r\frac{\sqrt{K}\alpha}{\sigma^2}\right), \tag{8}$$

where $\alpha = \sqrt{C}N/2$ is a term proportional to the received signal power C. The corresponding conditional detection probability is then the integral over the tail of $f_a^K(r \mid \Delta\tau, \Delta f_d = 0)$ (see [8, 15]), which leads to the expression:

$$P_{d|\Delta\tau,\Delta f_d=0}(V_t) = \int_{\sqrt{V_t}/\sigma}^{+\infty} f_a^K(x)dx = Q_K\left(\frac{\alpha}{\sigma}, \frac{\sqrt{V_t}}{\sigma}\right). \quad (9)$$

Equation (9) involves the kth-order Marcum Q function, Q_K discussed and defined in [15]. It is remarked how (9) does not still consider the shape of the correlation function of the signal being acquired.

This correlation function can be locally approximated around the peak as the product of the mono-dimensional correlations along the code delay and Doppler axes [7, 8], that is

$$R(\tau, \hat{\tau}, f_d, \hat{f}_d) \approx R_{\text{Doppler}}(f_d - \hat{f}_d) R_{\text{Code}}(\tau - \hat{\tau}). \quad (10)$$

It is evident that in real applications, where a residual error remains in the estimation of the code phase and Doppler shift, the acquisition does not work using the maximum possible correlation value. This situation can be modeled as additional losses or as an impairment, which depends both on the shape of $R_{\text{Code}}(\Delta\tau)$ and $R_{\text{Doppler}}(\Delta f)$.

The approximation reported in (10) is extremely important because it makes possible to separate the effects of the code errors to the one coming from Doppler shift, so to consider the total loss simply as the product of two single impairments.

As far as the code error loss is concerned, the reduction of the correlation output can be accounted in a dB amplitude scale as [8]

$$\alpha_{\text{loss}}\big|_{\text{dB}} = 20 \log \left| R_{\text{Code}}(\Delta\tau) \right|. \quad (11)$$

A plot of the code correlation losses for the CBOC(6,1,1/11), CBOC(6,1,4/33), and the BOC(1,1) is depicted in Figure 5.

Similarly to the code correlation loss, the residual Doppler phase error in the acquisition process produces a reduction of the correlation peak that is demonstrated, again in [8], to be equal to

$$\begin{aligned}\beta_{\text{loss}}\big|_{\text{dB}} &= 20 \log_{10} \left| R_{\text{Doppler}}(\Delta f) \right| \\ &\cong 20 \log_{10} \left| D_N[\pi(f_d - \hat{f}_d)] \right|.\end{aligned} \quad (12)$$

Being $D_N(x/2) = \sin(xN/2)/N\sin(x/2)$, the Dirichlet kernel function. Remembering that the term N is the number of samples coherently integrated, it is clear how the correlation loss β_{loss} depends on the integration time. Figure 6 reports the trend of the Doppler loss when the integration time goes from $T = 4$ milliseconds up to $T = 12$ millisecondss with 4 milliseconds of step.

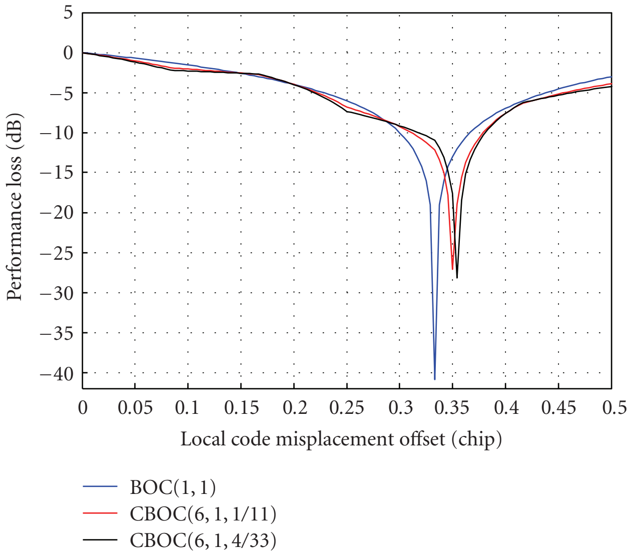

Figure 5: Performance loss as a function of the code offset for the BOC(1,1), CBOC(6,1,1/11), and CBOC(6,1,4/33).

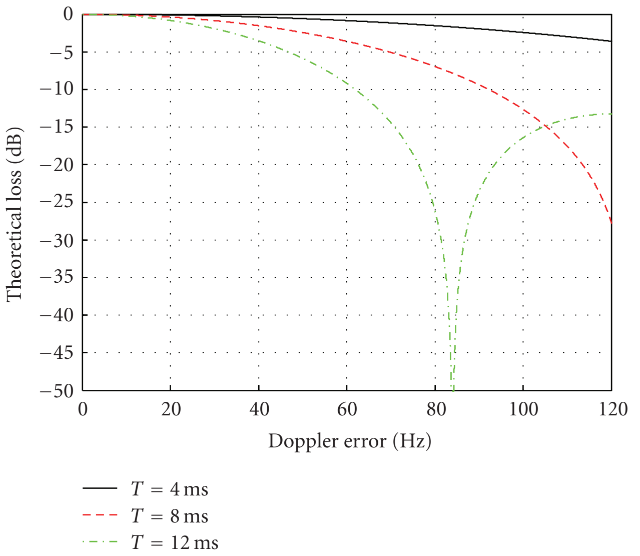

Figure 6: Logarithmic Doppler loss.

It is necessary to model the probability distribution of the code phase offset and Doppler shift in order to add up the different losses inside the conditional detection probability reported in (9). These two realistic hypotheses can be made on the basis of the functioning of the acquisition engine:

(i) the resolution used in the acquisition phase is usually of some integer fraction $\pm 1/L$ of chip, then the maximum absolute phase offset $\Delta\tau = \tau - \hat{\tau}$ can be assumed uniformly distributed between $\pm 1/(2L)$ chip;

(ii) similarly, the Doppler frequency $\Delta f_d = f_d - \hat{f}_d$ can be assumed to be uniformly distributed between zero and half the maximum absolute digital frequency, obtained by normalizing a natural frequency expressed in Hz with respect to the numerical frequency used to express a sequence of sample of a digital signal, bin width $\pm 1/(2M)$, where M is typically less or equal to N.

Furthermore, the Doppler frequency and code phase errors can be considered independent and uncorrelated. With all these assumptions, the combined loss simply becomes the sum (because expressed in dB) of the contributions α_{loss} and β_{loss}. Thus, according to the definition of [6, 8], an expected value of the detection probability, which also accounts for the particular shape of the cross ambiguity function and the impairments due to the residual code phase and Doppler errors, can be derived from the conditional detection probability defined in (9) integrating over the two assumed distribution for $\Delta\tau$ and Δf_d:

$$P_d = 2N\int_{-1/2L}^{1/2L}\int_{-1/2M}^{1/2M} Q_k\left(\frac{\sqrt{k}\alpha}{\sigma}R(f,\theta), \frac{\sqrt{V_t}}{\sigma}\right) df\, d\theta, \qquad (13)$$

with $R(f,\theta) = D_N(\pi f)R_{\text{Code}}(\theta)$.

Therefore, since different modulations have different $R_{\text{Code}}(\theta)$, clearly different detection rate must be expected considering what derived in (13).

The expected value of the detection rate P_d averages among all the possible code phase and Doppler offset; the acquisition can deal with, and it can be seen as an averaged probability even though in the following it will be referred to this quantity as a normal probability.

5. DETECTION PERFORMANCE OF THE CBOC MODULATION CANDIDATES

The CBOC candidates and BOC(1,1) modulations have been compared considering the impairments addressed in Section 4. Both false alarm and detection probabilities have been obtained by means of Monte Carlo simulations.

A classical acquisition technique not tailored for the new modulation has been considered, and the false alarm probability as well as the detection rate has been determined considering an integration period of 4 milliseconds (one Galileo primary code duration). All the simulated signals (BOC(1,1) and CBOCs) have been sampled at 12 MSamples/s considering the front end operating under the Nyquist criterion (i.e., 12 MHz two- sided bandwidth).

A common way to express the detection performance of an acquisition engine is by means of the so-called receiver operative characteristics (ROC) curves, where the detection probability is reported versus the false alarm probability at a specific signal to noise ratio. During this performance analysis, a C/N_0 of 40 dB·Hz has been considered to obtain all the ROC curves, where C/N_0 here refers to the single channel (pilot or data component) carrier to noise ratio.

In Figure 7, a comparison among the BOC(1,1) modulation and two different CBOC implementations is depicted. The ROC curves for the three modulations are reported changing by simulation to simulation and by the code search resolution starting from a value of half a chip down to an eighth of chip.

It is evident from this comparison that when the code search step is reduced, higher detection rates can be achieved for the same false alarm probabilities with all the modulations. These trends can be explained remembering that the larger is the code phase error $\Delta\tau$, the larger is the correlation loss averaged in (13), and then the lower is the detection rate.

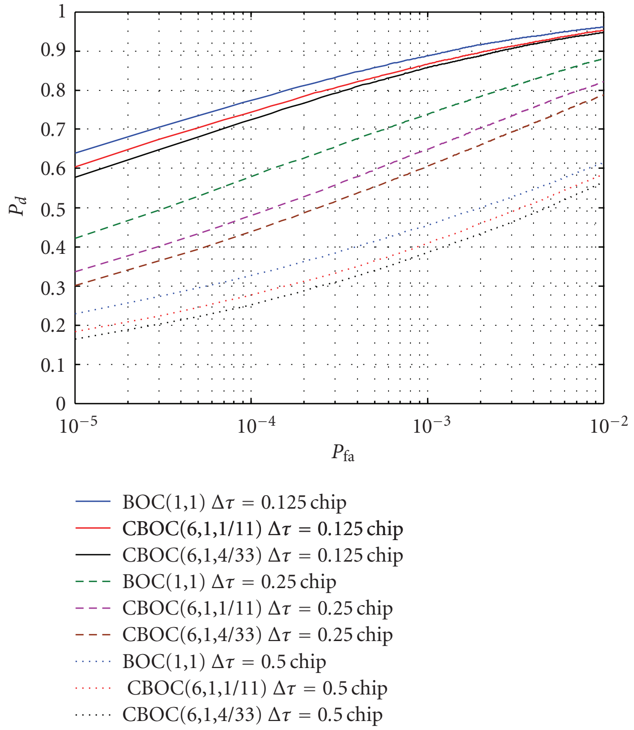

Figure 7: Receiver operative characteristic comparison among different CBOC implementations and BOC(1,1) for different search space spacing at C/N_0 of 40 dB·Hz.

The sharper correlation functions of the CBOC implementations lead to a more relevant code loss contribution with respect to the BOC(1,1). However, as demonstrated in Figure 7, the degradation which stems from the different code loss among BOC(1,1) and CBOCs can be reduced decreasing the code phase step, anyway often necessary to guarantee the pull-in phase of the tracking stages.

Another possibility to address the detection acquisition performance is given by graphs which depict the detection probability for a given false alarm probability versus the C/N_0, as done in the comparison of Figure 8.

Here, the BOC(1,1) and CBOCs modulations are compared considering a fixed false alarm probability of 10^{-4} varying the C/N_0 from a minimum of 30 up to 55 dB·Hz.

In this operative scenario, the C/N_0 necessary to acquire the CBOCs with a detection probability of 0.9 is reported in Table 2 as well as the degradation with respect to the case of using a BOC(1,1) modulation.

Considering that since MBOC has better self spectral separation coefficients (SSCs) than BOC(1,1), the intrasystem interference coming from satellites transmitting MBOC with a different PRN will be reduced.

In addition, the SSC between the MBOC and the C/A code is also lower and thus in summary the intersystem and intrasystem interference is also reduced [16]. Then, the equivalent noise due to interference from other satellites is around 0.1–0.2 dB lower for MBOC than for BOC(1,1), and

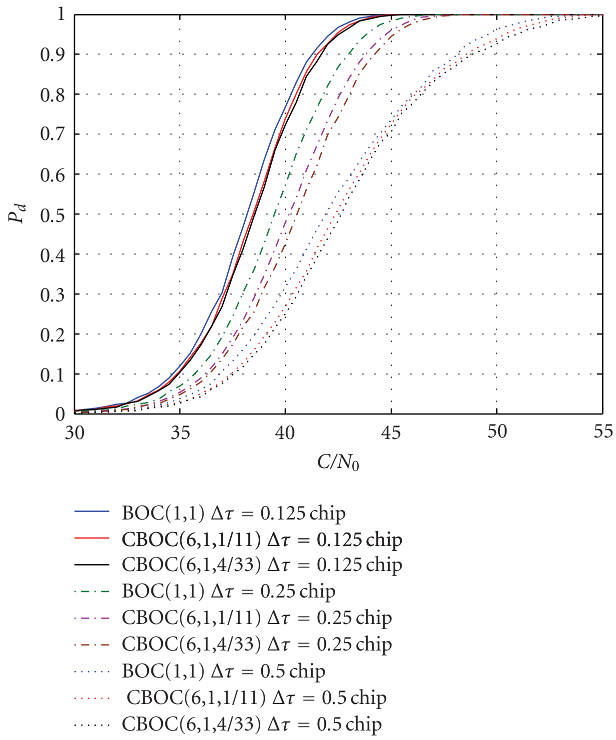

FIGURE 8: Detection probability versus the C/N_0 at a false alarm probability of 10^{-4}. Comparison among different CBOC implementation for different search space resolution.

TABLE 2: Carrier to noise ratio degradation. Comparison for CBOCs and BOC(1,1) modulations.

Modulation	Resolution [chip]	C/No @ Pd = 0.9 [dB-Hz]	Degradation w.r.t BOC(1,1) [dB-Hz]
BOC(1,1)	0.125	41.25	—
CBOC(6,1,1/11)	0.125	41.50	0.25
CBOC(6,1,4/33)	0.125	41.69	0.44
BOC(1,1)	0.25	42.95	—
CBOC(6,1,1/11)	0.25	43.78	0.83
CBOC(6,1,4/33)	0.25	44.21	1.26
BOC(1,1)	0.5	48.10	—
CBOC(6,1,1/11)	0.5	48.55	0.45
CBOC(6,1,4/33)	0.5	48.80	0.7

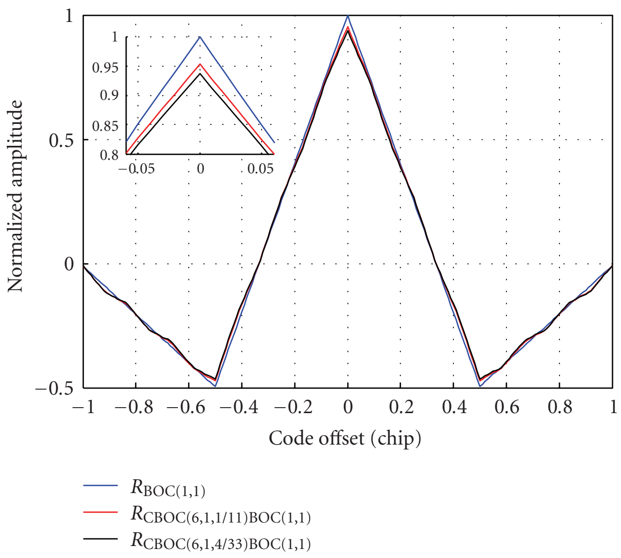

FIGURE 9: BOC(1,1) and CBOC cross-correlation functions comparison computed over an infinite bandwidth and zoom of correlation peaks.

the equivalent C/N_0 is expected to be 0.1–0.2 dB-Hz better [16].

In addition, the interplex modulation product with MBOC is around 4 dB lower with CBOC than with BOC(1,1) and thus the net effect is that at the end, for the same transmitted power from the satellite, at the ground there is an increase of the received power of approximately another half a dB.

Therefore, the degradation of the sharper correlation function is mostly compensated in all the cases by the increased power at the ground and by better SSC, and in some cases it should actually outperform the BOC(1,1) at least when code search step is reduced to less or equal to one quarter of chip.

It has not to be forgotten that one of the aim of the CBOC modulations is to maintain the interoperability and the compatibility with the existing systems. In fact, the contribution of the BOC(1,1) in the CBOC definition, (cfr. (3) and (4)), still assures a nonzero cross-correlation function among CBOCs and BOC(1,1).

Figure 9 reports the correlation functions obtained demodulating a CBOC signal with a local BOC(1,1) code.

This might be the working scenario of a BOC(1,1) legacy receiver processing the new optimized MBOC signal.

The cross-correlation functions $R_{\text{CBOC}(6,1,1/11)\text{BOC}(1,1)}$ and $R_{\text{CBOC}(6,1,4/33)\text{BOC}(1,1)}$ depicted in Figure 9 are practically identical.

They are mainly characterized by a reduction of the peak maximum due to the cross loss given by the BOC(6,1) term, but the correlation slope and widths are comparable one to the other.

This is the case of the ROC curves reported in Figure 10 where the detection performance of the CBOC(6,1,1/11) demodulated by a BOC(1,1) replica is reported together with the performance of the standalone BOC(1,1) and CBOC(6,1,1/11).

The comparison is made considering only a code delay step of 0.25 and 0.125 chip. The detection probability versus the C/N_0 for a false alarm probability of 10^{-4} is reported in Figure 11.

It is interesting to notice how, when the search space has a resolution of 0.25 chip for the code phase, higher detection probabilities can be obtained by demodulating the CBOC(6,1,1/11) with a local BOC(1,1) implementation. When the code step used in the search space is

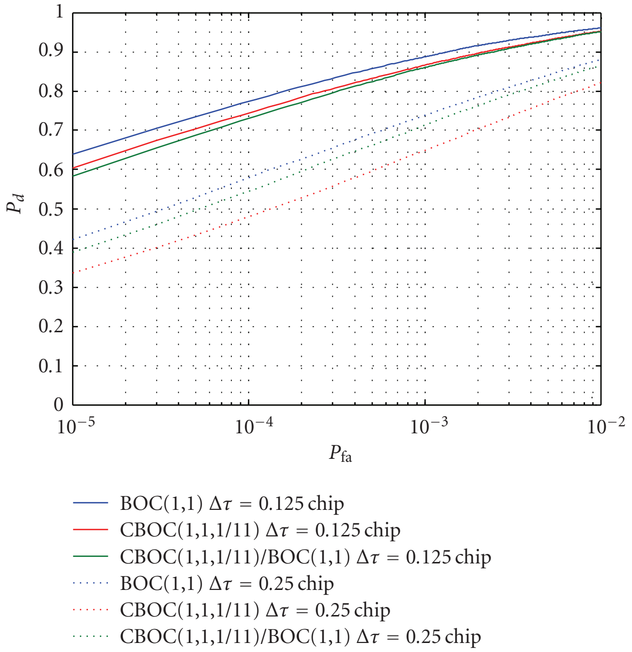

FIGURE 10: Receiver operative characteristic comparison, at C/N_0 of 40 dB·Hz and different spacing, among the standalone BOC(1,1), CBOC(6,1,1/11), and the CBOC(6,1,1/11) demodulated with a BOC(1,1) replica.

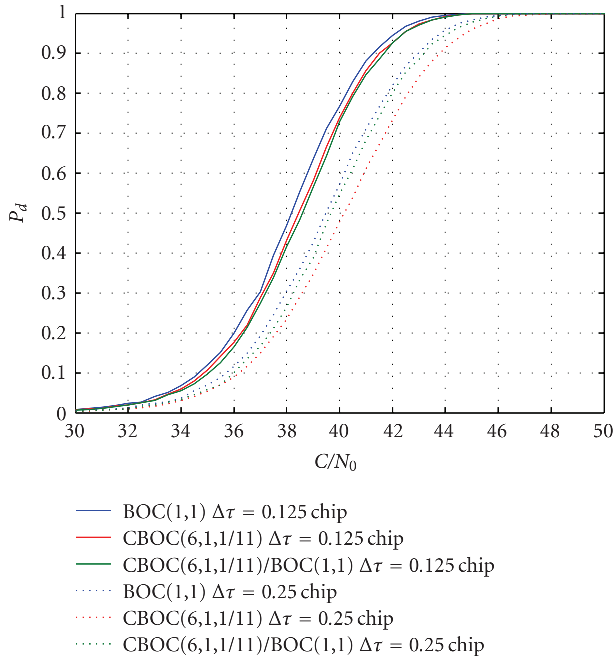

FIGURE 11: Detection probability versus the C/N_0 at a false alarm probability of 10^{-4} comparison among standalone BOC(1,1), CBOC(6,1,1/11), and the CBOC(6,1,1/11) demodulated with a BOC(1,1) replica.

reduced to 0.125 chip, then the solution to demodulate the CBOC(6,1,1/11) with a local BOC(1,1) does not outperform the pure CBOC(6,1,1/11) solution.

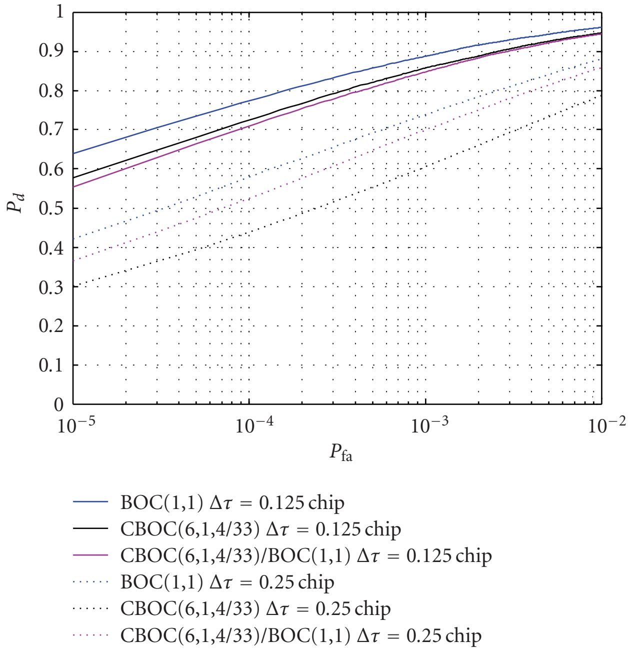

FIGURE 12: Receiver operative characteristic comparison, at C/N_0 of 40 dB·Hz and different spacing, among the standalone BOC(1,1), CBOC(6,1,4/33), and the CBOC(6,1,4/33) demodulated with a BOC(1,1) replica.

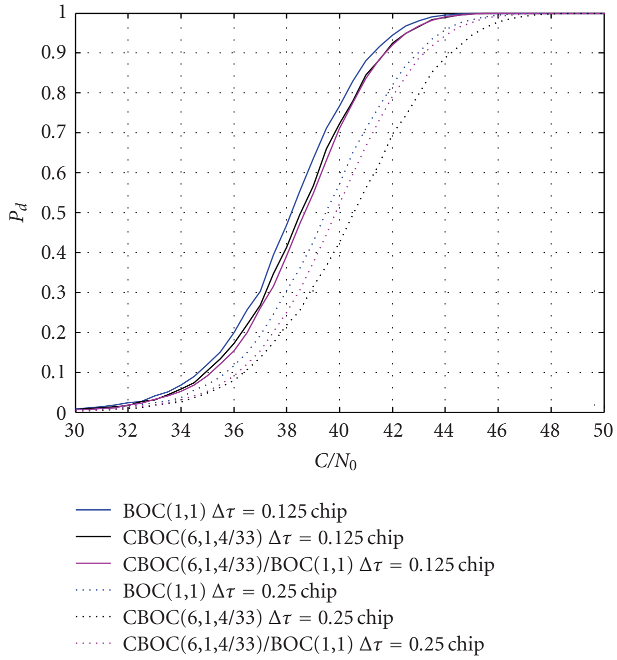

FIGURE 13: Detection probability versus the C/N_0 at a false alarm probability of 10^{-4} comparison among standalone BOC(1,1), CBOC(6,1,4/33), and the CBOC(6,1,4/33) demodulated with a BOC(1,1) replica.

Similar considerations can be made for the comparison of the CBOC(6,1,4/33) detection performance which have been reported in Figures 12 and 13.

When $\Delta\tau$ is reduced, then the maximum peak reduction of $R_{\text{CBOC}(6,1,1/11)\text{BOC}(1,1)}$ and $R_{\text{CBOC}(6,1,4/33)\text{BOC}(1,1)}$ plays a more significant role in the total averaged loss explaining the change of performance outlined in the previous comments.

6. CONCLUSIONS

On the basis of the modernization activities around the future Galileo E1 signals, this paper focuses on the analysis of the acquisition detection performance of two CBOC solutions, which are the CBOC(6,1,1/11) and CBOC(6,1,4/33).

Such activity, done with an acquisition engine implemented via software, is a key step for signals comparison considering that the CBOC modulation due to its sharper correlation function might present some acquisition losses with respect to the BOC(1,1). Through simulations, it has been proved that, in practical operative conditions and thanks to the better SSC derived by using an MBOC spectrum and thanks to the increased power level of the signal at the ground (which results in about 0.7 dB·Hz of improvement in the equivalent C/N_0 seen by the receivers antennas), those losses can be neglected.

Moreover, this work also shows how the CBOC candidate modulations still assure the compatibility and interoperability with BOC(1,1) legacy receivers in terms of acquisition.

All these considerations together with the major advantages in terms of better tracking performance and multipath rejections capabilities clearly justify the selections of the CBOC as implementation of the agreed MBOC.

REFERENCES

[1] United States-European Commission Agreement on the Promotion, "Provision and Use of Galileo and GPS Satellite-Based Navigation Systems and Related Application," http://pnt.gov//public/docs/2004-US-EC-agreement.pdf.

[2] "Joint Statement on Galileo and GPS Signal Optimization By the European Commission (EC) and the United States (US)," Bruxelles March 2006, http://useu.usmission.gov/Dossiers/Galileo_GPS/Mar2406_Joint_Statement.pdf.

[3] "United States and the European Union announce final design for GPS-Galileo common civil signal," http://europa.eu/rapid/pressReleasesAction.do?reference=IP/07/1180&format=HTML&aged=0&language=EN&guiLanguage=fr.

[4] G. W. Hein, J. A. Avila-Rodriguez, L. Ries, et al., "A candidate for the Galileo L1OS optimized signal," in *Proceedings of the Institute of Navigation (ION '05)*, Long Beach, Calif, USA, September 2005.

[5] G. W. Hein, J. A. Avila-Rodriguez, S. Wallner, et al., "MBOC: the new optimized spreading modulation recommended for GALILEO L1 OS and GPS L1C," in *Proceedings of the IEEE/ION Position, Location, and Navigation Symposium (PLANS '06)*, pp. 883–892, San Diego, Calif, USA, April 2006.

[6] D. Borio, M. Fantino, L. Lo Presti, and L. Camoriano, "Acquisition analysis for Galileo BOC modulated signals: theory and simulation," in *Proceedings of the European Navigation Conference (ENC '06)*, Manchester, UK, May 2006.

[7] H. Mathis, P. Flammant, and A. Thiel, "An analytic way to optimize the detector of a post-correlation FFT acquisition algorithm," in *Proceedings of the International Technical Meeting of the Satellite Division of the Institute of Navigation (ION GPS/GNSS '03)*, pp. 689–699, Portland, Ore, USA, September 2003.

[8] M. Fantino, "Study of architectures and algorithms for software Galileo receivers," Ph.D. dissertation, Electronic Department, Politecnico di Torino, Torino, Italy, May 2006.

[9] GPS-Galileo Working Group A MBOC Recommendations, "Recommendations on L1 OS/L1C Optimization," March 2006, http://www.galileoju.com/page3.cfm.

[10] J. W. Betz, "Design and performance of code tracking for the GPS M code signal," in *Proceedings of the 13th International Technical Meeting of the Satellite Division of the Institute of Navigation (ION GPS '00)*, Salt Lake City, Utah, USA, September 2000.

[11] J. A. Avila-Rodriguez, S. Wallner, G. W. Hein, et al., "CBOC—an implementation of MBOC," in *Proceedings of the 1st CNES Workshop on Galileo Signals and Signal Processing*, Tolouse, France, October 2006.

[12] S. K. Shanmugam, R. Watson, J. Nielsen, and G. Lachapelle, "Differential signal processing schemes for enhanced GPS acquisition," in *Proceedings of the 18th International Technical Meeting of the Satellite Division of the Institute of Navigation (ION GNSS '05)*, pp. 212–222, Long Beach, Calif, USA, September 2005.

[13] D. Borio, L. Camoriano, and L. Lo Presti, "Impact of the acquisition searching strategy on the detection and false alarm probabilities in a CDMA receiver," in *Proceedings of the IEEE/ION Position, Location, and Navigation Symposium (PLANS '06)*, pp. 1100–1107, San Diego, Calif, USA, April 2006.

[14] E. D. Kaplan and C. Hegarty, *Understanding GPS: Principles and Applications*, Mobile Communications Series, Artech House, Boston, Mass, USA, 2nd edition, 2006.

[15] J. I. Marcum, "A statistical theory of target detection by pulsed radar," *IEEE Transaction on Information Theory*, vol. 6, no. 2, pp. 59–267, 1947.

[16] S. Wallner, G. W. Hein, and J. A. Avila-Rodriguez, "Interference computations between several GNSS systems," in *Proceedings of the ESA Workshop on Satellite Navigation User Equipment Technologies (NAVITEC '06)*, Noordwijk, The Netherlands, December 2006.